

The characteristics and morphodynamics of sedimentary structure in  
gravel-bed rivers: implications for sediment entrainment

---

Thesis submitted for the degree of  
Doctor of Philosophy  
at the University of Leicester

by

David Mark Roger Ackerley  
Department of Geography  
University of Leicester

2018

## **Abstract**

The characteristics and morphodynamics of sedimentary structure in gravel-bed rivers: implications for sediment entrainment

By David M.R. Ackerley

While Earth Scientists acknowledge that bed structure influences flow resistance and sediment transport, relatively little is known about the structural properties of water-worked gravel beds and how bed structure influences particle stability. To address this concern, this research first explored the structural characteristics of 11 representative patches from nine gravel bars from six humid temperate and two dryland rivers. Streambed microtopography was analysed using a suite of statistical metrics, including bed elevation moments, variograms and local inclination, slope and aspect. To investigate how bed structure influences bed stability, for two humid temperate and three dryland patches, measurements of force balance parameters (pivoting angle, projection and exposure) were used to estimate sediment entrainment thresholds. Finally, the temporal dynamics of bed structure was examined through repeat surveys of two humid temperate patches over a 28-month period. These patches were divided into three sections to investigate the natural temporal variability of bed structure and the effects of shorter and longer periods of flow in reworking an unstructured surface. The humid temperate patches were characterised by a water-worked grain- and bedform-scale structure which, while variable, was comparable to previous observations (e.g. near-normal bed elevation pdfs; grain size dependent  $\sigma_z$ ). The dryland patches were, for the bed elevation pdfs, statistical moment  $Ku_z^*$  and variograms, structurally distinct from their humid temperate counterparts. Differences in bed structure between the humid temperate and dryland patches influenced grain pivoting angle and protrusion and, hence, particle stability. For the humid temperate patches, streambed structure was largely maintained over a range of competent flows. Following surface treatment, larger adjustments in bed structure occurred during initial water-working: subsequent changes were comparatively modest. However, since changes in bed structure were subtle, it was difficult to determine whether a natural bed structure had fully formed during the initial period of restructuring.

## Acknowledgements

It should come as no surprise that after a fair few years spent completing this work I am hugely indebted to a whole host of people for their various efforts in supporting me, for which I would like to express my heartfelt thanks.

I would like to start by acknowledging the help and guidance offered by my supervisors, Dr. Mark Powell and Dr. Andy Carr, throughout my PhD research, which was partially supported by a departmental PGR Research Training and Support fund. I have been particularly fortunate to have had a principal supervisor in Mark not only for his academic and financial support for this and previous studies over the past decade but also for his seemingly endless patience (which, I'm sure, I've sorely tested) and pure, infectious love of geomorphology that drew me to Leicester those many years ago as an undergraduate. Thank you, Mark.

I would like to extend my thanks to the technical and administrative team, to Bill Hickin, Gemma Black, Gary Hancox, Adam Cox, Simon Benson and Charlotte Langely, particularly for their understanding of the last-minute nature of my field work. Thanks also to Dr. Thao Nguyen, Dr. John Hillier and Dr. Rebecca Hodge for their computing wizardry and for supplying many of the scripts used to process, inspect and analyse the digital surfaces that form the foundations of this work.

Special thanks to Prof. John Laronne and Dr. Yael Storz-Peretz for enabling the research conducted in Israel, to all those postgraduate students at Ben-Gurion University who assisted in the field (usually in excessively warm conditions) and to Alex Hay for saving the day and flying over at short notice, TLS in arm. I also greatly appreciate the help given by those to my UK-based field studies - to Alex Cumming, Tom Potter, Gemma Ollerenshaw and Ros Nicholls – who, like me, learned to love the Zen art of pebble painting. I would like to, if I may, single out the help of Alex and Tom in assisting much of my field work, often with long drives involved and in sub-zero climes.

Thanks to those friends and departmental colleagues for their encouragement and humour during those most stressful times – in particular to Helena White, Hannah Brooking and to Sandor and Kirsty. I am also extremely thankful for the support of my parents, Roger and Anne, and brother, Ian.

Lastly, and by certainly no means least, I would like to express my most sincere thanks to my wife, Emma, for her unwavering love and support, which I am truly humbled by and eternally grateful for.

# Table of Contents

Abstract.....	i
Acknowledgements.....	ii
Table of Contents.....	iii
List of Tables.....	vii
List of Figures.....	viii
Chapter 1 Introduction.....	1
1.1. Research Hypotheses.....	4
Chapter 2 Streambed structure and its influence on boundary roughness and particle stability.....	5
2.1. Characterising boundary roughness and particle stability in terms of grain size.....	5
2.1.1. Bed texture and grain size adjustments.....	9
2.2. Influence of bed structure on boundary roughness and particle stability and implications for flow resistance and bed stability.....	11
2.2.1. Grain-scale bed structure.....	11
2.2.2. Bedform-scale bed structure.....	13
2.2.3. Influence of bed structure on flow resistance.....	15
2.2.4. Influence of bed structure on particle stability.....	17
2.3. Characterising bed structure and stability.....	20
2.3.1. Bed elevation pdfs and statistical moments ( $\sigma_z$ , $Sk_z$ and $Ku_z^*$ ).....	21
2.3.2. Variogram analysis: 1D and 2D approaches.....	25
2.3.3. Local metrics of streambed topography: inclination, slope and aspect.....	32
2.3.4. Parameters of particle stability: grain pivoting angle.....	35
2.3.5. Parameters of particle stability: grain protrusion.....	40
2.4. Temporal evolution of bed structure.....	42
2.5. Summary and research objectives.....	43
Chapter 3 Methods.....	47
3.1. Field sites.....	47
3.1.1. The River Ashop, UK: A <sub>1</sub> , A <sub>2</sub> .....	49
3.1.2. The Afon Elan, UK: E <sub>1.1</sub> , E <sub>1.2</sub> .....	50
3.1.3. The River Manifold, UK: M <sub>1</sub> , M <sub>2</sub> .....	52
3.1.4. The River Wharfe, UK: W <sub>1.1</sub> , W <sub>1.2</sub> .....	54
3.1.5. The Nahal Hever, Israel: H <sub>1</sub> , H <sub>2</sub> .....	57

3.1.6.	The Nahal Shafan, Israel: $S_1$ .....	58
3.2.	Surface grain size, sorting and shape .....	59
3.2.1.	Wolman count.....	59
3.2.2.	Digital gravelometry .....	61
3.3.	Bed microtopography.....	63
3.3.1.	Terrestrial laser scanning (TLS) .....	63
3.3.2.	Survey methodology .....	66
3.4.	Data processing .....	69
3.4.1.	$E$ -parameter.....	72
3.4.2.	Repeat Scan Error Value (RSEV) filter .....	73
3.4.3.	Statistical Outlier Removal (SOR) filter.....	77
3.4.4.	Cone filter .....	80
3.4.5.	High Point filter .....	84
3.4.6.	DTM generation.....	87
3.4.7.	DTM validation.....	87
3.4.8.	DTM detrending and surface measurements .....	89
3.5.	Characterising bed structure.....	89
3.5.1.	Bed elevation probability density functions (pdfs) and statistical moments ..	90
3.5.2.	1-D and 2-D variograms .....	90
3.5.3.	Inclination Index .....	92
3.5.4.	Slope and Aspect .....	93
3.6.	Bed stability parameters .....	94
3.6.1.	Pivoting angle .....	95
3.6.2.	Projection and exposure.....	96
3.6.3.	Grain entrainment model .....	97
Chapter 4	The characteristics of streambed structure in coarse-grained alluvial channels and their control on particle stability .....	99
4.1.	Introduction .....	99
4.2.	Bed material size, sorting and shape .....	99
4.3.	Digital elevation models .....	103
4.4.	Bed elevation probability density functions (pdfs) and statistical moments: standard deviation ( $\sigma_z$ ), skewness ( $Sk_z$ ) and kurtosis ( $Ku_z^*$ ).....	107
4.5.	2D variograms .....	111

4.6.	1D variograms.....	116
4.6.1.	1D variogram model assessment .....	116
4.6.2.	1D variogram characterisation.....	117
4.7.	Inclination Index .....	120
4.8.	Slope and Aspect.....	121
4.9.	Pivoting angle ( $\Phi$ ).....	126
4.10.	Grain protrusion: projection ( $p$ ) and exposure ( $e$ ).....	128
4.11.	Critical shear stress and dimensionless critical shear stress ( $\tau_c$ and $\tau_c^*$ ).....	130
4.12.	Discussion .....	132
4.12.1.	Structural characteristics of coarse-grained alluvial channels .....	132
4.12.2.	The influence of structure on bed stability.....	140
4.12.3.	Summary .....	144
Chapter 5 The temporal dynamics of sedimentary structure in coarse-grained alluvial river beds.....		149
5.1.	Introduction.....	149
5.2.	Temporal variability of streambed structure.....	152
5.2.1.	Grain size adjustments.....	152
5.2.2.	DTMs.....	153
5.2.3.	Bed elevation pdfs and their moments.....	158
5.2.4.	Variogram analyses.....	161
5.2.5.	Inclination index, local slope and aspect .....	162
5.3.	Temporal aspects of stream bed restructuring .....	167
5.3.1.	Effects of experimental surface treatments on bed structure.....	169
5.3.2.	Re(development) of streambed structure from an unstructured bed state ....	172
5.4.	Discussion .....	178
5.4.1.	Temporal variability of streambed structure.....	178
5.4.2.	Evaluating the (re)development of structure from a treated condition .....	181
5.4.3.	Summary .....	184
Chapter 6 Conclusion.....		185
6.1.	Further work.....	189
References.....		191
Appendix B: Flow-parallel and flow-transverse 1D variogram model assessment for the remaining humid temperate and dryland gravel patches. ....		213

Appendix C: Grain entrainment model preliminary analysis .....219

## List of Tables

Table 2.1 Summary of the coefficients in Equation 2.17 for tilting board (*) and force gauge measurements (**). Unworked and water-worked beds highlighted in white and grey respectively. ....	37
Table 3.1 Summary of catchment characteristics for the perennial rivers, where PROPWET is the catchment wetness index (PROPortion of time soils are WET), DPSBAR is an index of overall catchment steepness (mean Drainage Path Slope) and BFIHOST is a base flow index, a measure of the catchment responsiveness. Flow and local catchment information unavailable for the ephemeral rivers. ....	48
Table 3.2 The description of grain size sorting using the Logarithmic Folk and Ward (1957) Graphical Measure. ....	60
Table 3.3 Summary of selected work using TLS to map coarse-grained alluvial streambed topography. ....	64
Table 3.4 Overview of the TLS sensor used for each of the topographic surveys. ....	65
Table 4.1 Surface grain size statistics for the humid temperate perennial (blue) and dryland ephemeral (red) gravel patches. Note: only one representative grain size sample was collected from the Elan and Wharfe field sites. $D_n$ refers to the $n$ th percentile of the surface grain size distribution and $\sigma_G$ is the geometric Folk and Ward (1957) sorting coefficient. $D_{max}$ is the maximum grain size and is estimated as the geometric mean of the bounding sieve sizes containing the largest grain. ....	100
Table 4.2 Summary of bed elevation pdf moments for the measured surfaces. Humid temperate and dryland patches are highlighted in blue and red respectively. ....	108
Table 4.3 Summary of the power law coefficients recorded by previous workers from natural gravel streambeds. High $R^2$ values recorded by Buffington et al. (1992) and Johnston et al. (1998) reflect the choice of sampling placed or ‘available’ grains rather than the grid-based (random) approach employed in this study and by Hodge et al. (2013). ....	142
Table 4.4 Summary of the sedimentological and structural characteristics for the humid temperate and dryland patches. ....	147
Table 4.5 Summary of the bed stability parameters for regime-aggregated data from the humid temperate and dryland patches. Error ranges represent 95% confidence intervals. ....	148
Table 5.1 Hydrograph statistics for the 28-month survey period from November 2012 to April 2015. Flow information supplied by the Environment Agency gauge station site at Netherside Hall (ID: 8276) where bankfull ( $= 130 \text{ m}^3 \text{ s}^{-1}$ ), moderate ( $100 - 130 \text{ m}^3 \text{ s}^{-1}$ ) and low, shoaling flows ( $< 100 \text{ m}^3 \text{ s}^{-1}$ ) are highlighted in red, orange and yellow respectively. Surveys S1 – S8 and S9 – S13 conducted using the HDS 3000/SS2 and P20 sensors respectively. ....	150
Table 5.2 The bed elevation statistical moments $\sigma_z$ , $Sk_z$ and $Ku_z^*$ for the $W_{1.1}$ and $W_{1.2}$ patches over the monitoring period. ....	159
Table 5.3 Summary statistics describing the effects of treatment and the evolution of streambed texture and structure. Data are median values of textural and structural parameters calculated for the pre-treated (T-1), treated (T0), initial restructuring (T1) and subsequent development (T2-T $n$ ) surfaces. ....	169
Table A.1 Specifications for the Leica HDS 3000, ScanStation 2 and ScanStation P20 TLS sensors. ....	212

## List of Figures

Figure 2.1 Illustration of an a) armoured and b) unarmoured gravel bed. Adapted from Powell (1998).....	10
Figure 2.2 Illustrative schematic of three noncohesive bed conditions generated from the same grain size distribution but with differences in grain-scale bed structure (packing geometry). In a) and c) lines denote contact tangents between neighbouring grains. Diagram taken from Church (1978: 758). ....	12
Figure 2.3 Cross sectional view of a pebble cluster. Diagram adapted from Powell (1998). ....	14
Figure 2.4 Relationship between friction factor and boundary roughness geometry. The solid line marks the relationship of Rouse (1965) and the grey oval the envelope of values observed by Gomez (1993) for different shape gravel-sized sediments. Diagram adapted from Powell (2014).....	16
Figure 2.5 Critical shear stress vs. particle diameter for river and canal data (scatter of values approximated by grey bounding area). Values shown in relation to Shields criterion ( $\tau_c = f(D)$ , $f(0.4.D)$ , $f(2.D)$ ) and conceptual underloose and overloose boundaries. Diagram adapted from Church (1978).....	17
Figure 2.6 The force balance of an individual grain relative to the logarithmic velocity profile ( $u(z)$ ) above the local mean bed level ( $z$ ). After Kirchner et al. (1990).....	18
Figure 2.6 Illustration of particle mobility as a function of pivoting angle ( $\Phi$ ), projection ( $p$ ) and exposure ( $e$ ) relative to the local bed level. Size of sample grain and local bed in $D$ and $K$ respectively. After Kirchner et al. (1990). ....	19
Figure 2.7 Schematic bed elevation pdfs illustrating changes in skewness (solid lines) and kurtosis (dashed lines) relative to a normal distribution (dotted line). Adapted from Coleman et al. (2011).....	22
Figure 2.8 Change in bed elevation pdf form over time with a constant flow (Powell et al., 2016: 1502).....	23
Figure 2.9 Bed structure classification by $Sk_z$ and $Ku_z^*$ for a) water-worked and b) unworked beds. The boundaries marked by ‘ $W_{gm}$ ’ and ‘ $S_{gm}$ ’ approximate the structural classification of Coleman et al. (2011).....	24
Figure 2.10 The bifractal variogram model of Robert (1988, 1991) derived from bed profiles with a flow parallel direction. ....	27
Figure 2.11 a) Method of determining the characteristic scale $\Delta x_0$ (identical process for $\Delta y_0$ ) and b) illustration of non-dimensionless structure function. Both adapted from Nikora et al. (1998).....	29
Figure 2.12 Flow parallel 1D variogram for the a) River Feshie and b) Bury Green Brook gravel patches in Hodge et al., (2009b: 2033). In a) and b) a two-section line (black line) provides a poor approximation of the curved variograms (grey dots).....	30
Figure 2.13 Model and real examples (taken from Hodge et al., 2009b: 2032) of 2D variograms exhibiting a-b) isotropic and c-d) anisotropic changes in semivariance.....	31
Figure 2.14 a) 2D variogram for a water-worked flume bed (Powell et al., 2016: 1506) characterised by larger-scale flow-parallel anisotropy reflecting the flow-parallel alignment	

of meso-scale topography, as b) a 2D variogram for the meso-scale surface (following the removal of grain-scale topography) demonstrates. ....	32
Figure 2.15 Cross-sectional illustration of an imbricated layer of surface grains. Inclination index (positive = +, negative = -) shown for grain-scale lag pairs. ....	33
Figure 2.16 Slope distributions for a tightly packed ( <i>BGB E1</i> , solid line) and more loosely arranged bed structure ( <i>BGB R2</i> , dashed line) illustrated for gravel patches in Hodge et al. (2009b). ....	34
Figure 2.17 Polar density plots of grain-scale slope and aspect for simulated grains a) imbricated by 40° and resting parallel to the bed surface with a-axis orientated in a b) flow transverse and c) flow parallel direction. Plots shaded by density (high = black, low = grey) and taken from Hodge et al. (2009b: 2036-2037). ....	35
Figure 2.18 Illustration of the influence of a-b) relative particle size and c) packing arrangement on the stability of individual grains. After Kirchner et al. (1990). ....	38
Figure 2.19 Percentiles of the pivoting angle distribution ( $\Phi_i$ ) as a function of relative grain size ( $D_i/D_{50}$ ). Lines fitted from equation 2.17 to $i = 10, 50$ and $90$ . Adapted from Kirchner et al. (1990). ....	39
Figure 2.20 Friction angle distributions for unworked (dashed lines) and water-worked beds (solid lines). Large, medium and small test grain size diameter = c.1mm, c.4mm and c.6mm respectively. After Kirchner et al. (1990). ....	39
Figure 2.21 Median $\Phi$ values as a function of $D_i/D_{50}$ for the Pacific Creek and Pilgrim Creek reaches of Johnston et al. (1998). ....	40
Figure 2.22 Illustration of the influence of a-b) relative particle size and c) packing arrangement on the projection and exposure of surface grains. After Kirchner et al. (1990). ....	41
Figure 3.1 Regional location and course of the a) perennial and c) ephemeral rivers. ....	48
Figure 3.2 a) River Ashop field site location and b) photograph highlighting patch location with IDs. a) contains OS data © Crown copyright and database right 2017, in b) approximate direction of bank full flow displayed with white arrow. The upper reaches of the Ashop are dominated by a dendritic gully network delimited by wide interfluves (Lindsay and Evans, 2008). Here, the streams are steep, confined and adopt a step-pool morphology (Lee, 1998). At the confluence between the tributaries of Ashop Clough and Lady Clough (53°24'45" N 1°50'16" W; Figure 3.2a) the valley widens and a single thread, meandering channel flows within a 50 - 100 m wide floodplain, confined in several sections by deeply incised and terraced alluvium. The active erosion of upland headwaters and destabilisation of local hillslopes (Heaney, 2013) provides a source of sediment for the aggradation of coarse-grained point bars. Downstream from the site, the flow and sediment regime of the catchment is mediated by the abstraction of water into the Derwent Reservoir by the Ashop weir (Maddock et al., 2001). Although several workers have noted evidence of contemporary catchment erosion, e.g. rotational bank failures (Boon and Evans, 2008), analysis of change using historical maps (EDINA Historic Digimap Service) indicates that the course of the channel has not changed significantly since the 1880s. ....	49

Figure 3.3 a) Afon Elan field site location and b) photograph highlighting patch location with IDs. Key in a) as in Figure 3.2; contains OS data © Crown copyright and database right 2017. ....	51
Figure 3.4 a) River Manifold field site location, b) photographs highlighting patch location with IDs. Key in a) as in Figure 3.2; contains OS data © Crown copyright and database right 2017. ....	53
Figure 3.5 a) River Wharfe field site location, b) photographs highlighting patch location with IDs and schematic illustrations of the $W_{1.1}$ and $W_{1.2}$ sub patches for c) early (July 2013 – February 2014) and d) later surveys (November 2014 – April 2015). Key in a) as in Figure 3.2; contains OS data © Crown copyright and database right 2017. ....	55
Figure 3.6 Field site photographs for the a) $H_1$ and b) $H_2$ gravel patches. Approximate patch location is highlighted by ID labels and bankfull flow direction by the white arrow. ....	58
Figure 3.7 Field site photograph for the $S_1$ gravel patch. Approximate patch location is highlighted by the ID label and bankfull flow direction by the white arrow. ....	59
Figure 3.8 An illustration of the range of potential particle shapes calculated from the ratio between the long:intermediate and intermediate:short axis of grains using the Zingg (1935) classification and Krumbein (1941) sphericity statistic ( $\psi$ ). ....	61
Figure 3.9 Comparison between the manual Wolman count sample and the Sedimetrics digitised estimate for the $W_{1.1}$ natural and treated patches (open and grey-filled symbols respectively). Error bars represent 95% confidence intervals. ....	63
Figure 3.10 Illustration of survey setup in the field. Adapted from Hodge et al. (2009a) ...	68
Figure 3.11 The modular workflow used to collect and process TLS data and generate high-resolution DTMs for statistical analysis. Step [1] was used for the HDS 3000 and ScanStation 2 surveys and [3] for the $W_{1.1}$ and $W_{1.2}$ experimental series. ....	70
Figure 3.12 Stages of processing the $A_1$ (a, c, d, f, h, k) and $H_1$ (b, e, g, i, j) sub-patches using workflows for the HDS 3000/ScanStation 2 and P20 TLS sensors respectively. High-resolution (3mm) DTMs are generated at each stage of the workflow: for the a-b) raw data and after application of the c) RSEV, d-e) SOR, f-g) Cone and h-i) Local high point filters. Two 200 x 200 mm boxes highlight areas of error removed during this process. Lastly j-k) present orthogonal views of the final sub-patch DTMs for $A_1$ and $H_1$ respectively. Adapted from Hodge et al. (2009a). ....	71
Figure 3.13 Distributions of $E$ for the $A_1$ patch after the application of the RSEV filter using a range of threshold values. Boxes show inter-quartile range (IQR), upper and lower whiskers represent (25 <sup>th</sup> percentile) and (75 <sup>th</sup> percentile) respectively and circles the 5 <sup>th</sup> and 95 <sup>th</sup> percentiles. ....	74
Figure 3.14 Digital elevation models generated for a range of RSEV thresholds relative to the original, unfiltered $A_1$ patch. Two 200 x 200 mm boxes highlight areas of error removed using the RSEV filter. ....	76
Figure 3.15 The proportion of data retained across a range of RSEV thresholds for the humid temperate patches. b) Distributions of the $E$ parameter following the application of the 7 mm RSEV threshold to the humid temperate patches. ....	77

Figure 3.16 a-c) Comparison of DTMs for the SOR-filtered $H_1$ patches under various filter scenarios and d) the effects of filtering on the distributions of the $E$ parameter for the dryland patches. ....	79
Figure 3.17 Distributions of the $E$ parameter following the application of the SOR filter ( $6\sigma$ from a neighbourhood of 100 points) to the humid temperate patches. Statistical description of boxplot as in Figure 3.6. ....	80
Figure 3.18 Schematic diagram of the Cone filter, adapted from Hodge et al. (2009a: 959). ....	80
Figure 3.19 Distribution of $E$ for a) the $A_1$ patch across a range of Cone filter parameters and b) following the application of the optimal filter ( $5 \text{ mm } 10^\circ$ ) to all the humid temperate patches. c) The proportion of the unfiltered point cloud retained under each filter scenario for all humid temperate patches. ....	82
Figure 3.20 Distributions of $E$ for a) the $H_1$ patch across a range of Cone filter parameters and b) following the application of the optimal filter ( $2.5 \text{ mm } 5^\circ$ ) to the three dryland patches. c) The proportion of the unfiltered point cloud retained under each filter scenario for the dryland patches. ....	83
Figure 3.21 Schematic diagram of the local high point filter, adapted from Hodge et al. (2009a: 959). ....	84
Figure 3.22 Distributions of $E$ for a) the $A_1$ patch across a range of local high point filter parameters and b) the proportion of the unfiltered point cloud retained under each filter scenario (legend as in Figure 3.16c). The distributions of $E$ are also shown following the application of the optimal filter ( $7 \text{ mm } 15^\circ$ ) to the other humid temperate patches. ....	85
Figure 3.23 Distributions of $E$ for a) the $H_1$ patch across a range of local high point filter parameters and b) the proportion of the unfiltered point cloud retained under each filter scenario (legend as in Figure 3.17c). The distributions of $E$ are also shown following the application of the optimal filter ( $3 \text{ mm } 7^\circ$ ) to the other dryland patches. ....	86
Figure 3.24 Variations in the RMSE of residuals for the a) humid temperate and b) dryland patches with changes in DTM resolution. ....	88
Figure 3.25 The a) measured DTM and classified local parameters of b) aspect and c) slope, calculated within the $9 \text{ mm} \times 9 \text{ mm}$ moving window, for the $A_1$ patch. Direction of flow from left-to-right. In b) upstream and downstream facing cells are coloured in white and black respectively. In c) through an arbitrary classification, shallower ( $< 30^\circ$ ) and steeper slopes ( $> 60^\circ$ ) are coloured in white and black respectively. ....	94
Figure 3.26 Schematic illustration of the protrusion parameters, calculated within the dashed window, relative to a test grain: a) protrusion and b) exposure. In b) the dotted lines mark the boundary of streamwise strips which are averaged to estimate $e$ . ....	96
Figure 3.27 Workflow for the grain entrainment model, following Hodge et al. (2013). ....	98
Figure 4.1 Cumulative frequency distributions of surface grain size for the a) humid temperate and b) dryland patches (compared with the humid temperate patches, shown in grey). Grain size distributions are truncated at 2mm. ....	100
Figure 4.2 Zingg (1935) classification of particle shape. Distributions of particle shape are presented for the a) humid temperate patches, b) dryland gravel patches, c) humid temperate patches classified by lithology (limestone and gritstone) and d) limestone lithologies	

classified by flow regime (perennial and ephemeral). The large symbols indicate the mean particle shape calculated for each river with $\pm$ one standard deviation displayed as horizontal and vertical lines. ....	102
Figure 4.3 The measured (detrended) DTMs for the a-h) humid temperate and i-j) dryland gravel patches. Following Figures 3.9a-i, flow direction is orientated from left-to-right. In a) the DTM is overlain by a rough (solid line) trace around meso-scale topography. ....	106
Figure 4.4 The bed elevation pdfs for the a) humid temperate and b) dryland gravel patches. ....	108
Figure 4.5 Relationships between the statistical moments of the bed elevation pdfs - $\sigma_z$ , $Sk_z$ and $Kuz^*$ - and metrics of grain size, $D_{50}$ (a-c), sorting, $\sigma_G$ (d-f) and shape, $\psi$ (g-i). (Solid) Lines of best fit determined from least squares regression; 95% confidence intervals shown by the dotted lines. Horizontal error bars around $D_{50}$ and $\psi$ mark 95% confidence intervals (Bunte and Abt, 2001) and around $\sigma_G$ illustrate the compounded error from the 95% confidence intervals for $D_5$ , $D_{16}$ , $D_{84}$ and $D_{95}$ (Equation 3.1). Confidence intervals for $\sigma_z$ , $Sk_z$ and $Kuz^*$ too small to be visible ( $\leq 0.010$ mm, $\leq 0.021$ and $\leq 0.079$ , respectively; Wright and Herrington, 2011).....	110
Figure 4.6 Standardised 2D variograms for the a-h) humid temperate and i-k) dryland patches. Dashed lines mark where $h = 1$ , $h = h/D_{50}$ and $\gamma = \gamma/\sigma_z^2$ . ....	112
Figure 4.7 Variation in the ratio of normalised $\gamma$ in flow parallel ( $\gamma_x$ ) and flow transverse ( $\gamma_y$ ) directions as a function of normalised lag for the a) humid temperate patches, b) dryland patches, c) humid temperate patches classified by lithology (limestone vs. gritstone) and d) limestone lithologies classified by flow regime (perennial vs. ephemeral).....	115
Figure 4.8 a) Example flow-parallel variogram and fitted spline model for the a) $A_1$ humid temperate patch and b) residuals between the observed and expected $\gamma_x$ (note log $hx$ and $\gamma_x$ scales). In a) the dotted lines refer to the length of the $h_{1x}$ and $h_{2x}$ scales of roughness and the dashed lines represent the 95% confidence intervals around $h_{1x}$ and $h_{2x}$ . ....	117
Figure 4.9 Flow-parallel variograms for the a) humid temperate patches, b) dryland patches, c) humid temperate patches classified by lithology (limestone vs. gritstone) and d) limestone lithologies classified by flow regime (perennial vs. ephemeral). ....	119
Figure 4.10 a) The inclination index, $I$ , for the humid temperate and dryland patches (blue and red, respectively) and relationships between $I$ and b-d) surface grain size, sorting and shape. Vertical error bars represent range in $I$ calculated using 8 mm and 10 mm moving windows. ....	121
Figure 4.11 Distributions of local slope for the a) humid temperate patches and b) dryland patches. Relationships between the sedimentological parameters - $D_{50}$ , $\sigma_G$ , and $\psi$ - with c-e) median slope and f-h) the skewness of local slope distributions. 95% confidence intervals for $S_{50}$ and $Sk_s$ too small to be visible ( $\leq 0.09^\circ$ and $\leq 0.01$ , respectively).....	123
Figure 4.12 Polar plots of aspect and slope angle for the a-f) humid temperate gritstone, g-h) humid temperate limestone and i-k) dryland limestone patches, shaded by density (high = black, low = grey). Flow direction orientated from $270^\circ$ to $90^\circ$ .....	125
Figure 4.13 a) Cumulative distributions of $\Phi$ for the five patches and the relationship between $\Phi$ and $D_i/D_{50}$ for the b) humid temperate and c) dryland patches. In b) and c) lines represent	

the 25 <sup>th</sup> (dashed line), 50 <sup>th</sup> (solid) and 75 <sup>th</sup> (dotted) percentiles of data aggregated for bins that contain at least 30 grains.....	127
Figure 4.14 Cumulative distributions of a) grain projection and b) exposure normalised by grain size for the humid temperate (blue) and dryland patches (red). .....	129
Figure 4.15 Relationship between relative projection and relative exposure for a) the humid temperate and b) the dryland gravel patches. Lines of best fit determined from least squares regression for the regime-aggregated data, 95% confidence intervals illustrated by the dotted lines.....	129
Figure 4.16 Cumulative distribution of a) $\tau_c$ and b) $\tau_c^*$ for the humid temperate (black) and dryland (grey) patches predicted by the entrainment model.....	130
Figure 4.17 Relationship between relative grain size and dimensionless critical shear stress for the humid temperate (blue symbols) and dryland patches (red symbols) estimated by the grain entrainment model for a) individual patches and b) regime-aggregated data. Lines of best fit determined using least squares regression - in b) humid temperate: $\ln(\tau_c^*) = -0.76(\pm 0.02) - 1.32(\pm 0.09) \cdot \ln(D_i/D_{50})$ and dryland: $\ln(\tau_c^*) = -0.83(\pm 0.02) - 1.05(\pm 0.08) \cdot \ln(D_i/D_{50})$ . .....	132
Figure 4.18 Relationship between $Sk_z$ and $Ku_z^*$ for the humid temperate (blue) and dryland (red) patches, plotted in relation to previous observations. ....	136
Figure 5.1 Hydrograph for the 28-month monitoring period between November 2012 and April 2015. Discharge data gathered from the EA Netherside Hall gauge station with repeat surveys (S1–S13) illustrated by the red vertical bars and text.....	151
Figure 5.2 Cumulative grain size distributions for a) $W_{1.1}$ and b) $W_{1.2}$ . In a-c) $W_{1.1}$ and $W_{1.2}$ samples coloured in black and grey respectively. Digital grain size samples were not conducted for survey periods S6 and S9. In c) vertical error bars represent 95% confidence intervals.....	153
Figure 5.3 DTMs for the a) $W_{1.1}$ S1–S13 and b) $W_{1.2}$ S7–S13 surveys and significant changes in elevation (i.e. > LoD; cf. Wheaton et al., 2010) between the c) $W_{1.1}$ S1–S13 and d) $W_{1.2}$ S7–S13 surveys. In a) and b) the monotone elevation colour map is overlain by a semi-transparent layer representing elevation change, shown in c) and d). ....	157
Figure 5.4 The a) $W_{1.1}$ and b) $W_{1.2}$ bed elevation pdfs relative to the range of pdf form established from humid temperate surface characterisation (illustrated by dashed blue lines). .....	158
Figure 5.5 a) Variations in $\sigma_z$ over the monitoring period and changes in $\sigma_z$ for individual survey intervals with the b) magnitude and c) duration of competent flow. Lines of best fit determined from least squares regression for data aggregated from $W_{1.1}$ and $W_{1.2}$ ; 95% confidence intervals shown by the dotted lines. ....	159
Figure 5.6 a-b) Variations in $Sk_z$ and $Ku_z^*$ over the monitoring period and c-f) changes in $Sk_z$ and $Ku_z^*$ for individual survey intervals. ....	160
Figure 5.7 Flow-parallel variograms for the a) $W_{1.1}$ and b) $W_{1.2}$ patch series. In a-b) the bounds of humid temperate patch characterisation are illustrated by the dashed, blue lines. ....	161
Figure 5.8 The flow-parallel:flow-transverse ratio of $\gamma$ with $D_{50}$ -normalised lag for the a) $W_{1.1}$ and b) $W_{1.2}$ patch series. ....	162

Figure 5.9 a) Changes in  $I$  over the  $W_{1.1}$  and  $W_{1.2}$  survey series and b-c) changes in  $I$  for individual survey intervals. In a) the dashed lines refer to the envelope of values for the other humid temperate patches and the vertical bars the range in  $I$  calculated using 8 mm and 10 mm moving windows. In b) and c) the vertical bars represent the minimum and maximum absolute changes in  $I$  for the range of values recorded for a 9 mm ( $\pm 1$  mm) moving window. Lines of best fit determined from least squares regression; 95% confidence intervals shown by the dotted lines. .... 163

Figure 5.10 Local aspect for the a)  $W_{1.1}$  and b)  $W_{1.2}$  1 x 1m sub patch series. Direction of flow from left-to-right. In a-b) upstream and downstream facing cells are coloured in white and black respectively (see Figure 3.24). .... 164

Figure 5.11 The probability distributions of local slope for a)  $W_{1.1}$  and b)  $W_{1.2}$  and c-f) changes in  $S_{50}$  and  $Sk_s$  for individual survey intervals. In a-b) the envelope of values for the other humid temperate patches are illustrated by the dashed, blue lines. Lines of best fit determined from least squares regression; 95% confidence intervals shown by the dotted lines. .... 166

Figure 5.12 DTMs for the  $W_{1.1A}$ ,  $W_{1.2A}$  and  $W_{1.1B}$  sub patches. Pre-treated (T-1), treated (T0) and restructuring (T1-Tn) surfaces are differentiated by green, red and blue ID boxes respectively. Monotone elevation maps are overlain by a semi-transparent, coloured layer representing significant changes in elevation (i.e.  $>$  LoD; cf. Wheaton et al., 2010) between surveys. .... 168

Figure 5.13 Effects of surface treatment on a) grain size distributions, b) bed elevation pdfs, c) flow parallel 1D variograms, d) ratio of flow parallel and flow transverse standardised semivariance and e) pdfs of local slope as exemplified for the pre-treated (T-1; *green*) and treated surfaces (T0; *red*) at  $W_{1.1A}$  S3. In b), c) and e) the bounds of the data for the  $W_{1.1}$  series are illustrated by the solid, black lines. .... 171

Figure 5.14 Temporal evolution of a) grain size distribution, b) bed elevation pdfs, c) flow parallel variograms, d) ratio of flow-parallel and flow-transverse standardised semivariance and e) pdfs of local slope for the pre-treated surfaces (T-1; *green*) and restructuring surfaces (T1-T4; *blue*) for  $W_{1.1A}$  S3-S7. In b), c) and e) the bounds of the data for the  $W_{1.1}$  series are illustrated by the solid, black lines. .... 175

Figure 5.15 Relationship between peak discharge and duration of competent flow and absolute changes in a-b)  $D_{50}$ , c-d)  $\sigma_z$ , e-f)  $Sk_z$ , g-h)  $Ku_z$ , i-j)  $I$ , k-l)  $S_{50}$  and m-n)  $Sk_s$  between successive survey periods. Note: grain size information missing for the S6 survey (one T0-T1, T2-T3 and T3-T4 survey interval). The mean absolute changes observed over the  $W_{1.1}$  and  $W_{1.2}$  series are illustrated by the dotted lines. .... 177

Figure B.1 Flow-parallel variograms and fitted spline models and residual between the observed and expected  $\gamma_x$  for the (a-b)  $A_2$ , (c-d)  $E_{1.1}$ , (e-f)  $E_{1.2}$ , (g-h)  $M_1$ , (i-j)  $M_2$ , (k-l)  $W_{1.1}$ , (m-n)  $W_{1.2}$ , (o-p)  $H_1$ , (q-r)  $H_2$  and (s-t)  $S_1$  gravel patches. In a), c), e), g), i), k), m), o), q) and s) the dotted lines refer to the length of the h1x and h2x scales of roughness and the dashed lines represent the 95% confidence intervals around h1x and h2x. Note log hx and  $\gamma_x$  scales. .... 215

Figure B.2 Flow-transverse variograms and fitted spline models and residual between the observed and expected  $\gamma_x$  for the (a-b)  $A_1$ , (c-d)  $A_2$ , (e-f)  $E_{1.1}$ , (g-h)  $E_{1.2}$ , (i-j)  $M_1$ , (k-l)  $M_2$ ,

(m-n)  $W_{1.1}$ , (o-p)  $W_{1.2}$ , (q-r)  $H_1$ , (s-t)  $H_2$  and (u-v)  $S_1$  gravel patches. In a), c), e), g), i), k), m), o), q), s) and u) the dotted lines refer to the length of the h1x and h2x scales of roughness and the dashed lines represent the 95% confidence intervals around h1x and h2x. Note log hx and  $\gamma$ x scales. ....218

Figure C.1 Cumulative frequency distributions of (normally distributed) residuals from the relationship between dimensionless projection ( $p/D$ ) and dimensionless exposure ( $e/D$ ; Figure 4.15) for the  $W_{1.1}$  ( $\mu_{res} = 0$ ,  $\sigma_{res} = 0.06$ ),  $W_{1.2}$  ( $\mu_{res} = 0$ ,  $\sigma_{res} = 0.06$ ),  $H_1$  ( $\mu_{res} = 0$ ,  $\sigma_{res} = 0.10$ ),  $H_2$  ( $\mu_{res} = 0$ ,  $\sigma_{res} = 0.12$ ) and  $S_1$  patches ( $\mu_{res} = 0$ ,  $\sigma_{res} = 0.09$ ). ....219

## List of Acronyms and Abbreviations

1D	1-dimensional
2½D	2.5-dimensional
3D	3-dimensional
DTM	Digital terrain model
EA	Environment Agency
HDS	High Definition Surveying
IDW	Inverse Distance Weighting
LiDAR	Light Detection and Ranging
MP	Megapixel
OS	Ordnance Survey
PCL	Point Clouds Library
pdf	Probability density function
$S_{gm}$	Unworked gravel bed ( $Sk_z:Ku_z$ structural classification)
SOR	Statistical Outlier Removal filter
TLS	Terrestrial Laser Scanning
ToF	Time of Flight
TS	Total Station
WFD	Waveform Digitization technology
$W_{gm}$	Water-worked gravel bed ( $Sk_z:Ku_z$ structural classification)

## List of Symbols

$a$	Long grain-axis length
$A$	Aspect
$A_{rc}$	Cross-sectional area of the grain normal to $F_L$
$A_{rp}$	Photographed area
$b$	Intermediate grain-axis length
$b_1$	Coefficient describing the slope of the first, fitted log-linear segment
$b_2$	Coefficient describing the slope of the second, fitted log-linear segment
$c$	Short grain-axis length
$C_D$	Empirical drag coefficient
$C_L$	Empirical lift coefficient
$C_n$	Dimensionless multiplier to upscale roughness
$D$	Grain size diameter
$D_{50}$	Median grain size diameter
$D_i$	Diameter for the $i$ th grain size percentile
$D_{max}$	Maximum grain size diameter
$D_n$	Representative grain size
$D_{res}$	Diameter of the smallest resolvable grain
$dx$	Change in x-direction
$dy$	Change in y-direction
$dz$	Change in z-direction
$e$	Grain exposure
$E$	Mean elevation difference parameter
$E_i$	Percentile of the mean elevation difference parameter
$f$	Darcy-Weisbach friction factor
$F_D$	Drag force
$F_L$	Lift force
$F_W$	Force of particle weight

$g$	Acceleration due to gravity
$h$	Lag
$h_x$	Lag in x-direction
$h_y$	Lag in y-direction
$h_1$	Length of $H_1$
$h_2$	Length of $H_2$ (range of influence, sill)
$H$	Hurst exponent
$H_1$	First fractal band
$H_2$	Second fractal band
$Hd$	Hausdorff dimension
$ht$	Filter height
$ht_{opt}$	Optimal filter height
$I$	Inclination index
$I_+$	Number of positive changes in bed elevation between sampling pairs
$I_-$	Number of negative changes in bed elevation between sampling pairs
$I_N$	Total number of inclination samples
$k$	Height of a regular array of roughness elements
$K$	Grain size diameter of local bed
$k_s$	Boundary roughness length scale
$Ku_z^*$	Bed elevation kurtosis
$L$	Meander length
$LoD$	Minimum level of detectable change
$m$	Lift force multiplier
$n$	Number of observations
$p$	Grain protrusion
$P$	Number of pixels in an image
$Q$	Discharge
$r$	Filter radius

$r_{opt}$	Optimal filter radius
$R$	Hydraulic radius
$Re^*$	Grain Reynolds number
RMSE	Root Mean Square Error
RSEV	Repeat Scan Error Value
$RSEV_{opt}$	Optimal repeat scan error value threshold
$S$	Slope
$Sf$	Second-order structure function
$Sk_S$	Skewness of the slope distribution
$Sk_z$	Bed elevation skewness
$S_l$	Local slope
$Sn$	Survey ID
$T_{comp}$	Duration of competent flow
$Tn$	Treatment phase
$u$	Flow velocity
$u^*$	Shear velocity exerted by the flow on the boundary
$\nu$	Kinematic viscosity of the fluid
$W$	Grain cross-section width
$w$	Meander width
$z$	Bed elevation
$z_i$	Bed elevation of cell $i$

### ***Greek Letters***

$\alpha$	Relative grain size ( $D_i/D_{50}$ ) multiplier
$\beta$	Relative grain size ( $D_i/D_{50}$ ) exponent
$\gamma$	Coefficient describing the mode of particle movement
$\Gamma$	Grain size sorting exponent
$\gamma$	Power law exponent fitted by linear regression

$\gamma$	Semivariance
$\Delta x$	Second-order structure function in x-direction
$\Delta x_0$	Characteristic scale in x-direction
$\Delta y$	Second-order structure function in y-direction
$\Delta y_0$	Characteristic scale in y-direction
$\varepsilon$	Dimensionless exponent describing the relative importance of absolute or relative size effects for sediment transport
$\theta$	Divergence angle
$\kappa$	von Kármán's constant
$\lambda$	Spatial concentration of a regular array of roughness elements
$\rho$	Density of water
$\rho_s$	Density of sediment
$\sigma_G$	Sediment sorting
$\sigma_z$	Standard deviation of bed elevations
$\tau_c$	Critical shear stress for sediment entrainment
$\tau_c^*$	Dimensionless critical shear stress
$\tau_{c,i}^*$	Dimensionless critical shear stress for $D_i$
$\tau_{c,50}^*$	Dimensionless critical shear stress for $D_{50}$
$\Phi$	Grain pivoting angle
$\zeta$	Coefficient describing the mode of particle movement
$\chi$	Factors including the shape of the cross-section
$\psi$	Grain sphericity
$\vartheta$	Grain size in phi units

## **Chapter 1 Introduction**

The characteristics of alluvial rivers will result from the complex interplay between the driving variables of flow and sediment supply, boundary conditions which describe the morphological character of the local catchment and basin external factors including climate, tectonics and past-environmental conditions (Schumm and Lichty, 1965). Since river systems will naturally seek to attain an equilibrium state whereby the inputs and outputs of mass and energy are equal, the character of alluvial channels will reflect this balance (Nanson and Huang, 2008). Furthermore, given the elements that control the driving variables and boundary characteristics are spatially heterogenous, these characteristics will vary considerably within and between catchments (Schumm, 1981; Rosgen, 1994; van den Berg, 1995).

The geography of a catchment will determine various factors including local climate, topography, geology and soil cover which control the delivery of water and sediment into the river system. Rainfall regime – the intensity, duration and order of rainfall events – is one of the principal factors in determining the hydrological response and erosive capacity of a channel (Deal et al., 2018). Other factors will affect and add complexity to the relationship between discharge and sediment flux (Ibisate et al., 2011) including the morphometric characteristics of the catchment (e.g. steeper valleys will concentrate flows and increase sediment yield rates), the permeability of soils and underlying geology (e.g. karst geologies have a slower response to rainfall events and will generate less peaked flood events than more impermeable types) and vegetation cover (e.g. dense vegetation will protect the soil thereby reducing sediment yield rates and runoff). Owing to the sporadic, flashy nature of flooding and tendency of the watershed to be unvegetated in dryland environments, the rate of bedload transport in ephemeral channels is considerably greater, for a given stream power, than perennial channels (Laronne and Reid, 1993; Reid and Laronne, 1995). As a result of the nature of flooding in dryland environments, ephemeral channels are often in a state of disequilibrium (Renwick, 1992), limited in their ability to reach a stable condition (Bull, 1997). By comparison, perennial channels have the greater opportunity to attain an equilibrium provided by regular flooding and these differences in the geomorphic response between fluvial environments are, for instance, demonstrated by differences in the surface character and stability of alluvial streambeds (Wittenberg, 2002).

The character of alluvial channels will respond to changes in the driving variables and boundary conditions as the river system adjusts toward a new equilibrium. For example, land use practices which promote intensive grazing may act to modify the local catchment, by degrading soils, and indirectly increase runoff and sediment yield (Trimble and Mendel, 1995). In seeking to achieve a balance in the supply and transport of bedload, the channel may incise into the catchment and depending on reach variables (e.g. valley slope and confinement) change planform (Montgomery and Buffington, 1997; Buffington and Montgomery, 1999). Other channel management activities will more directly modify channel form and process and may ultimately lead to a change in system type (Surian and Rinaldi, 2003; Gregory, 2006). For instance, the creation of dams will modify the hydrological response of the downstream regulated reach by reducing flow magnitude and trapping sediment. These effects on flow and sediment regime change the capacity for the river to transport sediment, causing the channel to alter planform and degrade or aggrade depending on released flow and supply of sediment (Brandt, 2000; Petts and Gurnell, 2005). If the transport rate exceeds the local supply of sediment, the streambed will coarsen through the winnowing of fines which will in turn increase particle stability and reduce bedload flux (Dietrich et al., 1989).

The success of channel management strategies and the design of river works is predicated on understanding the stable form of a channel for a given flow and sediment regime or for a system in disequilibrium predicting likely morphological responses (Ward et al., 2001; Kondolf et al., 2002); for example, sedimentation from the construction of a reservoir which may require regular sediment flushing (Brandt, 2000). The ability to develop an understanding of the spatial character and temporal variability of alluvial systems and the response to changes in driving variables and boundary conditions for a range of different environments is, therefore, of fundamental importance to the effective administration of the natural environment; for example, for water resource management, the protection of the infrastructure, environmental sustainability and ecological connectivity (Ward and Stanford, 1995; Frey and Church, 2009).

The surface character of alluvial rivers is an important factor for controlling boundary roughness and hence the resistive force exerted by the bed on the flow, and particle stability, a function of the spatially averaged force exerted by the flow on the bed. Boundary roughness will affect flow resistance and how much a channel can convey for a given stage while particle stability will determine the shear stress required to mobilise

individual surface grains and hence moderate sediment transport. As a result, there is a clear need for Earth Scientists to characterise streambed microtopography to establish i) the flow resistance for stage-discharge relationships and models of flood prediction and ii) the shear stress for grain entrainment and sediment transport.

Conventionally, the influence of the surface on boundary roughness and particle stability has been characterised in terms of the size of surface grains. For example, a bed comprised of coarse, unconsolidated grains will offer a greater flow resistance (e.g. Keulegan, 1938) and surface grains will require a greater entrainment stress (e.g. Shields, 1936) than a bed comprised of finer-sized sediment. However, boundary roughness and particle stability are not singularly controlled by bed texture and the structure of the bed is also an important factor in affecting alluvial bed surface character (Naden and Brayshaw, 1987). For instance, an imbricated, tightly packed streambed will be topographically smoother (generate less boundary resistance) and increase the stability of individual particles (reduce bedload flux) relative to a more openly structured bed with an identical grain size distribution (Church, 1978). Moreover, the spatial distribution of structured, roughness elements will critically affect boundary resistance (Hassan and Reid, 1990) and the stability of the bed (Piedra et al., 2011).

While previous workers have acknowledged the need to consider bed structure within models of flow resistance and sediment transport, relatively little is understood about the structural characteristics of gravel bed surfaces in different environments and how this influences bed stability. Furthermore, much of what is known about streambed structure has been derived from flume experiments and, critically, may not be applicable to the natural environment. The few studies that have sought to characterise natural streambed structure *in-situ* were, for early workers, limited to qualitative assessments of bed packing arrangements and bedform typologies (e.g. Brayshaw, 1984; Naden and Brayshaw, 1987). More recent advancements in technology have allowed a handful of workers to characterise natural streambed topography using high resolution surface measurements (e.g. Butler et al., 2001; Hodge et al., 2009b) but, while the results from this vein of research are promising, these techniques have often been limited to single site surveys for a narrow range of perennial reaches. As a consequence, there is a clear need to establish the characteristics and temporal dynamics of streambed structure for a broader range of gravel bedded reaches in different fluvial environments to better describe boundary

roughness and particle stability and better inform models of flow resistance and sediment transport.

## **1.1. Research Hypotheses**

The main hypotheses of this research are, therefore, that:

- Coarse-grained alluvial streambeds from different fluvial environments, subject to different flow regimes, will exhibit different structural characteristics.
- Differences in the characteristics of streambed structure will cause particle stability and hence the nature of sediment transport to be different between fluvial environments.
- The characteristics of gravel bed structure in humid temperate reaches will remain within a dynamic equilibrium and will be broadly maintained over a series of interannual, sediment-transporting flood events.

## **Chapter 2 Streambed structure and its influence on boundary roughness and particle stability**

This chapter reviews the need to consider the characteristics and temporal dynamics of streambed structure and their implications for flow resistance and sediment transport. In doing so, the chapter starts by briefly summarising how previous workers have sought to characterise flow resistance and particle stability in terms of surface grain size in section 2.1. The control of bed structure on flow resistance and particle stability is then described in section 2.2 before moving on to how previous workers have characterised bed structure through various statistical approaches in section 2.3. Finally, the temporal dynamics of natural streambed structure are considered in section 2.4 and the research objectives set out in section 2.5.

### **2.1. Characterising boundary roughness and particle stability in terms of grain size**

The surface character of alluvial rivers is an important factor for controlling boundary roughness and particle stability and, hence, an important consideration for models of flood prediction and sediment transport. Conventionally, previous workers have characterised the influence of the surface on boundary roughness and particle stability through the size of surface grains. In terms of boundary roughness, using the work of Keulegan (1938) to apply earlier observations from flow in pipes to open channel flows, the roughness of the surface (parameter  $k_s$ ) can be related to flow resistance, by proxy of the Darcy-Weisbach friction factor ( $f$ ), and expressed in general terms using:

$$\frac{1}{\sqrt{f}} = \frac{\chi}{\sqrt{8}} + \frac{2.303}{\kappa\sqrt{8}} \cdot \log_{10} \left( \frac{R}{k_s} \right) \quad [2.1]$$

where,  $\chi$  refers to a variety of factors not accounted for by the analysis of Keulegan (1938) including the shape of the cross-section,  $\kappa$  is Von Kármán's constant and  $R$  is the hydraulic radius ( $R = \text{cross-sectional area/wetted perimeter}$ , m).

The accuracy to which  $f$ , and hence flow resistance, can be calculated, therefore, depends on the ability to characterise the roughness height of the surface ( $k_s$ ). For the early work of Nikuradse (1933) the experimental beds comprised tightly packed, uniformly-sized grains for which  $k_s$  was proportional to the size ( $D$ ) of bed material in hydraulically rough turbulent flows (i.e.  $k_s = D$ ; see also Moody, 1944). For planar beds, grain size can be thought to be one of the principal factors to control the shear stress necessary to mobilise

surface grains ( $\tau_c$ ,  $\text{Nm}^{-2}$ ). To test this assumption, Shields (1936) used measurements of flux to estimate critical shear stresses for different uniform grain sizes with considerations to the dimensionless critical shear stress ( $\tau_c^*$ ) and grain Reynolds number ( $Re^*$ ), calculated using:

$$\tau_c^* = \frac{\tau_c}{(\rho_s - \rho) g D} \quad [2.2]$$

where,  $\rho_s$  is the density of (quartz-grained) sediment ( $2650 \text{ kg m}^{-3}$ ),  $\rho$  is the density of water ( $1000 \text{ kg m}^{-3}$ ) and  $g$  is the acceleration of gravity ( $9.81 \text{ m s}^{-2}$ ) and

$$Re^* = \frac{u^* D}{\nu} \quad [2.3]$$

where,  $u^*$  is the shear velocity exerted by the flow on the boundary ( $\text{m s}^{-1}$ ) and  $\nu$  is the kinematic viscosity of the fluid ( $\text{m}^2 \text{ s}^{-1}$ ).

Shields (1936) observed  $\tau_c^*$  was constant for hydraulically rough turbulent flows, for  $Re^* \geq 500$ , and approximate to 0.06, although more recent research has identified a wider range of values between  $0.03 \leq \tau_c^* \leq 0.073$  (Miller et al., 1977; Yalin, 1977; Buffington et al., 1992; Buffington and Montgomery, 1997). From the findings of Shields (1936), equation 2.2 can be rearranged to give:

$$\tau_c \propto D \quad [2.4]$$

Therefore, for a planar bed and under flow conditions common to gravel-bedded rivers, the shear stress required to move surface grains is a function of particle diameter, i.e. coarse grains will require a greater shear stress to entrain than comparatively smaller grains. The basic inference that sediment transport is **size-selective** can explain various sedimentological phenomena in alluvial systems. For example, at the regional-scale, the observation that particle size decreases with increasing distance from the river's source, downstream fining, is, in-part rationalised by the greater mobility of finer sized sediment (Rice and Church, 1998). At the grain-scale, the size-selective nature of sediment transport can similarly explain the preferential entrainment of smaller surface grains during competent flows, i.e. the horizontal winnowing of fines (Gessler, 1971; Paola, 1988). The coarsening of the bed from horizontal winnowing can similarly help to explain the presence of a coarse armour layer characteristic of gravel streambed surfaces (Klingeman and Emmett, 1982; Gomez, 1983).

Most natural gravel beds, however, comprise a mix of sediment sizes and, as a consequence, boundary roughness is not strictly defined by particle size (Yen, 2002) and

the Shields' entrainment function has been found to inadequately predict critical shear stresses over graded beds (Graf, 1991; Reid et al., 1995). The role of the grain size distribution must therefore be acknowledged in predicting flow resistance and sediment transport. In terms of flow resistance, for planar bed conditions the dominant source of flow resistance will be generated from the viscous effects of skin friction (Powell, 2014). As the surface roughens, the pressure effects of form drag around coarse surface clasts will assume a greater role (Powell, 2014). Previous workers have sought to acknowledge the changing influence of skin friction and form drag on flow resistance by relating the roughness height to a representative grain size ( $D_n$ ), twinned with a dimensionless multiplier ( $C_n$ ):

$$k_s = C_n \cdot D_n \quad [2.5]$$

Although  $D_n$  varies widely between studies, previous workers have often used a coarser-than-average grain size percentile (Hey, 1979), since larger clasts will exert a greater role in modifying near-bed flow velocity compared to smaller grains which are often sheltered and hidden in the wakes of coarser bed material (Leopold et al., 1964). The  $C_n$  multiplier in equation 2.5 was required to upscale roughness to account for small-scale form drag associated with individual clasts (Clifford et al., 1992). For previous workers,  $C_n$  was found by analysing the data to be 3.5 and 6.8 for  $D_{84}$  and  $D_{50}$  respectively (Charlton et al., 1978; Hey, 1979; Bray, 1980, 1982; Yen, 2002).

The effect of a non-uniform grain size distribution on particle stability was acknowledged by early workers through the introduction of hiding functions (Einstein, 1950; Egiazaroff, 1965). These consider **relative size effects** whereby smaller surface grains are sheltered behind coarser, emergent surface grains and coarser surface grains project further into the flow. These relative size effects act to reduce the relative mobility of different grain sizes (Proffitt and Sutherland, 1983; Habersack et al., 2008). If the effects of particle exposure and sheltering (relative size effects) are sufficient to cancel out particle size and weight (absolute size effects) a condition of *equal mobility* prevails whereby all grain sizes are entrained at the same shear stress (Parker and Klingeman, 1982; Parker et al., 1982; Andrews, 1983; Andrews and Parker, 1987; Diplas, 1987; Wilcock and Southard, 1988; Wilcock, 1992; Habersack et al., 2008). Under equal mobility, critical shear stress does not vary with particle diameter and, once this shear stress is reached, surface grains of all sizes will be transported at rates in proportion of their existence on the bed surface

(Powell, 1998). Critically, size-dependent entrainment requires the surface to coarsen, under equilibrium transport conditions, from horizontal winnowing and an immobility of coarse surface grains (Gessler, 1970) whereas size-independent entrainment involves vertical winnowing and the movement of all grain size fractions (Parker and Klingeman, 1982; Parker et al., 1982; Andrews and Parker, 1987). The relative influence of size-selective transport and equal mobility represents two possible end points of a spectrum of sediment transport mechanisms which is described using:

$$\frac{\tau_{c,i}^*}{\tau_{c,50}^*} = \left( \frac{D_i}{D_{50}} \right)^\varepsilon \quad [2.6]$$

where,  $\tau_{c,i}^*$  is the dimensionless critical shear stress for the  $i$ th grain size ( $D_i$ ),  $\tau_{c,50}^*$  is the dimensionless critical shear stress for the median grain size and  $\varepsilon$  is a dimensionless exponent.

The power law exponent,  $\varepsilon$ , denotes the relative importance of the two competing theories of grain entrainment (Ferguson, 1987). In this respect,  $\varepsilon = 0$  and  $\varepsilon = -1$  if sediment entrainment is governed solely by absolute (Shields, 1936) and relative size effects (Parker et al., 1982), respectively. The concept of equal mobility was founded, in-part, by the experiments of Parker et al. (1982) who modelled transport events in two reaches and, in the process, derived an entrainment function during the breakup of surface armours. For these experiments,  $\varepsilon = -0.982$  which was deemed close enough to  $-1$  such that  $D_i$  exerts a negligible influence on  $\tau_c$  and, for flows capable of breaking apart the surface armour, grain size fractions are equally mobile and the size distribution of bedload matches that of bed material (Parker et al., 1982). The emerging consensus from more recent work has shown the power law exponent to occupy the wider range  $-1 \leq \varepsilon \leq -0.65$  (Andrews, 1983; Buffington and Montgomery, 1997; Whitaker and Potts, 2007). Thus, particle mobility in gravel-bedded rivers is, in general, governed more by relative particle size than absolute size and, at low excess shear stresses (i.e. at low discharges), the streambed will coarsen in response to the greater mobility of fines (Powell, 1998). In attempting to better define the mechanisms of sediment entrainment, previous workers have observed a scatter in values of  $\varepsilon$ , with 95% confidence intervals in the order of  $\pm 0.20$  (Ashworth and Ferguson, 1989; Ferguson et al., 1989; Petit, 1994). The variability of the exponent  $\varepsilon$  has been attributed to local factors, which vary between sites, including properties of the bed material (sorting, shape), bed structure (grain packing, bedforms) and the methods used to define incipient motion and characterise bed texture (Richards, 1990; Andrews, 1994; Buffington and Montgomery, 1997; Mao et al., 2008; Schneider et

al., 2015). However, despite the suggestion that the arrangement of bed material acts as a prominent factor, prohibitively little is understood about the effects of various physical processes on  $\varepsilon$  and, hence, grain entrainment (Recking, 2009).

### **2.1.1. Bed texture and grain size adjustments**

In seeking to better predict boundary roughness and particle stability, previous workers have characterised the bed texture of alluvial surfaces in different fluvial environments and investigated grain size adjustments over the course of flood events. In this regard, the streambeds of perennial channels are often characterised by a coarse armour layer which, as section 2.1 explains, develops from vertical winnowing under equal mobility (e.g. Parker and Klingeman, 1982) and horizontal winnowing from size-selective transport (Gessler, 1971). This coarse surface layer typically extends to depth approximately equal to  $c.2.D_{90}$  and overlies more poorly sorted and finer sediment (e.g. Figure 2.1a; Milhous, 1973; Andrews, 1983; Church et al., 1987). Past work studied the temporal dynamics of bed texture using flume experiments under steady discharge (e.g. Pender et al., 2001; Marion et al., 2003; Ockelford et al., 2010) and have often observed the grain size of bedload to increase under effective flows (Milhous, 1973; Parker et al., 1982; Dietrich et al., 1989; Kuhnle, 1992; Buffington and Montgomery, 1999). More recent research has illuminated the role of sediment supply on the maintenance of bed texture (Wilcock et al., 2001; Wilcock and DeTemple, 2005). For instance, under the presence of a persistent upstream sediment supply and flows capable of mobilising all grain size fractions the coarse surface layer is maintained and can be described as a ‘mobile armour’ (Parker et al., 1982). The surface will also respond to sustained imbalances in sediment supply and flow regime (Dietrich et al., 1989; Parker and Sutherland, 1990); for example, by degrading into a ‘static armour’ through a coarsening of the surface in supply-limited regimes such as those experienced in the outflow of dams (e.g. Vericat et al., 2006).

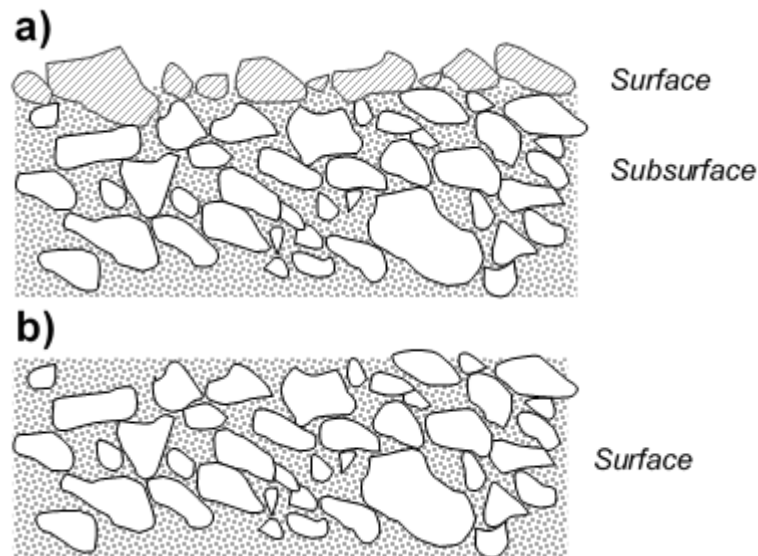


Figure 2.1 Illustration of an a) armoured and b) unarmoured gravel bed. Adapted from Powell (1998).

Two schools of thought exist regarding whether streambed armours are maintained over the full range of natural flows. The first has found the armour layer can be disturbed by more forceful events (e.g. Gomez, 1983). By contrast, other workers have found armour layers to remain relatively intact during high flows (Parker and Klingeman, 1982; Andrews and Erman, 1986; Wilcock and DeTemple, 2005). This, as Clayton and Pitlick (2008) suggest, is explained by the preference of entrained grains to be replaced by similarly-sized grains through bedload routing and the favourable sheltering properties around surface pockets. Thus, once established, an equilibrium bed texture is preserved over natural flows (Parker et al., 2007) and although an armour may break apart during the largest floods a similar condition reforms in the recession limb of the hydrograph (Parker and Klingeman, 1982; Vericat et al., 2006).

While the streambeds of perennial channels are generally considered to be well armoured, those of ephemeral channels are, by contrast, characterised by a lack of vertical layering between the surface and subsurface, i.e. a poor or undeveloped armour layer (Laronne and Reid, 1993; Laronne et al., 1994; Hassan et al., 2006). The condition illustrated in Figure 2.1b is generated from the scour-and-fill process during highly effective ephemeral flooding, where particles are deposited without size segregation (Reid and Laronne, 1995; Wittenberg and Newson, 2005; Powell et al., 2006); the lack of opportunity for the winnowing of fines owing to the flashy nature of flow recession and transmission losses

(Laronne et al., 1994; Shentsis et al., 1999) and high rates of sediment supply (Dietrich et al., 1989).

The characteristics of bed texture, i.e. the degree of armouring, will influence boundary roughness and the stability of surface grains (Parker and Sutherland, 1990). For example, the coarsening of the streambed will generate a rougher surface while the associated development of an armour layer will increase grain entrainment thresholds (Parker et al., 1982; Buffington and Montgomery, 1999). However, critically, the roughness of the bed and the stability of particles is also controlled by the arrangement of surface grains. Although the characteristics and temporal dynamics of bed texture are relatively well understood, much less is known about bed structure and its influence on flow resistance and particle stability.

## **2.2. Influence of bed structure on boundary roughness and particle stability and implications for flow resistance and bed stability**

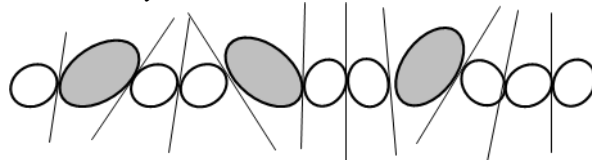
The development of the coarse surface layer characterising coarse-grained alluvial streambeds, described in section 2.1, is accompanied by the organisation of surface grains into discernible sedimentary structures (Naden and Brayshaw, 1987). These structures are generated from the organisation of surface grains into their most stable arrangement on the bed surface and are observed at the scale of individual particles and assemblages of particles, which Wolcott (1989) termed textural and geometrical structure, respectively. Textural structure refers to the characteristics of individual surface grains, e.g. imbrication and bed packing arrangements, whereas geometrical structure is concerned with the organisation of collections of grains into bedforms, e.g. cluster bedforms (Wolcott, 1989). For the purposes of this study, textural and geometrical structure are hereafter referred to as grain-scale and bedform-scale bed structure, respectively. The characteristics of grain- and bedform-scale structure is first outlined in subsections 2.2.1 and 2.2.2 respectively before concluding with a discussion on the influence of bed structure on flow resistance and bed stability in subsections 2.2.3 and 2.2.4 respectively.

### **2.2.1. Grain-scale bed structure**

The armoured surfaces of gravel streambeds are generally well structured and this bed structure can be considered at the grain-scale and the bedform-scale. The former, bed

structure at the scale of individual particles, is exhibited, for example, through the packing arrangement of surface grains. The effect of grain-scale bed structure can be conceptually illustrated through a comparison of three streambeds composed of the same size distribution of surface grains (i.e. an identical bed texture) but exhibiting different packing geometries: organised into loose, overloose and underloose boundaries (Figure 2.2; Church, 1978).

a) *Normally loose boundary*



b) *Overloose boundary*



c) *Underloose boundary*

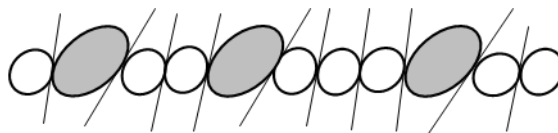


Figure 2.2 Illustrative schematic of three noncohesive bed conditions generated from the same grain size distribution but with differences in grain-scale bed structure (packing geometry). In a) and c) lines denote contact tangents between neighbouring grains. Modified after Church (1978).

As Laronne and Carson (1976) describe, grains within an overloose boundary are barely in contact and form an *open structure*. This condition characterises planar regions of the bed comprised of a relatively uniform size distribution of grains (Laronne and Carson, 1976; Billi, 1987). In contrast, the underloose boundary is more common and comprises a *closed structure* where surface grains are in close contact (Figure 2.2). In this instance, the tight packing of surface grains develops from the infilling of interparticle voids by fines and the imbrication of coarser grain size fractions (Laronne and Carson, 1976; Clifford, 1990). Imbrication describes the ‘fish-scale’ pattern of abutting water-worked particles orientated to the dominant flow direction (Johansson, 1976).

While particle packing is difficult to quantify, imbrication is one packing structure that has received some attention from previous workers. In this respect, the magnitude (relative degree) of particle imbrication has been found to be affected by several factors including grain shape. For example, beds comprised of bladed grains display a greater

tendency to imbricate than beds composed of more rounded grains (Johansson, 1963; Laronne and Carson, 1976). Grain-scale bed structure will also respond to local flow patterns (Laronne and Carson, 1976). For instance, preferential particle placement has been found to provide a reliable proxy for flow magnitude and flow direction (Millane et al., 2006). Previous workers have sought to describe the relative positioning of individual grains using the long, intermediate and short axes (a-, b- and c-axis lengths, respectively). In this regard, grain-scale structure has been characterised using the orientation of the a-axis and the angle of dip of the a-b axes plane relative to the local flow direction (e.g. Millane et al., 2006; Qin et al., 2012). The a-axis orientation of surface grains, for instance, is relatively easy to deduce in-situ and varies from reach-to-reach with flow regime and sediment supply. However, previous workers have disputed whether surface grains within mobile armours rest with their a-axes orientated in a flow transverse (e.g. Nikora et al., 1998; Nikora and Walsh, 2004) or flow parallel direction (Aberle and Nikora, 2006; Cooper and Tait, 2009). In addition, the relative alignment of surface grains may also vary within a stream course, as Hodge et al. (2009b) observed for pool (flow parallel), pool exit and riffle facies (flow transverse).

### **2.2.2. Bedform-scale bed structure**

At the larger, bedform-scale of bed structure, collections of surface grains assemble into a variety of geometrical features. Bed structure at scales larger than individual particles is characterised by the organisation of surface grains into small-scale bedforms – discrete depositional features that protrude above the local mean bed level (Brayshaw, 1984; Strom and Papanicolaou, 2008). Bedform-scale structure exhibits a variety of different geometric forms including clusters (Brayshaw, 1984; Reid et al., 1992; De Jong, 1995), coarse transverse ribs and clast dams (McDonald and Banerjee, 1971; Gustavson, 1974; Bluck, 1987) and poorly defined reticulate and longitudinal structures (Martini, 1977; Hassan and Church, 2000). Given the widespread presence of clusters in gravel beds across a range of flow conditions, sedimentologists have largely chosen to focus on these geometric forms in preference to other bedforms (e.g. Laronne and Carson, 1976; Brayshaw, 1984; Biggs et al., 1987; Church et al., 1998). To reflect this, clusters also provide the primary focus for this consideration of the characteristics of bedform-scale structure.

Previous workers have observed clusters are comprised of four or more abutting particles which surround on ‘obstacle’ clast, formed from a coarse surface grain typically greater than  $D_{84}$  (Brayshaw, 1984; De Jong, 1995; Wittenberg, 2002; Papanicolaou et al., 2003). As Figure 2.3 illustrates, obstacle clasts provide the nucleus for the cluster by sheltering the local area of the bed and, in doing so, anchors smaller grains which interlock with them (Strom and Papanicolaou, 2008). These interlocking grains take the form of stoss-side, imbricated accumulations ( $D_{74} \leq D_i \leq D_{94}$ ) and a wake tail largely composed of fines ( $D_8 \leq D_i \leq D_{46}$ ; Brayshaw et al., 1983). The former is constructed when moderately-sized material lodges against the stoss-side of the obstacle while the latter is formed from fine grains protected in the lee-side separation zone (Brayshaw et al., 1983; Buffin-Bélanger and Roy, 1998).

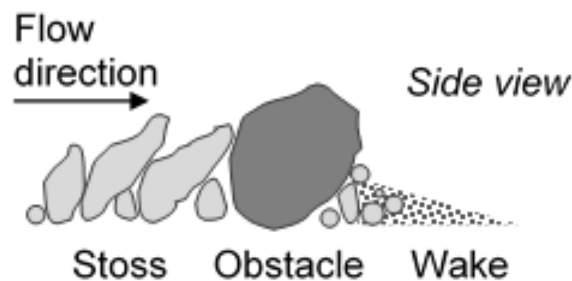


Figure 2.3 Cross sectional view of a pebble cluster. Diagram adapted from Powell (1998).

Previous workers have proposed a typological classification for cluster bedforms that includes pebble, line, comet, ring and heap geometries (De Jong, 1995; Kozłowski and Ergenzinger, 1999; Wittenberg, 2002; Strom and Papanicolaou, 2008; Hendrick et al., 2010). These different arrangements are distinguished by their geometry, composition and relative frequency across the streambed surface (Hendrick et al., 2010) and each vary in response to local slope and the size and sorting of surface grains (Wilcock, 1992; Wittenberg, 2002; Wittenberg and Newson, 2005; Wittenberg et al., 2007; Strom and Papanicolaou, 2008). For example, while clusters can occupy up to 50% of the surface in mountain streams (Billi, 1987, 1988; Diepenbrock and De Jong, 1994), they typically account for a smaller proportion of the streambed in lowland reaches (c.3-20%; Brayshaw, 1984; Reid et al., 1992; Wittenberg and Newson, 2005; Strom and Papanicolaou, 2008). The spatial extent of the cluster will also respond to bed texture, i.e. the coarser the streambed, the greater the height, width and length of the bedform (Wittenberg, 2002; Wittenberg and Newson, 2005; Wittenberg et al., 2007; Strom and Papanicolaou, 2008). Furthermore, in response to the lack of available medium-to-fine sized sediment, clusters may be incomplete and lack stoss and wake accumulations or

comprise a loose nesting of particles (Brayshaw, 1985; Billi, 1987; Hassan and Reid, 1990).

In addition to the effects of bed texture and sediment supply on bedform-scale structure, the spatial distribution and relative occurrence of clusters across gravel bed surfaces are affected by flow regime (Wittenberg, 2002). In this regard, the flashy nature of ephemeral flows, which limits the development of a coarse surface armour, also restricts the opportunity for grains to assemble into bedforms during receding flows (Wittenberg and Newson, 2005). As a result, previous workers have observed the streambeds of ephemeral channels are characterised by a smaller frequency of clusters compared to their perennial counterparts; occupying c.10% and c.30% of the surface respectively (Wittenberg, 2002). However, our understanding of bedform-scale structure in the beds of ephemeral channels is hampered by a lack of research.

### **2.2.3. Influence of bed structure on flow resistance**

The classical approaches of Nikuradse (1933) and Keulegan (1938) assume surface roughness is a strict function of surface grain size, based on observations derived over uniform beds. However, natural alluvial streambeds are topographically complex and comprise a wide range of grain sizes and shapes (Prestegard, 1983; Bathurst, 2002). Furthermore, as subsections 2.2.1-2 describe, the roughness of a surface is also a function of the way particles are arranged, e.g. grain packing densities and larger accumulations of grains, and the characteristics of this bed structure must be acknowledged within models of flow resistance. The discussion that follows is based on Powell (2014).

In seeking to acknowledge the influence of bed structure on boundary roughness, several workers have characterised  $k_s$  using statistics of streambed topography which include i) the size, shape and spatial distribution of roughness elements and ii) moments of the bed elevation distribution. Regarding the former, early flume work by Rouse (1965) characterised boundary roughness through the height ( $k$ ) and spatial concentration ( $\lambda$ ) of a regular array of roughness elements on an otherwise planar, artificial bed. In adapting equation 2.1, this relationship could be described, for  $\lambda < 0.125$ , by:

$$\frac{1}{\sqrt{f}} = 2 \cdot \log_{10} \left( \frac{R}{\lambda k} \right) - 0.82 \quad [2.7]$$

Subsequent flume-based research by Gomez (1993) considered water-worked beds comprised of a mix of grain shapes and similarly recorded a linear relationship between the Darcy-Weisbach friction factor and roughness geometry. However, the results of Gomez (1993) plotted below those of Rouse (1965), i.e. lower values of  $1/\sqrt{f}$  for a given  $R/\lambda k$ , which was attributed to several factors including the contribution of particle shape on bed structure and, hence, boundary roughness and flow resistance. Other workers considering the spatial distribution of roughness element have found the concentration of clusters to adjust to induce a maximum resistance to the flow (Hassan and Reid, 1990), however these preliminary observations require further validation.

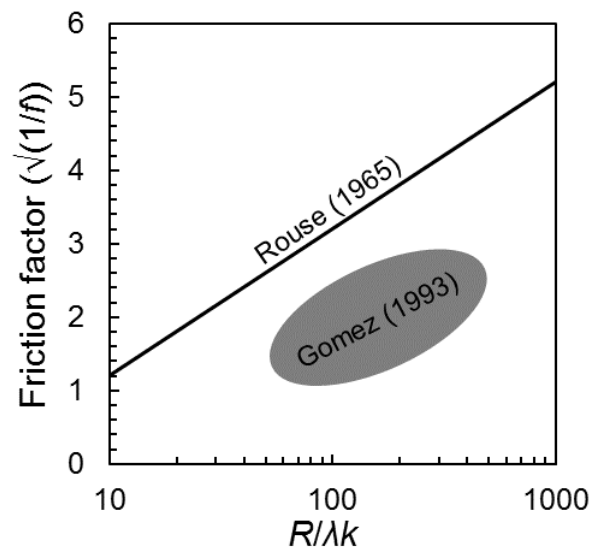


Figure 2.4 Relationship between friction factor and boundary roughness geometry. The solid line marks the relationship of Rouse (1965) and the grey oval the envelope of values observed by Gomez (1993) for different shape gravel-sized sediments. Diagram adapted from Powell (2014).

Several workers have also sought to relate the structural properties of the bed to boundary roughness and flow resistance using moments of the bed elevation distribution (Nikora et al., 1998). For example, Aberle and Smart (2003) characterised  $k_s$  in terms of the standard deviation of bed elevations ( $\sigma_z$ ). The use of  $\sigma_z$  as a roughness parameter was found to generate better predictive estimates of flow resistance compared to models based on particle size although there is some evidence that this approach is less suitable in steep streams (e.g. Nitsche et al., 2012). Recent advancements in remote sensing techniques (e.g. digital photogrammetry, laser scanning) have allowed workers to capture high resolution surface information from alluvial streambeds and, in the process, devise morphometric parameters to better characterise boundary roughness. However, these techniques have yet to be applied extensively across a broad range of gravel bed rivers in

different fluvial environments and, as such, the characteristics of bed structure remain relatively poorly understood. Given the complexity and scale-dependency of bed structure, it also remains unclear which structural metric best describes boundary roughness for predicting flow resistance.

#### 2.2.4. Influence of bed structure on particle stability

The presence of grain- and bedform-scale structure will modify the mobility of individual particles and, in doing so, bed stability. In terms of grain-scale structure, differences in packing arrangements will have important implications on bed stability. For instance, with a view to the illustrative bed conditions in Figure 2.2, surface grains resting in an overloose (open structured) boundary are comparatively less stable and require a smaller entrainment stress than grains resting in an underloose (tightly structured) boundary (Laronne and Carson, 1976; Reid and Frostick, 1984; Powell and Ashworth, 1995). The travel distances of grains within loosely packed beds will also be greater compared to more tightly packed arrangements (Laronne and Carson, 1976). The effects of grain-scale bed structure were demonstrated by Church (1978) to affect the relative influence of particle size on grain entrainment stresses. For instance, differences in grain packing between reaches (overloose and underloose boundaries) were observed to generate nearly an order of magnitude range in  $\tau_c$  for a given particle diameter (Figure 2.4; Church, 1978).

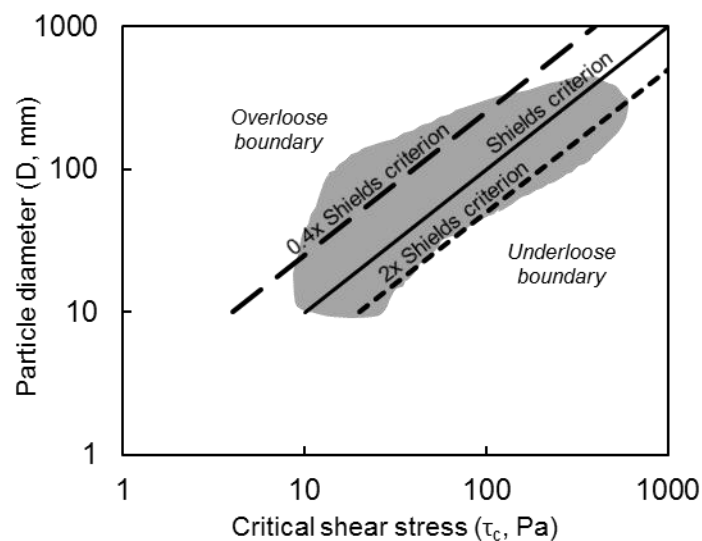


Figure 2.5 Critical shear stress vs. particle diameter for river and canal data (scatter of values approximated by grey bounding area). Values shown in relation to Shields criterion ( $\tau_c = f(D)$ ,  $f(0.4.D)$ ,  $f(2.D)$ ) and conceptual underloose and overloose boundaries. Modified after Church (1978).

In attempting to better define particle stability, previous workers have sought to explore the various factors that control grain-scale structure including sediment supply and flow regime (Recking, 2012; Bunte et al., 2013; Masteller and Finnegan, 2017). For instance, bed stability has been observed to increase from the conditioning of surface grains during antecedent flows, even those not capable of particle entrainment (Frostick et al., 1984; Reid et al., 1985; Monteith and Pender, 2005; Paphitis and Collins, 2005; Haynes and Pender, 2007; Turowski et al., 2011; Ockelford and Haynes, 2013) and through local site factors including bed material sorting (Johnson, 2016). Regarding the latter, the presence of a fine-grained interstitial matrix can generate an infilled packing arrangement of surface grains which increases bed cohesion and entrainment thresholds (Reid et al., 1985; Reid and Hassan, 1992; Wilcock, 2001; Haynes and Pender, 2007; Barzilai et al., 2013). The spatial arrangement of coarse surface clasts has more recently been found to affect bed stability and, in this respect, more stable beds are associated with an even distribution of  $D_{90}$ -sized grains (Piedra et al., 2011). However, many of these observations have been derived from flume experiments and few field-based studies have yet to explore the control of grain-scale structure on particle stability.

In seeking to parameterise particle stability, previous workers have sought to mechanistically predict the grain entrainment stresses by resolving the force balance of individual particles (Wiberg and Smith, 1985, 1987; Bridge and Bennett, 1992). Through this approach, the motion of surface grains is initiated once the imposing forces of the flow exceed the resistive forces of the grain and local surface and, following the schematic in Figure 2.5, grain entrainment stress is a function of the forces of fluid lift ( $F_L$ ), drag ( $F_D$ ) and particle weight ( $F_W$ ).

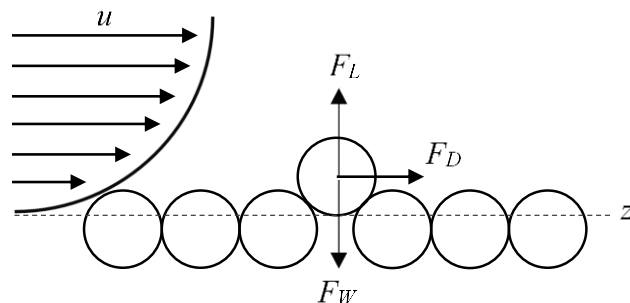


Figure 2.6 The force balance of an individual grain relative to the logarithmic velocity profile ( $u(z)$ ) above the local mean bed level ( $z$ ). After Kirchner et al. (1990).

The forces of lift, drag and weight are derived from various parameters which describe the positioning of surface grains and the sedimentological properties (size, shape and

sorting) of the grain and the local surface. As Figure 2.6 illustrates, the mobility of surface grains is a function of grain pivoting angle ( $\Phi$ ) and the projection ( $p$ ) and exposure ( $e$ ) of the grain to the flow, relative to the local bed level (Fenton and Abbott, 1977; Kirchner et al., 1990).

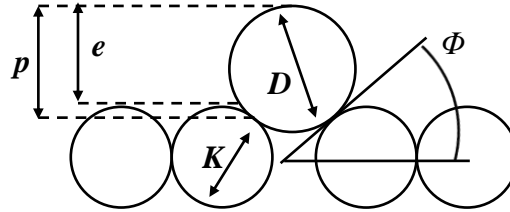


Figure 2.7 Illustration of particle mobility as a function of pivoting angle ( $\Phi$ ), projection ( $p$ ) and exposure ( $e$ ) relative to the local bed level. Size of sample grain and local bed in  $D$  and  $K$  respectively. After Kirchner et al. (1990).

At the threshold of particle motion, the forces of lift, drag and weight can be estimated using:

$$\frac{F_D}{\tan \Phi} + F_L = m \cdot F_W = \frac{1}{6} (\rho_s - \rho) g \pi D^3 \quad [2.8]$$

where  $m$  is the lift force multiple (Hodge et al., 2013), otherwise referred to as the ‘excess force ratio’ (Sanguinito and Johnson, 2012). For unconstrained sediment, the vertical force required to lift individual grains will equal particle weight and a neutral multiplier ( $m = 1$ ) will apply in  $F_L = m \cdot F_W$ . An increase in  $m$  away from 1 will reflect an increase in the vertical lift force in excess of particle weight, caused by various factors which impede sediment entrainment, e.g. in heavily mortared streambeds.

$$F_D = \frac{C_D}{2} \rho \int_{p-e}^p W(z) u(z)^2 dz \quad [2.9]$$

where,  $C_D$  is the empirical drag coefficient (0.4; Wiberg and Smith, 1985) and  $W(z)$  is the grain cross-section width at height  $z$ .

$$F_L = \frac{C_L}{2} \rho Ar_C [u(p)^2 - u(p - D)^2] \quad [2.10]$$

where,  $C_L$  is the empirical lift coefficient (0.2; Wiberg and Smith, 1985) and  $Ar_C$  is the cross-sectional area of the grain normal to the lift force.

However, as subsections 2.3.4-5 discuss in further detail, the characterisation of gravel bed surface stability using force balance parameters has only recently been applied in a natural setting and requires further exploratory work.

At larger scales, previous workers have generally found that bedform-scale structure will fundamentally affect particle stability (Sear, 1992; Church et al., 1998) although Billi (1988) and De Jong (1991) have contested that cluster bedforms play a negligible role on

bed stability and sediment transport. This research has largely relied on qualitative characterisation of bedforms and investigated the strength and stability of these features over natural flows. For example, coarse obstacle clasts have largely been observed to stabilise bedforms and shelter a local neighbourhood of grains (Strom and Papanicolaou, 2008). In addition, a positive feedback is derived from stoss and wake accumulations which protect the obstacle clast from the full force of the flow. As a result, clustered grains require a greater entrainment stress than fully exposed grains resting on an open-pane bed (Brayshaw et al., 1983; Brayshaw, 1985; Reid et al., 1992; Hassan and Church, 2000). In this respect, Sear (1992, 1995, 1996) and Sohag (1993) observed the additional mechanical strength generated from intergranular friction, interlock and shelter caused clusters to configure into some of the most stable artefacts in gravel streambeds (Reid et al., 1992). The presence of bedform-scale structure has also been found to delay the incipient motion of surface grains (Hassan and Church, 2000), reduce the distance and duration of transport events (Reid et al., 1992), decrease bedload flux (Strom et al., 2004) and increase the residence time of surface sediment (Iseya and Ikeda, 1987; Church et al., 1998). Furthermore, recent work has suggested coarse clasts which anchor bedforms exert a greater control over a wider area in moderating bed stability than has been established previously (Hendrick et al., 2010). However, critically, despite the acknowledged importance of structure on stability, this approach has often relied on subjective methods to identify bedform-scale structure. Further work should therefore seek to consider analytical (objective) approaches to characterise grain- and bedform-scale bed structure and investigate their influence on particle stability.

### **2.3. Characterising bed structure and stability**

Previous workers have used several metrics to describe the structural character of gravel bed microtopography. These include bed elevation pdfs (probability density functions) and their statistical moments (standard deviation, skewness and kurtosis; subsection 2.3.1), 1D and 2D variogram analyses (subsection 2.3.2) and the more local parameters of inclination, slope and combined slope-aspect (subsection 2.3.3). Bed stability is then considered through the force balance parameters: pivoting angle (subsection 2.3.4) and grain protrusion (subsection 2.3.5).

### 2.3.1. Bed elevation pdfs and statistical moments ( $\sigma_z$ , $Sk_z$ and $Ku_z^*$ )

The bed elevation pdf is a global measure of the distribution of elevations across a surface. In this regard, the form of the bed elevation pdf will reflect the nature of topographic variability within a streambed and can help to inform an understanding of bed structure. Previous workers have sought to characterise the bed elevation distribution through several statistical moments which quantify different aspects of the form of the pdf. This study considers the standard deviation of bed elevations ( $\sigma_z$ ), skewness ( $Sk_z$ ) and kurtosis ( $Ku_z^*$ ). The former, the standard deviation of bed elevations, is one of the most commonly cited statistical moments of the pdf and provides a quantitative measure of the spread of the distribution. It characterises the vertical roughness length of the surface and, in this respect, a higher standard deviation of bed elevation reflects a rougher surface while a smoother surface is described by a lower standard deviation of bed elevations (Nikora et al., 1998; Aberle and Smart, 2003; Smart et al., 2004; Aberle and Nikora, 2006; Coleman et al., 2011). Skewness describes the asymmetry of the distribution and, as Figure 2.7 illustrates, a neutral skewness ( $Sk_z = 0$ ) characterises a symmetrical Gaussian distribution. Away from a normal form, a positive skew ( $Sk_z > 0$ ) characterises a distribution where the modal bed elevation is less than the mean and the tail extends to high elevations whereas a negative skewness ( $Sk_z < 0$ ) reflects a distribution where the modal elevation falls below the mean and a tail of lower-than-average elevations (Coleman et al., 2011). Lastly, kurtosis describes the relative ‘tailedness’ or ‘peakedness’ of the distribution relative to a normal distribution (Figure 2.7; De Carlo, 1997; Coleman et al., 2011). A normal distribution has  $Ku_z = 3$  ( $Ku_z^* = 0$  where  $Ku_z^*$  is the excess kurtosis defined as  $Ku_z - 3$ ). Away from a Gaussian form, a *leptokurtic* distribution exhibits a high kurtosis ( $Ku_z^* > 0$ ) and is characterised by a narrower peak with a rapid decline in elevation density toward heavier tails than would be expected for a normal distribution while a *platykurtic* distribution exhibits a lower kurtosis ( $Ku_z^* < 0$ ) and is characterised by a flatter peak and lighter tails.

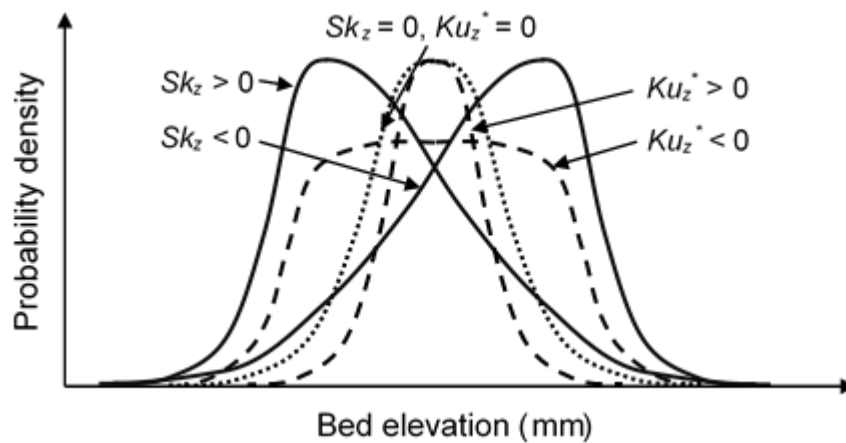


Figure 2.8 Schematic bed elevation pdfs illustrating changes in skewness (solid lines) and kurtosis (dashed lines) relative to a normal distribution (dotted line). Adapted from Coleman et al. (2011).

Previous workers have sought to examine the effects of bed structure on bed elevation pdfs by characterising the topography of unstructured and structured beds and studying shifts in the pdf form over time or with changes in flow strength. Much of this understanding has been derived from flume experiments. In terms of the effects of bed structure on the bed elevation distribution, the pdfs for unstructured beds are generally characterised by narrow, peaked distributions with slight negative skew and positive kurtosis (Figure 2.8; Aberle and Nikora, 2006; Cooper and Tait, 2009; Mao et al., 2011; Powell et al., 2016). A shift in the form of the bed elevation pdf is observed following water-working to reflect grain size adjustments and the development of bed structure. In this respect, the distributions for water-worked gravel beds in field and flume experiments are characterised by broader distributions with positive skew and kurtosis and that have almost universally been found to deviate from a Gaussian form in being asymmetric and more peaked (Figure 2.8; Brown and Willetts, 1997; Nikora et al., 1998; Marion et al., 2003; Aberle and Nikora, 2006; Hodge et al., 2009b; Coleman et al., 2011; Ockelford and Haynes, 2013; Qin et al., 2013; Bertin and Friedrich, 2014; Curran and Waters, 2014; Powell et al., 2016). The increase in the range and standard deviation of the distribution reflects an increase in surface roughness from the accumulation of coarse grains on the bed during armouring (through vertical and horizontal winnowing). The presence of bedforms and larger scales of sedimentary structure may also act to increase the range and standard deviation of bed elevations by supporting grains at higher elevations above the mean bed level than would otherwise be expected for a regionally planar surface (Gomez, 1993; Aberle et al., 2010; Coleman et al., 2011). The shift in the negative to

positive skew of the distribution and decline in kurtosis is similarly attributed to the armouring process and reflects the coarsening of the surface and the development of bedforms (Brown and Willetts, 1997; Aberle and Nikora, 2006; Aberle et al., 2010; Coleman et al., 2011; Bertin and Friedrich, 2014; Curran and Waters, 2014; Powell et al., 2016).

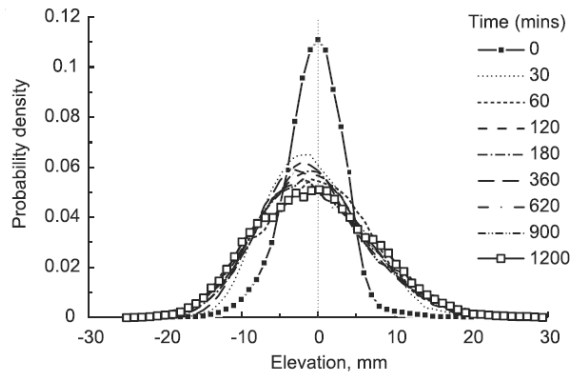


Figure 2.9 Change in bed elevation pdf form over time with a constant flow (Powell et al., 2016: 1502).

Coleman et al. (2011) was able to use the differences in  $Sk_z$  and  $Ku_z^*$  for a limited sample of unstructured and structured beds to classify the structure of gravel and sand bedded rivers (Figure 2.9). In this regard, water-worked field and flume gravels (' $W_{gm}$ ';  $0.2 \leq Sk_z \leq 1.0$ ,  $-0.2 \leq Ku_z^* \leq 2.4$ ) are clearly differentiated from a random collection of gravels (screeded, ' $S_{gm}$ ';  $-0.7 \leq Sk_z \leq -0.2$ ,  $0.6 \leq Ku_z^* \leq 1.6$ ) using a classification based on the ratio between  $Sk_z$  and  $Ku_z^*$ .

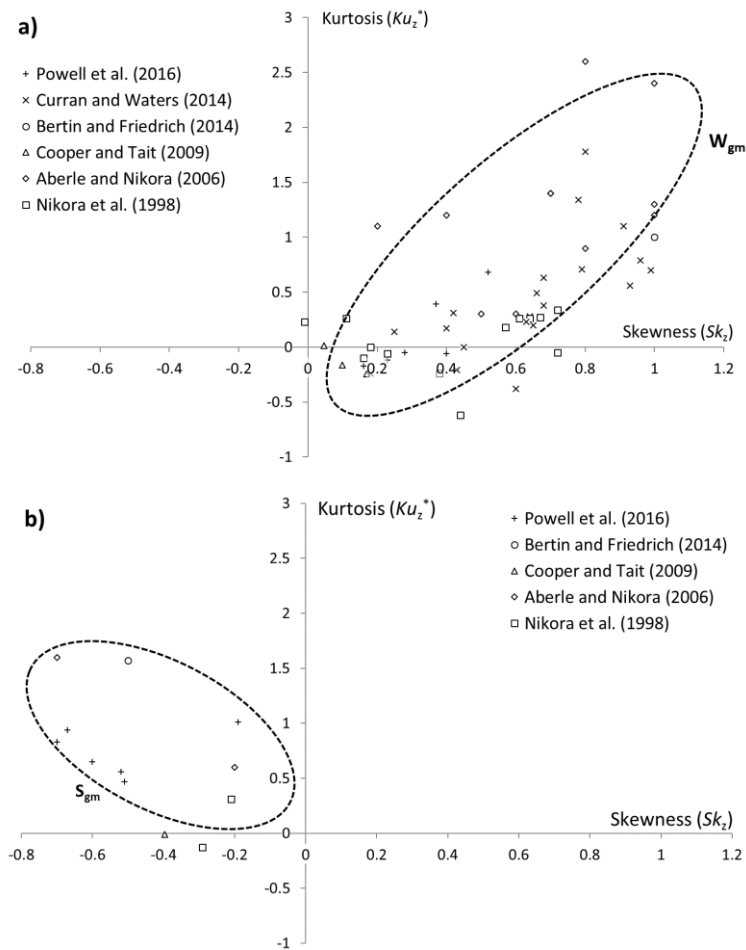


Figure 2.10 Bed structure classification by  $Sk_z$  and  $Ku_z^*$  for a) water-worked and b) unworked beds. The boundaries marked by ‘ $W_{gm}$ ’ and ‘ $S_{gm}$ ’ approximate the structural classification of Coleman et al. (2011).

Previous workers have also sought to study shifts in pdf form over time and with changes in flow strength to better understand the dynamics of water-worked beds. As Figures 2.8a and 2.8b illustrate, prolonged periods of effective flow and higher formative discharges generate distributions with a wider range and larger standard deviation than shorter formative flows or those with lower flow strengths (Aberle and Nikora, 2006; Mao et al., 2011; Mao, 2012; Powell et al., 2016). This can be explained by adjustments in surface grain size and bed structure. In terms of bed texture, for instance, the coarsening of the surface will increase with flow strength (Mao et al., 2011) while, considering bed structure, the packing of surface grains will loosen following an increase in shear stress to produce a rougher surface (Hodge et al., 2009b; Mao et al., 2011; Mao, 2012). Skewness has also been shown to increase with flow magnitude and duration and reflects the accelerated winnowing of fines and accumulation of coarse particles on the bed surface (Aberle and Nikora, 2006; Powell et al., 2016). Previous workers have, however,

debated about how long it takes for structure to become apparent in a skewed bed elevation pdf. For example, Mao et al. (2011) observed skewness to increase rapidly upon the onset of water-working toward a stable equilibrium whereas for Ockelford and Haynes (2013) changes in skewness were slower-forming and required prolonged periods of formative flow. Meanwhile, several workers have recorded a rapid decline in kurtosis toward a stable equilibrium in response to water-working (Coleman et al., 2011; Powell et al., 2016). During supply-limited, degradational phases of armour development this, in some cases, has led to a platykurtic distribution of bed elevations (Marion et al., 2003). The described shifts in pdf form largely reflect grain size adjustments, e.g. the coarsening of the surface over time or with discharge, since previous workers have found the standard deviation of bed elevations to be linearly correlated with particle size (Gomez, 1993; Nikora et al., 1998; Aberle and Nikora, 2006; Brasington et al., 2012). However, while some workers have found a similar relationship between  $\sigma_z$  and  $D_{50}$  persists for gravel patches subject to perennial and ephemeral flows (Brasington et al., 2012; Storz-Peretz and Laronne, 2013) others have recorded different linear relationships for different facies (Heritage and Milan, 2009) which may reflect differences in sedimentology and bed structure (Church et al., 1987; Gomez, 1993; Hodge et al., 2009b; Brasington et al., 2012; Rychkov et al., 2012; Curran and Waters, 2014; Bertin and Friedrich, 2016).

### **2.3.2. Variogram analysis: 1D and 2D approaches**

Conventional structural parameters, e.g. moments of the bed elevation distribution, are limited since they are aspatial (lumped) statistics and depend on the length of profile or size of surface under consideration. Since streambed structure is scale-dependent (e.g. Subsections 2.2.1 and 2.2.2), previous workers have sought an analytical approach that characterises surface roughness across a range of spatial scales but which is independent of sample size (Butler et al., 2001). In this respect, variograms have been used to characterise the roughness and scaling properties of gravel surfaces for streambed profiles sampled in flow parallel (e.g. Robert, 1988) and flow transverse directions (e.g. Nikora et al., 1998) and for surfaces (e.g. Butler et al., 2001).

A variogram quantifies the spatial dependency of point pairs across a surface using estimates of semivariance calculated for different lag distances through large, random samples of point pairs. In mathematical terms, the semivariance ( $\gamma$ ) at lag  $h$  is calculated for a profile using:

$$\gamma(h) = \frac{1}{2n-1} \cdot \sum_{i=1}^n (z_{i+h} - z_i)^2 \quad [2.11]$$

where  $z_i$  is the elevation of the point at the  $i$ th location from a total of  $n$  observations.

Early workers (Robert, 1988, 1991; Bergeron, 1996) identified several basic properties of 1D variograms plotted in log-log space (Figure 2.10). By definition,  $\gamma = 0$  when  $h = 0$  and  $\gamma$  will remain low at small lag distances. Semivariance will increase as  $h$  increases since point pairs sampled at large scales of separation will be more statistically dissimilar (less spatially dependent) than those taken at smaller lags. Semivariance will continue a finite rise until the variance of the surface is reached ( $\gamma = \sigma_z^2$ ) whereupon the variogram plateaus. This feature is termed the sill of the variogram and the corresponding lag abscissa defines the range of influence,  $h_2$  (Robert, 1988). For lags greater than  $h_2$  sample pairs are statistically independent and  $\gamma$  fluctuates about the sill. Therefore, the range  $0 < h < h_2$  defines the limit of statistical dependency of bed elevations. If the 1D variograms display power law behaviour within this region (linear sections in log-log space), it is possible to estimate the fractal dimension (Hausdorff dimension,  $Hd$ ) for that feature as the gradient of the linear segment<sup>2</sup>. For the bifractal variogram model of Robert (1988, 1991) the range  $0 < h < h_2$  was characterised by two linear sections delimited by a break in slope at lag  $h_1$  which could be modelled as power functions using:

$$\gamma_1(h) \propto h^{2H_1} \quad \text{for} \quad 0 < h \leq h_1 \quad \text{and} \quad [2.12]$$

$$\gamma_2(h) \propto h^{2H_2} \quad \text{for} \quad h_1 < h \leq h_2 \quad [2.13]$$

where the subscripts <sub>1</sub> and <sub>2</sub> refer to the first and second fractal bands of a bifractal surface.

The power law (Hurst) exponent,  $H$ , in equations 2.12 and 2.13 is related to the fractal dimension (through  $H = 2 - Hd$ ) and describes the irregularity of a feature relative to that generated from random process; for which the  $H$  is 0.5 (Robert, 1988, 1991; Bergeron, 1996).  $H > 0.5$  represents a smoothing of surface roughness while  $H < 0.5$  signifies an increase in the irregularity of the surface.

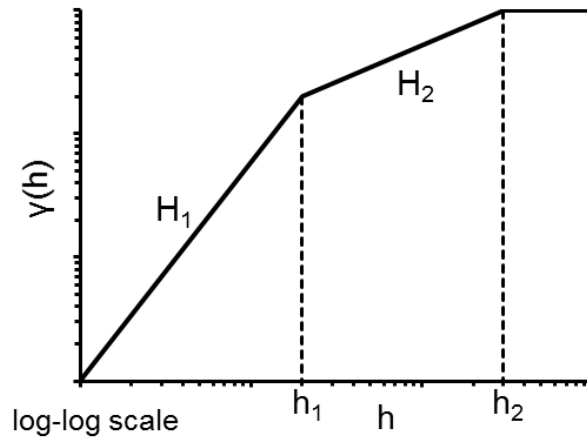


Figure 2.11 The bifractal variogram model of Robert (1988, 1991) derived from bed profiles with a flow parallel direction.

The two linear trends ( $H_1$  and  $H_2$ ) that define the bifractal variogram model of Robert (1988, 1991) correspond to two fractal bands each describing a distinct scale of roughness. In this respect, the length of the  $H_1$  fractal band,  $h_1$ , was found to closely approximate the textural properties of the surface (e.g.  $h_1 \approx D_{95}$ ; Robert, 1988, 1991) and was interpreted as the scale over which grain roughness operates. The length of the grain-scale fractal band has been observed by previous workers to increase under formative and conditioning flows in response to changes in grain-scale bed structure (Ockelford and Haynes, 2013; Powell et al., 2016). As the range of influence,  $h_2$ , extends to lags greater than the largest grains on the bed, larger scales of structure must explain the roughness properties of the  $H_2$  fractal band. For example, early workers have suggested  $h_2$  is a function of the maximal spacing of bedforms (Robert, 1988, 1991). More recent work by Butler et al. (2001), using high resolution topographic datasets of small gravel patches, also found the range  $0 < h < h_2$  to be largely characterised by two linear trends. The slight curvature between these linear sections was interpreted as a smoothing of two fractal bands (Butler et al., 2001). However, in contrast to Robert (1988, 1991), the fractal bands were found to operate over a comparatively smaller scale of application which reflected the small scale of study ( $0.6 \leq h_1/D_{84} \leq 1.3$ ,  $2.8 \leq h_2/D_{84} \leq 3.7$ ). The first and second log-linear fractal regions, therefore, refer to the roughness properties at the scale of grain surfaces (sub-grain) and of individual grains, respectively.

Butler et al., (2001) observed that values of the Hurst exponent were greater for the subgrain-scale fractal band compared to the grain-scale fractal band. This indicates that surface roughness was greater at the grain-scale compared to the subgrain-scale which was attributed to the smoothing of grain surfaces by *in-situ* abrasion (Butler et al., 2001).

Since  $H$  was found to vary little with direction this suggests an isotropic surface at subgrain-scales (Butler et al., 2001). For the bifractal model of Robert (1988, 1991), values of  $H$  were greater for the grain-scale fractal band than the bedform-scale fractal band which indicates that roughness at the scale of individual particles was smoother than that at the scale of bedforms. This was attributed to factors including particle size, sorting, shape and bed structure. In terms of grain size, for instance,  $H$  for the grain-scale fractal band (and unlike the bedform-scale fractal band) was found to increase with  $D_{50}$  (Bergeron, 1996). This was attributed to that fact that, at small scales of consideration, a bed profile will be less topographically complex for a bed comprised of a small number of large particles compared to a large number of small particles. A decrease in sorting was also found to increase values of  $H$  and the length of the grain- and bedform-scale fractal bands. This reflected the reduced irregularity of the surface and increased length of spatial dependency from the smoothing of the surface by fines (to generate an infilled bed structure). Previous workers have debated to what extent particle shape affects values of  $H$  and  $h$ . For example, Robert (1991) found particle shape to be a secondary factor and modulated the rate of increase in  $H$  and  $h$  with sorting while Nikora et al. (1998) found particle shape did not improve the relationship between grain size and grain-scale fractal length and so attributed other factors, e.g. particle orientation and packing, to act collectively to moderate the extent of grain-scale roughness. Previous workers have also questioned whether grain-scale fractal bands display isotropic (Nikora et al., 1998; Nikora and Walsh, 2004; Powell et al., 2016) or anisotropic behaviour (Butler et al., 2001; Mao et al., 2011; Curran and Waters, 2014). The latter, grain-scale surface anisotropy, was attributed to the preferential orientation of surface grains which developed during the formative phases of surface armouring and the development of grain-scale bed structure (Curran and Waters, 2014).

The bifractal model presented by Robert (1988, 1991) has, however, been contested by Nikora et al. (1998) and, more latterly, Hodge et al. (2009b). In the first instance, Nikora et al. (1998) used a second-order structure function  $Sf(\Delta x, \Delta y)$  of bed elevations  $z(x, y)$  in place of the variogram which was calculated using:

$$Sf(\Delta) = \frac{1}{n-1} \cdot \sum_{i=1}^n (z_{i+h} - z_i)^2 \quad [2.14]$$

Thus, the structure function is comparable to the variogram with only absolute values differing by a factor of two. The axes of the structure function were normalised to

compare flow parallel and flow transverse bed profiles sampled for a range of surfaces:  $Sf(\Delta x, \Delta y)$  as a proportion of  $2\sigma_z^2$  and  $\Delta x, \Delta y$  by  $\Delta x_0, \Delta y_0$ . The characteristic scale ( $\Delta x_0, \Delta y_0$ ), was calculated as the abscissa of the intercept between the power function for  $H_1$  ( $Sf(\Delta x) \sim \Delta x^{2H_1}$  and  $Sf(\Delta y) \sim \Delta y^{2H_1}$ ) and the sill (e.g. for  $\Delta x_0$  in Figure 2.11a). As Figure 2.11b illustrates, the structure function was found by Nikora et al. (1998) to be characterised by three regions: 1) a log-log linear increase in  $Sf(\Delta x, \Delta y)$  with  $\Delta x, \Delta y$  at small spatial scales termed the scaling region, 2) a saturation region over longer lags where the structure function is constant ( $Sf(\Delta x, \Delta y) = Sf(\text{inf}) = 2\sigma_z^2$ ) and 3) a curved transition region which separates the scaling and saturation regions. Critically, therefore, the variogram model of Nikora et al. (1998) contains only one linear (fractal) section compared to the bifractal model presented by Robert (1988, 1991). The first break in slope for the bifractal model,  $h_1$ , does however correlate with the boundary between the scaling and transition regions ( $\Delta x/\Delta x_0, \Delta y/\Delta y_0 \approx 0.6$ ; Nikora et al., 1998) while the range of influence,  $h_2$ , correlates with the boundary between the transition and saturation regions ( $\Delta x/\Delta x_0, \Delta y/\Delta y_0 \approx 2.5$ ; Nikora et al., 1998). As a consequence, the fractal band which characterises the scaling region describes the roughness properties of individual surface grains.

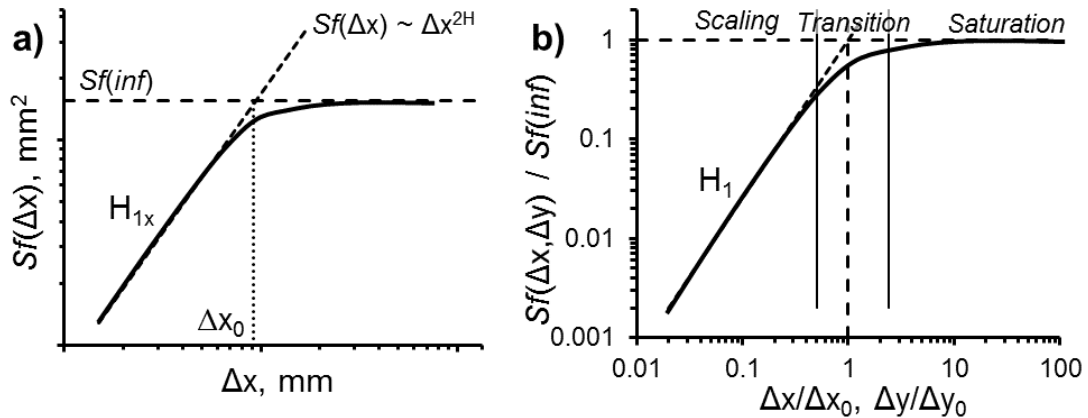


Figure 2.12 a) Method of determining the characteristic scale  $\Delta x_0$  (identical process for  $\Delta y_0$ ) and b) illustration of non-dimensional structure function. Both adapted from Nikora et al. (1998).

More recent research (e.g. Hodge et al., 2009b), considering a wider variety of gravel beds (from different geomorphic units (e.g. pool, riffles, etc) for different reaches) and a larger scale of study ( $1\text{m}^2$  patches), found the range  $0 < h < h_2$  to be characterised by an asymptotic increase in  $\gamma$  with  $h$  (Figure 2.12). In this regard, a curved variogram indicates multifractal behaviour, i.e. roughness varies continuously as a function of lag, unlike the models of Robert (1988, 1991) or Nikora et al. (1998). While a quadratic model was found

to best approximate this curvature, there is no *a priori* theoretical reason why gravel bed topography should exhibit multifractal behaviour that would warrant trying to fit a non-linear model (Hodge et al., 2009b). In place of quantitative analysis, the curved 1D variograms were assessed in qualitative terms which included a comparison of flow parallel and flow transverse profiles. This comparison of grain-scale semivariance revealed surface isotropy for one of the study reaches while the variograms for pool, pool exit and riffle facies at the other sample demonstrated evidence of anisotropic behaviour, implying preferential particle alignment.

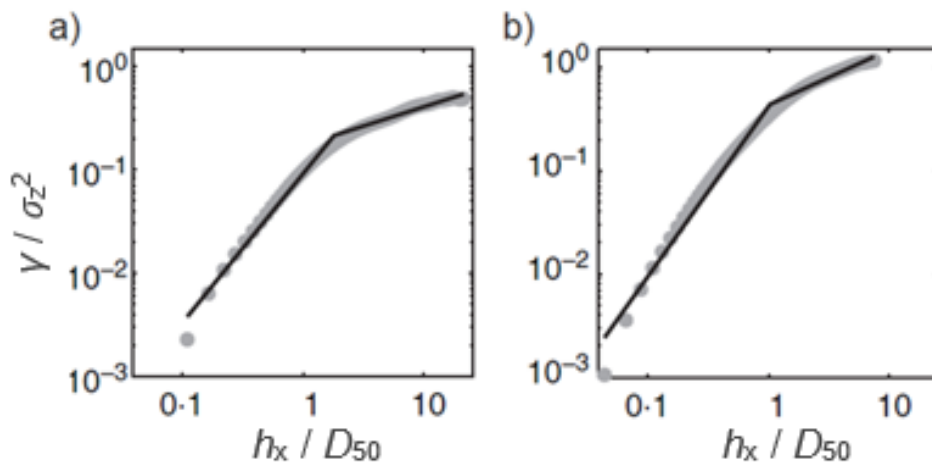


Figure 2.13 Flow parallel 1D variogram for the a) River Feshie and b) Bury Green Brook gravel patches in Hodge et al., (2009b: 2033). In a) and b) a two-section line (black line) provides a poor approximation of the curved variograms (grey dots).

In addition to 1D profiles, the variogram approach has also been applied to surfaces (e.g. Butler et al., 2001). Here, semivariance is estimated for a range of lag distances and across a spectrum of directions for lag pairs sampled from the surface using:

$$\gamma(h_x, h_y) = \frac{1}{2(x-h_x)(y-h_y)} \cdot \sum_{i=1}^{x-h_x} \sum_{j=1}^{y-h_y} (z_{i,j} - z_{i+h_x, j+h_y})^2 \quad [2.15]$$

where  $\gamma$  is estimated for the lags  $h_x$  and  $h_y$  in the x- and y-directions respectively and  $z(i,j)$  is the elevation at the surface location  $(i,j)$ .

The 2D variogram surfaces generated through equation 2.15 are used to visually interpret the directional properties of bed structure across a range of spatial scales. As such, they do not rely on conforming to a specific model. A 2D variogram surface plotted in log-log space will demonstrate isotropic changes in semivariance if isopleth contours are spherical (Figure 2.13a). Anisotropic changes in semivariance are indicated by non-spherical (elliptical) isopleth contours (Figure 2.13b). In addition, changes in the contour

spacing (the rate of increase in  $\gamma$  with  $h$ ) in a given direction suggest the surfaces are characterised by more than one scale of roughness, i.e. multiple fractal dimensions.

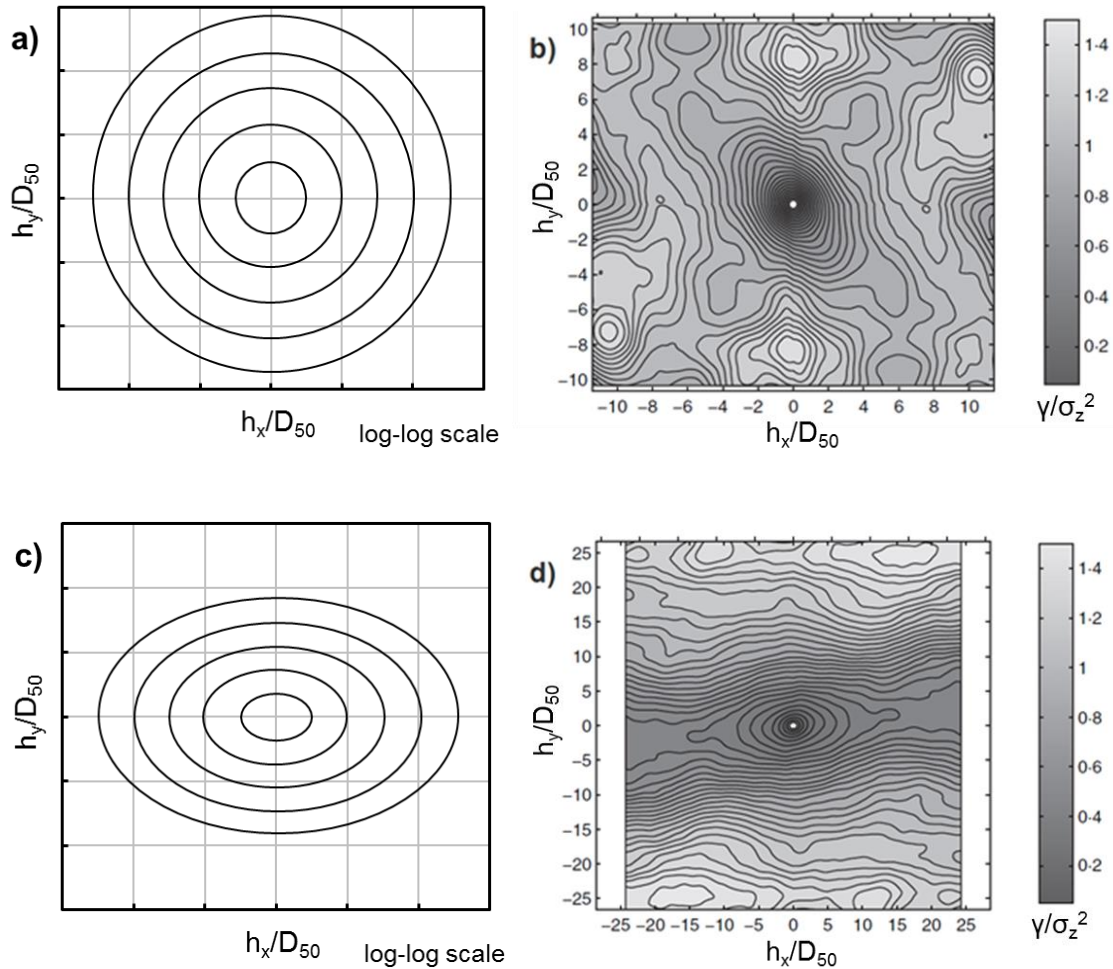


Figure 2.14 Model and real examples (taken from Hodge et al., 2009b: 2032) of 2D variograms exhibiting a-b) isotropic and c-d) anisotropic changes in semivariance.

Previous workers have characterised 2D variograms and structure functions across a range of spatial scales which relate to the roughness properties of grain surfaces, grains, bedforms and larger meso-scale topography (Butler et al., 2001; Mao et al., 2011; Powell et al., 2016). Over small spatial scales ( $0 < h/D_{50} < 1$ ) isopleth contours were found to be circular which for high resolution surface measurements (e.g. Butler et al., 2001) demonstrated subgrain-scale features were not directionally orientated. At coarser resolutions (e.g. Hodge et al., 2009b), small-scale noise masks subgrain-scale bed structure. At the scale of individual grains ( $h/D_{50} \approx 1$ ), the presence of elliptical contours demonstrates evidence of surface anisotropy which is driven by several factors including particle shape and orientation and the topography around coarse surface clasts (Nikora et al., 1998; Nikora and Walsh, 2004). Anisotropy at the scale of bedforms ( $h \approx 6.D_{50}$  for

Mao et al., 2011) may reflect their structural composition (Nikora and Walsh, 2004; Aberle and Nikora, 2006; Bertin and Friedrich); for example, Mao et al. (2011) observed diamond-shaped patterns of semivariance to be generated from diamond-shaped pebble clusters. Previous workers have tended to use the main axis of grain- and bedform-scale anisotropy (orientation of bed structure) to identify antecedent flow history, e.g. the direction of formative flows (Butler et al., 2001; Marion et al., 2003; Nikora and Walsh, 2004; Qin and Ng, 2011; Curran and Waters, 2014; Huang et al., 2016). For the exploratory flume work of Marion et al. (2003), surface anisotropy with a main axis in a flow parallel direction was observed to form rapid upon the onset of water-working, while slower-forming surface anisotropy with a main axis in a flow transverse direction was associated with a development of a stable bed structure. The presence of anisotropy at even greater scales was attributed to trends in meso-scale topography and refers to the organisation of extended patches of higher and lower bed elevation (Figure 2.14; Powell et al., 2016).

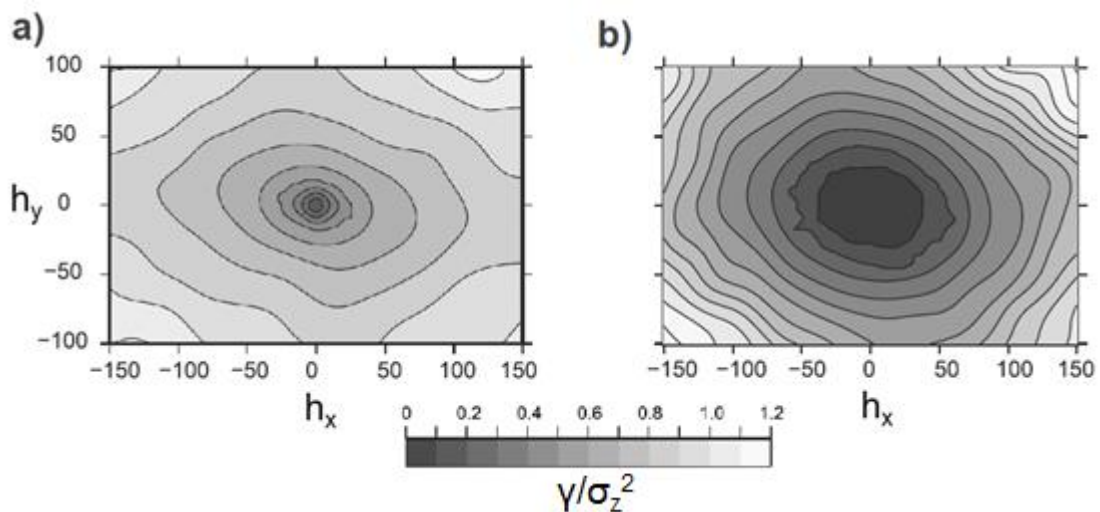


Figure 2.15 a) 2D variogram for a water-worked flume bed (Powell et al., 2016: 1506) characterised by larger-scale flow-parallel anisotropy reflecting the flow-parallel alignment of meso-scale topography, as b) a 2D variogram for the meso-scale surface (following the removal of grain-scale topography) demonstrates.

### 2.3.3. Local metrics of streambed topography: inclination, slope and aspect

The nature of grain-scale bed structure has been characterised by previous workers using several statistical parameters which describe various aspects of the local properties of streambed topography. The three local metrics used for the purposes of this study were

Smart's inclination index, slope and combined slope-aspect analysis which, when calculated at the scale of individual surface grains, help to define the i) orientation of the a-axis and ii) the angle of dip of the a-b axes plane of particles relative to the local flow direction and, hence, the characteristics of grain packing and particle arrangement.

The first of these metrics under consideration, the inclination index ( $I$ ), was devised by Smart et al. (2004) to describe the inclination of the surface over a range of lags. In doing so, the metric calculates slope between pairs of points separated by a lag distance, that typically ranges from the resolution of the DTM to several times the  $D_{50}$ . A negative value of slope is recorded for an increase in the elevation between sample pairs while a positive slope denotes a decrease in elevation and a zero value a neutral change in elevation (Figure 2.15). The inclination index is calculated by summing the positive, negative and neutral slopes between lag pairs across the surface. At the scale of individual grains, the inclination index will reveal information on the packing of surface grains. For example, a negative value of  $I$  would indicate an imbricated bed to reflect the dipping of grains in an upstream direction (Figure 2.15; Smart et al., 2004). The extension of the inclination index to larger lags reveals information on the organisation of larger scales of topography. For instance, a positive value of  $I$  indicates the surface over longer lengths typically faces downstream which may be generated from the centreline of bedforms dipping in a downstream direction (Smart et al., 2004).

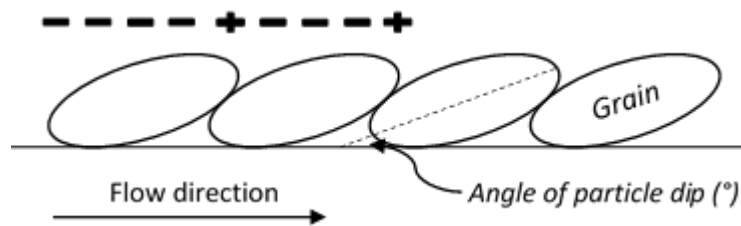


Figure 2.16 Cross-sectional illustration of an imbricated layer of surface grains. Inclination index (positive = +, negative = -) shown for grain-scale lag pairs.

The characteristics of bed structure can be examined further by considering how local slopes vary across the bed surface (Hodge et al., 2009b; Mao et al., 2011). At the grain-scale, imbrication will generate a topographically smooth surface characterised by many shallow slopes and few steep slopes. The infilling of interstices within the surface by fines may similarly smoothen the streambed and increase the relative frequency of shallow slopes. These tightly packed (imbricated) and infilled bed structures will narrow and positively skew the distribution of local slopes, calculated at the scale of individual grains

and grain surfaces (e.g. Figure 2.16 *BGB E1* slope distribution). By contrast, a bed with an open structure will be populated by a greater frequency of steeper pockets between neighbouring grains and a broader, less skewed distribution of local slopes (e.g. Figure 2.16 *BGB R2* slope distribution). The latter, for instance, has been recorded during the development of static armours and for higher formative discharges for both static and mobile gravel armours (Mao et al., 2011; Qin et al., 2012).

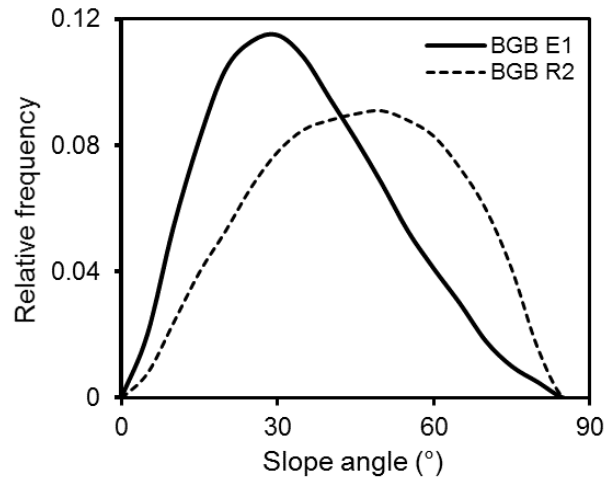


Figure 2.17 Slope distributions for a tightly packed (*BGB E1*, solid line) and more loosely arranged bed structure (*BGB R2*, dashed line) illustrated for gravel patches in Hodge et al. (2009b).

The distribution of grain-scale slopes can be considered along with local aspect to additionally characterise grain-scale bed structure (Hodge et al., 2009b). The analysis of the combined distributions of aspect and slope has been referred to, by previous workers, as the ‘AS’ method (Qin et al., 2012; Qin et al., 2013) and, when calculated at the scale of individual grains and grain surfaces, will reflect particle shape and the preferential orientation of grain-scale bed structure (Hodge et al., 2009b). The combined distributions of slope and aspect are commonly presented using polar density plots (Figure 2.17). The orientation of grain-scale bed structure can be explored using the ‘AS’ method by considering three structural conditions where i) the surface grains are strongly imbricated, ii) surface grains are preferentially aligned with their a-axis in a flow transverse or flow parallel direction or iii) no preference in the orientation of surface grains is observed. The first and second structural conditions are illustrated by Figures 2.17a and 2.17b-c respectively. For imbricated grains, the greatest density of local slopes will face in an upstream direction and maximum slope in a downstream direction. As such, the polar density plot describing such grain-scale bed structure will be characterised by a

distribution that contains one line of symmetry (e.g. Figure 2.17a; Hodge et al., 2009b; Qin et al., 2012; Qin et al., 2013). Where grain imbrication is less prominent, e.g. where the dipping angle of particles is lower for a topographically smoother surface, the density pattern of the polar plot may be split by two lines of symmetry (e.g. Figures 2.17b-c; Hodge et al., 2009b). Since the greatest change in local slope is found at the edges of surface grains, the axis of higher polar density will be normal to the preferential resting orientation of bed material; as illustrated for grains resting in a flow transverse (Figure 2.17b) and flow parallel (Figure 2.17c) direction. The ability to identify the preferential orientation of surface grains is affected by several factors including bed material sorting and the resolution of surface data. In terms of particle sorting, the noise from the local slopes of fines within poorly sorted beds may mask information on the resting orientation of larger grains while the latter, the use of low resolution surface data, may also inhibit the ability to accurately determine the direction of grain-scale bed structure (Qin et al., 2012).

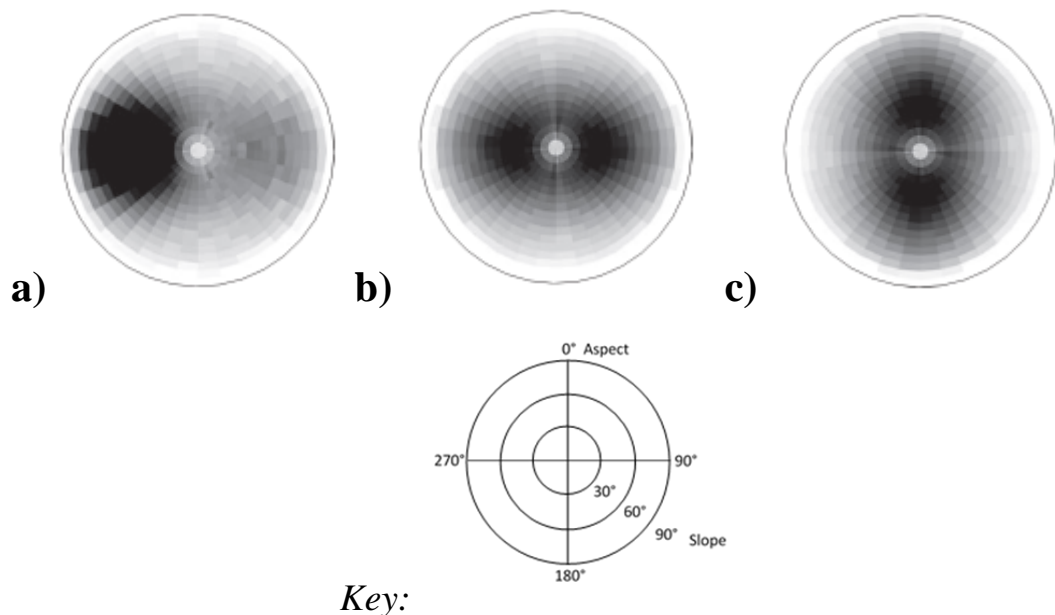


Figure 2.18 Polar density plots of grain-scale slope and aspect for simulated grains a) imbricated by  $40^\circ$  and resting parallel to the bed surface with a-axis orientated in a b) flow transverse and c) flow parallel direction. Plots shaded by density (high = black, low = grey) and taken from Hodge et al. (2009b: 2036-2037).

### 2.3.4. Parameters of particle stability: grain pivoting angle

Moving to particle stability, the force balance of surface grains is parameterised in terms of several metrics including grain pivoting angle and protrusion (see Figure 2.7;

subsection 2.2.4). Pivoting angle ( $\Phi$ ), describes the angle required to pivot a grain from its pocket within the surface (Komar and Li, 1986; Li and Komar, 1986). The parameter describes a particle's resistance to movement since grains with a larger  $\Phi$  are more difficult to entrain than those with a smaller  $\Phi$ . Early workers quantified pivoting angles using tilting boards. Chepil (1959), for instance, recorded a mean pivoting angle ( $\bar{\Phi}$ ) of  $33^\circ$  for the movement of sand over a cemented surface of similarly uniform sand-sized material. Eagleson and Dean (1961) and Miller and Byrne (1966) considered larger grains where  $\bar{\Phi} = 53^\circ$  and  $49^\circ$  respectively. These measurements were systematically larger than values predicted by the theoretical relationship for spheres of diameter ( $D$ ) resting on a bed of uniformly-sized grains ( $K$ ):

$$\tan \Phi = \frac{\zeta}{\sqrt{(D/K)^2 + 2(D/K) - \frac{1}{3}}} \quad [2.16]$$

where,  $\zeta$  is the coefficient describing the mode of particle movement. For a grain pivoting over the top of the base grain  $\zeta = 2/\sqrt{3}$  whereas through the saddle between two grains ensures  $\zeta = 1/\sqrt{3}$ .

Other workers (e.g. Miller and Byrne, 1966) describe the relationship between median pivoting angle and relative grain size using the negative power law function:

$$\Phi = \alpha(D_i/D_{50})^{-\beta} \quad [2.17]$$

where,  $\alpha$  and  $\beta$  are coefficients fitted by linear regression.

A summary of the coefficients describing Equation 2.17 is presented in Table 2.1. The preliminary results from tilting board measurements suggest the coefficients from this relationship,  $\alpha$  and  $\beta$ , vary as a function of particle shape and grain size sorting respectively (Miller and Byrne, 1966). In terms of particle shape, an increase in  $\Phi$  was found for bladed grains reflecting their tendency to imbricate and interlock (Li, 1985; Komar and Li, 1986; Li and Komar, 1986). The manner of particle movement was also affected by grain shape since bladed grains tended to slide while more rounded grains typically moved by rolling and pivoting (Li, 1985; Li and Komar, 1986). By contrast, the infilling of interstices by fines within poorly sorted beds reduces the depth and frequency of surface pockets which reduces a grain's pivoting angle.

Table 2.1 Summary of the coefficients in Equation 2.17 for tilting board (\*) and force gauge measurements (\*\*). Unworked and water-worked beds highlighted in white and grey respectively.

Study	Site/surface character	$\Phi = \alpha(D_i/D_{50})^{-\beta}$		
		$\alpha$	$\beta$	$R^2$
<b>Miller and Byrne (1966) *</b>	Natural sand	57.3	0.30	0.98
	Glass spheres, poorly sorted	45.7	0.32	0.91
	Glass spheres, well sorted	44.9	0.44	0.99
<b>Li and Komar (1986) *</b>	Crushed basalt	51.3	0.33	0.98
	Spheres	20.4	0.75	0.99
	Ellipsoidal natural grains	31.9	0.36	0.87
<b>Kirchner et al. (1990) *</b>	Natural grains, poorly sorted, water worked	55.2	0.31	0.91
	Natural grains, poorly sorted, unworked	66.1	0.46	0.99
<b>Buffington et al. (1992) *</b>	Natural sediment, $D_{50} = 4.1\text{mm}$	60	0.26	0.99
	Natural sediment, $D_{50} = 11.4\text{mm}$	51	0.28	0.99
	Natural sediment, $D_{50} = 14.0\text{mm}$	54	0.21	0.91
	Natural sediment, $D_{50} = 14.5\text{mm}$	46	0.21	0.92
	Natural sediment, $D_{50} = 45.0\text{mm}$	52	0.24	0.93
<b>Johnston et al. (1998) **</b>	Pacific Creek	61.9	0.28	0.94
	Van Duzen River	49.1	0.45	0.92
	Sagehen Creek	51.6	0.30	0.86
	Colorado River	55.5	0.14	0.98
<b>Hodge et al. (2013) **</b>	Bury Green Brook (pool facies)	62		
	Bury Green Brook (pool exit)	83		
	Bury Green Brook (riffle)	76		
<b>Prancevic and Lamb (2015) **</b>	Sespe Creek (Thalweg)	66.4	-0.01	
	Sespe Creek (Bar)	73.5	-0.01	
	Rose Valley Tributary	67.5	-0.01	
	Arroyo Seco	69.2	-0.01	
	Block Creek	69.9	0.18	
	San Oline Creek	67.7	0.18	
	Tumble Creek	64.3	0.18	
	Rattlesnake Creek	67.3	0.18	

Note: The  $\alpha$  coefficient has been defined differently by previous workers and may describe the mean (Miller and Byrne, 1966; Li and Komar, 1986; Hodge et al., 2013) or median pivoting angle of the median grain size (Kirchner et al., 1990; Buffington et al., 1992; Johnston et al., 1998; Prancevic and Lamb, 2015).

Early work (e.g. Miller and Byrne, 1966; Li and Komar, 1986), considered the pivoting angle of grains for artificially constructed beds, i.e. those where a sediment mixture was fixed to a tilting board. Subsequent research sought to establish grain pivoting angles for water-worked artificial beds through tilting boards (e.g. Kirchner et al., 1990) and for natural beds through force gauge measurements (e.g. Johnston et al., 1998). In general, the earlier relationships derived over unconsolidated, artificially-constructed beds were

not applicable to water-worked beds since they did not fully account for the effects of i) grain size sorting, ii) the pocket-to-pocket variation in  $\Phi$  and iii) grain-scale bed structure.

In terms of grain size sorting ( $\sigma_G$ ), the effect of  $\sigma_G$  on  $\Phi$  was considered more explicitly by Buffington et al. (1992) who adapted equation 2.17 to produce the empirical equation 2.18 from tilting board measurements conducted over natural gravel peels (where  $\alpha$ ,  $\beta$  and  $\Gamma = 52$ , 0.25 and 0.38 respectively).

$$\Phi = \alpha(D_i/D_{50})^{-\beta} \sigma_G^{-\Gamma} \quad [2.18]$$

where  $\Gamma$  is the power law exponent fitted using linear regression.

Data gathered by Johnston et al. (1998), using *in-situ* load cell measurements from natural beds, was found to similarly fit the equation 2.18 ( $\alpha$ ,  $\beta$  and  $\Gamma = 52.2$ , 0.28 and 0.72 respectively) although the  $\Gamma$  exponent was significantly higher than Buffington et al. (1992). This was attributed to the larger sample size and greater variety of field sites considered in Johnston et al. (1998).

Turning to pocket-to-pocket variations in  $\Phi$ , as Figure 2.18 illustrates, particle size acts collectively with the size, sorting and packing of the bed to fundamentally control the resting position of surface grains and their relative stability (Kirchner et al., 1990). For example, a lower pivoting is necessary to pivot a larger grain resting on the surface (Figure 2.18a) than a comparatively smaller grain (Figure 2.18b) or one residing more deeply within the bed (Figure 2.18c).

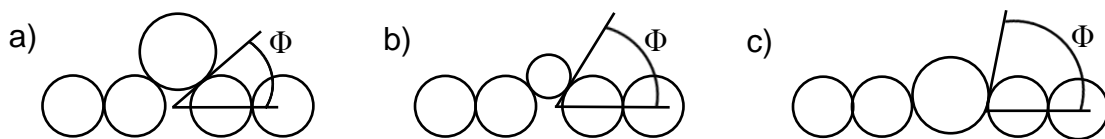


Figure 2.19 Illustration of the influence of a-b) relative particle size and c) packing arrangement on the stability of individual grains. After Kirchner et al. (1990).

Given the mix of sediment sizes and heterogeneity of natural streambed topography, critical shear stress will vary widely from grain-to-grain and pocket-to-pocket. For instance, the pivoting angle at the median particle diameter ( $D_i/D_{50} = 1$ ) was found to range between  $34.5^\circ$  and  $80.5^\circ$  for the 10<sup>th</sup> and 90<sup>th</sup> grain size classes, respectively (Figure 2.19; Kirchner et al., 1990). This represents an eightfold difference in the entrainment stress of different grain size classes, assuming  $\tan(\Phi)$  maintains a proportional dependency on  $\tau_c$  (Kirchner et al., 1990). Grain pivoting angle will also vary widely

within size classes and, as a consequence,  $\Phi$  for an individual grain size fraction (and  $\tau_c^*$ ) is better characterised as a probability distribution than a single value (Buffington et al., 1992; Kirchner et al., 1990; Johnston et al., 1998).

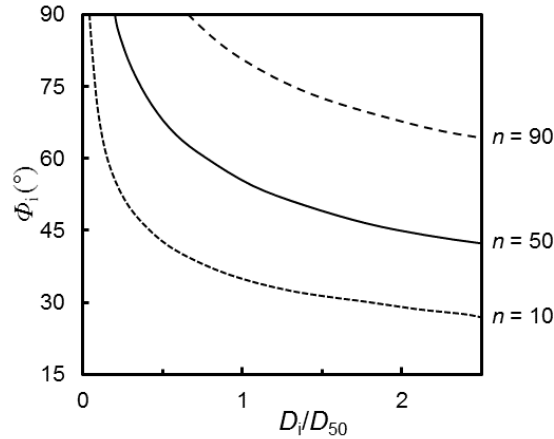


Figure 2.20 Percentiles of the pivoting angle distribution ( $\Phi_i$ ) as a function of relative grain size ( $D_i/D_{50}$ ). Lines fitted from equation 2.17 to  $i = 10, 50$  and  $90$ . Adapted from Kirchner et al. (1990).

Lastly, the use of artificially constructed beds neglects the influence of bed structure, e.g. grain packing, on particle stability. In this regard, Kirchner et al. (1990) found values of  $\Phi$  were greater for unworked beds compared to their water-worked counterparts (Figure 2.20). This reflected the effects of water-working to generate a topographically smooth, imbricated beds which decreases the pivoting angle of available surface pockets.

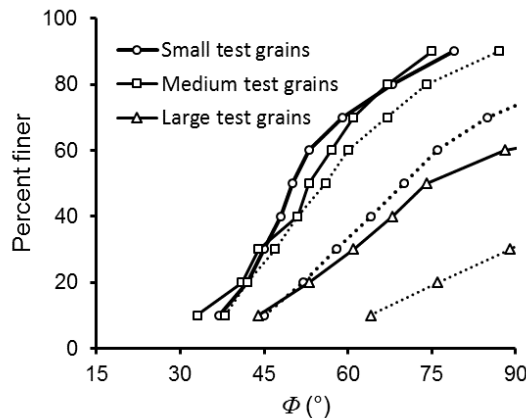


Figure 2.21 Friction angle distributions for unworked (dashed lines) and water-worked beds (solid lines). Large, medium and small test grain size diameter = c.1mm, c.4mm and c.6mm respectively. After Kirchner et al. (1990).

Pivoting angle trends (i.e. how  $\Phi$  varies as a function of  $D_i/D_{50}$ ) have also been found to differ between reaches on the basis of grain-scale structure. For example, for an infilled bed, the embedding and partial burial of grains within a fine-grained matrix will reduce

the influence of relative grain size on pivoting angle by increasing a particle's resistance to movement greater than would be expected solely from grain-on-grain contact (Johnston et al., 1998). This infilling of interstices will narrow the range of bed pockets and reduce the variability of pivoting angles. As a consequence, values of  $\Phi$  remain relatively consistent for all grain size classes for a bed with an infilled structure (e.g. Figure 2.21 *Pilgrim Creek*) and comparatively higher with  $D_i/D_{50}$  than beds where embedding is less prevalent (e.g. Figure 2.21 *Pacific Creek*; Johnston et al., 1998). The presence of bedform-scale structure may similarly position coarse grains more deeply within the bed and modify pivoting angle trends (Hodge et al., 2013).

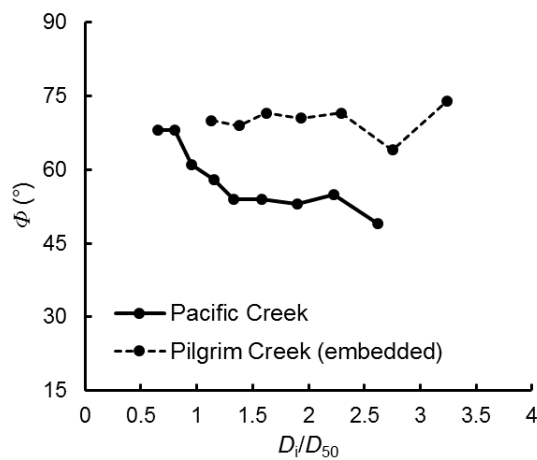


Figure 2.22 Median  $\Phi$  values as a function of  $D_i/D_{50}$  for the Pacific Creek and Pilgrim Creek reaches of Johnston et al. (1998).

### 2.3.5. Parameters of particle stability: grain protrusion

The stability of particles within mixed-grain beds is not only a function of pivoting angle but also of the relative protrusion of surface grains into the flow. The position of grains within the bed can be characterised in terms of the i) **projection** of the grain relative to the local mean bed level ( $p$ ; Figure 2.22) and ii) **exposure** of the grain relative to the local upstream neighbourhood of grains ( $e$ ; Figure 2.22). The former,  $p$ , is calculated as the elevation difference from the top of the surface grain to the height of the local mean bed level while the latter,  $e$ , refers to the elevation difference from the top of the surface grain to the highest point within a local area upstream from the leading edge of the particle of interest. Previous workers have taken the local neighbourhood over which grain projection and exposure to be related to the  $D_{84}$  grain size percentile, since this length is

associated with the hydraulic properties of mixed-grain beds (Leopold et al., 1964; Kirchner et al., 1990).

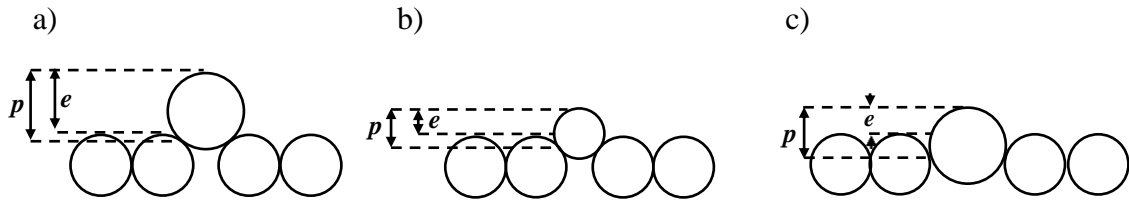


Figure 2.23 Illustration of the influence of a-b) relative particle size and c) packing arrangement on the projection and exposure of surface grains. After Kirchner et al. (1990).

For a bed comprised of spherical, uniformly-sized grains, the distributions of the force balance parameters of grain exposure and projection can be estimated from the pivoting angle distribution using empirical relationships defined by Kirchner et al. (1990):

$$p_i = e_i + \frac{\pi}{12} D_{50} \quad [2.19]$$

$$e_i = \frac{1}{2} [D - D_{50} + (D + D_{50}) \cos \Phi_{100-i}] \quad [2.20]$$

The ability to estimate force balance parameter values using a stochastic approach (e.g. random sampling using a Monte Carlo simulation) is, however, complicated by the effects of the grain size distribution and bed structure. There is, therefore, a need to measure grain protrusion from natural water-worked beds which has only recently been made possible from advancements in the ability to capture high resolution information of streambed topography (e.g. Hodge et al., 2013). In terms of bed texture, as Figures 2.22a-b illustrate, projection and exposure are affected by particle size since larger grains tend to protrude further into the flow. Unsurprisingly, therefore, previous workers have observed that the projection of individual particles was, in-part, a function of grain size and that normalised projection (i.e.  $p/D$ ) is relatively consistent for all grain size classes ( $0.37 \leq \overline{p/D} \leq 0.47$ ; Hodge et al., 2013). The exposure of surface grains is likely to be greater for those that project further into the flow and this is reflected by the dependency of normalised projection on normalised exposure ( $e/D$ ; Hodge et al., 2013). In terms of bed structure, as Figure 2.22c illustrates, the packing of surface grains can also affect projection and exposure and may explain differences in the distributions of  $p/D$  recorded by previous workers between reaches (e.g. Hodge et al., 2013).

## 2.4. Temporal evolution of bed structure

Further to the characteristics of grain- and bedform-scale structure, described in subsections 2.2.1 and 2.2.2, there is a pressing need to document and understand the temporal dynamics of sedimentary organisation in coarse-grained alluvial surfaces. In this regard, previous workers have sought to establish how streambed structure develops, often in an artificial environment, and whether structured bed conditions persist over competent flows.

In terms of grain-scale structure, surface grains have been observed to rapidly structure in stable positions that offer the least resistance to the near-bed flows. Under low flows, coarse bladed grains tend to roll or slide along the bed and be deposited with their a-axis resting transverse to the flow (Millane et al., 2006). This rolling/sliding motion is responsible for the imbrication of coarse surface grains and generates tight bed packing arrangements (Johansson, 1963). By contrast, under higher flows or for smaller or more rounded grains, particles tend to skip along the bed and be deposited with their a-axis parallel to the direction of flow (Johansson, 1963). The properties of grain-scale structure (e.g. magnitude of particle imbrication and geometry of bed packing) will respond to local sediment supply and flow regime. For instance, a highly imbricated surface armour will develop under static (sediment starved) conditions whereas mobile armours are comprised of a comparatively looser packing of grains (Mao et al., 2011). In addition, grain imbrication has been observed to mature during the recession limb of a flood hydrograph (Mao, 2012) and, owing to the flashy nature of flows and high rates of sediment supply, can explain the lack of imbrication within the streambeds of ephemeral channels (Hassan, 2005).

Turning to the temporal dynamics of bedform-scale structure, previous workers have primarily focused on understanding how pebble clusters develop and whether they persist over flood events (Brayshaw et al., 1983; Hassan and Reid, 1990; Pender et al., 2001; Strom et al., 2004; Wittenberg and Newson, 2005). As explained in Subsection 2.2.2, flow recession plays an important role in promoting the formation of pebble clusters (De Jong and Ergenzinger, 1995) and differences in flow regime explain differences in the frequency of bedforms within the streambeds of perennial and ephemeral channels (Wittenberg, 2002). However, the persistence of bedform-scale structure over competent flows, particularly in a natural setting, is less well understood and remains poorly

researched. The handful of studies that have sought to document the temporal dynamics of bedform structures in the field have found coarse obstacle clasts and, hence, the largest cluster bedforms within an established surface armour typically remain in place even over the highest observed flows (Oldmeadow and Church, 2006; Lamarre and Roy, 2008). While smaller cluster bedforms are comparatively more mobile, no appreciable changes in bedform-scale structure were observed over flood events (Oldmeadow and Church, 2006; Lamarre and Roy, 2008). This suggests larger scales of bed structure stay relatively intact over natural flows but subsequent research to confirm these initial observations is limited. In an attempt to account for a broader range of flows, several workers have studied the development of bedforms from a manually unstructured bed (treated by breaking apart and dispersing existing clusters) while bed texture remained unaltered. Lamarre and Roy (2008) found that bedforms redeveloped toward a natural, stable condition after two low magnitude flow events whereas Oldmeadow and Church (2006) found a longer sequence of flows was required for bedforms to reassemble. In addition, Oldmeadow and Church (2006) observed a complete reversion in bed structure, toward an unstructured state, after a major flood event (4.5-year return interval) which occurred during the initial period of recovery. The incipient bedform structure that had developed prior to the major event was, therefore, not sufficiently resilient to withstand the larger flow (Oldmeadow and Church, 2006). In this regard, Wittenberg and Newson (2005) and the consolidatory flume work of Ockelford and Haynes (2013) have suggested antecedent flow history plays an important role in the resilience of bed structure and the capacity for bedforms to persist over subsequent flood events. However, despite the initial promise offered by these studies, very little is understood about the temporal dynamics of bed structure, particularly in comparison to the adjustments in bed texture discussed in subsection 2.1.1.

## **2.5. Summary and research objectives**

In summary, previous workers acknowledge the need to consider the roughness properties of gravel streambeds to generate better predictive models for boundary resistance and bed stability (Sections 2.1-3). However, previous attempts to characterise bed structure have predominantly relied on the observations from flume experiments or modelling approaches, with the former constrained by grain size distribution and sediment supply

feed (e.g. Naden, 1987; Church et al., 1998), and may not be applicable to the natural environment. The few studies that have sought to characterise natural gravel bed structure have often been limited to a small sample of humid temperate reaches or small patches which fail to document larger scales of topography (e.g. Hodge et al., 2009b). As a consequence, there is a pressing need to establish the variability in natural streambed structure, defined through various statistical parameters, by considering a greater range of sediments (size, shape, sorting, etc.) and a wider range of fluvial environments (perennial, ephemeral). Regarding the latter, no study has investigated the structural characteristics of ephemeral streambeds despite speculation that suggests they may differ in significant ways from their humid temperate counterparts due to an undeveloped surface armour, lacking grain- and bedform-scale structure (Wittenberg, 2002).

Further to structural character, relatively little is known about how bed structure influences bed stability. Only recently have workers derived grain protrusion from natural water-worked beds, e.g. for riffle, pool and pool exit facies in a humid temperate reach (Hodge et al., 2013). In addition, the effects of bed structure on pivoting angle trends remain poorly understood since research has been limited to a handful of studies considering a narrow range of field sites. Further work is, therefore, required to consolidate these preliminary observations and extend this initial research to understand the control of alluvial bed surface structure on particle stability and investigate how this varies for different reaches in different fluvial environments. For example, while previous workers have suggested that grain- and bedform-scale structure differs between streambeds from perennial and ephemeral channels (e.g. Hassan et al., 2009), and that this may be exhibited through different pivoting angle trends, no studies to-date have sought to explicitly compare grain pivoting angles from channels subject to distinct flow regimes.

There is also a need for a greater understanding of the temporal dynamics of streambed structure. Much of what is known has been derived from flume experiments and studies in a natural setting have largely been limited to single site surveys or focused on grain size adjustments over time. Temporal changes in bed structure have generally been viewed through coarse, qualitative assessments of bedform presence and the inferred movements of pebble clusters over repeated surveys (e.g. Oldmeadow and Church, 2006). As a consequence, the temporal dynamics of bed structure using various structural parameters has yet to be explored. In this respect, while several workers have suggested

natural streambed structure is maintained over flood events (e.g. Oldmeadow and Church, 2006; Lamarre and Roy, 2008), a persistence of bed structure remains to be demonstrated through statistical approaches. The limited amount of research conducted in a natural setting has also incorporated surface treatments to investigate how structure develops from an unstructured condition (e.g. Wooldridge and Hickin, 2002; Oldmeadow and Church, 2006; Entwistle et al., 2007; Lamarre and Roy, 2008). However, previous workers have disputed the timescale necessary for bed structure to fully develop. For example, Lamarre and Roy (2008) found that bed structure formed after two low magnitude events while Oldmeadow and Church (2006) observed that a stable structure developed over a longer sequence of flows and incipient structure was not resilient to larger flows. Further work is necessary to confirm these preliminary observations.

There are three principal objectives to this research. The first of these research objectives is to quantify and compare the structural characteristics of naturally water-worked gravel beds across a variety of field sites subject to perennial and ephemeral flow regimes using a suite of statistical metrics. Since qualitative differences in the structure of streambeds from perennial and ephemeral channels have been observed by previous workers (e.g. Wittenberg, 2002), it is expected these differences will be demonstrated quantitatively by the suite of structural metrics. For example, the local metrics of inclination, aspect and slope are predicted to confirm differences in grain-scale structure between streambeds from different regimes – lower values of the inclination index, a more positively skewed distribution of shallow, local slopes and local aspect more aligned in a flow-parallel direction for the humid temperate beds to reflect a more tightly packed, imbricated arrangement of surface grains compared to the dryland beds. Meanwhile, at larger scales, the absence of bedforms within the dryland streambeds is anticipated to be reflected, in the variogram analyses by a shorter range of influence, accounting for differences in bed texture, relative to the humid temperate beds. The second of these research objectives is to evaluate the significance of differences in perennial and ephemeral streambed structure for bed stability using parameters that determine bed stability and through entrainment threshold modelling. In this regard, it is hypothesized that surface grains will be more exposed and project further into the flow for the more loosely packed dryland beds than the humid temperate beds. Grain pivoting angle may, however, be greater for the dryland beds owing to embedding of surface grains (e.g. Johnston et al., 1998). Sediment transport is expected to be closer to equal mobility for the dryland beds, given the relative lack of

sedimentary structure. Finally, the third research objective is to investigate the temporal variability of streambed structure by exploring how quickly structure develops and to what extent a structured bed condition is preserved over a series of competent flows. Since bed texture and structure (through a coarse, qualitative classification of bedforms) have previously been observed to be maintained over natural flows (Wilcock and DeTemple, 2005; Oldmeadow and Church, 2006), it is expected that the statistical metrics will remain relatively constant, and hence structure will remain stable, over the monitoring period. Furthermore, structure is predicted to develop rapidly from an unstructured to stable condition after a handful of competent flows events, although a reversion in structure to an unstructured state may be observed following a large flood (e.g. Oldmeadow and Church, 2006).

## Chapter 3 Methods

High-resolution digital elevation models (digital terrain models; DTMs) of gravel surface microtopography were generated from terrestrial laser scanning (TLS) data and characterised using a suite of statistical techniques. In order to satisfy the first research objective concerning the variability in the structural characteristics of gravel bed rivers, data was obtained from 11 patches from nine gravel-cobble bars in six alluvial rivers. For this objective, each patch was surveyed once. For the second research objective concerning the temporal evolution of bed surface structure, repeat surveys of the bed condition were undertaken at a single site over individual flood events (experiment A) and over a series of competent flow events (experiment B). This chapter describes the 3.1) field sites and their locations, 3.2) methodology for data capture, 3.3) data processing workflow adopted for creating and validating the DTMs, the techniques used to characterise 3.4) bed surface grain size and parameterise 3.5) sedimentary structure and 3.6) particle stability, concluding with 3.7) a description of the experimental methodologies for studying the temporal evolution of bed surface structure.

### 3.1. Field sites

Field data was gathered from a number of gravel-bed rivers in two contrasting environments: four humid temperate perennial rivers in the uplands of the UK (Wharfe, Ashop, Manifold and Elan; Figure 3.1a) and two dryland ephemeral rivers in the Judean Desert, Israel (Hever and Shafan; Figure 3.1b). In selecting rivers from the Judean desert, the gravel bed structures and roughness properties were not affected by accumulations of silt and clay that characterise rivers in the neighbouring Beersheva depression (Barzilai et al., 2013). In order to capture the diversity of alluvial streambed structure, the sampled reaches were chosen to exhibit a range of sedimentological and hydrological characteristics; e.g. differences in grain size, shape, sorting and flow regime. At each of the field sites, locally-representative and regionally-planar patches were sampled from coarse-grained bars in areas devoid of vegetation. Two patches from neighbouring bars were sampled in the Ashop (A<sub>1</sub>, A<sub>2</sub>), Manifold (M<sub>1</sub>, M<sub>2</sub>) and Hever (H<sub>1</sub>, H<sub>2</sub>) whilst two patches from a single bar were sampled in the Wharfe (W<sub>1.1</sub>, W<sub>1.2</sub>) and Afon Elan (E<sub>1.1</sub>, E<sub>1.2</sub>); the lattermost data were collected by Ewen (2010). Only one patch was sampled in

the Shafan ( $S_1$ ). A description of the geomorphic setting and hydrological character of each river is outlined in the following subsections (3.1.1–6).

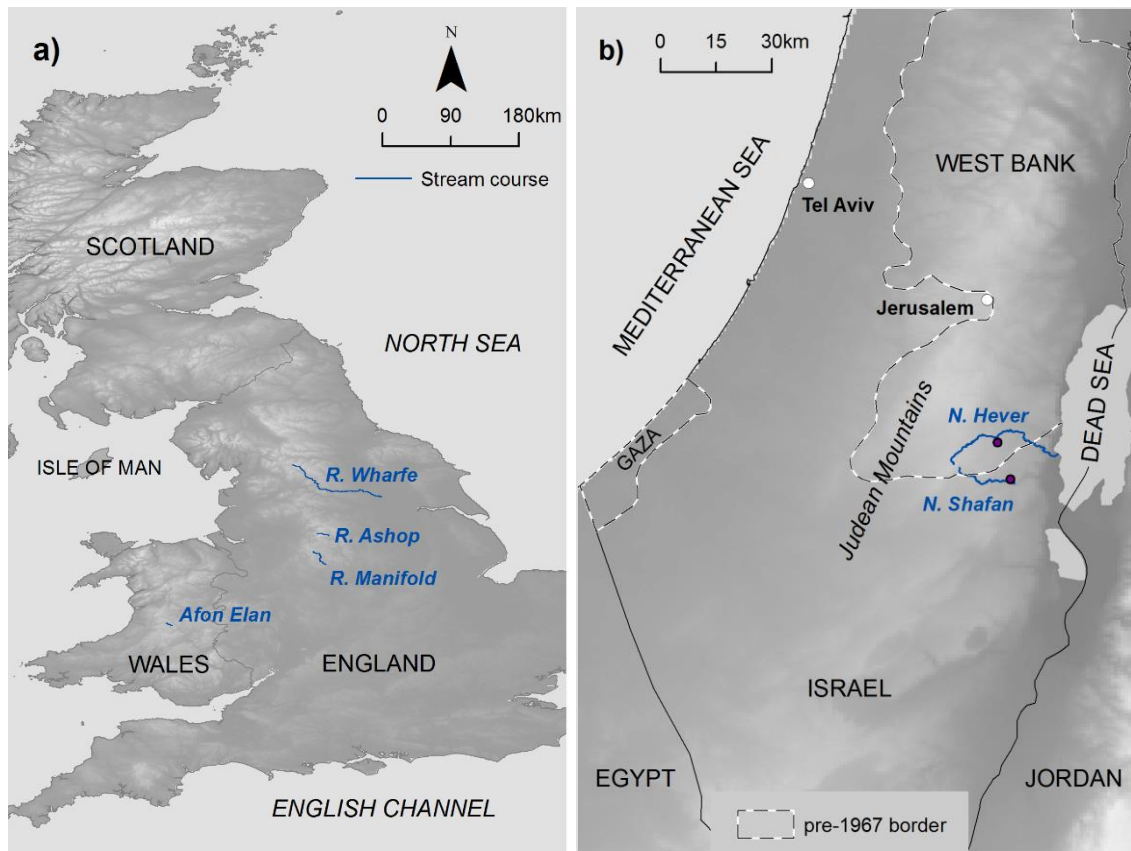


Figure 3.1 Regional location and course of the a) perennial and c) ephemeral rivers.

Table 3.1 Summary of catchment characteristics for the perennial rivers, where PROPWET is the catchment wetness index (PROPortion of time soils are WET), DPSBAR is an index of overall catchment steepness (mean Drainage Path Slope) and BFIHOST is a base flow index, a measure of the catchment responsiveness. Flow and local catchment information unavailable for the ephemeral rivers.

	Ashop	Elan	Manifold	Wharfe	Hever	Shafan
Catchment (km <sup>2</sup> )	44	184	149	912	175	260
Lithology	Gritstone			Limestone		
PROPWET (%) *	48	65	44	62		
DPSBAR (m km <sup>-1</sup> ) *	191	146	117	138		
BFIHOST *	0.36	0.35	0.46	0.37		
Local site catchment (km <sup>2</sup> ) **	28	39	22	212		
Stream Order **	4 <sup>th</sup>	4 <sup>th</sup>	4 <sup>th</sup>	6 <sup>th</sup>		

\* Flood Estimation Handbook (FEH) catchment descriptors for gauging stations downstream from the field sites (National River Flow Archive, 2012a, 2012b, 2012c, 2012d).

\*\* Estimated in ArcGIS from catchment topography; Stream Order through the Strahler (1957) method.

### 3.1.1. The River Ashop, UK: A<sub>1</sub>, A<sub>2</sub>

The River Ashop drains a 44 km<sup>2</sup> catchment area within the Peak District National Park, central England. It flows in a south easterly direction for 10 km from the Bleaklow and Kinder upland plateaus to the Ladybower Reservoir (Figure 3.2a). The catchment geology comprises interbedded coarse-grained sandstones and shales from the Millstone Grit (Carboniferous) series (Lindsay and Evans, 2008; Pawson et al., 2012). The upland plateaus are characterised by deep blanket peatland soils whilst the lower reaches consist of a mixture of coniferous plantations and improved grassland. Land use is primarily dedicated to forestry and rough grazing by sheep and cattle (Lindsay and Evans, 2008). The average annual rainfall is 1554 mm (Pawson et al., 2012). The extensive dissection of the upper catchment and surface run-off over the saturated peat blanket results in a flashy hydrological regime (Tallis, 1985; Rothwell et al., 2005) and, as a result, flows commonly recede to base level within 24 hours of the hydrograph peak (Tallis, 1973).

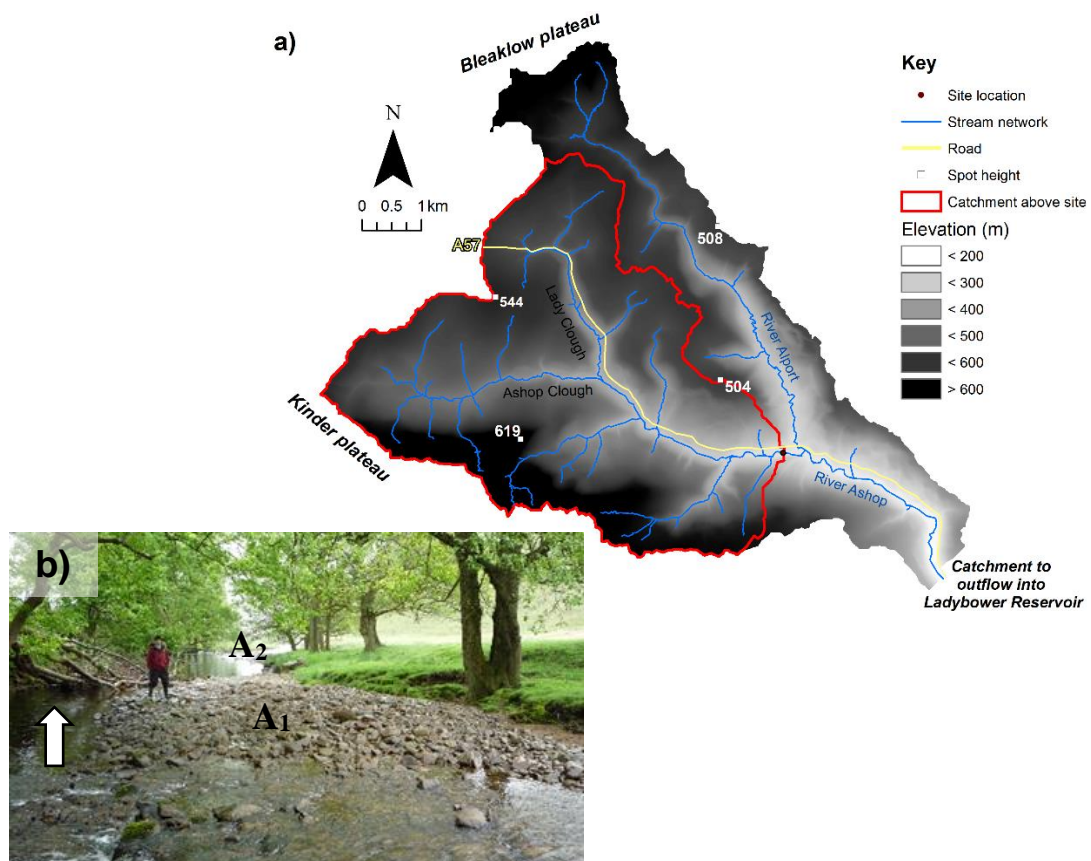


Figure 3.2 a) River Ashop field site location and b) photograph highlighting patch location with IDs. a) contains OS data © Crown copyright and database right 2017, in b) approximate direction of bank full flow displayed with white arrow.

The upper reaches of the Ashop are dominated by a dendritic gully network delimited by wide interfluves (Lindsay and Evans, 2008). Here, the streams are steep, confined and

adopt a step-pool morphology (Lee, 1998). At the confluence between the tributaries of Ashop Clough and Lady Clough (53°24'45" N 1°50'16" W; Figure 3.2a) the valley widens and a single thread, meandering channel flows within a 50 - 100 m wide floodplain, confined in several sections by deeply incised and terraced alluvium. The active erosion of upland headwaters and destabilisation of local hillslopes (Heaney, 2013) provides a source of sediment for the aggradation of coarse-grained point bars. Downstream from the site, the flow and sediment regime of the catchment is mediated by the abstraction of water into the Derwent Reservoir by the Ashop weir (Maddock et al., 2001). Although several workers have noted evidence of contemporary catchment erosion, e.g. rotational bank failures (Boon and Evans, 2008), analysis of change using historical maps (EDINA Historic Digimap Service) indicates that the course of the channel has not changed significantly since the 1880s.

The two gravel patches on the Ashop (A<sub>1</sub> and A<sub>2</sub>; 53°24'07" N 1°47'37" W) were sampled from neighbouring coarse-grained point bars located c.200 m upstream of the Ashop weir (local catchment: 28 km<sup>2</sup>). The bars were approximately 6 x 10 m and 2 x 5 m (A<sub>1</sub> > A<sub>2</sub>), from which 3 x 3 m and 2.5 x 2 m patches were sampled, and comprised of disc-shaped, gravel- to cobble-sized sediment. The coarse surface material was imbricated and structured into a variety of larger-scale bedforms (e.g. transverse ribs and pebble clusters) which were noted from a walkover of the reach section between the two bars. At both sites the bankfull width was approximately 8 m and low flows shoaled from right to left across the bar heads to concentrate down the right-hand side of the channel (Figure 3.2b). At higher discharges, however, the flow overtops the bar and straightens in-line with the course of the reach.

### **3.1.2. The Afon Elan, UK: E<sub>1.1</sub>, E<sub>1.2</sub>**

The Afon Elan rises in the Cambrian Mountains and drains a catchment of 184 km<sup>2</sup> (Scullion and Sinton, 1983; Figure 3.3a). The stream flows in a south-easterly direction for about 10 km before entering into a sequence of reservoirs (Craig Goch, Penygarreg, Garreg-ddu and Caban-coch). A 6.5km regulated section then follows until the river reaches a confluence with the River Wye just south of Rhyader. The upland plateau is characterised by blanket peatland and acidic grassland which is underlain by an impermeable geology of Silurian shales and slates from the Glanyrafon, Pysgotwr and

Rhuddnant formations (Llandovery epoch; National River Flow Archive, 2012b). Land use, here, is primarily dedicated to sheep grazing. The upper catchment has a mean annual rainfall of 1874 mm (The Met. Office, 1986) which generates a flashy flow regime, common to the tributaries of the River Wye (Howe et al., 1967). Downstream of the headwaters, the river adopts a meandering planform and flows within a floodplain up to 300 m wide, though the river is locally confined by outcrops of bed rock (Higgs, 1997), valley side bluffs (Richards, 1982) and unconsolidated glacial periglacial deposits (Lewin and Brindle, 1977). The field site is located within a 1 km sequence of meander bends where reworked Devensian tills are deposited as riffles and point bars (Anderson and Richards, 1979). Despite the reworking of sediment during periods of high flow, Thorne (1995) characterises the Afon Elan as a confined stream with passive meandering. Meander wavelength ( $L$ ) greatly exceeds width ( $w$ ;  $10w \leq L \leq 14w$ ) and the Elan is unable to generate the stream power necessary to modify channel boundaries through bed and bank erosion (Richards, 1982; Thorne, 1995).

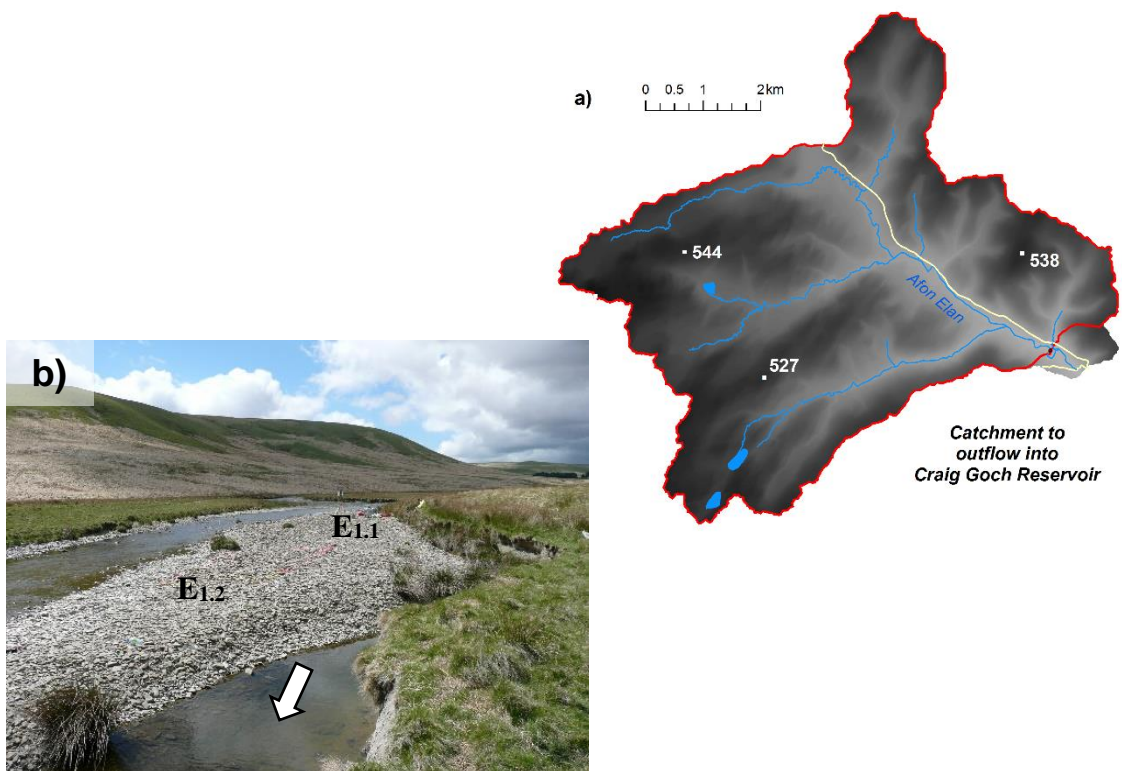


Figure 3.3 a) Afon Elan field site location and b) photograph highlighting patch location with IDs. Key in a) as in Figure 3.2; contains OS data © Crown copyright and database right 2017.

A single 8 x 30 m point bar comprising very coarse gravel- to cobble-sized, poorly sorted, bladed material located c. 1 km upstream from the outflow to the Craig Goch Reservoir was selected for study ( $52^{\circ}20'04''$  N  $3^{\circ}37'11''$  W; local catchment: 39 km<sup>2</sup>; Figure 3.3b).

The two gravel patches (E<sub>1.1</sub> and E<sub>1.2</sub>) were sampled from the bar head and tail facies and encompass areas of 3 x 2.5 m and 3 x 3 m respectively. Although both patches shared similar surface grain size distributions, textural streambed structuring (e.g. a tighter grain packing arrangement) was less apparent for the downstream, bar tail facies (E<sub>1.2</sub>; Bluck, 1982).

### **3.1.3. The River Manifold, UK: M<sub>1</sub>, M<sub>2</sub>**

The River Manifold is found within the Peak District National Park, rising just south of Buxton before heading in a southerly and south-easterly direction for 41 km to a confluence with the River Dove downstream from the village of Ilam (Figure 3.4a). The catchment encompasses an area of 149 km<sup>2</sup> and is underlain by a geology of Carboniferous gritstones, sandstones and black shales from the Millstone Grit formation (Namurian stage; National River Flow Archive, 2012c; Johnson et al., 2014). Soils are acidic to weakly calcareous in nature and the catchment is primarily dedicated to grassland used to graze sheep and cattle. The mean annual rainfall is 1100 mm and like the Ashop and Elan, the quick draining headwaters result in a flashy hydrological response (National River Flow Archive, 2012c). The river follows a sinuous course, flowing from headwater gullies to a wide valley downstream from Longnor. Historical mapping of the 6 km reach between Longnor and Hulme End shows evidence of planform instability over the past century as evidenced by a network of palaeochannels (EDINA Historic Digimap Service). More contemporary processes, such as bank erosion, provide a source of sediment for the aggradation of coarse-grained point bar features, which are actively remobilised during periods of moderate- to high- flows (Rice and Toone, 2011). The severity of the bank erosion has necessitated remedial bank stabilisation efforts (Everall, 2010; Everall et al., 2012; Angelopoulos, 2013).

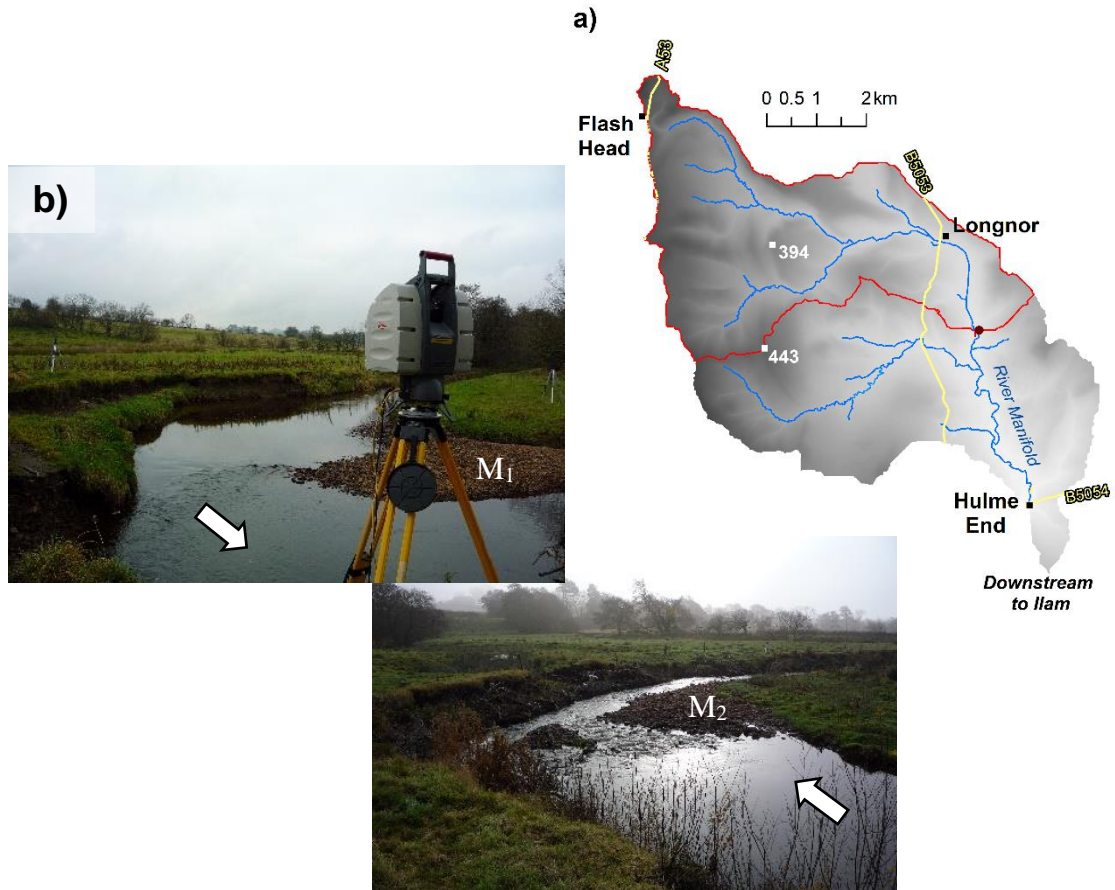


Figure 3.4 a) River Manifold field site location, b) photographs highlighting patch location with IDs. Key in a) as in Figure 3.2; contains OS data © Crown copyright and database right 2017.

Two gravel patches ( $M_1$  and  $M_2$ ) were sampled from neighbouring coarse-grained point bars ( $53^{\circ}09'46''$  N  $1^{\circ}51'35''$  W; local catchment:  $22 \text{ km}^2$ ; Figure 3.4b) which exhibited different sedimentological and morphological characteristics. The upstream patch ( $M_1$ ) was located on a  $2 \times 3 \text{ m}$  low relief bar which comprised a loose arrangement of small- to medium- sized gravels that, on inspection, appeared to lack extensive grain-scale structure and bedform development. In contrast, the downstream patch ( $M_2$ ) sampled from a  $4 \times 8 \text{ m}$  higher relief bar was characterised by a tightly packed, imbricated and clustered gravel- to cobble- sized sediment. Each patch was  $2 \times 1 \text{ m}$  long and orientated with the long axis aligned in the direction of flow. Owing to the sinuous channel planform, both patches were affected by flow straightening where flow direction varies with stage (see subsection 3.1.1; Wittenberg and Newson, 2005).

### **3.1.4. The River Wharfe, UK: W<sub>1.1</sub>, W<sub>1.2</sub>**

The River Wharfe drains a 912 km<sup>2</sup> catchment as it flows for 105 km through the Yorkshire Dales National Park before reaching a confluence with the River Ouse to the south of York (Figure 3.5a). The upper valleys are deeply incised into Carboniferous limestones of the Great Scar formation and sandstone and schist facies from the Yoredale Bed and Millstone Grit sequences (Black, 1950; Walling et al., 1999). Soils within this region comprise of blanket peatland and the open moorland of the upper catchment is dedicated to forestry and rough pasture to graze sheep. The headwaters receive c.2000 mm of precipitation annually (Merrett and Macklin, 1999; Reid et al., 2002). The combination of a quick draining limestone geology and steep catchment hillslopes gives rise to a relatively flashy flow regime (Lane et al., 2008), though the hydrological response of the catchment has been modified considerably by recent catchment management practises (e.g. gripping of the upland drainage system, bedload trapping, channel dredging and the raising of channel banks; Hey and Winterbottom, 1990; Reid, 2002) which has resulted in a reduction in flood magnitude and the time to hydrograph peak (Lane and Milledge, 2012).

The channel upstream of Hubberholme is confined by local outcrops of bedrock and steep valley sides (Lane et al., 2008; Raven et al., 2009). The river downstream from Hubberholme is, by contrast, characterised by a gentler slope wherein a single thread channel adopts a meandering planform (Lane et al., 2008). Coarse-grained, rounded limestone sediment from reworked glacial tills and hillslope failures is stored extensively as lateral and point bars which are frequently remobilised during periods of high flow (Hey and Winterbottom, 1990; Reid et al., 2007). Despite prominent flood events (e.g. in 1686; Coulthard et al., 1998) and a record of historical channel aggradation, which prompted the installation of a gravel trap downstream from Hubberholme (Hey and Winterbottom, 1990; Lane et al., 2007; Raven et al., 2009), the local course of the river has not changed appreciably over the past 140 years (Howard et al., 2000; EDINA Historic Digimap Service).

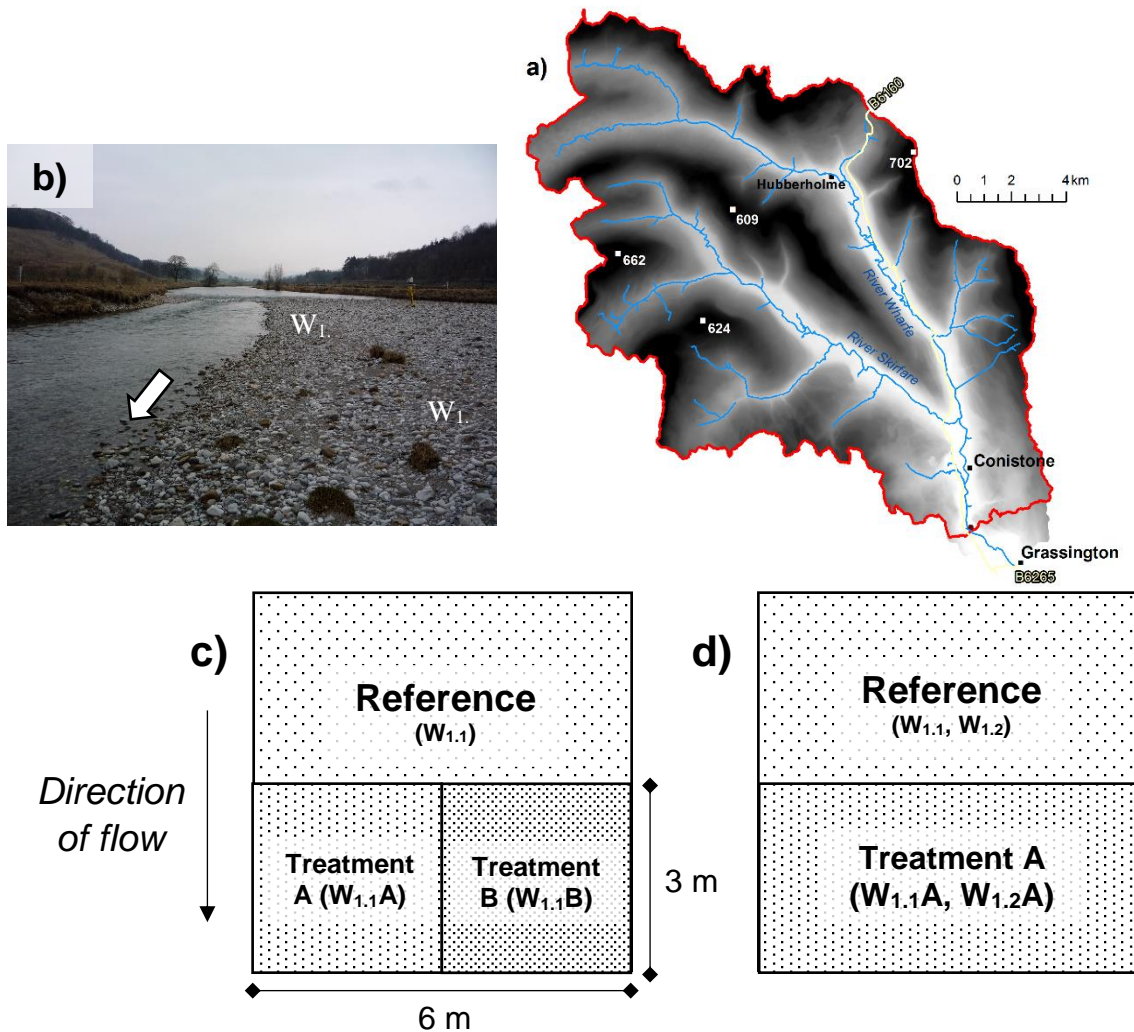


Figure 3.5 a) River Wharfe field site location, b) photographs highlighting patch location with IDs and schematic illustrations of the  $W_{1.1}$  and  $W_{1.2}$  sub patches for c) early (July 2013 – February 2014) and d) later surveys (November 2014 – April 2015). Key in a) as in Figure 3.2; contains OS data © Crown copyright and database right 2017.

The two gravel patches on the River Wharfe were chosen from the bar head and tail facies of a large (100 x 50 m) gravel- to cobble- sized, low relief point bar found c.2 km upstream of Grassington (54°04'59" N 2°01'53" W; local catchment: 212 km<sup>2</sup>; Figure 3.5a). The surfaces of both patches showed grain imbrication and the development of cluster microforms. Low flows visibly shoaled over the bar head and were concentrated down the righthand side of the channel whilst water ponded in a chute formed down the lefthand bar margin. At higher flows, the bar topography was drowned out and the flow straightened (cf. subsection 3.1.1; Wittenberg and Newson, 2005). Owing to its upstream location, the  $W_{1.1}$  bar head facies was particularly sensitive to these changes in flow direction.

Unlike the other field sites, where the patches were only surveyed once, those on the Wharfe were used to conduct two experiments that required repeat surveys in order to investigate the temporal dynamics of alluvial streambed structure. To facilitate the experiments, the two gravel patches were each subdivided into sub patches. Two 3 x 6 m sub patches (Figures 3.5c-d) were used to characterise the bed structure for objective 1. These ‘reference’ patches (cf. Oldmeadow and Church, 2006) also provided an experimental control for two experiments performed on two 3 x 3 m patches ( $W_{1.1}A$  and  $W_{1.1}B$  immediately downstream from the  $W_{1.1}$  reference patch) between July 2013 and February 2014 and one experiment performed on two 3 x 6 m patches ( $W_{1.1}A$  and  $W_{1.2}A$ ) between November 2014 and April 2015 for objective 2. The two experiments involved the application of surface treatments to generate unstructured surfaces (e.g. Oldmeadow and Church, 2006; Lamarre and Roy, 2008). The aim of the treatment process was to manipulate the bed to produce an unstructured condition which involved the removal of structure at various spatial scales. In generating an unstructured bed, surface sediment was turned over by hand so that clusters of grains were dispersed and individual grains no longer exhibited any preferential alignment or orientation (disturbing bedform and grain scale structure, respectively). In addition, local depressions were infilled by neighbouring areas of relief to produce a planar surface (remove larger scale structure; Lamarre and Roy, 2008). Care was taken during the treatment process not to introduce finer surface material to the surface or to leave the subsurface exposed (Oldmeadow and Church, 2006). A 1 m buffer between each patch minimised the cross-contamination of newly unstructured (i.e. mobile) material between experiments.

The first experiment (experiment A) used sub patches  $W_{1.1}A$  and  $W_{1.2}A$  to investigate how sedimentary structure re-established over a series of competent flows. The second experiment (experiment B) utilised sub patch  $W_{1.1}B$  and characterised bed restructuring over a smaller collection of events and involved the repeated application of surface treatments after each repeat survey. During each experiment, the reference patches were not manipulated and acted as a control to the surface treatments. Over the entire 28-month experiment period, flows between surveys were characterised using the discharge record gathered at a nearby Environment Agency station at Netherside Hall (ID: 8276) located c.300 m downstream from the field site.

### **3.1.5. The Nahal Hever, Israel: H<sub>1</sub>, H<sub>2</sub>**

The Nahal Hever rises in the Judean Mountains in Israel and follows an easterly and south-easterly course for c.17 km to the Dead Sea. The 175 km<sup>2</sup> catchment is dominated by heavily faulted Late Cretaceous carbonates (limestone, dolomite and chalk) and clays (Turonian and Cenomanian stages; Raz, 1986; Gilat, 1987; Frumkin, 2001). Hillslopes throughout the region are sparsely vegetated with thin soils and large areas of exposed bedrock (Yair and Kossovsky, 2002). Land use in the upper catchment is restricted to the grazing of sheep and goats by local Bedouin. Mean annual rainfall is highly variable over the catchment and varies from c.500 mm in the semi-arid Judean desert to 50 mm in the hyper-arid regions closer to the Dead Sea (Bowman et al., 2007; Shamir et al., 2013). The rainy season extends from October to April and the ephemeral discharge regime is characterised by periodic flash flooding (Nahal Eshtemoa a few km to the east is hydrologically dormant for 98% of the time; Reid et al., 1998). Flooding within the catchment (and catchments within the surrounding area) is characterised by needle hydrographs (short lag and recession times, high peaks), and is typically confined within a 12-hour period (Cohen and Laronne, 2005). Given the short lag times, the lack of base flow and the high bedload transport rates generated during flood events (Reid and Laronne, 1995), opportunities for sediment restructuring are limited to recession limbs which rarely exceed 2 – 3 hours (Cohen and Laronne, 2005).

The Nahal Hever is a deeply incised, coarse-grained braided channel which, in the lower reaches, meanders through a deep canyon with numerous knick-points (Frostick and Reid, 1989). The gravel patches H<sub>1</sub> and H<sub>2</sub> (31°26'16" N 35°14'34" E and 31°26'11" N 35°14'47" E; Figures 3.6a and 3.6b) were sampled from two bars within a 0.5 km reach of the upper catchment. The bars comprised coarse-grained, poorly sorted, rounded limestone material which appeared to lack both grain-scale structure and bedform development.

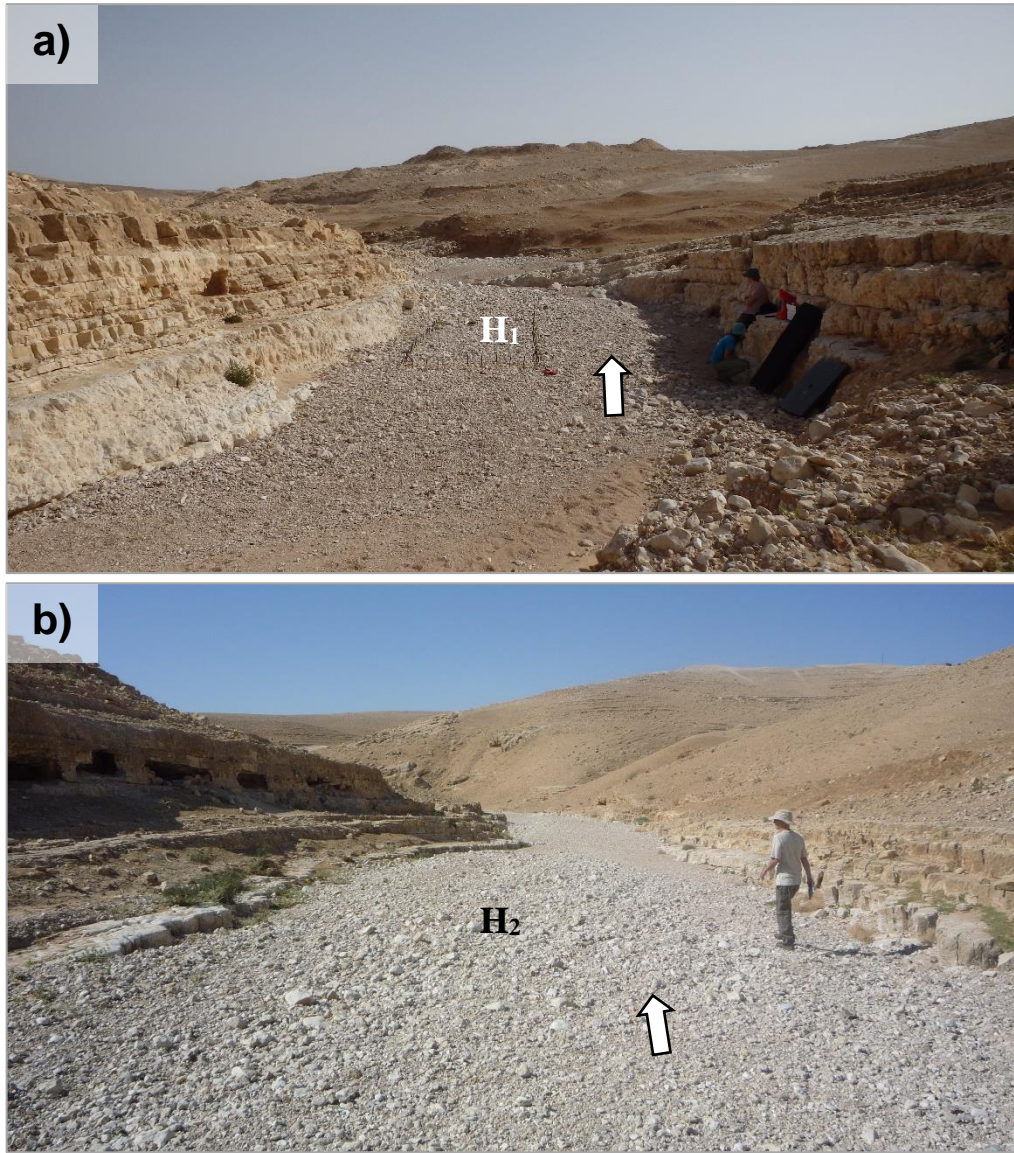


Figure 3.6 Field site photographs for the a) H<sub>1</sub> and b) H<sub>2</sub> gravel patches. Approximate patch location is highlighted by ID labels and bankfull flow direction by the white arrow.

### 3.1.6. The Nahal Shafan, Israel: S<sub>1</sub>

The Nahal Shafan is a tributary of the Nahal Ze'elim, one of the largest streams in the region, and drains c.260 km<sup>2</sup> of the southern Judean desert into the Dead Sea (Polak, 1988; Bowman et al., 2007). The catchment shares a similar geology, soils and land use to the Hever (Gilat, 1987). The gravel patch S<sub>1</sub> (31°20'57" N 35°16'27" E; Figure 3.7) was sampled from a coarse-grained bar in the lower catchment, located approximately 1 km upstream from the confluence between the Shafan and Ze'elim within a deeply incised gorge. The sedimentological character of the patch is very similar to the H<sub>1</sub> and H<sub>2</sub> patches

in that it comprises a loose arrangement of poorly sorted, rounded gravels with no obvious bedform development.



Figure 3.7 Field site photograph for the  $S_1$  gravel patch. Approximate patch location is highlighted by the ID label and bankfull flow direction by the white arrow.

## 3.2. Surface grain size, sorting and shape

In this study, surface grain size, sorting and shape were determined by two techniques: a Wolman count and plan-view digital photography (Subsections 3.2.1 and 3.2.2 respectively). The Wolman count was used to characterise bed surface grain size, sorting and shape at the single survey sites while digital photography was introduced as a non-destructive alternative for multiple site revisits (Subsection 3.3.1).

### 3.2.1. Wolman count

A Wolman count was conducted at each of the field sites by selecting a minimum of 150 particles across a regular grid with nodes spaced at greater than  $2.D_{max}$ . The choice of a grid spacing which exceeds the diameter of the largest grain avoids the possibility of sampling the same particle twice (Wolman, 1954). Grains were sampled immediately below the grid node which, for the dryland patches, required the use of tweezers to collect the finer fractions of bed material. The intermediate, b-axis of grains provided an index of the size of particles and sediment sorting ( $\sigma_G$ ) was calculated through Equation 3.1 and interpreted using Table 3.2.

$$\sigma_G = \frac{\vartheta_{84} - \vartheta_{16}}{4} + \frac{\vartheta_{95} - \vartheta_5}{6.6} \quad [3.1]$$

where,  $\vartheta_i$  is the  $i$ th percentile of the grain size distribution in phi units ( $\vartheta = -\log_2(D)$ ).

Table 3.2 The description of grain size sorting using the Logarithmic Folk and Ward (1957) Graphical Measure.

Sorting ( $\sigma_G$ )	Description
<b>&lt; 0.35</b>	Very well sorted
<b>0.35 – 0.70</b>	Well sorted
<b>0.50 – 0.70</b>	Moderately well sorted
<b>0.70 – 1.00</b>	Moderately sorted
<b>1.00 – 2.00</b>	Poorly sorted
<b>2.00 – 4.00</b>	Very poorly sorted
<b>&gt; 4.00</b>	Extremely poorly sorted

For the patches A<sub>1</sub>, A<sub>2</sub>, E<sub>1.1</sub>, E<sub>1.2</sub>, W<sub>1.1</sub>, W<sub>1.2</sub>, H<sub>1</sub>, H<sub>2</sub> and S<sub>1</sub>, the long (a-) and short (c-) axis of all particles >2 mm were additionally measured in order to define particle shape (Zingg, 1935) and sphericity (Krumbein, 1941). Grain roundness was not observed. The former defines four particle shapes ('Bladed', 'Discoid', 'Prolate' and 'Spheroid'; Figure 3.8), while the latter is estimated using:

$$\psi = \left(\frac{b \cdot c}{a^2}\right)^{1/3} \quad [3.2]$$

where, values of  $\psi$  occupy the range 0 – 1, where  $\psi = 1$  for a perfect sphere (Figure 3.8).

At M<sub>1</sub> and M<sub>2</sub> only the b-axis of grains were recorded and so only particle size can be determined for these surfaces. Field observations do, however, suggest the Ashop and Manifold sites, had similar particle shapes which might be expected given they share the same lithology.

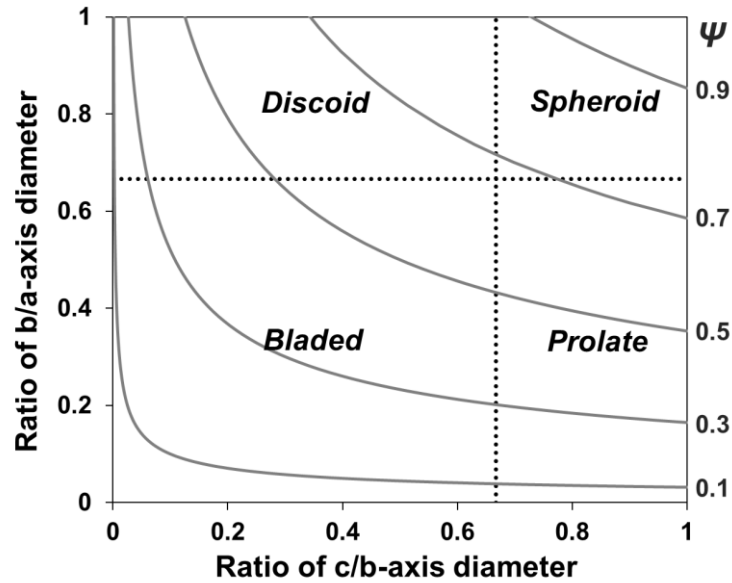


Figure 3.8 An illustration of the range of potential particle shapes calculated from the ratio between the long:intermediate and intermediate:short axis of grains using the Zingg (1935) classification and Krumbein (1941) sphericity statistic ( $\psi$ ).

Grain size sampling was conducted immediately after measurements of surface topography (Section 3.3) since the Wolman count disturbs the surface. For this reason, an alternative solution was sought to document bed texture at sites where repeat revisits were required. This took the form of automated grain sizing from digital photography (Butler et al., 2001; Carbonneau et al., 2003; Graham et al., 2005a, 2005b).

### 3.2.2. Digital gravelometry

The grain size of the gravel patches that required repeat revisits was determined using the photo sieving method of Graham et al. (2005a). This approach involves the collection of planform images from which surface grain size was digitally extracted. For this study, photographs were taken using a Panasonic Lumix DMC-FS5 camera with a 10 MP resolution (3648 x 2736 maximum image resolution) and an internal flash from a vertical height of approximately 1.5 m above the patch surface. Following the recommendations of Graham et al. (2005b) the photographed patches were shaded from direct sunlight and a flash was used to enhance the contrast between grains and interstices and minimise image-processing errors. Photographs conducted under suboptimal lighting conditions may, for instance, promote the inexact identification of grains and lead to the incorrect measurement of surface grains. An oversized frame was placed over each patch with intruding pins marking a sampling area of 1.2 m<sup>2</sup> (1.27 x 0.95 m to match the aspect ratio

of the digital images). The size of the sampling area was found to provide an adequate sample of the number of grains required for image analysis ( $\geq 300$  particles for beds where  $D_{50} \approx 64$  mm; Graham et al., 2005a). Moreover, the combination of sample area coverage and image resolution was sufficient to resolve grains with a diameter in excess of 8 mm as calculated by Equation 3.3 (Graham et al., 2005a, 2005b). For this reason, the grain size distributions generated for each of the patches by the technique were truncated at 8 mm. Equation 3.3 is given by:

$$D_{res} = \frac{23000 \cdot \sqrt{Ar_p}}{P} \quad [3.3]$$

where,  $Ar_p$  refers to the photographed areas ( $m^2$ ),  $D_{res}$  is the diameter of the smallest resolvable grain (mm) and  $P$  is the number of pixels in the image and assumes that the smallest grain of interest has a diameter which is greater than 23 pixels (Graham et al., 2005a).

The digital photographs were processed using the *Sedimetrics* Digital Gravelometer software (version 1.0.0; Graham et al., 2005a) which previous workers have found to provide reliable estimates of surface grain size from coarse-grained streambeds in humid temperate (Graham et al., 2005b) and dryland (Storz-Peretz and Laronne, 2013) environments. The software operates by firstly converting images to binary, grayscale where high intensity values represent grains and low intensity shaded interstices. A bottom-hat transformation then enhances the contrast of grain interstices while a median filter reduces the effects intra-grain noise (Graham et al., 2005a). The transformed image is finally segmented by a watershed algorithm to identify and measure individual grains.

The validity of the technique was tested by comparing the surface grain size estimates derived from a grid-by-number sample and from automated grain digitisation. The grain size distributions were compared after a  $D^2$  weighting conversion had been applied to translate the area-by-number digitised sample to a grid-by-number estimate (Kellerhals and Bray, 1971). The results are displayed in Figure 3.9 through a comparison between selected grain size percentiles ( $D_{16}$ ,  $D_{50}$ ,  $D_{84}$  and  $D_{95}$ ) calculated for both methods. There is a good agreement in surface grain size estimated from the Wolman count and *Sedimetrics* software although there is some evidence that the digital gravelometer underestimates coarser surface grains. The grain size error between methods for coarser fractions does not, however, exceed values observed by previous workers. For example, Rice and Church (1996) recorded errors in the range  $\pm 0.2 \leq \vartheta \leq \pm 0.5$  whereas for this

study the errors were  $\pm 0.05 \leq \vartheta \leq \pm 0.45$  and  $\pm 0.09 \leq \vartheta \leq \pm 0.35$  for the natural and treated patches respectively.

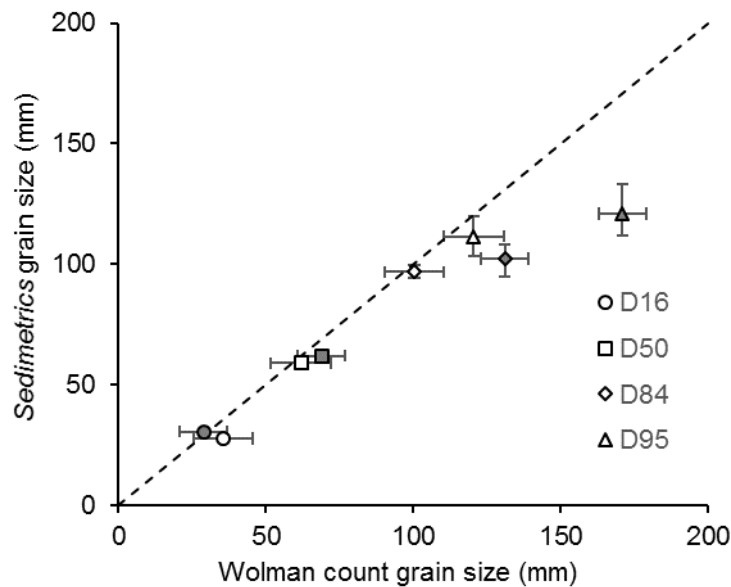


Figure 3.9 Comparison between the manual Wolman count sample and the Sedimetrics digitised estimate for the  $W_{1.1}$  natural and treated patches (open and grey-filled symbols respectively). Error bars represent 95% confidence intervals.

### 3.3. Bed microtopography

The ability to capture the micro-topography of coarse-grained alluvial surfaces accurately is essential to achieve the main aims and objectives of this research. For the purposes of this study a terrestrial LiDAR system, hereafter referred to as Terrestrial Laser Scanning (TLS), was employed to capture high resolution bed elevation data. An overview of the technique and the survey methodology employed for this study is described in subsections 3.3.1 and 3.3.2 respectively.

#### 3.3.1. Terrestrial laser scanning (TLS)

Terrestrial Laser Scanning (TLS) is an active remote sensing technique which uses the principles of laser ranging to construct a 3D cloud of points from discrete surface measurements. The technique was originally developed with a narrow engineering-focus but has since been exploited within a wide realm of pure and applied scientific research to include mapping and monitoring fluvial form and process (Alho et al., 2011; Hohenthal et al., 2011). As summarised in Table 3.3, TLS has been used to characterise streambed

morphology across a range of spatial scales: from wider, reach-scale investigations (e.g. Brasington et al., 2012) to local, patch-scale inspection (e.g. Hodge et al., 2009b; Wang et al., 2011).

Table 3.3 Summary of selected work using TLS to map coarse-grained alluvial streambed topography.

Reference	Study site/s	Survey area (m <sup>2</sup> )	Sampling resolution (m)
<b>Heritage and Hetherington (2007)</b>	River Wharfe, UK	2,250	0.010*
<b>Milan et al. (2007)</b>	Mont Miné and Ferpècle glaciers, Switzerland	5,881	0.019**
<b>Entwistle and Fuller (2009)</b>	River South Tyne, UK River Coquet, UK Kingsdale Beck, UK	180 10,600 c.600	0.012* 0.040* 0.009*
<b>Heritage and Milan (2009)</b>	River South Tyne, UK	180	0.012*
<b>Heritage et al. (2009)</b>	River Nent, UK	9,900	0.090**
<b>Hodge et al. (2009b)</b>	Bury Green Brook, UK River Feshie, UK	1	0.002
<b>Wang et al. (2011)</b>	Nan-Shih and Pei-Shih Rivers, Taiwan	4 – 36	0.003 – 0.010
<b>Brasington et al. (2012)</b>	River Feshie, UK	140,000	0.013*
<b>Storz-Peretz and Laronne (2013)</b>	Nahal Rahaf, Ze'elim and Roded, Israel	612 – 4,280	0.003 – 0.008
<b>Storz-Peretz et al. (2016)</b>	Nahal Ze'elim and Rahaf, Israel Barranca-de-los-Pinos, Spain La-Bléone River, France Saisera and Cimoliana, Italy	52 – 4,280	0.003 – 0.008

\*mean spacing

\*\*median spacing

The TLS technique operates by measuring the distance between the sensor and a neighbouring surface using laser pulses. While older sensors (e.g. Leica HDS 3000, ScanStation 2) rely on the ‘time of flight’ (ToF) principle of ranging to infer surface locations, newer models (e.g. Leica ScanStation P20) collect data through a combination of ToF and phase shift technologies, e.g. waveform digitization (WFD; Leica Geosystems, 2013). Recent advancements in TLS have also led to an increase in the rate of data acquisition from 4,000 to 1,000,000 points sec<sup>-1</sup> and the levelling of individual scan views from a dual-axis tilt compensator (Leica Geosystems, 2006, 2007, 2013).

The humid temperate gravel patches chosen for surface characterisation (objective 1) and the initial surveys of the temporal morphodynamics work (objective 2; 12.12.12 – 04.02.14) were carried out using Leica HDS 3000 and ScanStation 2 models of TLS (Table 3.4). The Leica ScanStation P20 was used for the later survey series of W<sub>1.1</sub> and W<sub>1.2</sub> (i.e. post 18<sup>th</sup> November 2014 surveys) and the surveys of the dryland patches (H<sub>1</sub>, H<sub>2</sub> and S<sub>1</sub>). TLS instrument key technical specifications are presented in Appendix A.

Table 3.4 Overview of the TLS sensor used for each of the topographic surveys.

Field Site	Patch ID	Survey date/s (dd.mm.yy)	TLS sensor
<b>Ashop</b>	A <sub>1</sub>	22.07.13	HDS 3000
	A <sub>2</sub>		
<b>Afon Elan</b>	E <sub>1.1</sub>	26.05.10	HDS 3000
	E <sub>1.2</sub>	27.05.10	
<b>Manifold</b>	M <sub>1</sub>	14.11.12	HDS 3000
	M <sub>2</sub>		
<b>Wharfe</b>	W <sub>1.1</sub>	12.12.12 – 06.11.13	HDS 3000
		04.02.14	ScanStation 2
		18.11.14 – 15.04.15	ScanStation P20
	W <sub>1.2</sub>	06.11.13	HDS 3000
		04.02.14	ScanStation 2
		18.11.14 – 15.04.15	ScanStation P20
<b>Hever</b>	H <sub>1</sub>	03.05.14	ScanStation P20
	H <sub>2</sub>	07.05.14	
<b>Shafan</b>	S <sub>1</sub>	04.05.14	ScanStation P20

Topographic surveys, including those conducted using the TLS, are subject to various sources of error that can be classed as random, systematic and gross (Hodge et al., 2009a). Random errors represent the variability of repeated measurements and reflect the precision of the sensor, while systematic errors signify the difference between the sampled and real surface and dictate the accuracy of point measurements (Hodge et al., 2009a). Gross errors are caused by human error or malfunctioning equipment and denote the reliability of the method of data collection.

Scanner hardware design, surface reflectivity and imaging geometry have been identified as important factors which influence the magnitude of error in TLS data (Lichti et al., 2005). For example, angular displacement errors and mixed pixels result from the inexact measurement of points from geometrically rough surfaces. The former is caused where a point location is misplaced, e.g. from the edge of the laser footprint but attributed to the centre, whereas the latter is produced from the integration of multiple returns within the laser footprint causing a false record of the interacting surface (Reschetyuk, 2006; Hodge et al., 2009a). Mixed pixels are most commonly observed as a trailing edge of points extending beyond the edges of coarse, emergent grains (cf. Hodge et al., 2009a: 963).

The significance of the errors in TLS data is highly dependent on the scale of study; small errors will radically affect the quality of high resolution measurements but are less consequential as the signal/noise ratio increases, i.e. for low resolution, reach-scale inspection (Hodge et al., 2009a). As this study is focused on characterising patch-scale morphology, the management of errors during data collection and processing is of fundamental importance for generating surfaces suitable for statistical examination. In this regard, the adoption of recommended strategies for surveying (e.g. Heritage and Hetherington, 2007) can help to minimise error during the acquisition of data while the application of filters during processing can further eradicate sources of error (e.g. angular displacement errors, mixed pixels; Hodge et al., 2009a) within collected point cloud data.

### **3.3.2. Survey methodology**

The methodology employed to conduct topographic, LiDAR surveys was guided by recommendations of previous workers to inform choices regarding patch size, spatial resolution of scans and correct surveying protocol. For instance, in the humid temperate rivers, field work was undertaken during periods of low flow when bar features were subaerially exposed and could be surveyed without recourse to through-water sensing techniques (e.g. Smith et al., 2012). Moreover, previous work on the characterisation of river bed structure has typically relied on relatively small patches (e.g. 1 x 1m; Hodge et al., 2009b). However, recent research has revealed that larger patches may be necessary to fully document large scales of roughness associated with bedforms such as pebble clusters (Huang and Wang, 2009). Given the limited timeframe available for field work, a compromise had to be made between patch size and the spatial resolution of the

topographic surveys. This balance was achieved by extending patches to 2 – 18 m<sup>2</sup> while maintaining a minimum sampling resolution of 3 mm at a distance of 10 m across each of the surveys. The choice of scan resolution was designed to ensure a minimum point spacing of 3 mm across the patch, which was deemed sufficient to capture surface microtopography. Further increases in the spatial resolution of scans are limited by the size of the laser footprint (c.6 mm at 50 m; Leica Geosystems, 2006) and do not improve the quality of patch surveys, i.e. by revealing additional surface information (Hodge et al., 2009a, 2009b).

The data capture methodology was optimised to account for the complex nature of gravel streambed topography (Soudarissanane et al., 2011). For the majority of patches, the coarse calibre of sediment resulted in a rough microtopography. The use of isolated scanning viewpoints may, therefore, undersample those areas of a patch that are shadowed from the sensor position by coarse, prominent clasts (Heritage and Hetherington, 2007). This was mitigated by taking scans from a minimum of three locations around the patch. Scan positions were preferentially located downstream of the patch (Figure 3.10) in recognition that much of the bed material was imbricated, i.e. with the greatest surface relief orientated in a downstream direction (Heritage and Hetherington, 2007). A maximum of four scan positions were used as previous workers have found no evidence that further increasing the number of scanning viewpoints yields any additional surface information (Hodge et al., 2009a; Huang and Wang, 2009). For each scan, the TLS was mounted on a fibreglass tripod at a height c.1.7 m above the patch surface. The elevated position of the sensor helped to increase the incidence angle and further reduce the proportion of the bed surface prone to shadowing (Heritage and Hetherington, 2007).

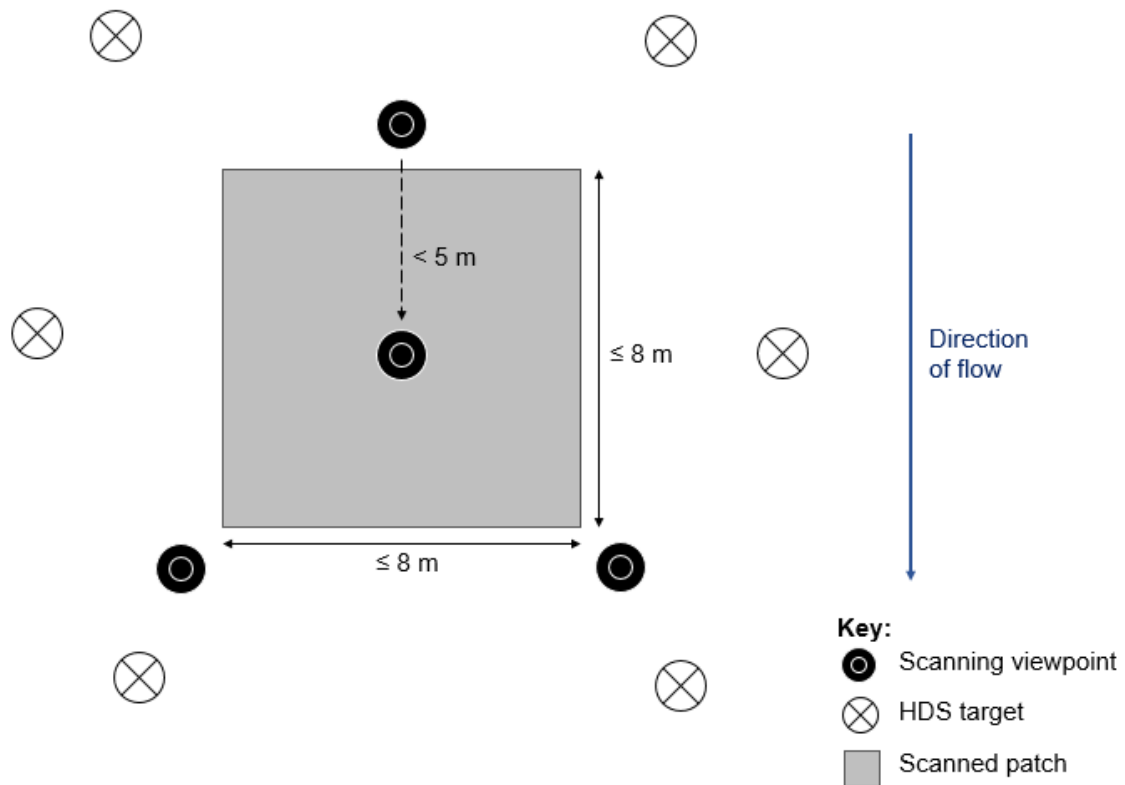


Figure 3.10 Illustration of survey setup in the field. Adapted from Hodge et al. (2009a)

The precision of HDS 3000 and ScanStation 2 sensor measurements were improved by averaging two-three repeated scans from each viewpoint using an identical surveying strategy and equipment settings (e.g. spatial resolution and field-of-view). The use of up to three replicate scans provided the optimum compromise between increased point precision and the limited time constraints for collecting data in the field (Hodge et al., 2009a). As the Leica ScanStation P20 is unable to store repeat scans in an accessible format, the surveys with this instrument relied on the use of an adjustable ‘quality setting’ which also operates by considering a local neighbourhood of points to reduce range noise and improve data quality.

Another potential source of error concerns the registration of individual scan viewpoints using a network of static Leica high definition (HDS) targets placed around the extremities of the survey area. The relative positions of these targets were recorded from each of the scan positions and used to co-register the individual surveys into one locally-defined coordinate system. This registration process was handled with the Leica Geosystems’ proprietary Cyclone software (Version 9.0) using a 3D bundle adjustment algorithm. The use of three-six targets placed at different heights around the survey area (e.g. Heritage and Hetherington, 2007) ensured registration bias, from a poorly designed target network geometry, was minimised. High target-to-target displacement distances

were disabled from the registration process to restrict 3D mean absolute error to 1 mm for all surveys. For the repeat surveys, the registered point clouds of the individual surveys were subsequently referenced into a coordinate system defined from a total station (TS) survey. The use of an independent coordinate system was necessary to level the initial surveys conducted using the Leica HDS 3000 TLS. Although a dual-axis compensator was later added to the Leica ScanStation 2 and P20 models of TLS sensor, the TS coordinate transformation is applied across all repeated surveys. The 3D positional errors associated with the transformation from the HDS target-defined to TS-derived coordinate system were c.10 mm for the field sites on the River Wharfe. Consequently, the level of minimum detectable change between repeat surveys (LoD) was in the order of 10 mm (Brasington et al., 2000, 2003; Wheaton et al., 2010).

### **3.4. Data processing**

Despite following an optimised survey strategy, errors are still present in high resolution TLS data collected from geometrically rough surfaces, e.g. through angular displacement errors and mixed pixels. These are detrimental to point cloud and DTM quality and prompt the inclusion of various filtering steps to the data processing workflow to improve data quality. As shown in Figure 3.11, this involved the application of four potential filters: the Repeat Scan Error Value (RSEV; Step 1), Cone (Step 4) and Local high point (Step 5) filters devised by Hodge et al. (2009a) and implemented in MATLAB and the Statistical Outlier Removal (SOR) filter (Step 2) designed by the Point Clouds Library (PCL) open source project and available as a plug-in within the open source CloudCompare software (Version 2.8.1). A methodological description of the four filters and their role in removing error from TLS data (i.e. Figure 3.12) is described through the subsections 3.4.2-5. Once a filtered dataset had been generated, the point cloud was then converted into a surface (Step 7) which was detrended (Step 9) ready for statistical evaluation (Step 10). The quality of the filtered point cloud and associated surface were evaluated through the respective (Step 6) error analysis and DTM assessment (Step 8) workflow steps following Hodge et al., (2009a).

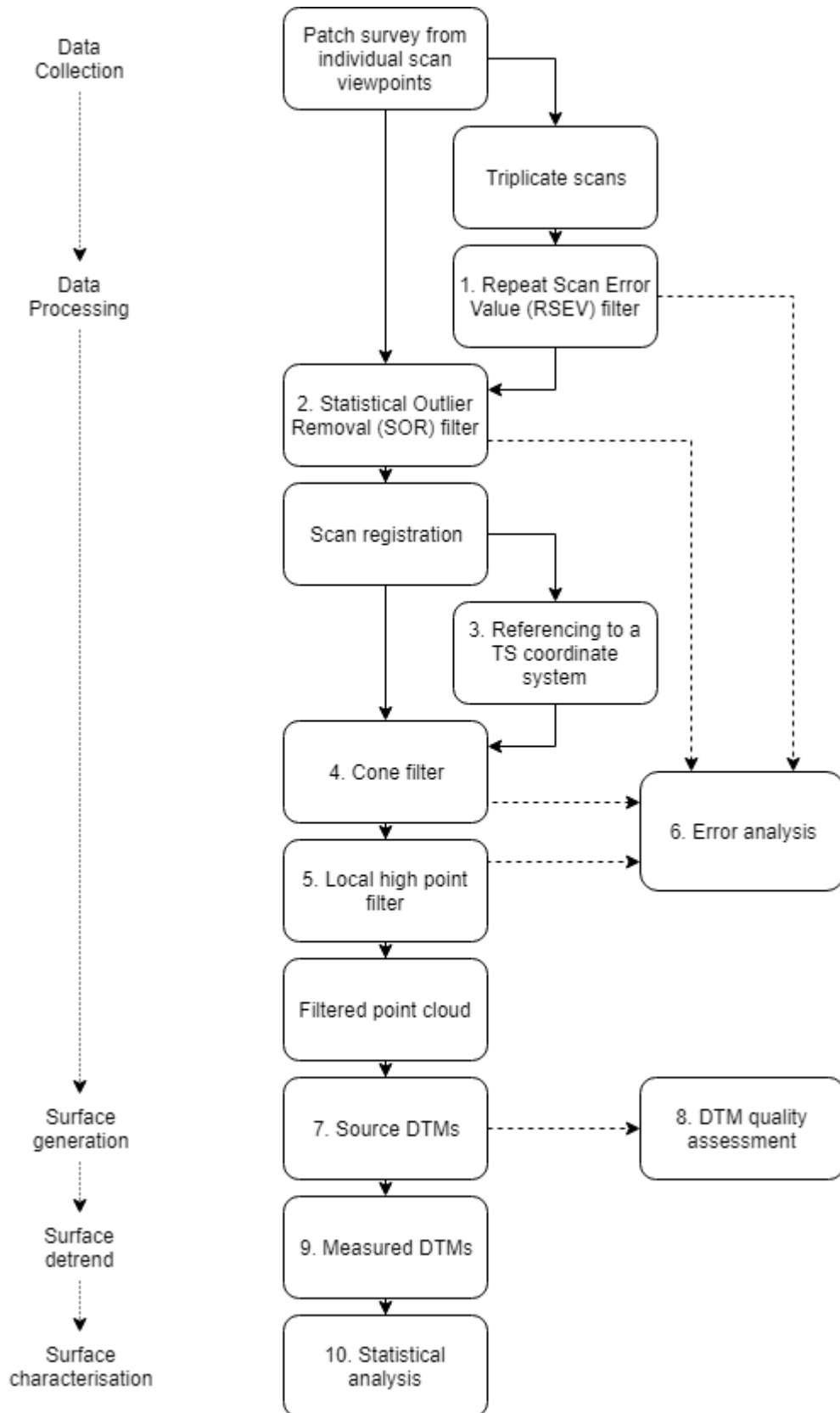


Figure 3.11 The modular workflow used to collect and process TLS data and generate high-resolution DTMs for statistical analysis. Step [1] was used for the HDS 3000 and ScanStation 2 surveys and [3] for the  $W_{1.1}$  and  $W_{1.2}$  experimental series.

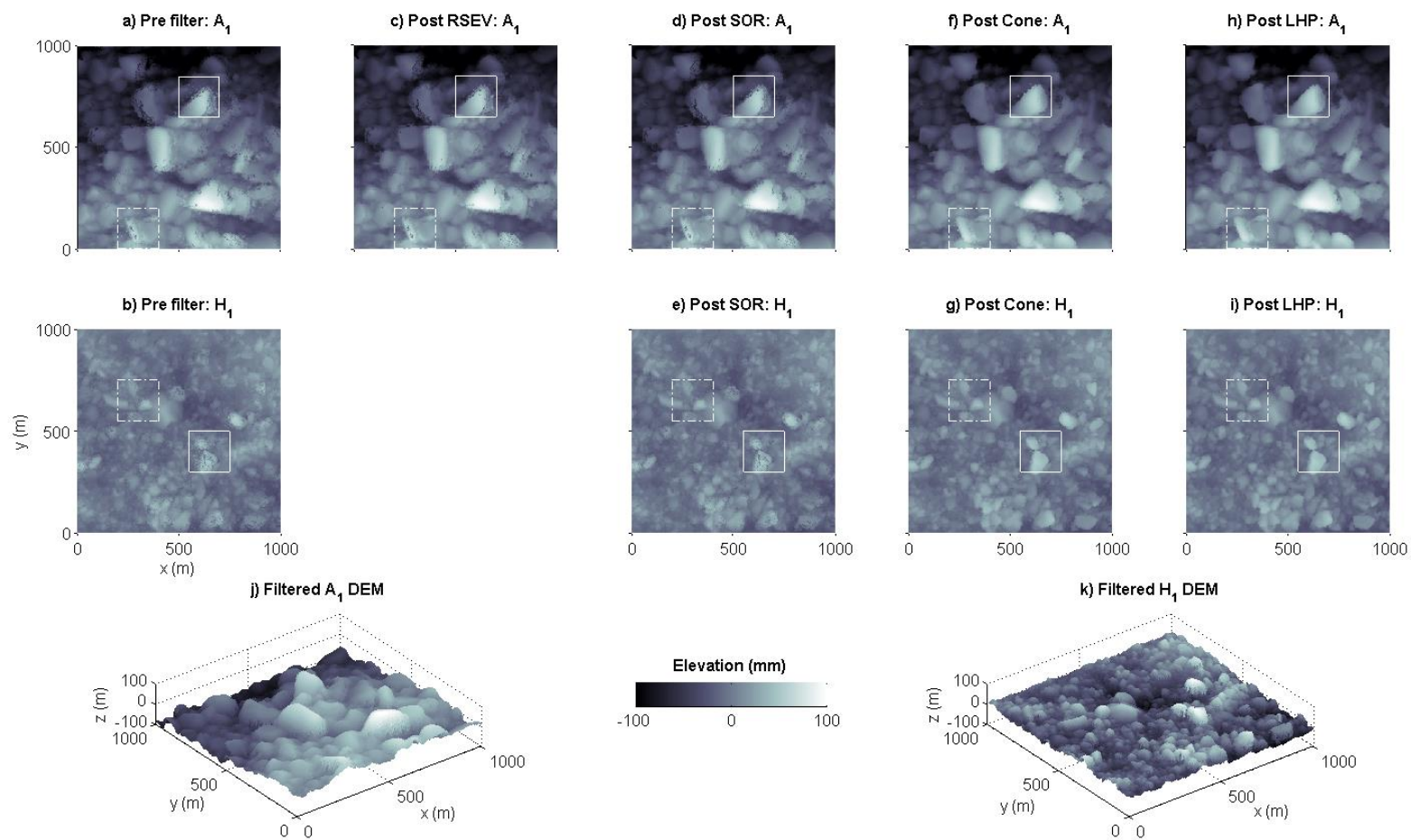


Figure 3.12 Stages of processing the  $A_1$  (a, c, d, f, h, k) and  $H_1$  (b, e, g, i, j) sub-patches using workflows for the HDS 3000/ScanStation 2 and P20 TLS sensors respectively. High-resolution (3mm) DTMs are generated at each stage of the workflow: for the a-b) raw data and after application of the c) RSEV, d-e) SOR, f-g) Cone and h-i) Local high point filters. Two 200 x 200 mm boxes highlight areas of error removed during this process. Lastly j-k) present orthogonal views of the final sub-patch DTMs for  $A_1$  and  $H_1$  respectively. Adapted from Hodge et al. (2009a).

### 3.4.1. *E*-parameter

On inspection, the pre-filtered DTMs were subject to two sources of error, those associated with trailing mixed pixels and local outliers. These errors are likely to significantly impact the quality of surfaces produced from unfiltered point clouds and necessitated the addition of the RSEV, SOR, Cone and Local high point filters. As the quality of TLS data at this scale is comparable to other surveying methods (e.g. TS; Pandzic et al., 2014), alternate remotely sensed datasets cannot provide a reference dataset suitable for error and filter parameter assessment. Consequently, the choice and sequencing of filters and selection of appropriate parameter values for point cloud filtering was guided by internal validation. Although the filters are designed to remove different sources of error, they all operate by excluding outliers which lie beyond a threshold distance from a local collection of points. For large values of the threshold (i.e. coarse filters), only the largest outliers will be removed from the point cloud. As the filter threshold decreases, the amount of data excluded increases until, at very low thresholds, the filter will undersample the true surface. A compromise must, therefore, be made between the amount of data and the magnitude of error retained. This balance was resolved through a combination of visual assessment and iterative sensitivity analysis. The former involved a visual examination of the interpolated point cloud (source DTM), generated under various filter scenarios, to provide a qualitative assessment of surface quality (e.g. identify isolated outliers in elevation; cf. Hodge et al., 2009a: 962). The latter considered the distribution of the mean elevation difference parameter (*E*; equation [3.4]) calculated across the DTM using a three-by-three moving window (e.g. Hodge et al., 2009a; Hodge, 2010).

$$E = \frac{(\sum_{i=2}^9 z_1 - z_i)}{8} \quad [3.4]$$

where,  $z_1$  is the elevation of the centroid cell of a three-by-three moving window and  $z_2$ - $z_9$  are the elevations of the surrounding perimeter cells.

High values of *E* represent significant differences in local elevation between the point at the centre of the moving window and the surrounding perimeter cells and can be attributed to erroneous points in the point cloud (Hodge et al., 2009a). The choice of parameter settings was advised by 1 m<sup>2</sup> sub patches extracted from of the patch surveys. These patches were

used to train the filters using a range of parameter values and evaluating the difference between surfaces created from the resultant point clouds. The patches were carefully selected to provide a good representation of the patch surface (e.g. to be inclusive of high- and low-relief topography) to ensure parameter values were not biased toward particular bed conditions.

### 3.4.2. Repeat Scan Error Value (RSEV) filter

The initial step in processing the Leica HDS 3000 and ScanStation 2 point clouds was provided by the *RSEV* filter (Step 1; Figure 3.12c). The *RSEV* metric documents the precision of individual points by calculating the maximum 3D distance between points gathered from replicate scans along the same path lines (Equation 3.5), i.e. from topographic surveys repeated from an individual scan position using identical scanning parameters. The filter was, therefore, primarily designed to isolate and remove points which are subject to range-bias errors, i.e. those identified as mixed pixels. Values of *RSEV* are given by:

$$RSEV = \max \left[ \sqrt{(x_i - x_j)^2 + (y_i - y_j)^2 + (z_i - z_j)^2} \right] \quad [3.5]$$

where  $x_i, y_i, z_i$  and  $x_j, y_j, z_j$  are  $x, y, z$  coordinates for the scans  $i$  and  $j$  respectively.

The *RSEV* filter was applied to the raw point cloud data for a range of threshold values, from 10 mm to 1 mm at 1 mm intervals. The choice of an optimal *RSEV* threshold was determined by a combination of 1) the distribution of *E*-parameter values, 2) visual inspection of the points clouds and associated DTMs generated for different thresholds and 3) an assessment of the amount of data retained for each *RSEV* threshold. By way of illustration, a typical example of the effect of varying the *RSEV* threshold is shown for A<sub>1</sub> in Figure 3.13. The main outcome of reducing the *RSEV* threshold is to narrow the distribution of *E*. For the example shown, the range between the 5<sup>th</sup> and 95<sup>th</sup> percentiles of the *E* distribution ( $E_{95}-E_5$ ) decreases from 7.1 mm for the unfiltered dataset to 2.8 mm after the 1 mm *RSEV* threshold. The greatest reduction in the distribution of *E* occurs for the lower threshold values ( $1 \text{ mm} \leq RSEV \leq 4 \text{ mm}$ ;  $2.7 \text{ mm} \leq E_{95}-E_5 \leq 5.4 \text{ mm}$ ) with little, observed change for higher thresholds ( $5 \text{ mm} \leq RSEV \leq 10 \text{ mm}$ ;  $5.7 \text{ mm} \leq E_{95}-E_5 \leq 6.4 \text{ mm}$ ).

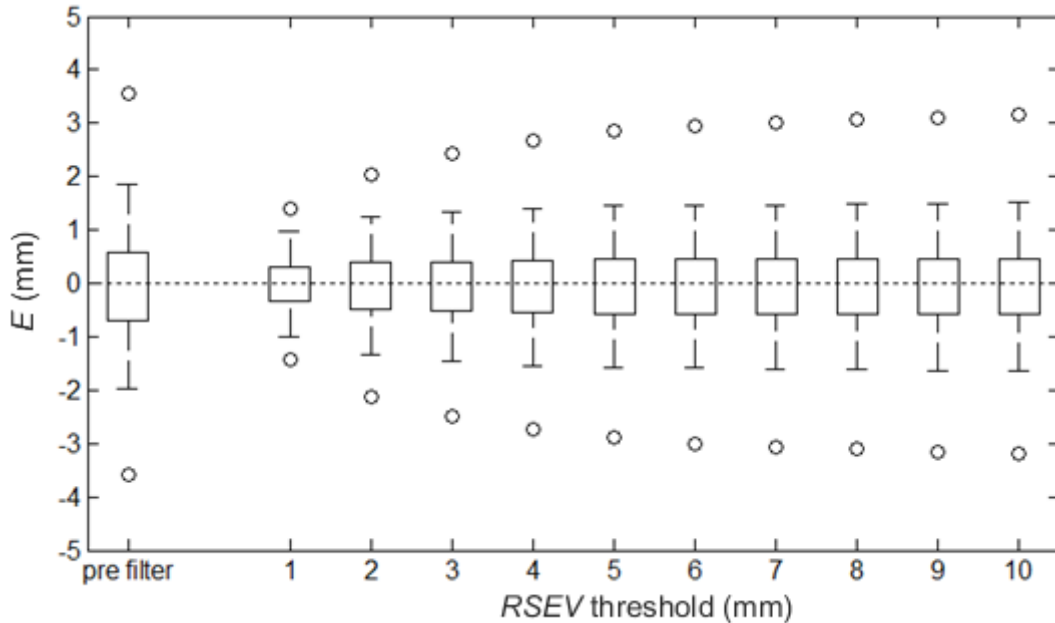


Figure 3.13 Distributions of  $E$  for the  $A_1$  patch after the application of the  $RSEV$  filter using a range of threshold values. Boxes show inter-quartile range (IQR), upper and lower whiskers represent (25<sup>th</sup> percentile) and (75<sup>th</sup> percentile) respectively and circles the 5<sup>th</sup> and 95<sup>th</sup> percentiles. Diagram adapted from Hodge et al. (2009a).

The progressive removal of erroneous points from the raw dataset as the threshold is reduced is also evident in the resultant DTMs (Figure 3.14). Outliers of high or low elevation relative to the local surface highlight topographic discontinuities and the presence of error in the raw point cloud (see inside the boxed areas boxes of the pre-filtered DTM; Figures 3.12a-b). The filter acts to remove points around grain edges where mixed pixels occur until, at the lowest  $RSEV$  thresholds (e.g. for the 1 mm and 2 mm DTMs), the dataset has been undersampled to such an extent that the finer details of microtopography (e.g. the boundaries of the grains) cannot be easily distinguished. In this study, an  $RSEV$  threshold of 7 mm was found to be the optimal threshold ( $RSEV_{opt}$ ) for all surfaces, eliminating 8 – 41% of the point cloud (Figure 3.15a) and narrowing the distribution of  $E$  to  $3.9 \text{ mm} \leq E_{95} - E_5 \leq 8.8 \text{ mm}$  (Figure 3.15b). The greatest reduction in data using the 7 mm  $RSEV$  threshold was found for the  $M_1$  and  $E_{1,2}$  patches. This is unsurprising since both surfaces comprised fine gravels and a relatively smooth surface for which mixed pixel errors are expected to be more likely (because individual laser pulses are more likely to interact with multiple grain edges; Hodge et al., 2009a). Previous workers (e.g. Hodge et al., 2009a) have found a 5 mm  $RSEV$  threshold was most effective in removing mixed pixel errors, i.e.  $RSEV_{opt} = 5 \text{ mm}$ . However, in using the 5

mm the filter was found to remove an excessive proportion of the merged point cloud (Figure 3.15a: 0.43 – 0.76; cf. 0.23 – 0.53 in Hodge et al., 2009a). The difference in point precision is attributed to several factors including i) the lower scanning resolution of this study (3 mm vs. 2 mm) and ii) the greater difference between the sensor and the patches and an associated reduction in the incidence angle that resulted from the larger patch sizes under consideration. The latter is considered a more significant factor as the quality of TLS measurements is not necessarily improved once the sampling resolution falls below the laser spot size (Hodge et al., 2009a).

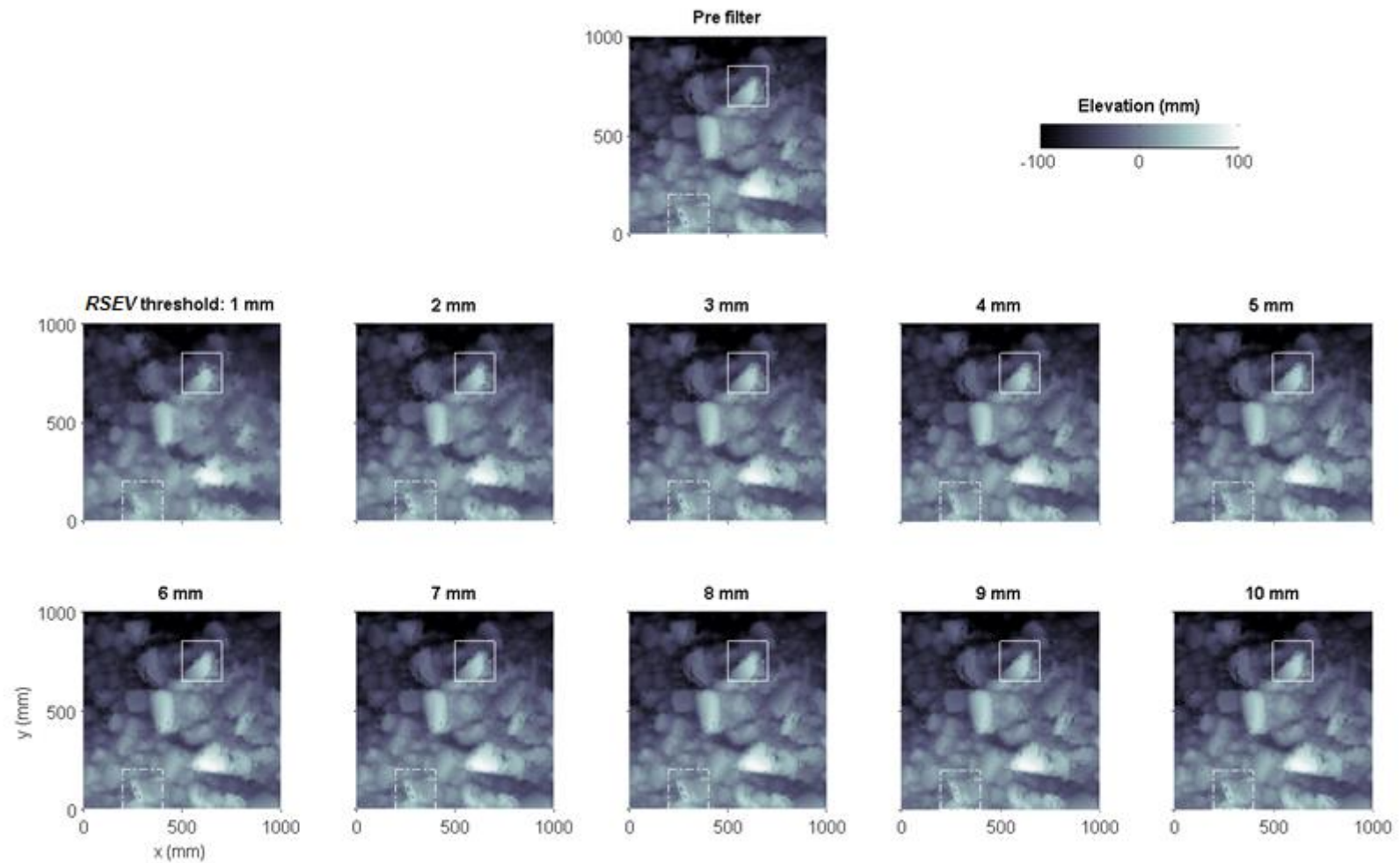


Figure 3.14 Digital elevation models generated for a range of *RSEV* thresholds relative to the original, unfiltered  $A_1$  patch. Two 200 x 200 mm boxes highlight areas of error removed using the *RSEV* filter.

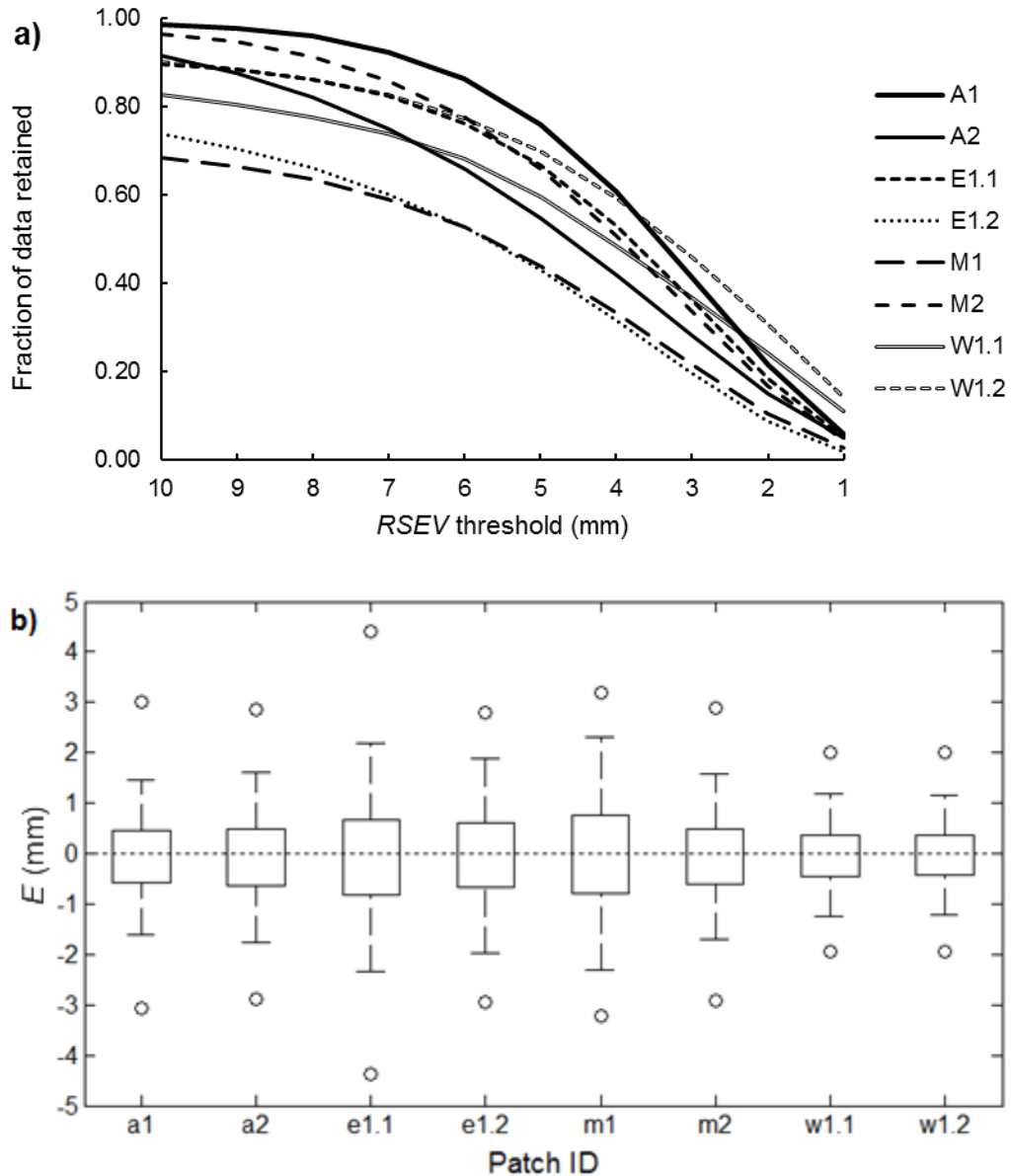


Figure 3.15 The proportion of data retained across a range of *RSEV* thresholds for the humid temperate patches. b) Distributions of the *E* parameter following the application of the 7 mm *RSEV* threshold to the humid temperate patches.

### 3.4.3. Statistical Outlier Removal (SOR) filter

The second step in processing the Leica HDS 3000/ScanStation 2 and first for the ScanStation P20 clouds was through the application of the SOR filter (Step 2; Figure 3.12d-e). The SOR filter works by calculating the average location of a local neighbourhood of points and then removes points further than a specified distance (a multiple of the local

standard deviation of points) from the average. The filter was chosen in preference to CloudCompare's Noise filter since the latter removes points relative to a locally fitted plane and is therefore more suited to low relief (topographically simple) surfaces. Given the close similarities between the RSEV and SOR filters, this workflow step was also designed to remove mixed pixel errors that remain within the point clouds derived using the HDS 3000 and ScanStation 2 after application of the RSEV filter (Figure 3.16a).

Aside from the proprietary filters provided by Leica Geosystems (e.g. the undefined and unspecified 'data quality' setting), the SOR filter provides the first step in actively filtering point cloud data collected using the P20 TLS sensor. Through an iterative inspection of point clouds cleaned by the SOR filter, two sequential steps were found to provide the most effective method in removing mixed pixels from individual scan views. The first stage removes points outside  $4\sigma$  from the mean distance between a neighbourhood of 10 points (SOR filter 1; Figure 3.16b), while the second retains values within a  $6\sigma$  distance set by a larger collection of 100 points (SOR filter 2; Figure 3.16c). Standalone filters (i.e. using SOR filter 1 or 2) are not capable of sufficiently filtering the data to remove visually prominent, outliers. Through this process, the distributions of  $E$  narrow from  $E_{95}-E_5 = 8$  mm for the unfiltered surfaces to  $5.3 \text{ mm} \leq E_{95}-E_5 \leq 7.4$  mm for the dryland patches (Figure 3.16d) while removing 1% of the point cloud.

As the point clouds collected using the HDS 3000 and ScanStation 2 had already been initially filtered using the RSEV filter, the two-stage filtering step used for the P20 scans was found to remove too much surface detail from the DTMs. Consequently, an alternate solution was sought to filter any remaining mixed pixels from the HDS 3000 and ScanStation 2 scans. This took the form of a single, moderate filtering step which involved retaining points within  $6\sigma$  from the mean distance between a neighbourhood of 100 points (i.e. SOR filter 2) and was responsible for removing less than 1% of points from the RSEV-filtered datasets. The distributions of  $E$  after the application of the SOR filter (Figure 3.17) range between  $3.9 \text{ mm} \leq E_{95}-E_5 \leq 8.5$  mm and compare favourably with the SS2 SOR-filtered scans. This would suggest the quality of the point cloud data after these filtering steps is broadly comparable despite differences in sensor and the initial stages of the filtering workflow.

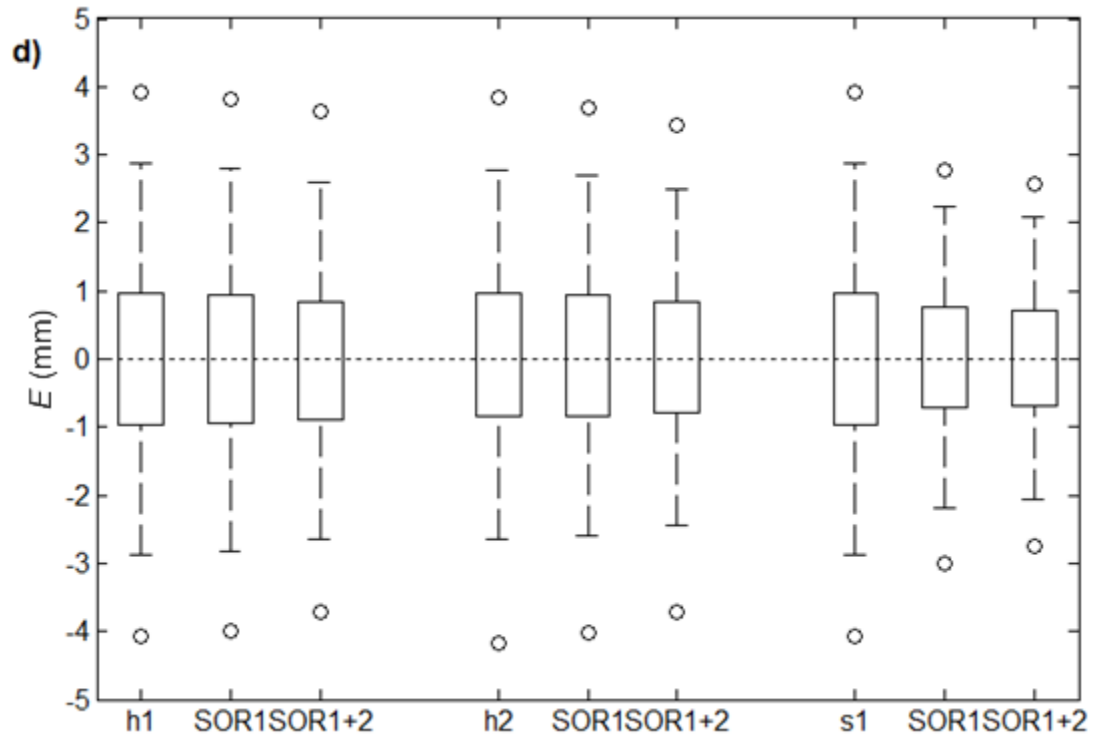
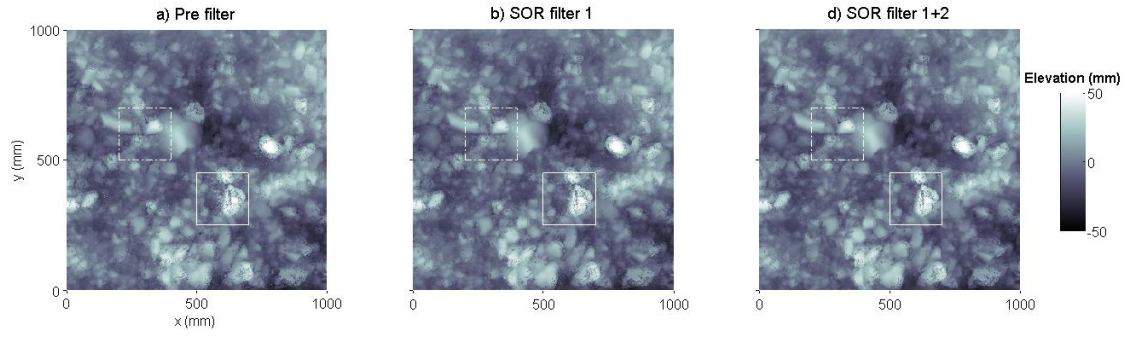


Figure 3.16 a-c) Comparison of DTMs for the SOR-filtered  $H_1$  patches under various filter scenarios and d) the effects of filtering on the distributions of the  $E$  parameter for the dryland patches.

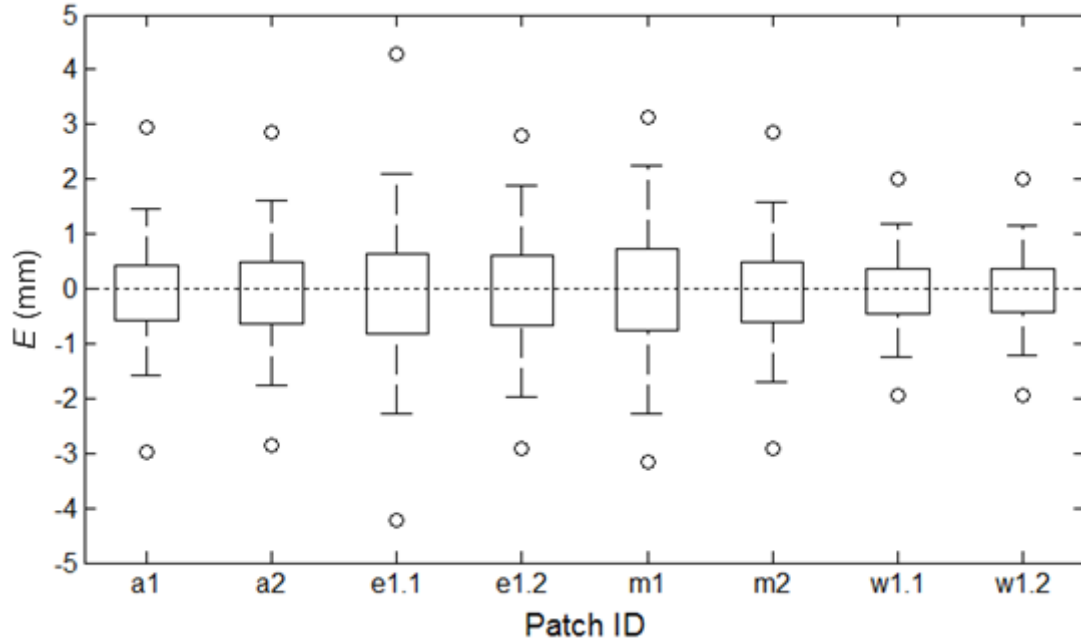


Figure 3.17 Distributions of the  $E$  parameter following the application of the SOR filter ( $6\sigma$  from a neighbourhood of 100 points) to the humid temperate patches. Statistical description of boxplot as in Figure 3.6.

### 3.4.4. Cone filter

The Cone filter (Step 4; Figure 3.12f-g) operates by removing all underlying points within a local geometric cone as defined by two parameters: a filter radius ( $r$ ) and a divergence angle ( $\theta$ ). This step was required to eliminate multiple  $z$  values for single  $x$ - $y$  coordinates which arise from scanning the upper and lower faces of grains (Figure 3.18) and can affect the quality of  $2\frac{1}{2}$ D interpolation. Moreover, the majority of conventional statistical approaches (e.g. variograms and surface slope and aspect analyses) are designed to operate over  $2\frac{1}{2}$ D surfaces.

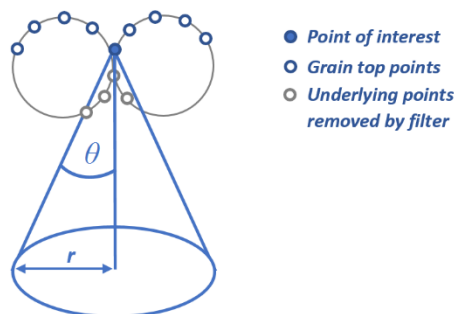


Figure 3.18 Schematic diagram of the Cone filter, adapted from Hodge et al. (2009a: 959).

The assessment of the cone filter was performed for a range of divergence angles ( $2.5 \leq \theta \leq 20^\circ$ ) and filter radii ( $1.25 \leq r \leq 10$  mm) following Hodge et al. (2009a). The results of this assessment are presented for  $A_1$  and  $H_1$  in Figures 3.19a and 3.20a respectively. As the divergence angle increases the number of points removed by the filter increases and consequently the distribution of  $E$  narrows. The narrowing of the  $E$  distribution during this process was accentuated by an increase in the size of the filter radius such that the Cone filter was more sensitive to changes in  $r$  than  $\theta$ . In terms of the post-filtered DTMs (e.g. Figures 3.12f and 3.12g), ineffective filters were found to either fail to remove points from the undersides of grains, causing small-scale fluctuations in the DTM, or to discard excessive data below the edges of emergent grains which resulted in a loss of surface detail. Despite the similarities in the quality of the SOR-filtered data from the different TLS sensors, this study found that two different parameter setups were most effective in removing subsurface points for data collected using the Leica HDS 3000/ScanStation 2 and ScanStation P20. In the first instance, an optimal cone filter with  $r_{opt} = 5$  mm radius and  $\theta_{opt} = 10^\circ$  was found most appropriate for the HDS 3000/SS2 scans and reduced the spread of the  $E$  distribution from  $3.9 \text{ mm} \leq E_{95}-E_5 \leq 8.5 \text{ mm}$  (SOR-filtered data) to  $3.2 \text{ mm} \leq E_{95}-E_5 \leq 5.0 \text{ mm}$  (Figure 3.19b). Through this process 39 – 74% of the original dataset was retained (removing a further 18 – 33% of the SOR-filtered point clouds; Figure 3.19c). The P20 scans required a different filter –  $r_{opt} = 2.5$  mm and  $\theta_{opt} = 5^\circ$  - which narrowed the distribution of  $E$  for the dryland patches from  $5.3 \text{ mm} \leq E_{95}-E_5 \leq 7.4 \text{ mm}$  to  $4.7 \text{ mm} \leq E_{95}-E_5 \leq 6.6 \text{ mm}$  (Figure 3.20b) and in the process preserved 76 – 82% of the unfiltered dataset (removing 17 – 24% of the SOR-filtered data; Figure 3.20c). Meanwhile, Hodge et al. (2009a) found  $r_{opt}$  and  $\theta_{opt} = 5$  mm and  $10^\circ$  respectively which removed an additional 15 – 26% of the RSEV-filtered point cloud (retaining 38 – 66% of the unfiltered dataset). Thus, an identical Cone filter was used to process the HDS 3000/SS2 scans for this study and by previous workers while a smaller filter was required for the P20 scans.

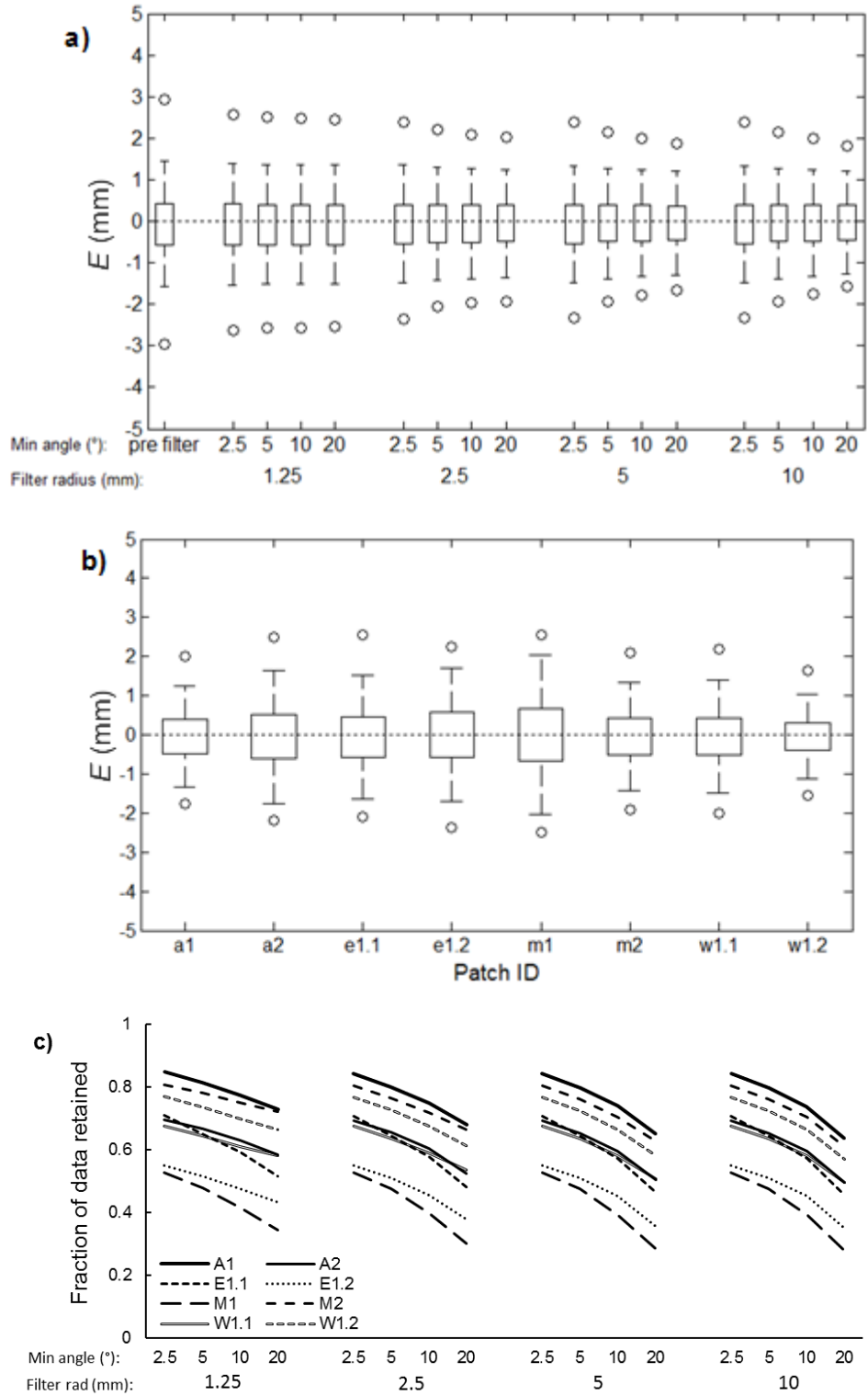


Figure 3.19 Distribution of  $E$  for a) the A<sub>1</sub> patch across a range of Cone filter parameters and b) following the application of the optimal filter (5 mm 10°) to all the humid temperate patches. c) The proportion of the unfiltered point cloud retained under each filter scenario for all humid temperate patches. a) adapted from Hodge et al. (2009a).

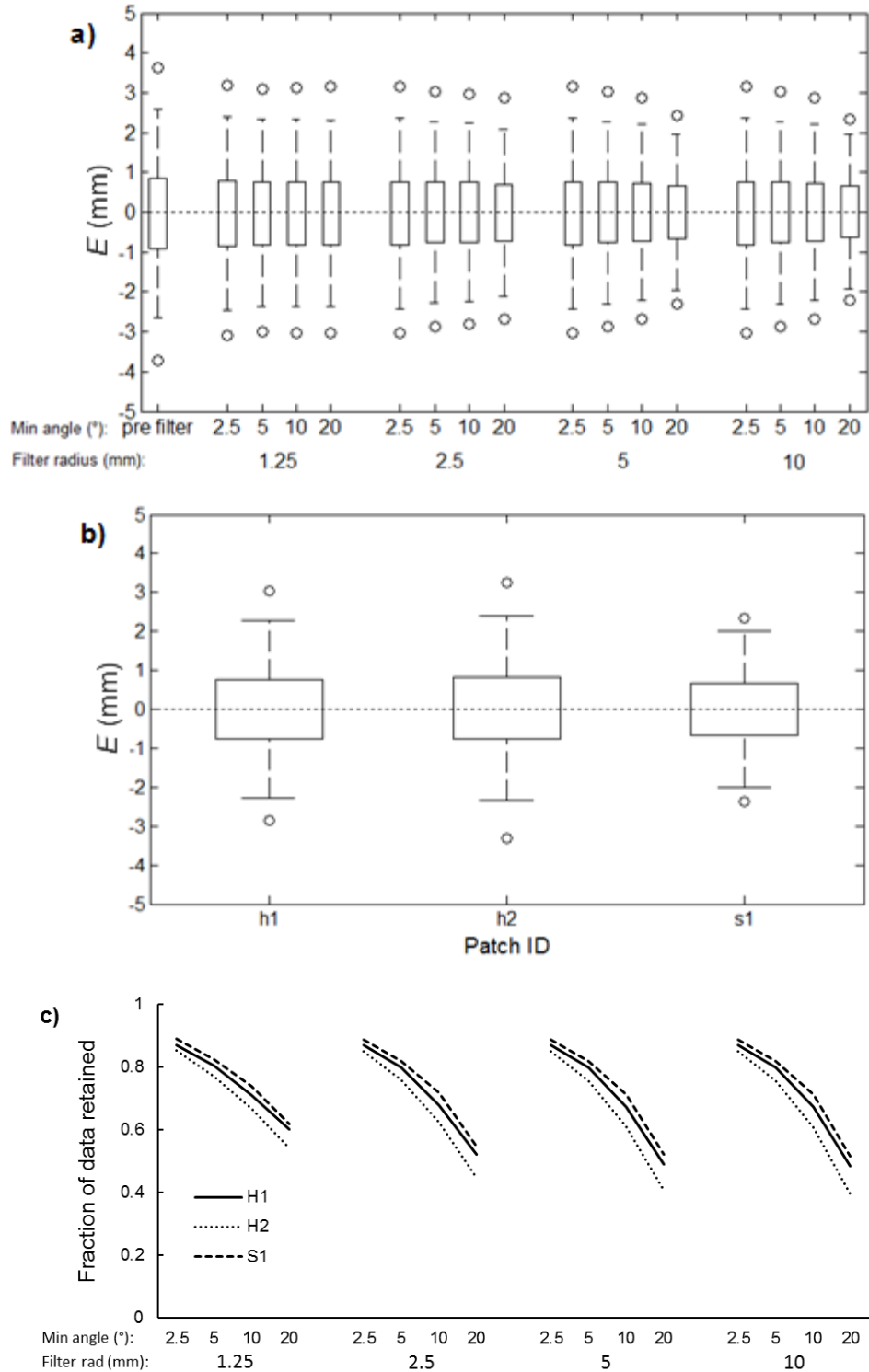


Figure 3.20 Distributions of  $E$  for a) the H<sub>1</sub> patch across a range of Cone filter parameters and b) following the application of the optimal filter (2.5 mm 5°) to the three dryland patches. c) The proportion of the unfiltered point cloud retained under each filter scenario for the dryland patches. a) adapted from Hodge et al. (2009a).

### 3.4.5. High Point filter

The final stage of the filtering workflow (Step 5; Figure 3.12h-i) used a local high point filter, informed by a filter radius ( $r$ ) and threshold height ( $ht$ ) relative to the average elevation of points within the local window (Figure 3.21). The filter was designed to remove rare, spatially unsupported elevation data that persisted within the point clouds and was used after the application of RSEV, SOR and Cone filters.

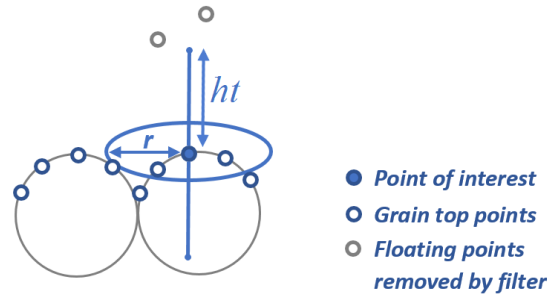


Figure 3.21 Schematic diagram of the local high point filter, adapted from Hodge et al. (2009a: 959).

The parameter assessment for this filter was run for a range of threshold heights ( $3 \leq ht \leq 10$  mm) and filter radii ( $5 \leq r \leq 15$  mm) - the results for  $A_1$  and  $H_1$  sub patches are displayed in Figures 3.22a and 3.23a respectively. As the threshold height falls and the filter radius widens, the amount of data removed by the local high point filter increases and the distribution of  $E$  narrows. In the case of the  $A_1$  patch, the choice of an optimal parameter setting was unclear from interrogation of the  $E$  distribution. Consequently, the final choice was based on the visual inspection of the point clouds and variation in data retention with different parameter settings. In the first instance, ineffective filters were found to either insufficiently remove local outliers or lose surface detail. For this study, the optimal parameter values for the HDS 3000/ScanStation 2 and ScanStation P20 datasets were  $r_{opt} = 7$  mm and  $ht_{opt} = 15$  mm (39 – 73 % data retained; Figure 3.22b) and  $r_{opt} = 3$  mm and  $ht_{opt} = 7$  mm respectively (69 – 74 % data retained; Figure 3.23b). This accounted for a universal c.1% reduction of the point cloud and narrowed the distributions of  $E$  for the humid temperate to  $3.1 \text{ mm} \leq E_{95} - E_5 \leq 4.6 \text{ mm}$  (Figure 3.22c) and dryland sub patches to  $3.6 \text{ mm} \leq E_{95} - E_5 \leq 4.4 \text{ mm}$  (Figure 3.23c). Hodge et al. (2009a), meanwhile, found  $r_{opt}$  and  $ht_{opt} = 5$  mm and 7 mm respectively with the local high point filter similarly found to remove only a small proportion of the point cloud.

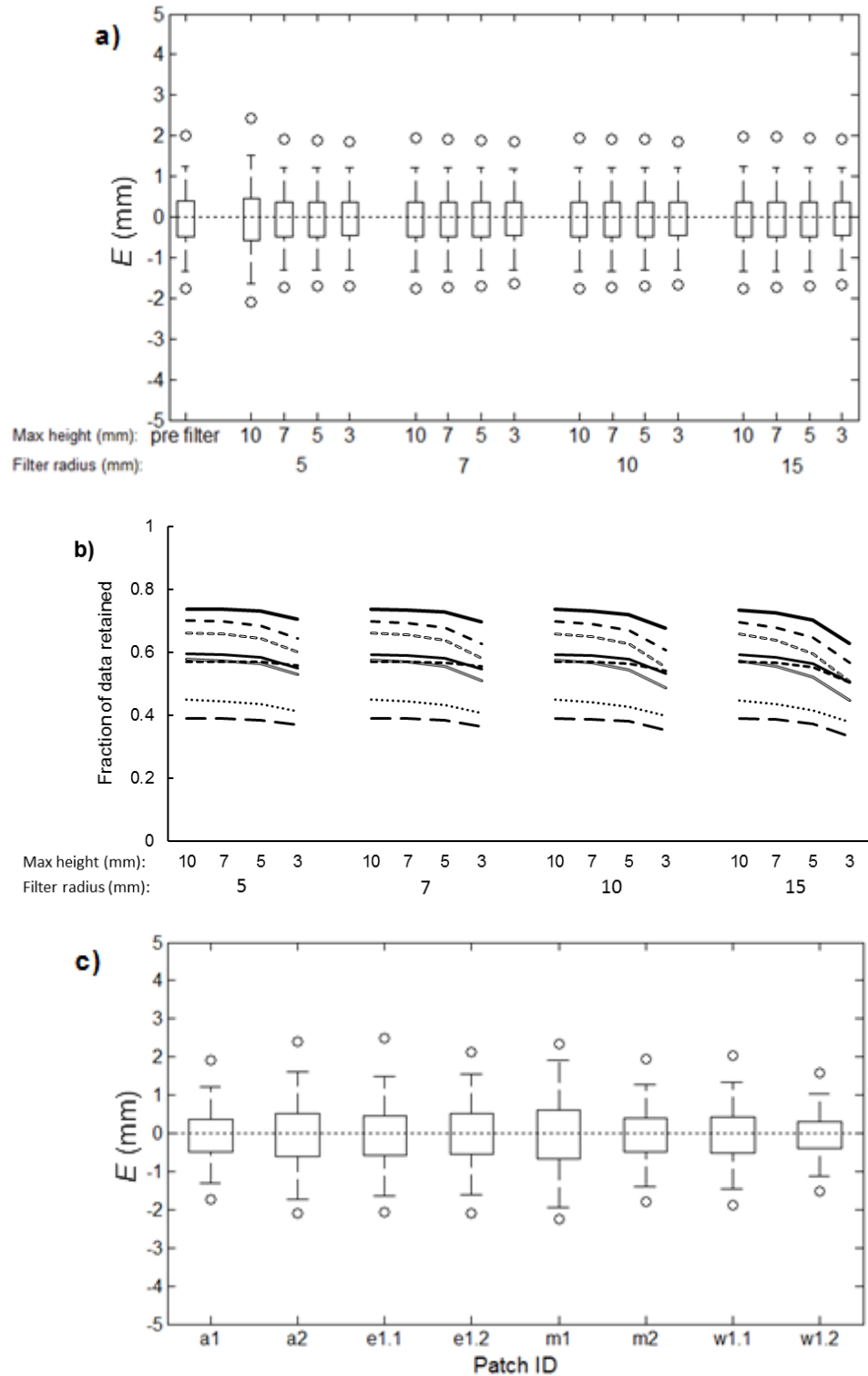


Figure 3.22 Distributions of  $E$  for a) the A<sub>1</sub> patch across a range of local high point filter parameters and b) the proportion of the unfiltered point cloud retained under each filter scenario (legend as in Figure 3.16c). The distributions of  $E$  are also shown following the application of the optimal filter (7 mm 15 mm) to the other humid temperate patches. a) adapted from Hodge et al. (2009a).

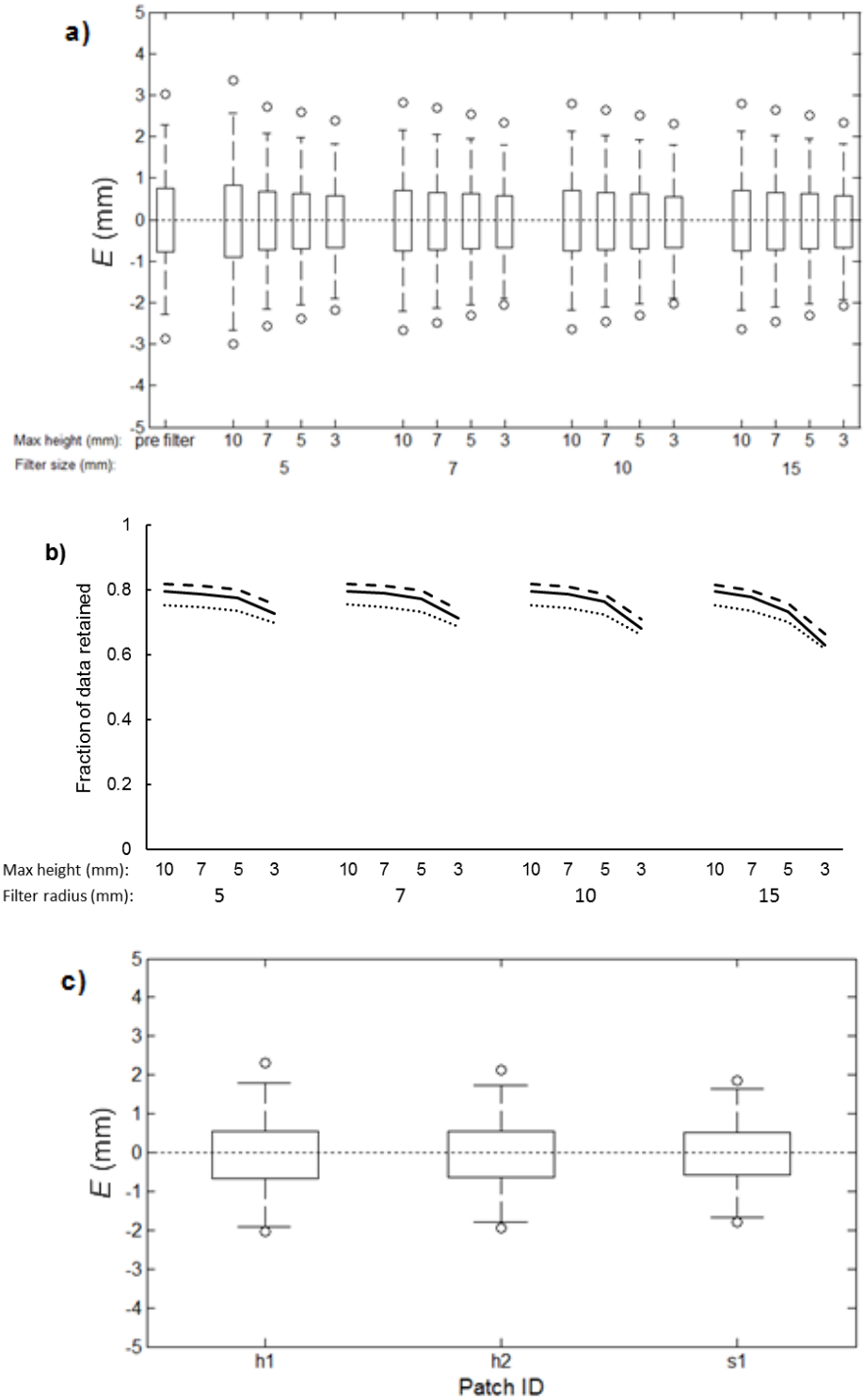


Figure 3.23 Distributions of  $E$  for a) the  $H_1$  patch across a range of local high point filter parameters and b) the proportion of the unfiltered point cloud retained under each filter scenario (legend as in Figure 3.17c). The distributions of  $E$  are also shown following the application of the optimal filter (3 mm 7 mm) to the other dryland patches. a) adapted from Hodge et al. (2009a).

### **3.4.6. DTM generation**

The penultimate stage of data processing involved the conversion of the filtered 2½D point cloud to a digital elevation model – the source DTM (Step 7). The interpolation process responsible for raster generation was performed using the inverse distance weighting (IDW) algorithm as implemented using the ArcMap 3D Analyst toolbox (ESRI, 2011. ArcGIS Desktop: Version 10.5). The selection of the DTM generation technique over other exact interpolators (e.g. Delaunay triangulation; Brasington et al., 2000, 2003) was guided by previous studies of this type (e.g. Storz-Peretz and Laronne, 2013; Powell et al., 2016; Storz-Peretz et al., 2016) and the results are probably insensitive to this choice. The grid spacing of the source DTMs was 3 mm since error propagation is least for surfaces created at the same resolution of the sampling density (Behan, 2000). Moreover, Hodge et al. (2009a) observed no gains in DTM precision from further increases in grid resolution.

### **3.4.7. DTM validation**

The quality of the final DTMs was assessed through a combination of qualitative and quantitative analysis (Step 8). The former demonstrates the processing steps were successful in removing the majority of erroneous data values; as exemplified upon visual inspection of the source DTMs generated from both workflows for the A<sub>1</sub> and H<sub>1</sub> patches (Figures 3.9j and 3.9k respectively). The DTMs were, therefore, thought to provide a good representations of the gravel microtopography at each of the field sites. Any errors that remain within the processed datasets are small and, from visual inspection of the surfaces, appear confined to areas of lesser point density; for example, in the deep interstices between coarse grains and in regions shadowed by larger, emergent grains.

Independent quantitative validation of the final point clouds and DTM counterparts was, however, hindered by the inability to gather a similarly precise, control dataset. For this study, the method of jack-knifing was used to generate an internal set of ‘check’ data to provide a check on the DTM generation process for a given elevation data set (Deutsch and Journal, 1998). This involved extracting a 5% random subsample from the filtered point cloud to provide a control dataset. The remaining 95% of the point cloud was used to

construct the DTMs which the check point dataset was compared against. The results of surface validation are expressed in terms of the root mean square error (RMSE, mm) of residuals between the jack-knifed subset and the modelled surface. The magnitude of residual error is then evaluated against the size of bed material ( $\widetilde{RMSE} = RMSE/D_{50}$ ). The jack-knife analysis was repeated with changes in the resolution of the measured DTM for grid steps ranging between 1 – 20 mm at 1 mm increments. A positive relationship between RMSE and grid step demonstrates that as the resolution of the DTM coarsens the magnitude of residual error increases. For the humid temperate sub patches (Figure 3.24a) this led to a reduction in RMSE from 4.9 – 6.5 mm for the coarsest DTM produced (20 mm grid step) before falling to 1.8 – 3.7 mm for the 3mm DTM. The M<sub>2</sub>, W<sub>1.1</sub> and W<sub>1.2</sub> patches account for the highest RMSE errors:  $3.5 \leq RMSE \leq 3.7$  mm compared to  $1.8 \leq RMSE \leq 2.7$  mm recorded for the other humid temperate patches. Increased surface errors are likely to be caused from an increase in the distance between the sensor and patch, and amplified by a coarse bed texture, which reduces incidence angle and the ability to map the deep interstices between grains. While the magnitude of RMSE was greatest for these patches, the signal-noise ratio between error and surface relief was still relatively low ( $\widetilde{RMSE} = 0.06$ ), and within the range of the other humid temperate gravel patches ( $0.03 \leq \widetilde{RMSE} \leq 0.12$ ), owing to their coarse surface grain size ( $D_{50} = 62$  mm; Hodge et al., 2009b). Consequently, there is sufficient signal to extract valid surface measurements from the DTMs.

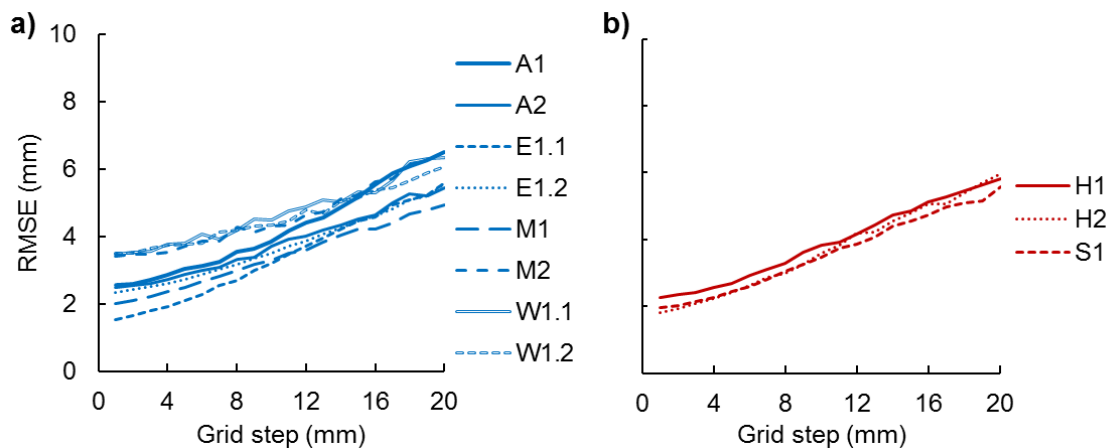


Figure 3.24 Variations in the RMSE of residuals for the a) humid temperate and b) dryland patches with changes in DTM resolution. a) and b) adapted from Hodge et al. (2009a).

Meanwhile, residual RMSE was similarly observed to fall with reducing DTM resolution for the dryland sub patches (Figure 3.24b): from 5.6 – 6.0 mm to 2.1 – 2.4 mm for the 20 mm and 3 mm DTMs respectively. These errors broadly consistent with the humid temperate patches, particularly when accounting for grain size ( $0.05 \leq \overline{RMSE} \leq 0.13$ ), despite differences in filtering workflow and optimal parameter settings. Moreover, the magnitude of surface residuals is comparable to Hodge et al. (2009a: 1.5 – 2.5 mm) notwithstanding differences in data capture (patch size, sampling resolution), point cloud filtering (workflow and parameter settings) and DTM generation (raster resolution) used for this study. As Hodge et al. (2009a) reflect, the quality of the DTM will be greater than RMSE values suggest as residual error propagates from both the surface and check points.

### **3.4.8. DTM detrending and surface measurements**

Prior to the characterisation of the DTMs it was necessary to detrend the surfaces to remove any larger-scale trends such as that due to the slope of the bed and which may confound the analysis of the grain-scale properties of the surface. In this study, a linear detrend was sufficient to remove the larger-scale trends in the surfaces. This reduced the range of bed elevations by an average of 75 mm for the humid temperate and dryland patches considered for surface characterisation (Objective 1). Following the linear detrend, the surfaces are referred to as measured DTMs and it is these surfaces that form the basis of the subsequent statistical analyses.

## **3.5. Characterising bed structure**

The structural properties of the humid temperate and dryland gravel patches were evaluated using a suite of morphometrics parameters. Some of these consider lumped, aspatial measures of surface topography while others are calculated at a variety of scales and in different directions relative to the direction of formative flow. The measured DTMs of the gravel patches were characterised initially through analysis of the bed elevation distribution and associated statistical moments (Subsection 3.5.1). Several additional metrics were introduced to provide further information on the direction and scaling properties of

sedimentary structure including 1D and 2D variograms (3.5.2), Inclination Indices (3.5.3) and slope-aspect analysis (3.5.4).

### 3.5.1. Bed elevation probability density functions (pdfs) and statistical moments

The structure of bed microtopography was initially examined by investigating the probability density functions (pdfs) of surface elevations and their statistical properties: standard deviation ( $\sigma_z$ ), Skewness ( $Sk_z$ ) and Kurtosis ( $Ku_z^*$ ). Although this is not a particularly sophisticated analysis, previous workers have found it useful in identifying a water worked bed geometry; for example, in documenting the stages of armour layer development from an unstructured surface in laboratory flume experiments (Marion et al., 2003; Mao et al., 2011; subsections 2.5.1–3). The surface elevation statistics  $\sigma_z$ ,  $Sk_z$  and  $Ku_z^*$  were calculated from the measured DTMs using:

$$\sigma_z = \sqrt{\frac{1}{n} \sum_{i=1}^n (z_i - \bar{z})^2} \quad [3.6]$$

$$Sk_z = \frac{1}{n} \sum_{i=1}^n \left( \frac{z_i - \bar{z}}{\sigma_z} \right)^3 \quad [3.7]$$

$$Ku_z^* = \frac{1}{n} \sum_{i=1}^n \left( \frac{z_i - \bar{z}}{\sigma_z} \right)^4 - 3 \quad [3.8]$$

where,  $z_i$  refers to the bed surface elevation at the  $i$ th location and  $n$  the number of observations.

### 3.5.2. 1-D and 2-D variograms

As discussed in Subsection 2.3.2, variograms can help to provide a view on the scaling properties of surface microtopography, e.g. by revealing the spatial dependency of sedimentary structure. In this study, variograms were produced to assess the degree of surface anisotropy (see Subsection 2.3.2) and quantify the topographic irregularity of the surfaces (via the Hurst exponent,  $H$ ) and the scales of roughness (via  $h_1$  and  $h_2$ ; see Subsection 2.3.2). 2D variogram surfaces (e.g. Subsection 2.3.2) were generated by calculating semivariance for lags ( $h$ ) in all directions ( $h_x, h_y$ ; Equation 3.9).

$$\gamma(h_x, h_y) = \frac{1}{2(n-1)} \cdot \sum_{i=1}^n (z_{i+h} - z_i)^2 \quad [3.9]$$

where,  $\gamma$  was estimated from 10,000 point pairs sampled for each lag ( $h$ ) in all directions ( $h_x, h_y$ ) and  $n$  is the number of observations. 1D variograms are produced for lags constrained in downstream ( $h_x$ ) and cross stream directions ( $h_y$ ).

Semivariance was sampled for a range of lags ( $h_x, h_y$ ) from the raster resolution to half the downstream and cross stream patch dimensions to ensure undersampling at larger lags were avoided (Journel and Huijbregts, 1978; Klinkenberg, 1994; Butler et al., 2001; Hodge et al., 2009b). In this study, the variograms are presented using dimensionless scales where  $\gamma$  and  $h$  are normalised by the variance of bed elevations and median surface grain size respectively (i.e.  $\tilde{\gamma} = \gamma/\sigma_z^2$ ,  $\tilde{h} = h/D_{50}$ ). This facilitates the comparison of variograms from patches with different grain size distributions. 1D variograms were extracted from the 2D variogram surfaces for lags constrained in downstream ( $h_x$ ) and cross stream ( $h_y$ ) directions. As described in subsections 3.1.1, 3.1.3 and 3.1.4, flow direction can vary with discharge. For example, flows may shoal across the patch during moderate events and straighten during larger events. These effects may cause sedimentary structure to develop obliquely across the patches (Wittenberg and Newson, 2005) which were aligned in the direction of bankfull flow. To allow for the effects of the variations in flow direction with discharge, the downstream and cross stream 1D variograms and any subsequent direction-based analyses were extracted along and across the main axis of any coherent, larger-scale anisotropy that was present within the 2D variogram surfaces. If structure was isotropic at larger spatial scales, the downstream and cross stream 1D variograms were sampled in directions downstream and cross stream relative to bankfull flow respectively.

As outlined in Subsection 2.3.2, two alternative methods have been proposed to model the 1D variogram of a gravel surface. The first considers the variogram to exhibit two log-linear segments corresponding to grain- and bedform-scale roughness and a sill of constant semivariance (Robert, 1988, 1991; Figure 2.5). The second considers the variogram to exhibit a single log-log linear section, a curved region and a horizontal sill (termed the scaling, transition and saturation regions respectively of Nikora et al., 1998; Figure 2.6). Inspection of the 1D variograms in this study indicate that they conform to the model of Nikora et al. and were analysed accordingly. The coefficients  $\tilde{h}_1$  ( $h_1/D_{50}$ ),  $H$  and  $\tilde{\gamma}_1$  ( $\tilde{\gamma}/\sigma_z^2$ ) were estimated

by fitting a linear spline model where the joint (or knot) of a segmented polynomial of degree two lies at lag  $h_l$ . The linear regression is performed in log-log space and expressed through Equations 3.10 and 3.11. The iterative regression process was undertaken using the PROC NLIN function within the SAS software package using an initial parameter set informed by visual inspection of the variograms (cf. Powell et al., 2016).

$$\log \tilde{\gamma}(h) = a + b_1(\log \tilde{h}) \quad \text{for } 0 < \log \tilde{h} \leq \tilde{h}_1 \quad [3.10]$$

$$\log \tilde{\gamma}(h) = a + b_1(\log \tilde{h}) + b_2(\log \tilde{h} - \log \tilde{h}_1) \quad \text{for } \tilde{h}_1 < \log \tilde{h} \leq \tilde{h}_2 \quad [3.11]$$

where the coefficients of regression  $a$ ,  $b_1$  and  $b_2$  correspond to the intercept and the slope of the two, fitted log-linear segments respectively.

### 3.5.3. Inclination Index

The inclination index ( $I$ ) of Smart et al. (2004), as discussed in Subsection 2.3.3 and illustrated by Figure 2.15, provides a quantitative measure of scale-dependent bed orientation that is not accounted by the analysis of bed elevation pdfs or variograms. The metric describes how surface relief varies between sample pairs separated by a range of lag distances and can inform how surface alignment varies with scale (Smart et al., 2004). Values of  $I$  represent the relative proportion of positive and negative surface inclinations and are calculated using:

$$I = \frac{I_+ - I_-}{I_N} \quad [3.12]$$

where,  $I_+$  and  $I_-$  represent the number of positive and negative changes in bed elevation between successive sampling pairs and  $I_N$  the total number of inclination samples.

The inclination index occupies the range  $-1 \leq I \leq 1$  where minimum and maximum values represent monotonically decreasing and increasing surface elevations respectively (Smart et al., 2004). Negative values of  $I$  thereby indicate a preponderance of negative inclinations which at the grain-scale is indicative of particle imbrication. Conversely positive values of  $I$  denotes a greater proportion of positive inclinations. The index will be zero if the proportion of positive and negative inclinations is equal. For the purposes of this study, values of  $I$  were used to identify grain-scale imbrication and were calculated at lags extending to three times the raster spacing (9 mm). This length scale has been shown to provide an optimal balance

in minimising noise from grain-edge effects (Millane et al., 2006) while retaining information that would otherwise be blurred by adopting larger sampling windows (Qin et al., 2013). The inclination index was calculated along the main axis of larger-scale anisotropy informed by the 2D variogram analysis.

### 3.5.4. Slope and Aspect

The grain-scale roughness properties of the patches were further evaluated by studying the local parameters of slope ( $S$ ) and aspect ( $A$ ). The magnitude and distribution of these local parameters are likely to reflect the textural structure exhibited by the streambed and can help to further characterise particle imbrication (e.g. Millane et al., 2006; Hodge et al., 2009b). Local slope and aspect were calculated by estimating the gradient (units = degrees) within a 3-by-3 cell moving window applied across the measured DTMs, as expressed by:

$$S = \arctan \sqrt{\left(\frac{dz}{dx}\right)^2 + \left(\frac{dz}{dy}\right)^2} \quad [3.13]$$

$$A = \arctan \left(\frac{dz/dx}{dz/dy}\right) \quad [3.14]$$

where,  $dz/dx$  and  $dz/dy$  express the rate of change in bed elevation in the x- and y- directions and where cell aspect is adjusted for  $dz/dx < 0$  such that  $A = A + 180^\circ$  for bankfull flows. In this instance, downstream facing cells within the measured DTMs are found where  $A = 90^\circ$  and upstream facing cells where  $A = 270^\circ$ .

The 9 mm cell width of the moving window matches the scale of inspection used for the inclination index (subsection 3.5.3). As Figure 3.25 demonstrates for the  $A_1$  measured DTM (Figure 3.25a), the local parameters of aspect and slope calculated at this scale (Figures 3.25b and 3.25c respectively) represent the roughness properties of individual grains within the patches.

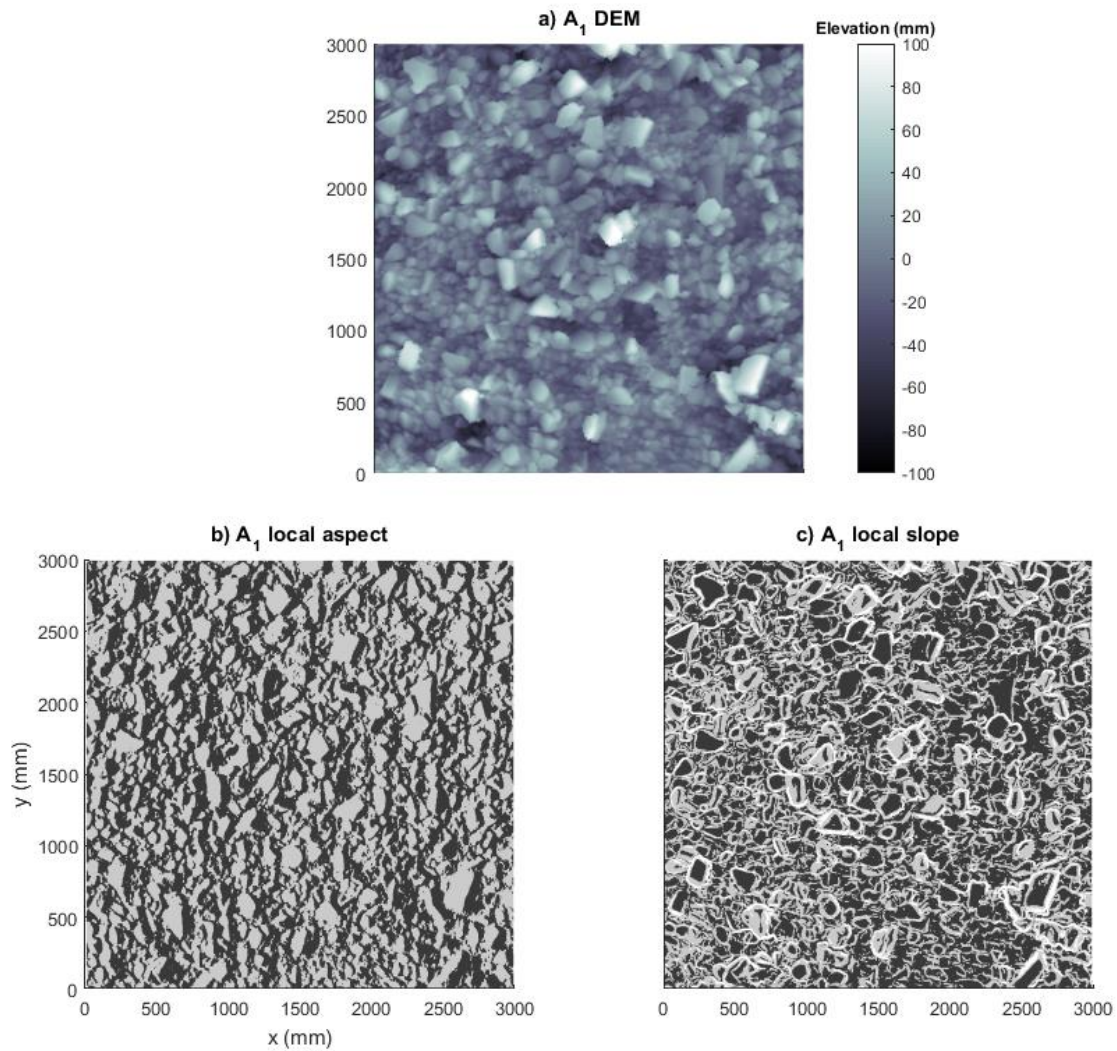


Figure 3.25 The a) measured DTM and classified local parameters of b) aspect and c) slope, calculated within the 9 mm x 9 mm moving window, for the  $A_1$  patch. Direction of flow from left-to-right. In b) upstream and downstream facing cells are coloured in white and black respectively. In c) through an arbitrary classification, shallower ( $< 30^\circ$ ) and steeper slopes ( $> 60^\circ$ ) are coloured in white and black respectively.

### 3.6. Bed stability parameters

Further to the statistical metrics describing the structural properties of the streambed, several additional parameters were introduced to evaluate how sedimentary structure influences bed stability. This initially involved gathering measurements of three key components of the force balance of individual surface grains: pivoting angle (Subsection 2.3.4) and projection and exposure above the local bed surface (Subsection 2.3.5). These parameters were sourced

through a combination of *in-situ* sampling ( $\Phi$ ) and DTM derivation ( $p$  and  $e$ ). As the former is an inherently destructive technique, the particle stability parameters were only recorded for the final surveys conducted on the W<sub>1.1</sub> and W<sub>1.2</sub> humid temperate gravel patches. A contrasting dataset was also obtained from the H<sub>1</sub>, H<sub>2</sub> and S<sub>1</sub> dryland patches. The parameters  $\Phi$ ,  $p$  and  $e$  were used to inform an entrainment model which predicted  $\tau_c$  and  $\tau_c^*$  for a gridded sample of surface grains and, in doing so, the model described the stability of the streambed and the relative influence of structure on particle mobility.

### 3.6.1. Pivoting angle

The first of the force balance parameters, the grain pivoting angle ( $\Phi$ ), describes the angle required to release a grain from its pocket with the surface. As Figure 2.18 illustrates, the magnitude of  $\Phi$  is a function of the size and resting position of the particle relative to the size and packing geometry of neighbouring grains. In this study, values of  $\Phi$  were calculated by rearranging Equation 2.8 and resolving the horizontal drag force ( $F_D$ ), grain weight ( $F_W$ ) and local slope ( $S_l$ ):

$$\tan \Phi = \frac{F_D - F_W \sin S_l}{F_W \cos S_l} \quad [3.15]$$

The horizontal drag force was measured as the force acting parallel to the bed surface, able to mobilise a grain, as recorded by a MecMesin Basic Force Gauge. Once the grain had been dislodged out of pocket, particle axes and mass were recorded. As Subsection 2.2.4 discusses, previous workers have applied a force multiplier to grain weight, e.g.  $m$  in Equation 2.8 (Hodge et al., 2013), in order to account for additional factors which may impede particle movement. Such factors include packing geometry and mortaring and there may increase the force required to lift surface grains in excess of their weight. As the embedding of grains was not a significant factor at any of the field sites, a separate sample of vertical lift force measurements was not undertaken for the purposes of this study. Meanwhile, local slope was assumed to approximate zero ( $S_l \approx 0$ ) since the Force Gauge measurements were gathered with consideration to larger-scale components of bed topography.

### 3.6.2. Projection and exposure

Projection ( $p$ ) and exposure ( $e$ ) describe the resting position of a particle relative to the surrounding surface and will reflect the sheltering properties of surface grains. The parameters  $p$  and  $e$  are defined as the elevation difference between the height of the grain to the local mean bed elevation and the maximum upstream elevation respectively (Figures 2.6 and 2.22). In this study, the size of the local neighbourhood area used to define  $p$  and  $e$  was a function of the  $D_{84}$  grain size percentile, since the  $D_{84}$  roughness length is linked to the hydraulic properties of graded beds (Section 2.1; Kirchner et al., 1990). For example, grain projection was estimated over an area equal to  $D_{84}$  surrounding the clast (Figure 3.26a) while grain exposure was calculated as a mean of streamwise strips extending to  $D_{84}$  upstream from the grain's leading edge (Figure 3.26b). The latter, the averaging of strips, was necessary to account for variations in sheltering across the upstream face of the grain. Where the grain was entirely sheltered, i.e. residing at a lower elevation than the maximum upstream element with the local neighbourhood window, the exposure was set to zero ( $e = 0$ ). Grain projection and exposure were derived from the DTM aided by grain boundaries created from a classification of sampled grains based on point cloud intensity (e.g. Franceschi et al., 2009). In order to distinguish sampled grains from their unsampled counterparts, they were painted prior to the topographic surveys. Following laboratory testing using natural grains, black paint was found to provide the best contrast in intensity between the dark, sampled grains and lighter-coloured, (limestone) parent bed material. Slight, final adjustments were made to the intensity-classified grain boundaries with the guidance of plan view photographs.

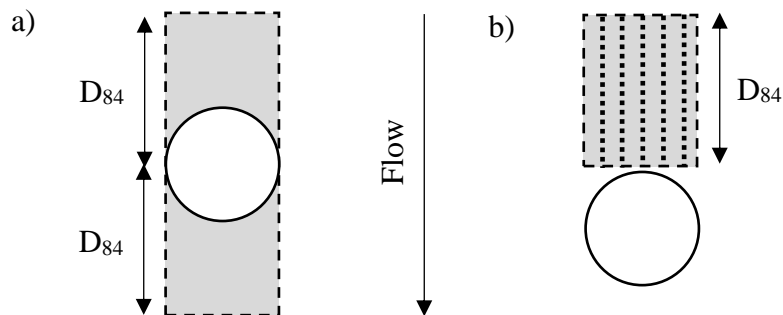


Figure 3.26 Schematic illustration of the protrusion parameters, calculated within the dashed window, relative to a test grain: a) protrusion and b) exposure. In b) the dotted lines mark the boundary of streamwise strips which are averaged to estimate  $e$ .

### 3.6.3. Grain entrainment model

The force balance parameters, calculated by the methods described in Subsections 3.6.1 and 3.6.2, were introduced into an entrainment model to investigate bed stability through estimates of  $\tau_c$  and  $\tau_c^*$ . While the diameter, axis length and weight and the parameters of pivoting angle, projection and exposure were calculated for individual grains, these values were not used as a direct input into the entrainment model. Instead, given the exclusion of fines during *in-situ* sampling,  $\tau_c$  and  $\tau_c^*$  were predicted through a random sampling approach which involved a Monte Carlo simulation of 3000 simulated grains (divisible by the number of humid temperate and dryland patches while of a similar magnitude in the number of simulated grains, and standard error of predicted variables, used by previous workers, e.g. Hodge et al., 2013). Using the methodological workflow illustrated in Figure 3.27, the former,  $\tau_c$ , was estimated using Equation 3.16 while the latter,  $\tau_c^*$ , was predicted using Equation 2.2.

$$\tau_c = 0.1m(\rho_s - \rho)g \left( \frac{\pi D^3}{6} \right) \cdot \left\{ \frac{C_D}{\tan \phi 2\kappa^2} \int_{p-e}^p \sqrt{D^2 - [2z - (2p - D)]^2} f(z)^2 dz + \frac{\pi C_L}{8\kappa^2} D^2 [f(p)^2 - f(p - D)^2] \right\}^{-1} \quad [3.16]$$

for:

$$f(z) = \ln \left( \frac{z+z_0}{z_0} \right) \quad z > 0$$

$$f(z) = 0 \quad z \leq 0$$

The grain entrainment model described here follows that of Hodge et al. (2013) which is predicated on several key assumptions including i) a lognormal surface grain size distribution, ii) a statistically significant relationship between dimensionless projection ( $p/D$ ) and dimensionless exposure ( $e/D$ ) and iii) the errors from the correlation between  $p/D$  and  $e/D$  are normally distributed. Preliminary analysis (Figure 4.1, Figure 4.15 and Appendix C), revealed these three assumptions are valid for each of the sampled patches which allows for the use of the model to estimate grain size information and the force balance parameters and hence  $\tau_c$  and  $\tau_c^*$  without significant adaption.

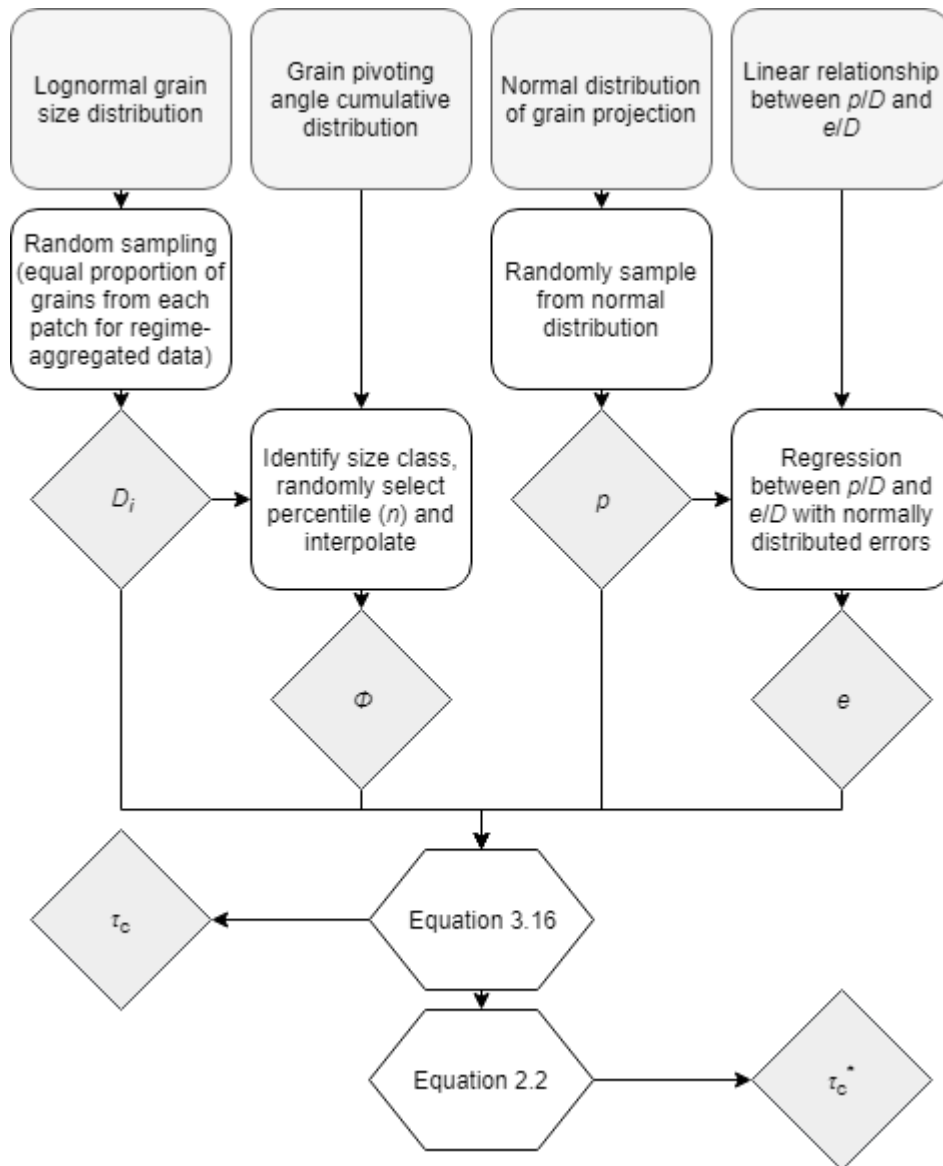


Figure 3.27 Workflow for the grain entrainment model, following Hodge et al. (2013).

## **Chapter 4 The characteristics of streambed structure in coarse-grained alluvial channels and their control on particle stability**

### **4.1. Introduction**

Using the 11 gravel patches sampled from six gravel-bed rivers, this chapter seeks to i) describe and compare the surface characteristics of a range of coarse-grained alluvial streambeds and ii) investigate how bed surface grain size and structure affect particle stability. In doing so, the chapter firstly describes bed surface character in terms of surface grain size, sorting and shape (4.2). Bed surface structure is then considered via qualitative descriptions of surface microtopography as revealed by visual inspection of the DTMs (4.3) and the interpretation of a series of quantitative metrics including bed elevation pdfs and their associated statistical moments (standard deviation, skewness and kurtosis; 4.4), 2D and 1D variograms (4.5 and 4.6 respectively), surface inclination (4.7), slope and aspect (4.8) and the force balance parameters: pivoting angle (4.9), projection and exposure (4.10). The chapter concludes by considering the relationships between bed surface grain size, structure and particle stability through the calculation of entrainment thresholds using a force-balance modelling approach (4.11).

### **4.2. Bed material size, sorting and shape**

Surface grain size distributions for the 11 gravel patches and a summary of particle size and sorting statistics are presented in Figure 4.1 and Table 4.1 respectively. In terms of the humid temperate rivers, the grain size distributions for E<sub>1.1</sub>, E<sub>1.2</sub>, M<sub>2</sub>, W<sub>1.1</sub> and W<sub>1.2</sub> are broadly comparable (Figure 4.1a;  $53 \leq D_{50} \leq 62$  mm;  $107 \leq D_{\max} \leq 215$  mm). The grain size distributions for A<sub>1</sub> and A<sub>2</sub> are similar but have a tail of coarser bed material ( $D_{50} = 68$  and 78 mm respectively and  $D_{\max} = 304$  mm). In contrast, M<sub>1</sub> is considerably finer ( $D_{50} = 18$  mm,  $D_{\max} = 76$  mm). Despite the differences in surface grain size, the bed material of all eight humid temperate patches is poorly sorted with little variation in the coefficient,  $\sigma_G$  ( $1.6 \leq \sigma_G \leq 1.9$ ). On the other hand, H<sub>1</sub>, H<sub>2</sub> and S<sub>1</sub> on the ephemeral Hever and Shafan comprise considerably finer ( $19 \leq D_{50} \leq 39$  mm) and more poorly sorted bed material ( $2.4 \leq \sigma_G \leq 2.8$ ) which extends to coarser grain sizes ( $215 \leq D_{\max} \leq 429$  mm).

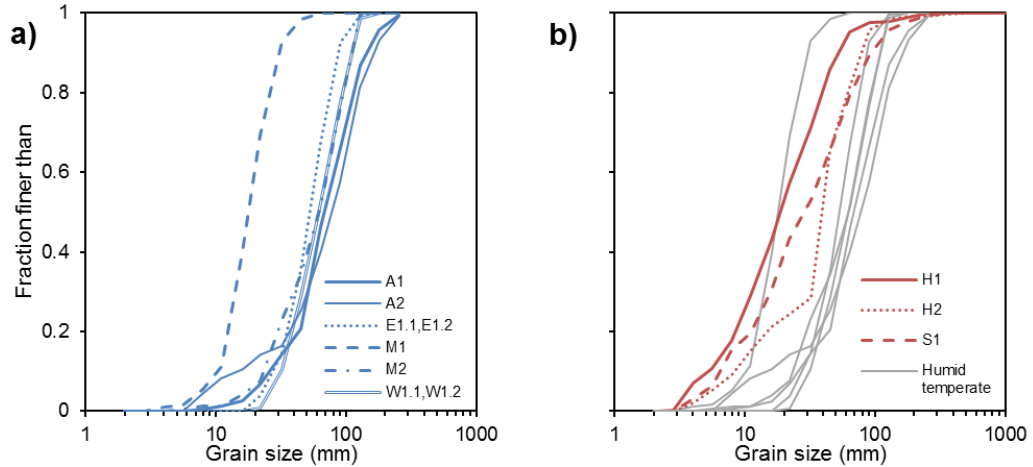


Figure 4.1 Cumulative frequency distributions of surface grain size for the a) humid temperate and b) dryland patches (compared with the humid temperate patches, shown in grey). Grain size distributions are truncated at 2mm.

Table 4.1 Surface grain size statistics for the humid temperate perennial (blue) and dryland ephemeral (red) gravel patches. Note: only one representative grain size sample was collected from the Elan and Wharfe field sites.  $D_n$  refers to the nth percentile of the surface grain size distribution and  $\sigma_G$  is the geometric Folk and Ward (1957) sorting coefficient.  $D_{max}$  is the maximum grain size and is estimated as the geometric mean of the bounding sieve sizes containing the largest grain.

Site	Patch ID	Grain size (mm)					Sorting $\sigma_G$
		$D_{16}$	$D_{50}$	$D_{84}$	$D_{95}$	$D_{max}$	
Ashop	A <sub>1</sub>	35	68	122	177	304	1.9
	A <sub>2</sub>	30	78	138	200	304	2.4
Elan	E <sub>1.1</sub>	33	53	80	102	215	1.6
	E <sub>1.2</sub>						
Manifold	M <sub>1</sub>	12	18	28	36	76	1.6
	M <sub>2</sub>	27	62	101	119	107	1.9
Wharfe	W <sub>1.1</sub>	36	62	100	120	215	1.6
	W <sub>1.2</sub>						
Hever	H <sub>1</sub>	7	19	43	64	215	2.4
	H <sub>2</sub>	12	39	68	89	429	2.4
Shafan	S <sub>1</sub>	8	29	75	123	304	2.8

The distributions of particle shape for the humid temperate and dryland gravel patches are illustrated using the classification of Zingg (1935) in Figures 4.2a and 4.2b respectively. The average particle shape is discoid for A<sub>1</sub>, A<sub>2</sub>, W<sub>1.1</sub>, W<sub>1.2</sub>, H<sub>1</sub>, H<sub>2</sub> and S<sub>1</sub> and bladed for E<sub>1.1</sub> and E<sub>1.2</sub>. This difference in grain shape may reflect lithological controls (e.g. Knighton, 1982) as,

considering the perennial rivers, the limestone parent material of the Wharfe catchment weathers to produce rounded sediment whereas the gritstone-dominated reaches of the Ashop and Elan abrade to more bladed grains (Figure 4.2c). Flow regime may also play a secondary role in affecting particle shape since, for the limestone patches, the average shape for the humid temperate patches is slightly more spherical than the average shape of the dryland patches (Figure 4.2d). This may reflect the greater frequency of flooding in perennial reaches which increases the potential for particle movement and in-situ abrasional processes (e.g. Schumm and Stevens, 1973; Brewer et al., 1992). The statistical significance of the differences in particle shape identified in Figures 4.2c and 4.2d were evaluated using a two-sample t-test to determine whether the population means were equal. In this regard, mean sphericity ( $\bar{\psi}$ ) was found to be i) greater for the humid temperate limestone patches than the humid temperate gritstone patches ( $\bar{\psi} = 0.71$  and  $0.56 \leq \bar{\psi} \leq 0.61$ , respectively;  $p < 0.001$ ) and ii) slightly, but significantly, greater for the humid temperate limestone patches compared to the dryland limestone patches ( $\bar{\psi} = 0.71$  and  $0.69$ , respectively;  $p < 0.03$ ).

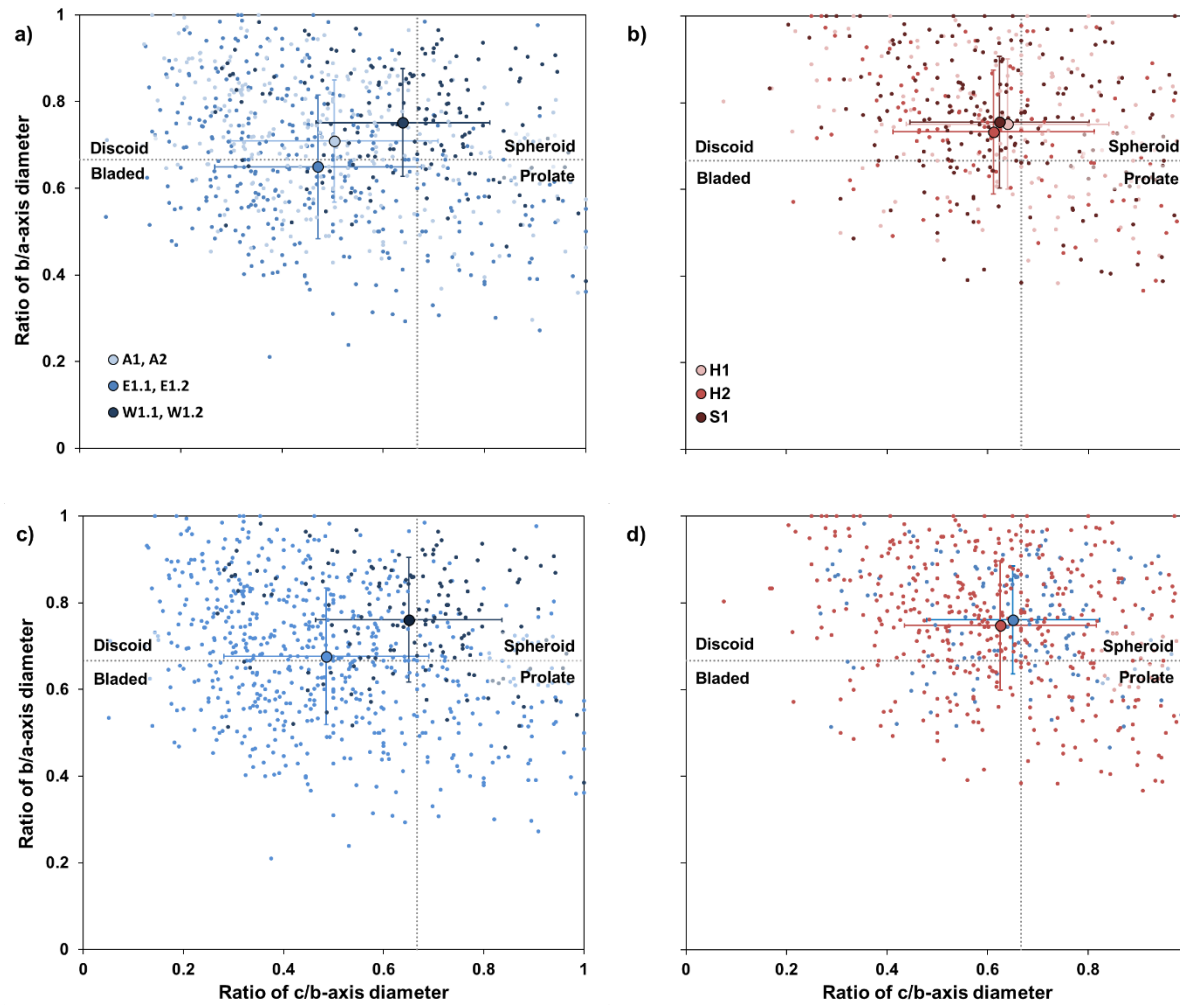


Figure 4.2 Zingg (1935) classification of particle shape. Distributions of particle shape are presented for the a) humid temperate patches, b) dryland gravel patches, c) humid temperate patches classified by lithology (limestone and gritstone) and d) limestone lithologies classified by flow regime (perennial and ephemeral). The large symbols indicate the mean particle shape calculated for each river with  $\pm$  one standard deviation displayed as horizontal and vertical lines.

### 4.3. Digital elevation models

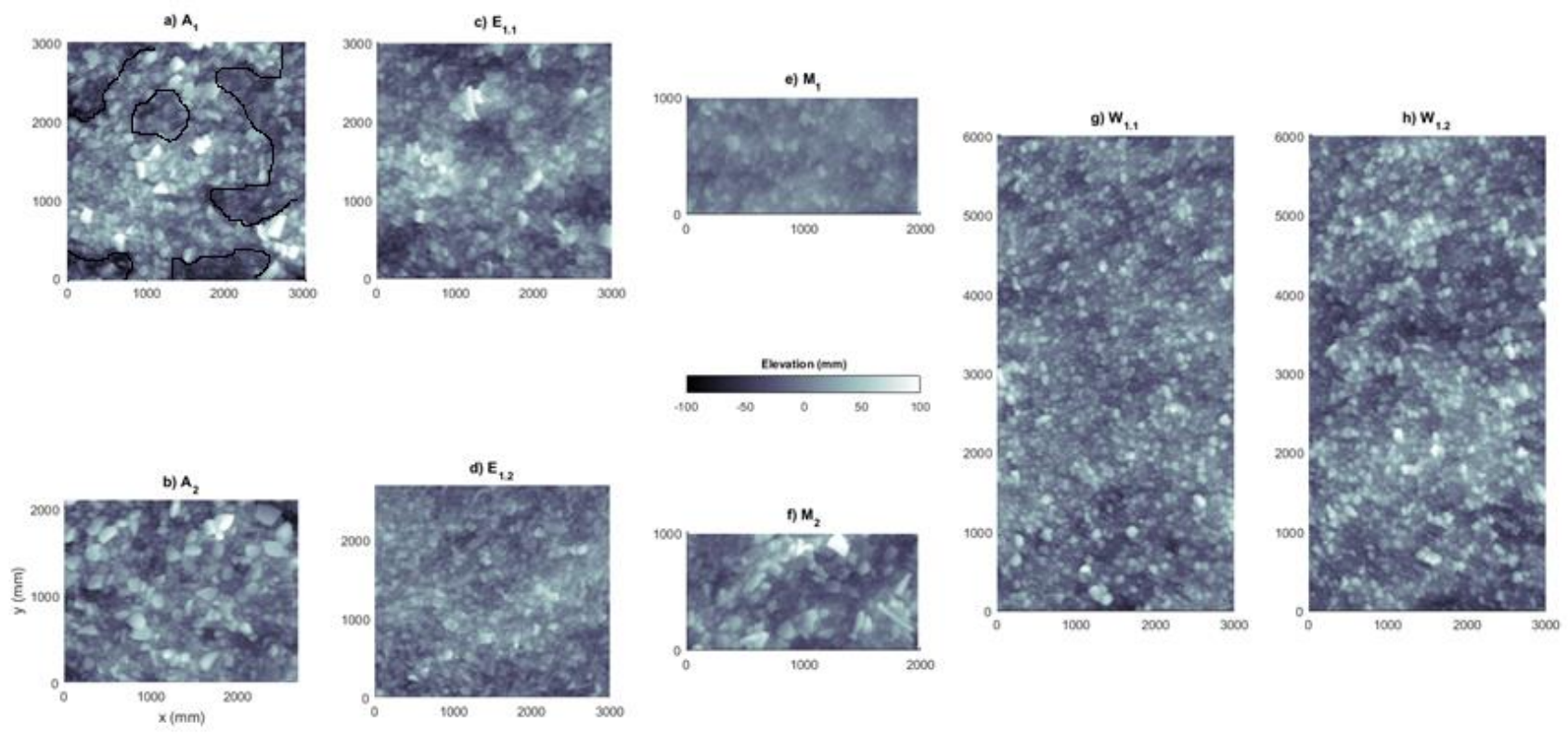
The measured digital elevation models (DTMs) for the humid temperate and dryland gravel patches are presented in Figure 4.3. A visual assessment of the DTMs reveals two scales of topographic variation. The first of these arises from the arrangement of individual particles and groups of particles on the streambed and is hereafter collectively referred to as grain-scale microtopography. The second refers to larger-scale (100-1000 mm) patches of higher and lower bed elevations which form the meso-scale component of surface topography.

At the grain-scale, the humid temperate patches were typically composed of a coarse surface armour comprised of imbricated, tightly packed grains (Figures 4.3a-d and 4.3f-h). Surface grains, on occasion, grouped into cluster bedforms that appeared to be irregularly distributed across the patches and which, from DTM inspection and qualitative field observation, packed into tighter, streamwise-aligned configurations for the bladed gritstone facies (Figures 4.3a-d and 4.3f) compared to their comparatively more rounded limestone counterparts (Figures 4.3g-h). In both instances, the development of bedforms roughened the surface by elevating the grains within pebble clusters up to 50 mm above the surrounding local bed level. In contrast, the  $M_1$  patch (Figure 4.3e) gave the impression of a comparatively looser arrangement of particles with surface grains showing little preference to imbricate or assemble into bedforms.

The dryland patches (Figures 4.3i-k) appeared to lack the coarse armour characteristic of the humid temperate patches and the poorly sorted surfaces comprised fine grains, punctuated by coarse particles which reach 50-100 mm above the local mean bed level. These prominent grains were commonly aligned with their longest axes transverse to the flow and, in some instances, trapped and anchored smaller fractions of bed material as stoss imbricates. The downstream region from these obstacle clasts was often characterised by scour which extended to 50 mm below the local bed level (Storz-Peretz and Laronne, 2013). Surrounding these obstacle clasts and scour holes, the dryland surfaces comprised grains which lacked a tendency to imbricate and bedforms were largely absent. As a result, the ephemeral gravel patches were broadly planar at the grain-scale.

At the meso-scale, the humid temperate patches were largely characterised by regions of higher and lower bed elevations up to 50-100 mm above/below the mean bed level; for

example, as illustrated for the A<sub>1</sub> humid temperate patch by the solid line trace in Figure 4.3a. In contrast, the M<sub>1</sub> patch was devoid of meso-scale surface topography since bed elevations fluctuated at the scale of individual grains, i.e. < 20 mm about the mean bed level. The dryland patches similarly lacked meso-scale topography as the variations in bed elevation were accounted for by grain-scale topography, e.g. individual coarse clasts and their associated scour holes.



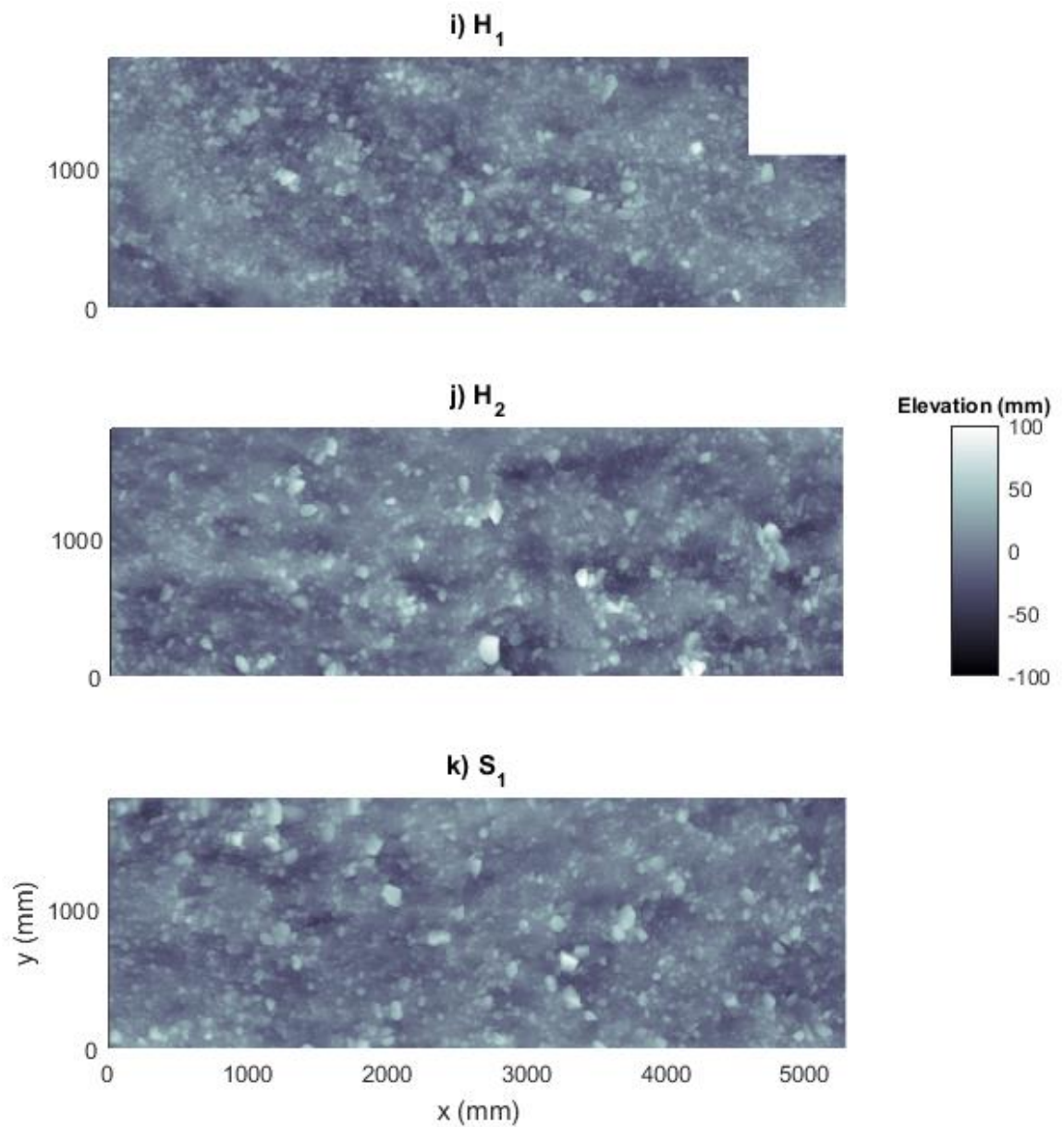


Figure 4.3 The measured (detrended) DTMs for the a-h) humid temperate and i-j) dryland gravel patches. Following Figures 3.9a-i, flow direction is orientated from left-to-right. In a) the DTM is overlain by a rough (solid line) trace around meso-scale topography.

#### 4.4. Bed elevation probability density functions (pdfs) and statistical moments: standard deviation ( $\sigma_z$ ), skewness ( $Sk_z$ ) and kurtosis ( $Ku_z^*$ ).

The probability density functions (pdfs) of bed elevations for the measured DTMs are shown in Figure 4.4 and the statistical moments which describe the form of the bed elevation pdfs – the standard deviation of bed elevations ( $\sigma_z$ ), skewness ( $Sk_z$ ) and kurtosis ( $Ku_z^*$ ) – are presented in Table 4.2. The bed elevation pdfs for the 11 surfaces typically exhibit a similar bell-shaped form but are sufficiently peaked ( $Ku_z^* > 0$ ) and positively skewed ( $Sk_z > 0$ ) that they fail to conform to a normal distribution as determined by a chi-square goodness of fit test ( $p < 0.05$ ). In general, the pdfs of the humid temperate gravel patches are broader ( $17.5 \leq \sigma_z \leq 32.9$  mm,  $\bar{\sigma}_z = 24.9$  mm; Figure 4.4a) than the dryland patches ( $15.0 \leq \sigma_z \leq 17.3$  mm,  $\bar{\sigma}_z = 15.9$  mm; Figure 4.4b). However, the exception is patch M<sub>1</sub> for which the pdf is notably narrower ( $\sigma_z = 10.9$  mm) with a smaller range of elevations. The positive skew ( $Sk_z > 0$ ) indicates the distributions extend to a longer tail of higher elevations than would be expected for a normal distribution which ensures that modal bed elevations lie below the mean bed level. The pdfs are generally more positively skewed for the dryland patches compared to their humid temperate counterparts ( $0.49 \leq Sk_z \leq 0.89$ ,  $\overline{Sk}_z = 0.76$  and  $0.37 \leq Sk_z \leq 0.65$ ,  $\overline{Sk}_z = 0.55$  respectively) although the distribution of M<sub>2</sub> is considerably more positively skewed ( $Sk_z = 1.08$ ) relative to the average of the dryland patches. In terms of kurtosis, the bed elevation distributions for all 11 patches are leptokurtic, i.e. characterised by heavier tails and narrower peaks than would be expected for a normal distribution ( $Ku_z^* > 0$ ). Values of  $Ku_z^*$  are typically greater for the dryland patches than the humid temperate patches ( $1.31 \leq Ku_z^* \leq 2.27$ ,  $\overline{Ku}_z^* = 1.76$  and  $0.10 \leq Ku_z^* \leq 1.46$ ,  $\overline{Ku}_z^* = 0.70$  respectively).

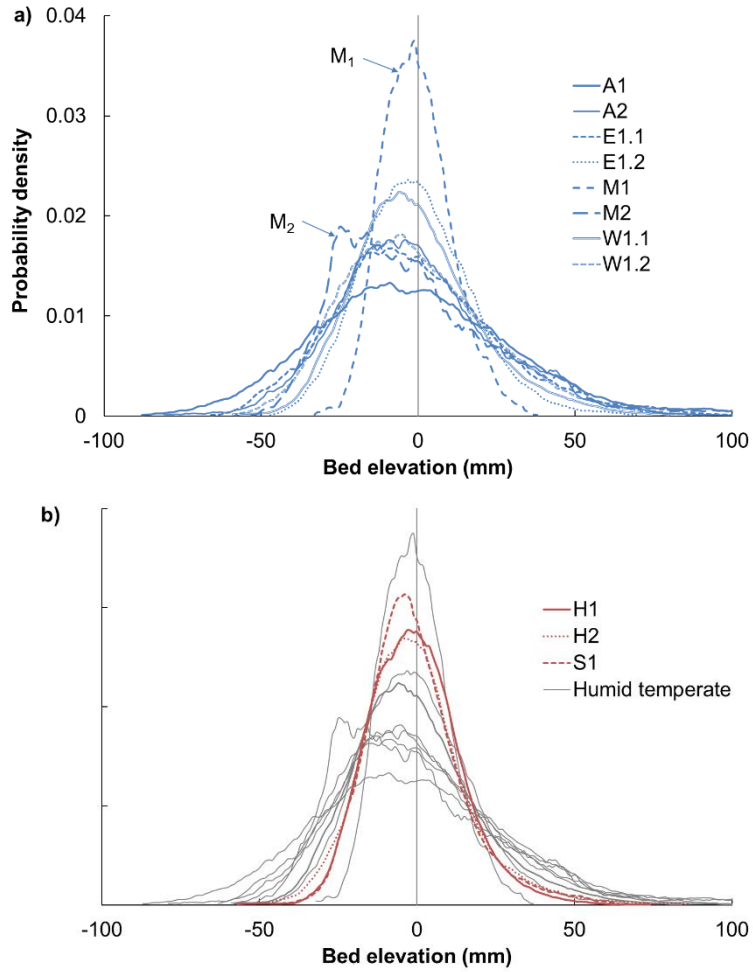


Figure 4.4 The bed elevation pdfs for the a) humid temperate and b) dryland gravel patches.

Table 4.2 Summary of bed elevation pdf moments for the measured surfaces. Humid temperate and dryland patches are highlighted in blue and red respectively.

Patch iD	$\sigma_z$ (mm)	$Sk_z$	$Ku_z^*$
<b>A<sub>1</sub></b>	32.9	0.56	0.79
<b>A<sub>2</sub></b>	25.8	0.56	0.90
<b>E<sub>1.1</sub></b>	26.3	0.59	0.55
<b>E<sub>1.2</sub></b>	17.5	0.46	0.47
<b>M<sub>1</sub></b>	10.9	0.37	0.10
<b>M<sub>2</sub></b>	26.8	1.08	1.46
<b>W<sub>1.1</sub></b>	20.1	0.65	0.87
<b>W<sub>1.2</sub></b>	24.0	0.62	0.56
<b>H<sub>1</sub></b>	15.0	0.49	1.31
<b>H<sub>2</sub></b>	17.3	0.89	2.27
<b>S<sub>1</sub></b>	15.5	0.88	1.71

The statistical moments  $\sigma_z$ ,  $Sk_z$  and  $Ku_z^*$  were compared against patch surface grain size ( $D_{50}$ ), sorting ( $\sigma_G$ ) and particle shape ( $\bar{\psi}$ ) to establish whether the characteristics and differences described in the form of the bed elevation distribution were influenced by sedimentology (Figure 4.5). Previous workers have observed a common relationship between the standard deviation of the bed elevation distribution and particle size (see subsection 2.3.1). A similar correlation was found for the 11 gravel patches considered in this study ( $R^2 = 0.71$ ,  $p < 0.002$ ; Figure 4.5a). The breadth of the bed elevation distribution, a proxy for surface roughness, is therefore largely controlled by particle size. The sorting of bed material was similarly found to exert a significant influence on the kurtosis of the bed elevation distribution ( $R^2 = 0.57$ ,  $p < 0.007$ ; Figure 4.5f). The movement in the frequency of bed elevations from the tails to the shoulders of the distribution (subsection 2.3.1; De Carlo, 1997) under increasing  $\sigma_G$  reflects a greater tendency for poorly sorted beds to be infilled by fine material which reduces the frequency of extremes in bed elevation (Coleman et al., 2011). No statistically significant relationships were observed between the remaining bed elevation pdf moments and metrics of surface grain size, sorting and particle shape ( $p > 0.05$ ; Figures 4.5b-e and 4.5g-i).

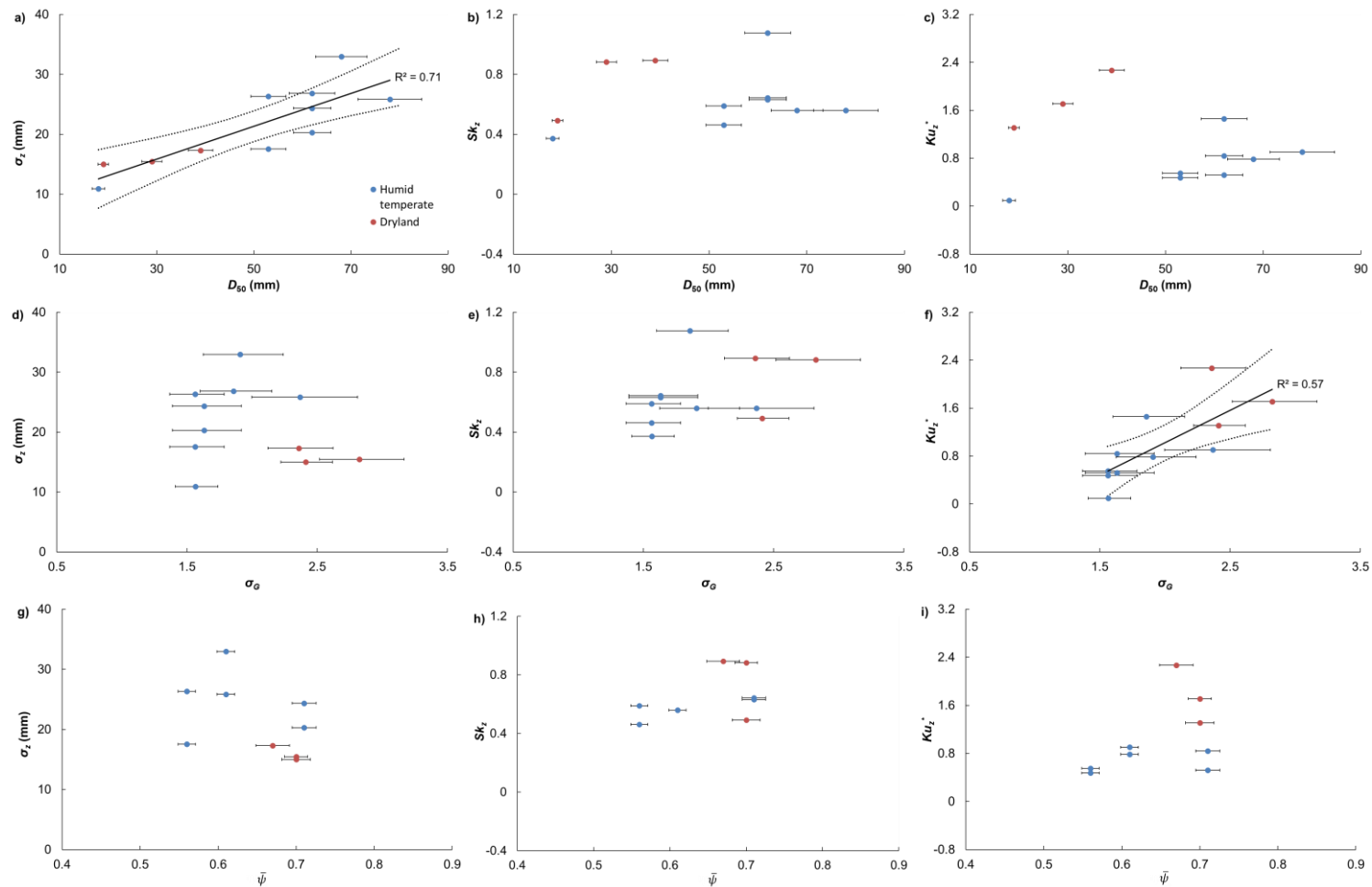


Figure 4.5 Relationships between the statistical moments of the bed elevation pdfs -  $\sigma_z$ ,  $Sk_z$  and  $Ku_z^*$  – and metrics of grain size,  $D_{50}$  (a-c), sorting,  $\sigma_G$  (d-f) and shape,  $\bar{\psi}$  (g-i). (Solid) Lines of best fit determined from least squares regression; 95% confidence intervals shown by the dotted lines. Horizontal error bars around  $D_{50}$  and  $\bar{\psi}$  mark 95% confidence intervals (Bunte and Abt, 2001) and around  $\sigma_G$  illustrate the compounded error from the 95% confidence intervals for  $D_5$ ,  $D_{16}$ ,  $D_{84}$  and  $D_{95}$  (Equation 3.1). Confidence intervals for  $\sigma_z$ ,  $Sk_z$  and  $Ku_z^*$  too small to be visible ( $\leq 0.010$  mm,  $\leq 0.021$  and  $\leq 0.079$ , respectively; Wright and Herrington, 2011).

## 4.5. 2D variograms

The normalised 2D variograms for the humid temperate and dryland patches are presented in Figure 4.6. Close inspection of the variogram surfaces reveals the existence of three regions. The first occurs at subgrain scales, for the range of normalised lags  $0 < \tilde{h} < 0.5$ , and describes the roughness properties of individual grain surfaces. The second region occurs at the grain-scale,  $\tilde{h} \approx 1$ , and reflects the roughness properties of the surface at grain-scales, e.g. preferential particle orientation. Meanwhile, the final region extends to lags  $3 \leq \tilde{h} \leq 10$  and describes the structure associated with meso-scale topography, e.g. extended patches of higher and lower elevations. To help facilitate identifying the preferential alignment of structure, e.g. particle orientation at the grain-scale and the larger-scale alignment of structure at the meso-scale, the ratio of  $\tilde{\gamma}$  between flow parallel and flow transverse variograms ( $\tilde{\gamma}_x/\tilde{\gamma}_y$ ) was calculated over the range  $0.5 < \tilde{h}_{x,y} < 10$  (Figure 4.7).

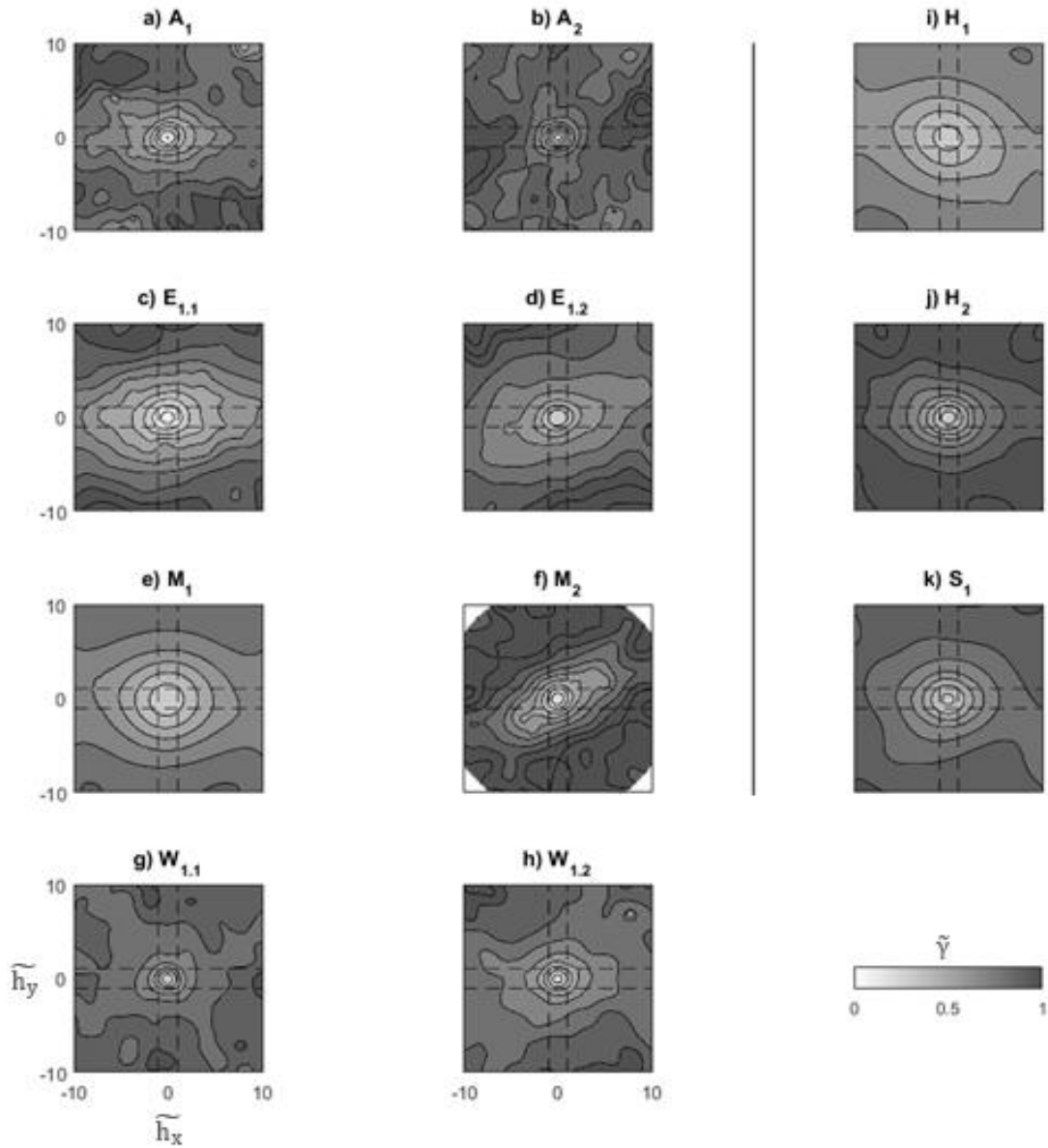


Figure 4.6 Standardised 2D variograms for the a-h) humid temperate and i-k) dryland patches. Dashed lines mark where  $\tilde{h} = 1$ ,  $\tilde{h} = h/D_{50}$  and  $\tilde{\gamma} = \gamma/\sigma_z^2$ .

In this study, the 2D variogram surfaces for all 11 patches appeared to exhibit circular contours at subgrain and grain scales. This indicates that  $\tilde{\gamma}$  increased at an equal rate in all directions, i.e. surface isotropy, over the range  $0 < \tilde{h} < 3$ . Previous workers have similarly recorded circular isobars of  $\tilde{\gamma}$  at subgrain scales which, in some cases, reflected the use of high resolution surface data; where lag pairs were sampled from the same grain at small scales of separation (section 2.3.2; Hodge et al., 2009b). At grain scales, surface isotropy suggests individual particles are not preferentially orientated with respect to the direction of

flow, unlike the observations of previous workers for artificial (e.g. Mao et al., 2011; Curran and Waters, 2014) and natural beds (e.g. Hodge et al., 2009b). Interestingly, the ratio of flow parallel and flow transverse standardised semivariance was not as isotropic as the 2D variograms suggest (typically  $\tilde{\gamma}_x/\tilde{\gamma}_y \approx 0.9$ ; Figures 4.7a and 4.7b) and was potentially too small to be detected from visual inspection of the surfaces.

Over longer lags ( $3 \leq \tilde{h} < 10$ ), the contour pattern of the humid temperate gritstone variogram surfaces tended to become elliptical, e.g. A<sub>1</sub>, E<sub>1.1</sub>, E<sub>1.2</sub>, M<sub>1</sub> and M<sub>2</sub>. In these cases,  $\tilde{\gamma}$  increased at a greater rate in the flow transverse direction than the flow parallel direction (reflected by a decrease in  $\tilde{\gamma}_x/\tilde{\gamma}_y$ ) which indicates surface anisotropy at larger scales. This could be explained by the presence of flow aligned pebble clusters, identified from the visual inspection of measured DTMs. For the M<sub>1</sub> variogram surface (Figure 4.6e), the increase in  $\tilde{\gamma}$  with  $\tilde{h}_{x,y}$  was lower when compared to the other humid temperate gritstone patches and indicates a smoother surface (cf. Figure 4.3; section 4.3). This was consistent with the smaller surface grain size (Figure 4.1a; Table 4.1). Conversely, the tighter contouring pattern for the M<sub>2</sub> variogram surface (Figure 4.6f) indicates the increase in  $\tilde{\gamma}$  with  $\tilde{h}_{x,y}$  was comparatively greater than the other humid temperate gritstone patches. This suggests the surface is comparatively rougher which is reflected in higher values of  $\sigma_z$  (Table 4.2) and the coarser grain size distribution (Figure 4.1a; Table 4.1). In contrast to their humid temperate gritstone counterparts, the humid temperate limestone 2D variograms were characterised by a circular contouring pattern at larger scales (Figures 4.6g-h). In addition, the ratio of flow parallel and flow transverse standardised semivariance was broadly maintained over full range of lags ( $\tilde{\gamma}_x/\tilde{\gamma}_y \approx 0.9$  for  $0.5 < \tilde{h} < 10$ ; Figure 4.7c). This larger-scale surface isotropy is thought to reflect the role of particle shape in moderating the alignment of bed structure. In this regard, the humid temperate limestone patches were comprised of rounded grains which displayed less of a tendency to imbricate and combine into cluster bedforms compared to their gritstone counterparts (see section 4.3; Figure 4.3). The effect of particle shape on larger-scale bed structure was also demonstrated for the dryland limestone 2D variograms which are similarly characterised by circular contours and surface isotropy over longer lags (Figures 4.6i-k and 4.7d). However, like the M<sub>1</sub> patch, the increase in  $\tilde{\gamma}$  with  $\tilde{h}_{x,y}$  was lower when compared to the humid temperate limestone counterparts. This reflects the smoother dryland patch bed

topography (Figures 4.3i-k) generated, in-part, by a poorly sorted and fine surface grain size distribution (Figure 4.1; Table 4.1).

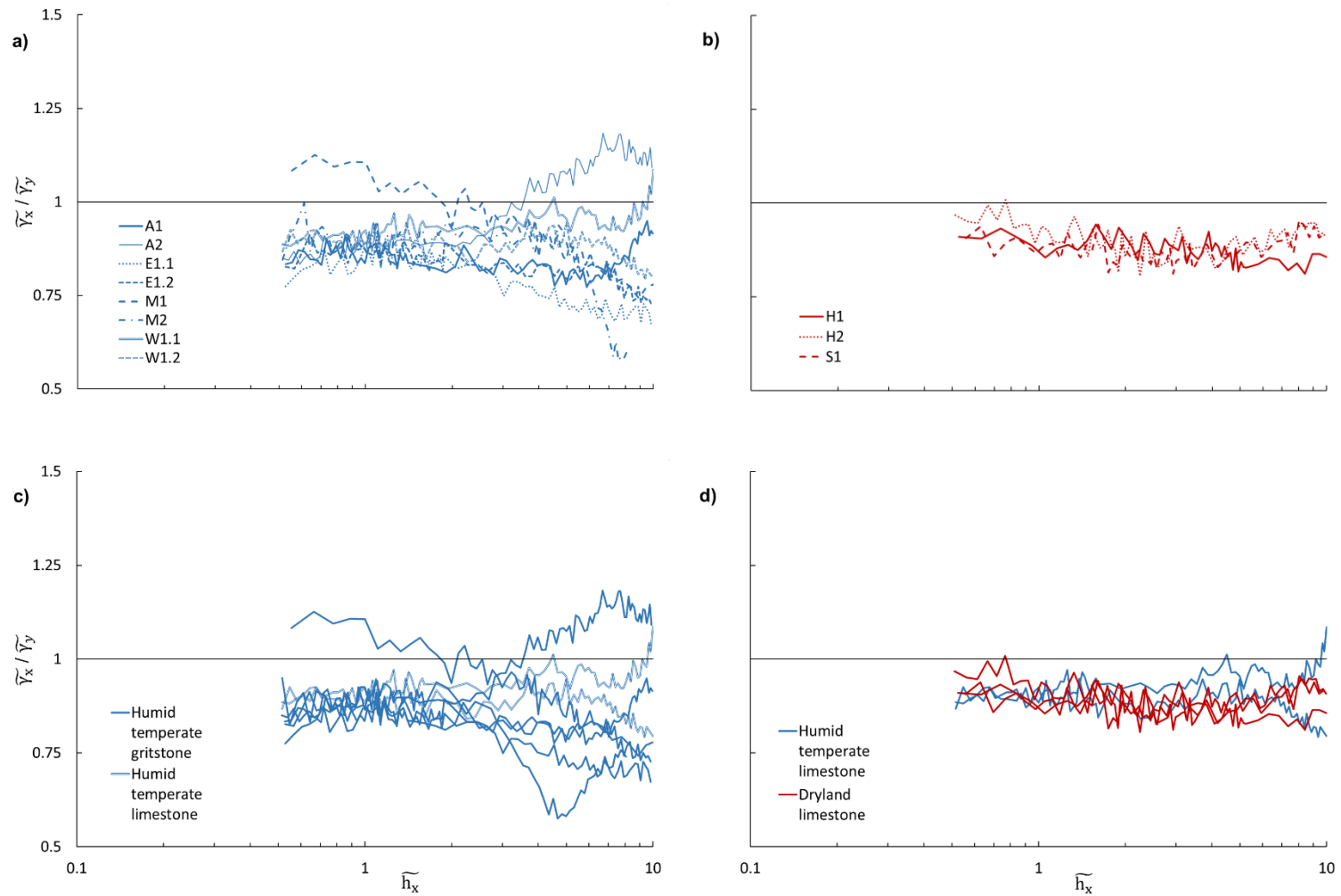


Figure 4.7 Variation in the ratio of normalised  $\gamma$  in flow parallel ( $\gamma_x$ ) and flow transverse ( $\gamma_y$ ) directions as a function of normalised lag for the a) humid temperate patches, b) dryland patches, c) humid temperate patches classified by lithology (limestone vs. gritstone) and d) limestone lithologies classified by flow regime (perennial vs. ephemeral).

## 4.6. 1D variograms

This section investigates the scaling characteristics of the surfaces by considering the flow-parallel and flow-transverse 1D profiles in further detail. In doing so, an assessment is firstly made on the validity of the variogram model of Nikora et al. (1998) to describe the 1D profiles (Subsection 4.6.1) before moving onto characterising the form of the 1D variograms (Subsection 4.6.2) between patches on the basis of grain and meso-scale topographies, particle shape (gritstone vs. limestone) and flow regime (perennial vs. ephemeral).

### 4.6.1. 1D variogram model assessment

On inspection, the 1D variograms in flow parallel and flow transverse directions for all 11 patches appear to conform to the model of Nikora (subsection 2.3.2 and 3.5.2). In this regard, the 1D variograms seem to be subdivided into three regions at short, intermediate and long lags which approximate the scaling, transition and saturation regions described by Nikora et al. (1998). As an example, the flow parallel variograms for the  $A_1$  patch is presented in Figure 4.7a in which estimates of the topographic irregularity of the surface ( $H$ ) and two scales of roughness ( $h_1$  and  $h_2$ ) are highlighted. The two-knot, three-segment spline model used to characterise the form of the 1D variograms (Subsection 3.5.2; Figure 4.8a) was found to provide a good statistical approximation of the data. This is confirmed by high values of the  $R^2$  goodness of fit statistic which, for all 11 patches, was found to range between  $0.988 \leq R^2 \leq 0.998$  and by the narrow 95% confidence intervals estimated for  $h_1$ ,  $H$  and  $h_2$  (2–4 mm; 2–4%; 6–99 mm). However, despite the good statistical approximation of the data provided by the model, the systematic pattern of residuals around the knots ( $\tilde{h}_1$  and  $\tilde{h}_2$ ; Figure 4.8b) suggests a degree of non-linearity within the region  $\tilde{h} < \tilde{h}_1$ . The curvature in this region is present across all the flow parallel and flow transverse 1D variograms (see Appendix B) and reflects multifractal behaviour (Subsection 2.3.2; Hodge et al., 2009b). Therefore, the 1D variograms did not follow the model of Nikora where a single log-log linear section (scaling region) is present, described by a single fractal dimension. As a consequence, the analysis of 1D variograms that follows in Subsection 4.6.2 relies on the qualitative interpretation of variogram character.

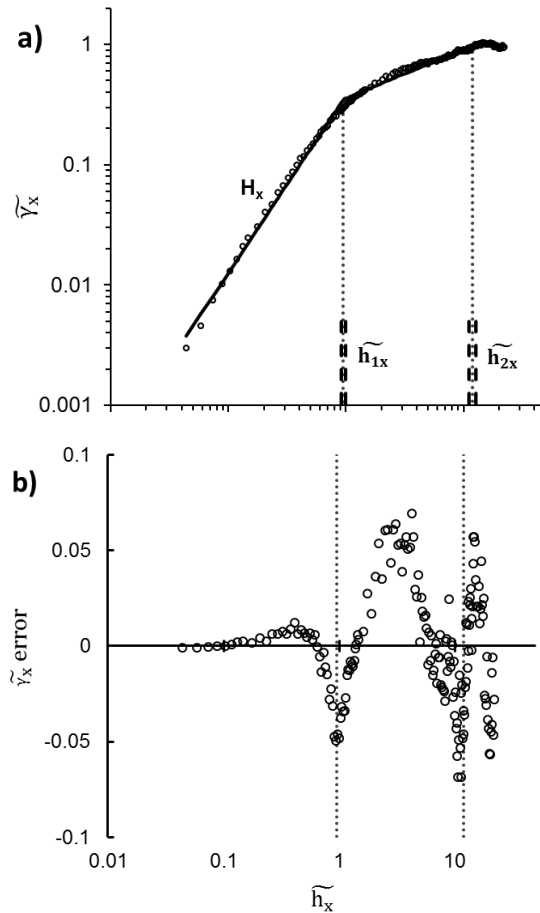


Figure 4.8 a) Example flow-parallel variogram and fitted spline model for the a)  $A_1$  humid temperate patch and b) residuals between the observed and expected  $\tilde{\gamma}_x$  (note  $\log \tilde{h}_x$  and  $\tilde{\gamma}_x$  scales). In a) the dotted lines refer to the length of the  $\tilde{h}_{1x}$  and  $\tilde{h}_{2x}$  scales of roughness and the dashed lines represent the 95% confidence intervals around  $\tilde{h}_{1x}$  and  $\tilde{h}_{2x}$ .

#### 4.6.2. 1D variogram characterisation

The 1D, flow-parallel variograms for the humid temperate and dryland patches are presented in Figures 4.9a and 4.9b respectively. As Subsection 4.6.1 discusses, the 1D variograms for all 11 patches follow a broadly curved form in log-log space as the rate of increase in  $\tilde{\gamma}_x$  decreases with increasing  $\tilde{h}_x$ . For the majority of humid temperate patches, the point at which the rate of increase in  $\tilde{\gamma}_x$  begins to markedly reduce (start of the apex of curvature) is approximate to the median surface grain size diameter ( $\tilde{h}_x \approx 1$ ). This reflects the important control of particle size on surface roughness (Figure 4.5a). For the  $M_1$  patch, the start of the apex of curvature begins at slightly longer lags, equivalent to the size of coarser surface

grains ( $\widetilde{h}_x \approx 2$ ), which reflects the greater influence of coarse clasts on surface roughness for the comparatively planar patch topography (cf. Figure 4.3c). This is similarly found for the dryland patches and can be attributed to the pronounced grain-scale topography associated with coarse surface grains and scoured wake depressions (Figures 4.3i-k).

Over longer lags  $\widetilde{\gamma}_x$  continues a finite, asymptotic rise until, in most instances, a defined sill is reached. Thereafter, increases in  $\widetilde{h}_x$  do not lead to systematic changes in  $\widetilde{\gamma}_x$ , which fluctuate about the patch variance. However, for E<sub>1.1</sub> and W<sub>1.2</sub> it was unclear whether a sill was attained over the range of lags, i.e.  $\widetilde{\gamma}_x$  continued to rise with  $\widetilde{h}_x$ . In these isolated cases, this may suggest the statistical dependency of the surface exceeds the patch extent. In addition,  $\widetilde{\gamma}_x$  is comparatively lower for E<sub>1.1</sub> and M<sub>1</sub> within the range  $0.1 \leq \widetilde{h}_x \leq 3$  relative to the other humid temperate patches which demonstrates these surfaces are topographically smoother over this scale. When the gritstone and limestone humid temperate patches are compared in Figure 4.9c,  $\widetilde{\gamma}_x$  tends to be greater for the latter particularly within the range of grain-scale lags  $0.1 \leq \widetilde{h}_x \leq 2$ . This suggests the humid temperate limestone patches are generally rougher at the scale of individual grains compared to their humid temperate gritstone counterparts. Furthermore, the 1D variograms for the humid temperate gritstone patches appear to reach a sill at longer lags relative to the humid temperate limestone patches ( $\widetilde{h}_x \approx 15$  and  $\widetilde{h}_x \approx 10$  respectively). This reflects the greater tendency for larger-scale, flow aligned structure to develop with streambeds comprised of bladed, gritstone material compared to more rounded, limestone grains. Meanwhile, a comparison between the limestone patches from both flow regimes (Figure 4.9d) reveals  $\widetilde{\gamma}_x$  remains comparatively lower at grain-scales ( $0.1 \leq \widetilde{h}_x \leq 2$ ) and the sill was attained at shorter lag lengths for the dryland patches ( $\widetilde{h}_x \approx 5$ ). Thus, the grain-scale topography of the dryland limestone patches was smoother than their humid temperate counterparts and larger scales of bed structure are limited to the roughness properties around prominent, coarse surface clasts and not any larger- (meso-) scale topography.

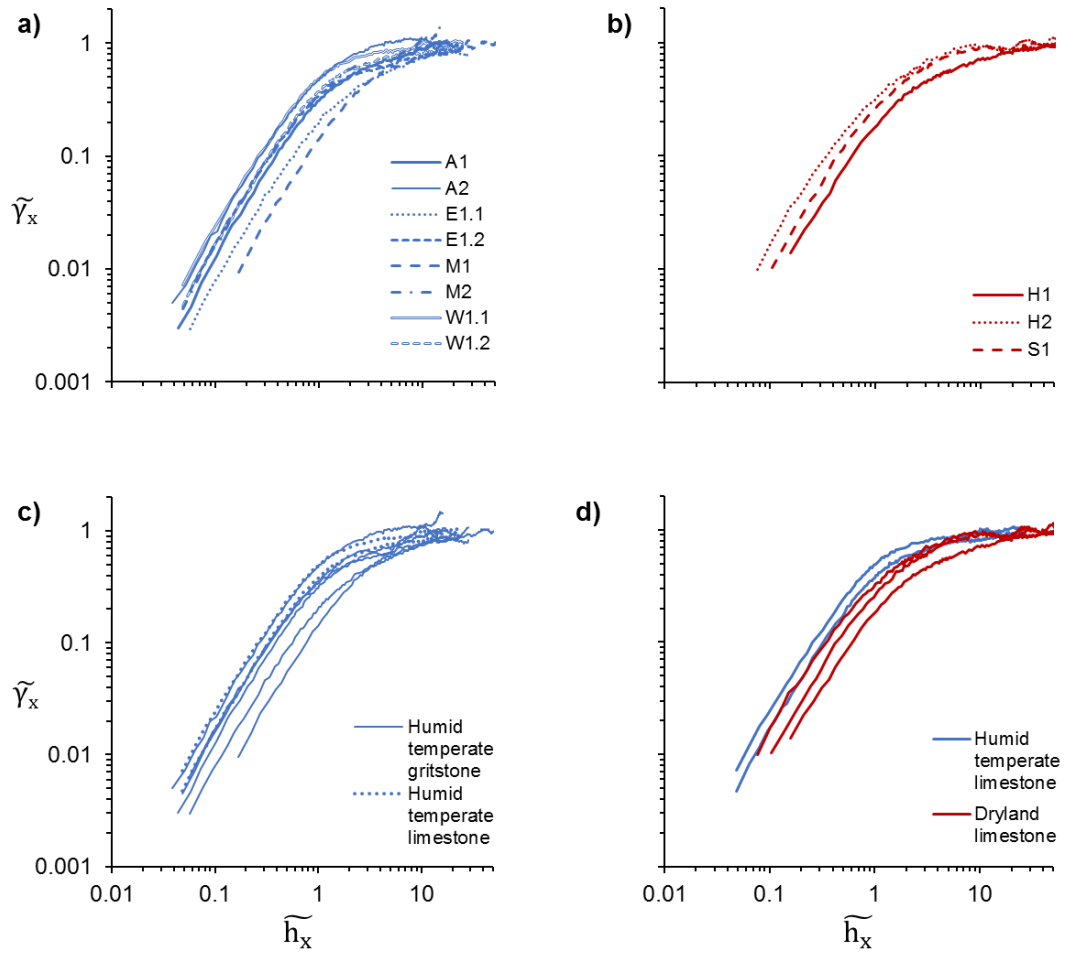


Figure 4.9 Flow-parallel variograms for the a) humid temperate patches, b) dryland patches, c) humid temperate patches classified by lithology (limestone vs. gritstone) and d) limestone lithologies classified by flow regime (perennial vs. ephemeral).

## 4.7. Inclination Index

The inclination index of Smart et al. (2004),  $I$ , helps to further characterise the grain-scale properties of the surface. As Figure 3.24b demonstrated with a binary classification of upstream (black) and downstream (white) facing slopes (corresponding to negative and positive values of  $I$  respectively), the metric calculated over a 9 mm length clearly identifies the faces of individual grains and is therefore suitable for characterising particle imbrication. Figure 4.10a shows  $I$  is typically negative for the humid temperate gravel patches ( $-0.094 \leq I \leq -0.004$ ) which indicates surface grains tend to face in an upstream direction. This demonstrates the streambed surfaces are largely comprised of imbricated grains. However, in contrast, the inclination index for the A<sub>2</sub> patch is positive ( $I = 0.039$ ) which indicates grains typically face in a downstream direction. This suggests a preference for particles to be imbricated against the direction of flow. In addition, the inclination index for the patches A<sub>1</sub>, M<sub>1</sub> and W<sub>1.1</sub> was found to approximate zero ( $-0.004 \leq I \leq 0$ ) which demonstrates the frequency of positive and negative inclinations were approximately equal. However, differences in particle imbrication between the humid temperate patches were not evident from a visual inspection of the DTMs (Section 4.3) which casts doubt on the ability to infer preferential particle positioning from qualitative analysis. Meanwhile, the inclination index is broadly comparable for the dryland patches ( $-0.051 \leq I \leq -0.004$ ;  $\bar{I} = -0.032$ ) compared to their humid temperate patches ( $-0.094 \leq I \leq -0.039$ ;  $\bar{I} = -0.028$ ) which shows there is little evidence that the humid temperate patches are any more imbricated than the dryland patches. The inclination index was compared against patch surface grain size, sorting and shape (Figures 4.10b, 4.10c and 4.10d respectively) to investigate whether the imbrication of surface grains was influenced by sedimentology. In this regard, no statistically significant relationships were observed  $I$  and  $D_{50}$ ,  $\sigma_G$  and  $\bar{\psi}$  from least squares regression ( $p > 0.05$ ) which demonstrates surface grain size, sorting and shape does not moderate particle imbrication.

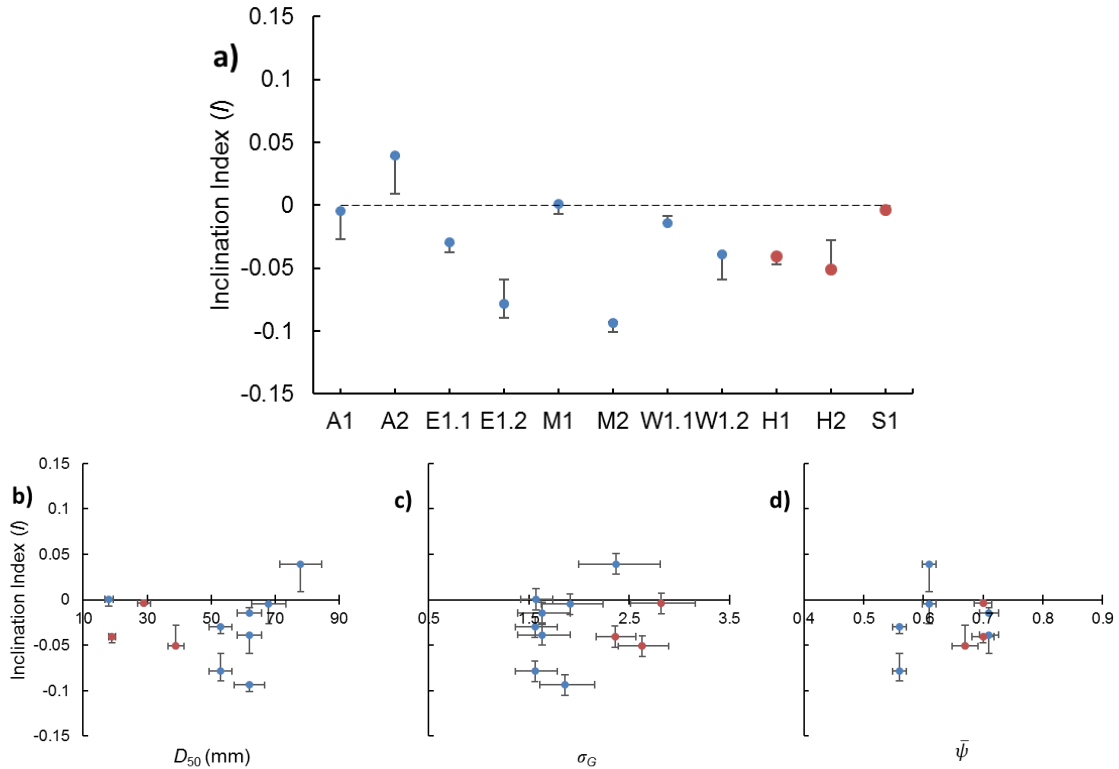


Figure 4.10 a) The inclination index,  $I$ , for the humid temperate and dryland patches (blue and red, respectively) and relationships between  $I$  and b-d) surface grain size, sorting and shape. Vertical error bars represent range in  $I$  calculated using 8 mm and 10 mm moving windows.

#### 4.8. Slope and Aspect

An analysis of local slope and aspect can help to provide a further view on the grain-scale properties of the surface (Figure 3.24c). The metric is calculated over a 3-by-3 cell (9 x 9 mm) window, which matches the spatial length used to estimate the Inclination Index in Section 4.7. When considering local slope at the scale of individual grains, a high proportion of shallow slopes (i.e. median slope,  $S_{50}$ :  $0 < S_{50} < 30^\circ$ ) indicates a relatively smooth surface whereas a preponderance of steeper gradients ( $60 < S_{50} < 90^\circ$ ) will indicate a rougher surface. The distributions of local slope for the humid temperate and dryland patches are presented in Figures 4.11. The surfaces of all 11 patches exhibit a greater proportion of shallow slopes than steep slopes and, in response, the distributions of local slope are characterised by a positive skew. The form of the slope distribution was described through two metrics: median slope ( $S_{50}$ ), and the skewness of the slope distribution ( $Sk_s$ ). The skewness of the distributions

was broadly comparable between the humid temperate patches ( $26.0 \leq S_{50} \leq 30.8^\circ$ ,  $\overline{S_{50}} = 28.9^\circ$ ;  $0.37 \leq Sk_s \leq 0.65$ ,  $\overline{Sk_s} = 0.51$ ; Figure 4.11a) although the slope distribution for  $M_1$  was significantly more peaked and positively skewed compared to the other patches ( $S_{50} = 20.5^\circ$ ,  $Sk_s = 0.76$ ). The higher proportion of shallow slopes for the  $M_1$  patch indicates the surface was topographically smoother than the other humid temperate patches which is consistent with the DTM and bed elevation pdf analyses (Sections 4.3 and 4.4 respectively). Meanwhile, the distributions of local slope for the dryland patches exhibit a largely similar form to their humid temperate counterparts ( $26.5 \leq S_{50} \leq 29.9^\circ$ ,  $\overline{S_{50}} = 27.8^\circ$ ;  $0.43 \leq Sk_s \leq 0.62$ ,  $\overline{Sk_s} = 0.55$ ; Figure 4.11b). The metrics of the slope distribution were compared against surface grain size, sorting and shape (see Section 4.7) to establish whether local slope was a function of patch sedimentology. The results of this assessment are presented in Figures 4.11c-h. Considering all 11 patches, the null hypothesis of least squares regression was accepted ( $p > 0.05$ ) and so the form of the local slope distributions was not significantly influenced by  $D_{50}$ ,  $\sigma_G$  and  $\bar{\psi}$ . Therefore, the local slopes of the humid temperate and dryland patches were unaffected by patch sedimentology.

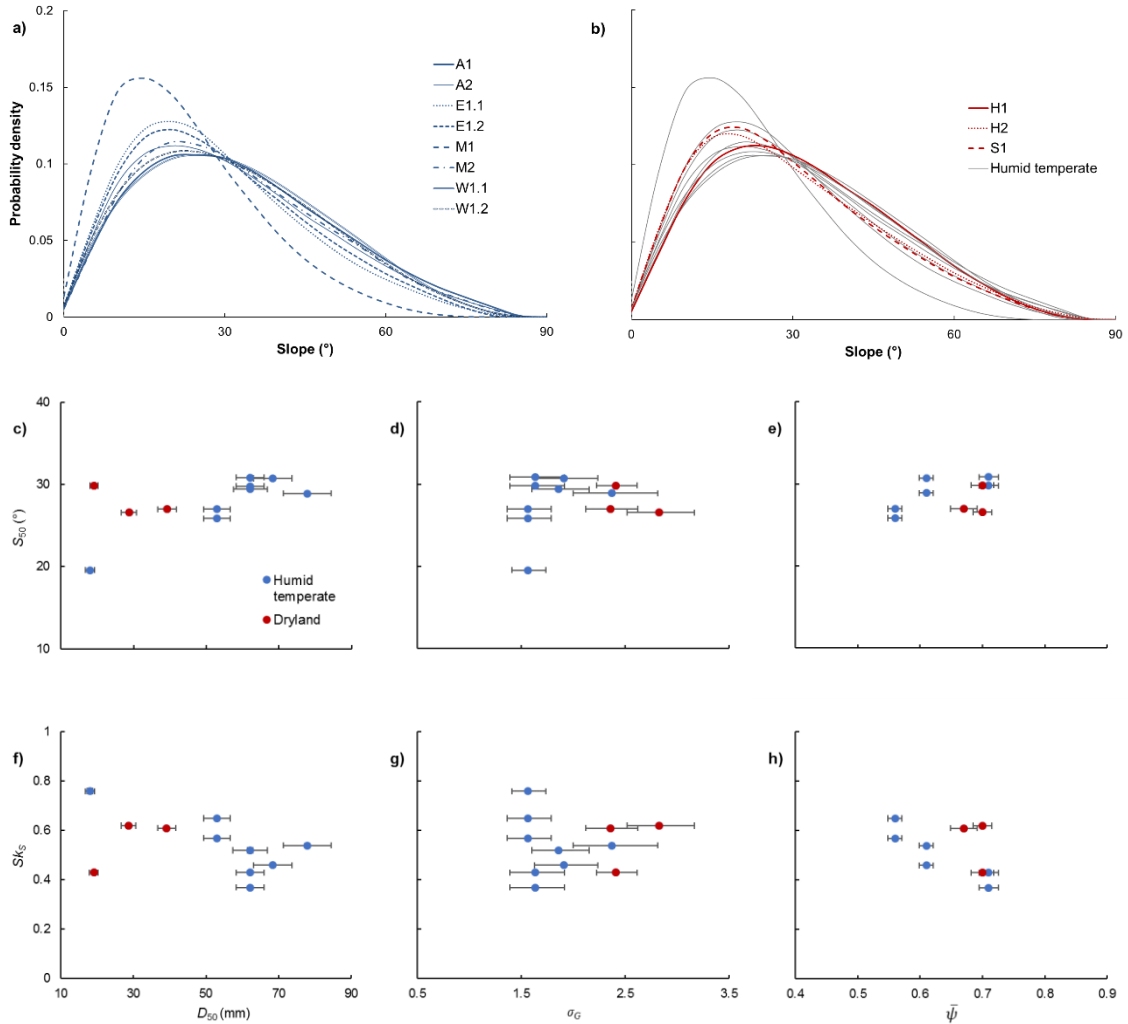


Figure 4.11 Distributions of local slope for the a) humid temperate patches and b) dryland patches. Relationships between the sedimentological parameters -  $D_{50}$ ,  $\sigma_G$ , and  $\bar{\psi}$  – with c-e) median slope and f-h) the skewness of local slope distributions. 95% confidence intervals for  $S_{50}$  and  $Sk_S$  too small to be visible ( $\leq 0.09^\circ$  and  $\leq 0.01$ , respectively).

The combined distributions of local slope and aspect are presented from the humid temperate and dryland patches in Figures 4.12a-h and 4.12i-k respectively. Previous workers have used polar plots of slope and aspect to further explore grain-scale properties of the surface and identify preferential particle imbrication and orientation (Subsection 2.3.3). Grain imbrication, for example, is demonstrated by a greater proportion of cells with upstream facing aspects and by a tendency for the cells associated with the highest angles to be sloping in a downstream direction. Particle shape influences the density pattern with the polar plot of combined slope and aspect while grain orientation can be deduced from symmetrical axes of density (Subsection 2.3.3). In this study, the polar plots of slope and aspect are generally

characterised by a greater proportion of upstream to downstream facing cells, thereby demonstrating a tendency for grains to be imbricated. However, the density patterns within the polar plots are highly variable and systematic differences are not apparent between patches on the basis of particle shape (Figures 4.12a-f vs. 4.12g-h) or flow regime (Figures 4.12g-h vs. 4.12i-k). Moreover, this variability inhibits the ability to identify symmetrical axes of density to infer the preferential orientation of grains. The polar plots are, however, able to highlight the contrast in the distribution of slopes for the  $M_1$  patch.

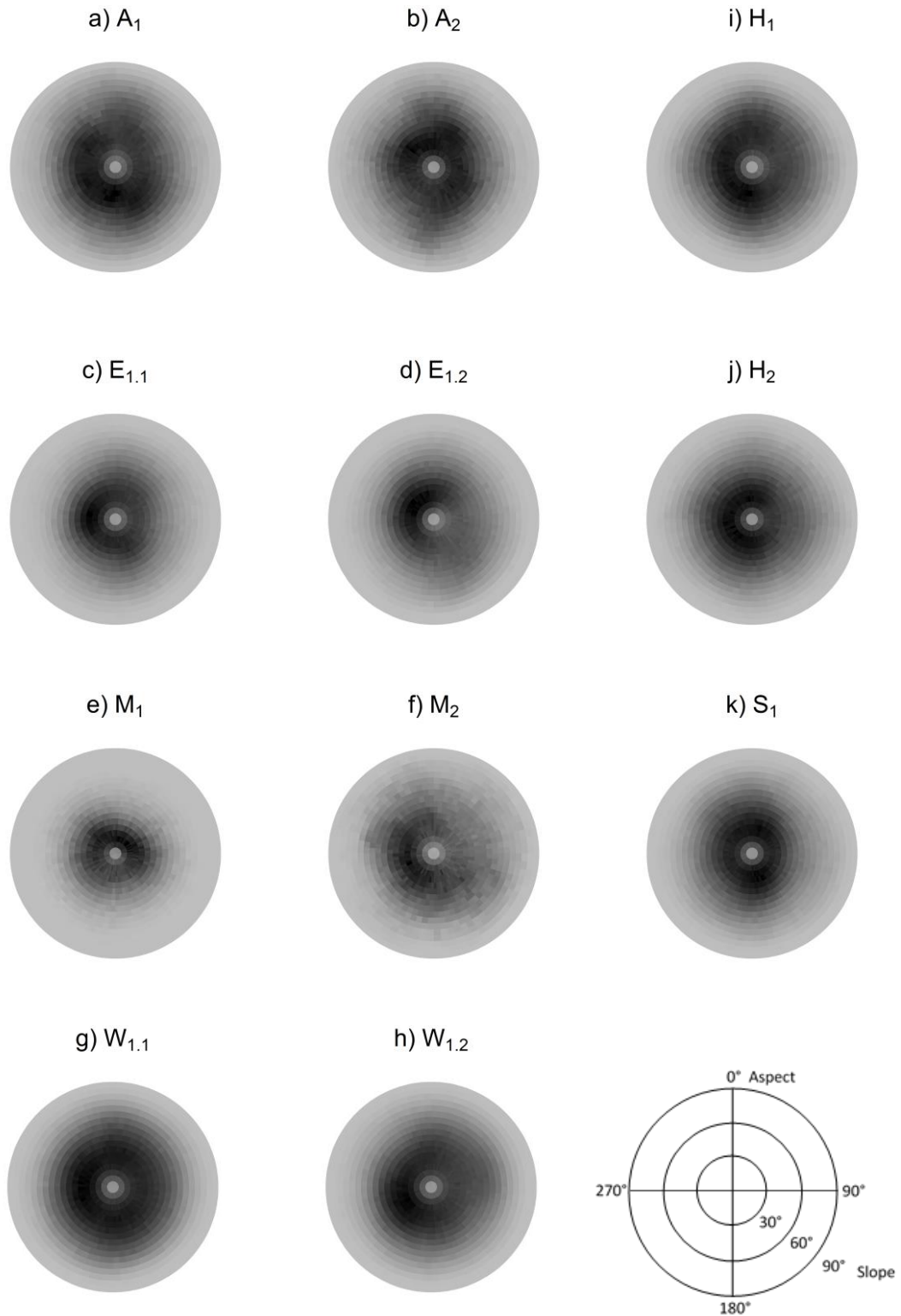


Figure 4.12 Polar plots of aspect and slope angle for the a-f) humid temperate gritstone, g-h) humid temperate limestone and i-k) dryland limestone patches, shaded by density (high = black, low = grey). Flow direction orientated from 270° to 90°.

#### 4.9. Pivoting angle ( $\Phi$ )

The characteristics of alluvial streambed structure, as discussed through sections 4.2 – 4.8, will influence the mobility of surface grains and, hence, the transport of sediment. To explicitly explore the control of bed structure on particle stability, the force balance of individual grains can be parameterised in terms of the parameters  $\Phi$ ,  $p$  and  $e$  (see subsections 2.3.4-5). In this study, measurements of  $\Phi$ ,  $p$  and  $e$  were obtained from two humid temperate ( $W_{1.1}$  and  $W_{1.2}$ ) and the three dryland patches ( $H_1$ ,  $H_2$  and  $S_1$ ). Differences between the parameters for the humid temperate and dryland patches were evaluated using regime-aggregated (combined) datasets. An analysis of  $\Phi$  is firstly considered through section 4.9 before moving onto the components of grain protrusion –  $p$  and  $e$  – in section 4.10.

Previous workers have commonly observed values of  $\Phi$  are lognormally distributed (e.g. Johnston et al., 1998). In this study, however, the distributions of  $\ln(\Phi)$  were sufficiently peaked ( $Ku_{\ln(\Phi)} > 0$ ) and negatively skewed ( $Sk_{\ln(\Phi)} < 0$ ) such that they were significantly different from a normal distribution following a chi-square goodness-of-fit test ( $p < 0.05$ ). A non-parametric Wilcoxon rank sum test revealed  $\Phi$  was significantly lower for regime-aggregated data from the humid temperate patches relative to the dryland patches ( $\Phi_{50} = 73^\circ$  and  $84^\circ$ , respectively;  $p < 0.001$ ; Figure 4.13a). The distributions of  $\Phi$  were also comparatively broader for the humid temperate patches ( $\Phi_{16} = 53^\circ$ ,  $\Phi_{84} = 83^\circ$ ) than their dryland counterparts ( $\Phi_{16} = 73^\circ$ ,  $\Phi_{84} = 88^\circ$ ) which reflects a greater variation in the geometry of bed surface pockets. Furthermore, a greater difference was observed in the distributions of  $\Phi$  between the humid temperate patches ( $70 \leq \Phi_{50} \leq 77^\circ$ ) compared to the dryland patches ( $84 \leq \Phi_{50} \leq 85^\circ$ ). This reflects the wider variety in the geometry of bed surfaces pockets for the patches subject to perennial flows whereas those subject to ephemeral flows exhibit a narrow range of high pivoting angles. Figure 4.13b and 4.13c illustrate how pivoting angle varies with relative particle size ( $D_i/D_{50}$ ) for the humid temperate and dryland patches respectively. Previous workers observed that  $\Phi$  decreases with  $D_i/D_{50}$ , although the embedding of surface grains can cause  $D_i/D_{50}$  to be invariant (e.g. Pilgrim Creek; Johnston et al., 1998). In this study,  $\Phi$  was found to decrease with  $D_i/D_{50}$  for all five patches with the humid temperate patches showing the greatest rate of decrease. Consequently, higher values of  $\Phi$  were sustained for a given  $D_i/D_{50}$  for the dryland patches which may be linked with the

embedding of surface grains within a fine-grained matrix-supported streambed (Johnston et al., 1998).

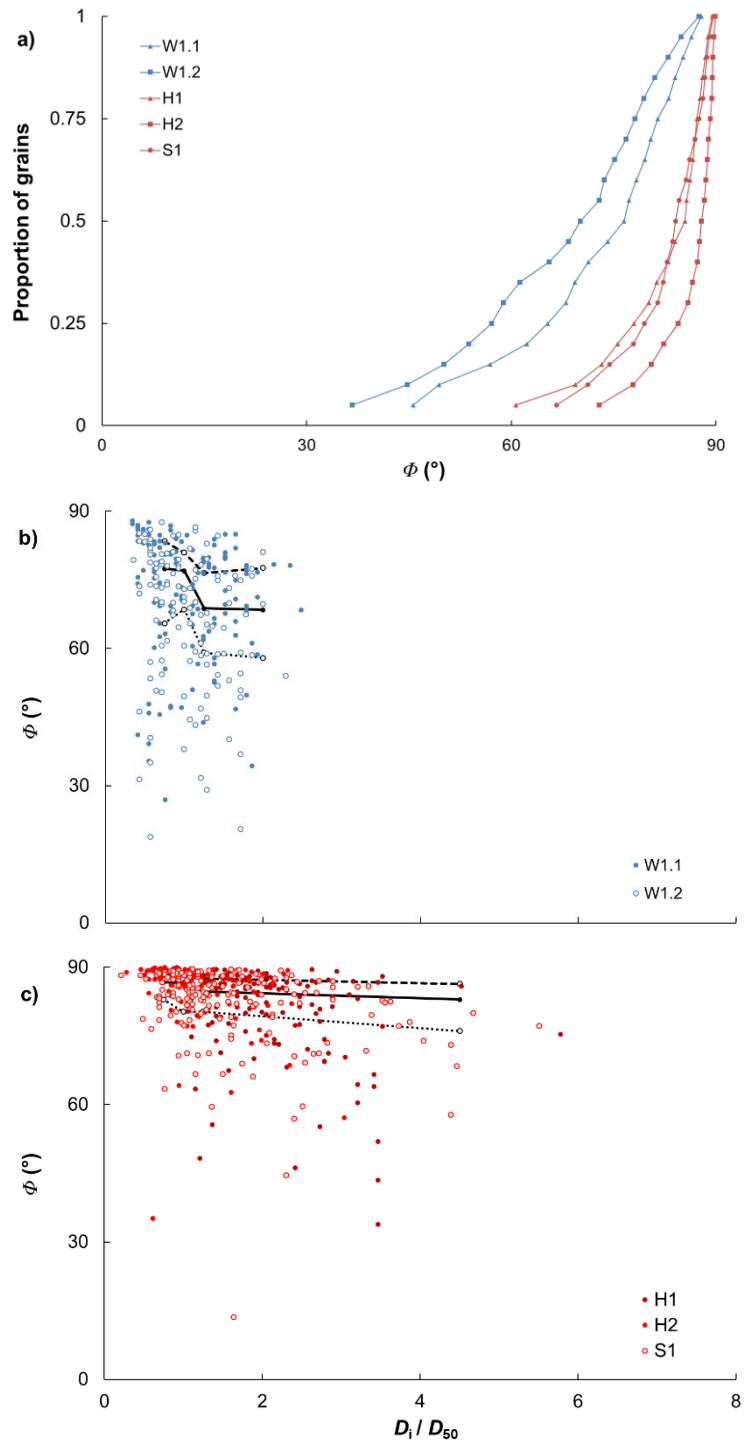


Figure 4.13 a) Cumulative distributions of  $\Phi$  for the five patches and the relationship between  $\Phi$  and  $D_i/D_{50}$  for the b) humid temperate and c) dryland patches. In b) and c) lines represent the 25<sup>th</sup> (dashed line), 50<sup>th</sup> (solid) and 75<sup>th</sup> (dotted) percentiles of data aggregated for bins that contain at least 30 grains.

Following Miller and Byrne (1966), a power law function was fitted to define the trends between  $\Phi$  and  $D_i/D_{50}$  for all five patches (see Subsection 2.3.4). A statistically significant relationship was only observed for the dryland patches ( $R^2 = 0.04-0.11$ ,  $p < 0.02$ ) while the lack of a statistically significant relationship for the humid temperate patches ( $R^2 = 0.01-0.02$ ,  $p > 0.05$ ) reflects the wide spread in  $\Phi$  with  $D_i/D_{50}$ . The coefficients  $\alpha$  and  $\beta$  in the power law functions for the dryland patches were found to range between  $78.9 \leq \alpha \leq 86.0$  and  $0.06 \leq \beta \leq 0.19$ . Values of  $\alpha$  were higher and for  $\beta$  were lower in comparison to previous workers (see Table 2.1; Subsection 2.3.4) demonstrating that  $\Phi$  for the dryland patches was both greater and shows less variation across all grain size classes than might be expected.

#### **4.10. Grain protrusion: projection ( $p$ ) and exposure ( $e$ )**

Distributions of dimensionless projection ( $p/D$ ) for the humid temperate and dryland patches are presented in Figure 4.14a. Previous workers have observed that distributions of  $p/D$  are normally distributed (e.g. Hodge et al., 2013). In this study, the distributions of  $p/D$  for all five patches are also approximated by a Gaussian form, as confirmed by a chi-square goodness of fit test ( $p > 0.05$ ). Despite a broad agreement in the general form of the distribution, a t-test performed on regime-aggregated data found values of  $p/D$  were significantly greater for the dryland patches than the humid temperate patches ( $\overline{p/D} = 0.34$  and  $0.27$ , respectively;  $p < 0.001$ ). The distributions of dimensionless exposure ( $e/D$ ), on inspection, appeared non-normal and positively skewed (Figure 4.14b). A non-parametric Wilcoxon rank sum test between regime-aggregated data revealed median values of  $e/D$  were significantly greater for the dryland patches than the humid temperate patches ( $e/D_{.50} = 0.007$  and  $0$ , respectively;  $p < 0.001$ ). The differences in values of  $p/D$  and  $e/D$  indicates that grains found within the dryland patches projected further into the flow and were more exposed than an equivalently-sized particle from the humid temperate patches.

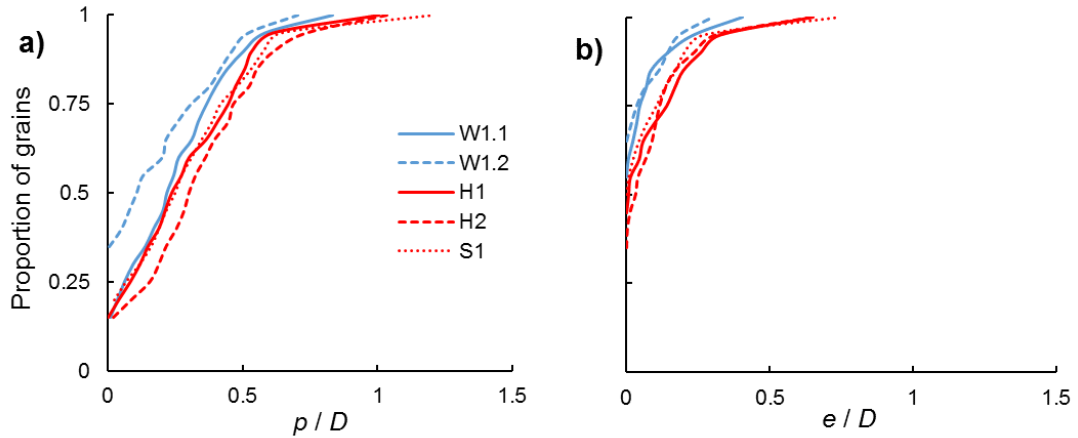


Figure 4.14 Cumulative distributions of a) grain projection and b) exposure normalised by grain size for the humid temperate (blue) and dryland patches (red).

The relationship between projection and exposure is explored further by plotting  $p/D$  against  $e/D$  for the humid temperate and dryland patches, as shown in Figures 4.15a and 4.15b respectively. For the regime-aggregated data, a weak but significant relationship is recorded between  $p/D$  and  $e/D$  for the humid temperate ( $R^2 = 0.49$ ,  $p < 0.001$ ) and dryland patches ( $R^2 = 0.09-0.46$ ,  $p < 0.001$ ) which confirms that grains projecting further above the local bed surface are also likely to be more exposed to the flow. Previous workers have observed the residuals from the significant relationship between  $p/D$  and  $e/D$  are normally distributed (e.g. Hodge et al., 2013). In this study, the residual error between  $p/D$  and  $e/D$  was also found to adhere to a Gaussian form, as a chi-squared goodness of fit test confirmed for the humid temperate and dryland patches ( $p > 0.05$ ).

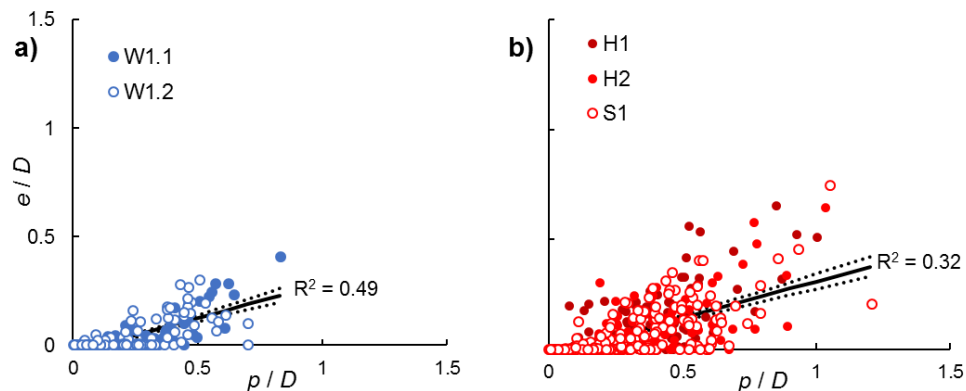


Figure 4.15 Relationship between relative projection and relative exposure for a) the humid temperate and b) the dryland gravel patches. Lines of best fit determined from least squares regression for the regime-aggregated data, 95% confidence intervals illustrated by the dotted lines.

#### 4.11. Critical shear stress and dimensionless critical shear stress ( $\tau_c$ and $\tau_c^*$ )

Bed stability was described through critical shear stress ( $\tau_c$ ) and dimensionless critical shear stress ( $\tau_c^*$ ) which were estimated by resolving the force balance model outlined in section 3.6.3 using a Monte Carlo simulation. The distributions of  $\tau_c$  and  $\tau_c^*$  predicted by the entrainment model are presented in Figures 4.16a and 4.16b respectively. Despite appearing to follow a lognormal form, the distributions of  $\ln(\tau_c)$  for regime-aggregated humid temperate and dryland data reject the null hypothesis of a chi-squared goodness of fit test ( $p < 0.05$ ), owing to long tails of modelled critical shear stresses. A non-parametric Wilcoxon rank-sum test revealed  $\log(\tau_c)$  was significantly higher for the humid temperate patches compared to their dryland counterparts ( $\tau_{c.50} = 118$  and  $51$  Pa, respectively;  $p < 0.001$ ). This largely reflected the differences in bed texture since the grain size distributions were coarser for the humid temperate patches than the dryland patches.

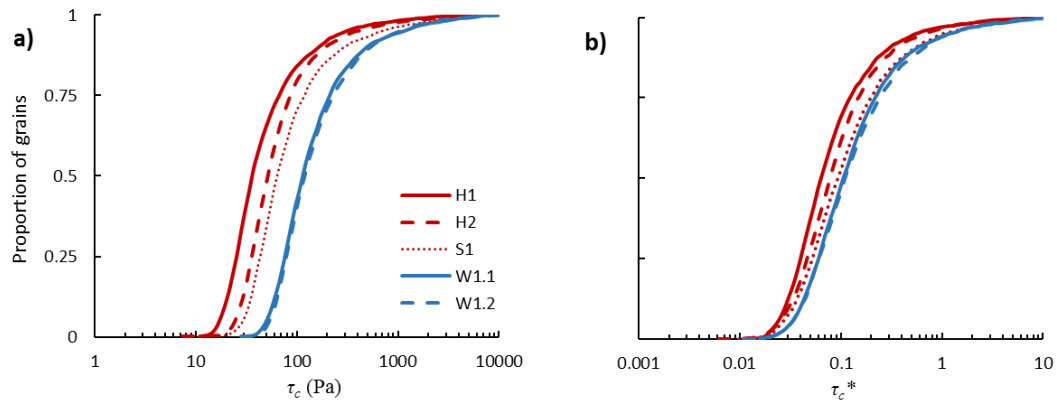
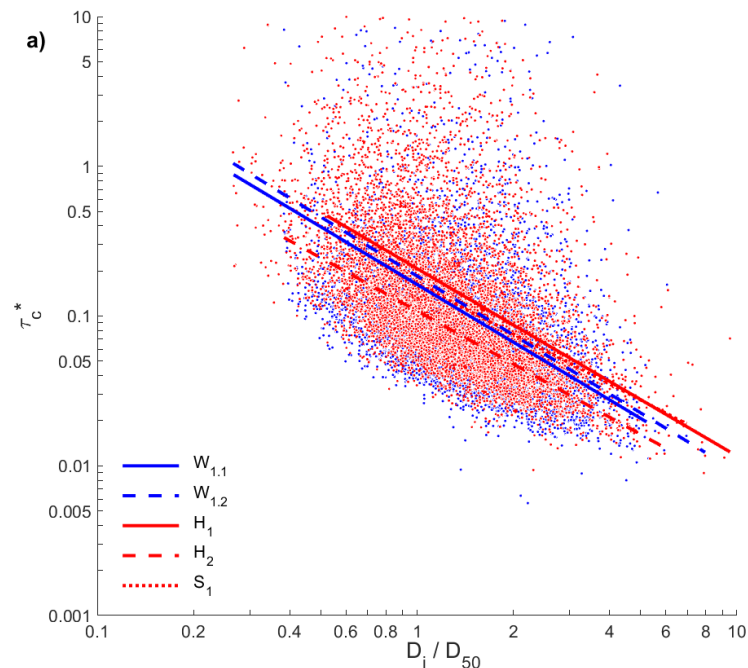


Figure 4.16 Cumulative distribution of a)  $\tau_c$  and b)  $\tau_c^*$  for the humid temperate (black) and dryland (grey) patches predicted by the entrainment model.

Accounting for the grain-size dependency of  $\tau_c$ , a Wilcoxon rank-sum test between regime-aggregated data revealed  $\tau_c^*$  was significantly higher for the humid temperate patches compared to their dryland counterparts ( $\tau_{c^*.50} = 0.11$  and  $0.08$ , respectively;  $p < 0.001$ ). This indicates that bed stability, irrespective of differences in grain size, was significantly greater for the humid temperate patches relative to the dryland patches. Values of  $\tau_c^*$  for both regime-aggregated datasets lie toward the uppermost limit of previous observations (Section 2.1; Buffington and Montgomery, 1997) and reflects the selective choice of coarser surface grains

for *in-situ* sampling which may bias the entrainment model and lead to the possible overestimation of  $\tau_c$  and  $\tau_c^*$ .

The relationship between dimensionless critical shear stress and relative grain size is illustrated for the humid temperate and dryland patches in Figure 4.17 with lines of best fit generated from least squares regression between  $\ln(\tau_c^*)$  and  $\ln(D_i/D_{50})$ , i.e.  $\ln(\tau_c^*) = \alpha_0 + \alpha_1 \ln(D_i/D_{50})$ . The slope coefficient for the line of best fit ( $\alpha_1$ ) is in the order of -1 for the regime-aggregated data from the humid temperate and dryland patches. Consequently,  $\tau_c^*$  is inversely proportional to  $D_i/D_{50}$ . The finding of a negative log-log linear correlation between  $D_i/D_{50}$  and  $\tau_c^*$  with an exponent of -1 is consistent with the equal mobility hypothesis (Parker and Klingeman, 1982; Parker et al., 1982) where critical shear stress is independent of particle size (Section 2.1). Although the intercept of the log-log linear relationship between  $D_i/D_{50}$  and  $\tau_c^*$  ( $\alpha_0$ ) was lower for H<sub>2</sub> ( $\alpha_0 = -0.96$ ) compared to the other patches ( $-0.78 \leq \alpha_0 \leq -0.67$ ), values of the dimensionless critical shear stress are not sufficiently lower to significantly skew the distribution of  $\tau_c^*$  (Figure 4.16b). The relative mobility of different grain sizes is, therefore, broadly comparable between the humid temperate and dryland patches despite differences in hiding effects (e.g. grain protrusion; Section 4.10), pivoting angle and factors including the structure and packing of sediment (Sections 4.2-9).



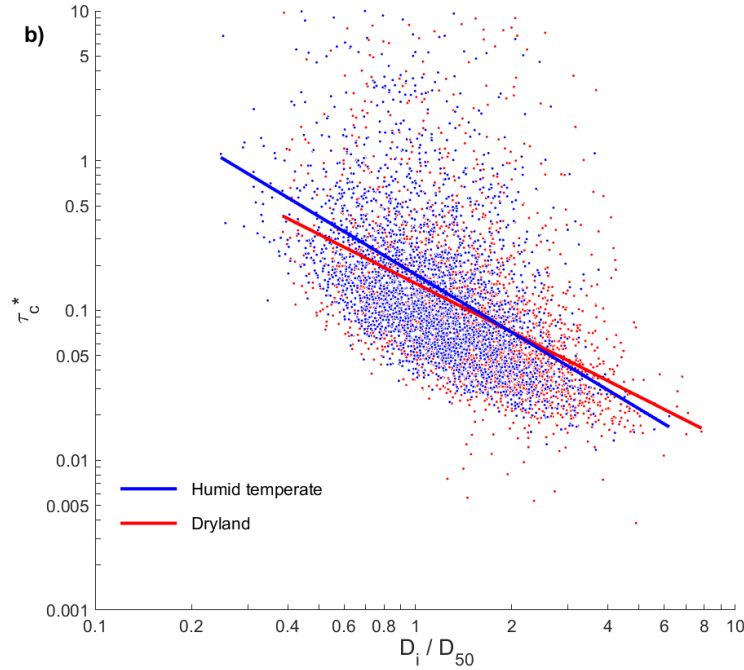


Figure 4.17 Relationship between relative grain size and dimensionless critical shear stress for the humid temperate (blue symbols) and dryland patches (red symbols) estimated by the grain entrainment model for a) individual patches and b) regime-aggregated data. Lines of best fit determined using least squares regression - in b) humid temperate:  $\ln(\tau_c^*) = -0.76(\pm 0.02) - 1.32(\pm 0.09) \cdot \ln(D_i/D_{50})$  and dryland:  $\ln(\tau_c^*) = -0.83(\pm 0.02) - 1.05(\pm 0.08) \cdot \ln(D_i/D_{50})$ .

## 4.12. Discussion

This chapter seeks to broaden our understanding of the structural characteristics of coarse-grained alluvial streambeds. This was achieved by applying a suite of geostatistical analyses to a range of gravel-bed surfaces sampled from rivers within perennial and ephemeral flow regimes. In addition, the effect of bed surface structure on bed stability was assessed using estimates of dimensionless critical shear stress derived from a force balance model of particle entrainment.

### 4.12.1. Structural characteristics of coarse-grained alluvial channels

The structural characteristics of streams subject to a perennial flow regime were assessed using eight gravel patches sampled from four UK rivers. The humid temperate gravel patches

exhibited a range of bed material sizes ( $18 \leq D_{50} \leq 78$  mm), sorting ( $1.6 \leq \sigma_G \leq 2.4$ ) and shapes ( $0.56 \leq \bar{\psi} \leq 0.71$ ) with differences in shape reflecting the different lithologies of the catchments (either limestone  $\bar{\psi} = 0.71$  or gritstone  $0.56 \leq \bar{\psi} \leq 0.61$ ). The structural characteristics of the humid temperate patches were compared against three, dryland gravel patches sampled from two Israeli rivers which are governed by an ephemeral flow regime. In this study, the dryland patches were composed of limestone and were characterised by a smaller surface grain size ( $19 \leq D_{50} \leq 39$  mm), poorer sorting of bed material ( $2.4 \leq \sigma_G \leq 2.8$ ) and broadly comparable particle shape ( $0.67 \leq \bar{\psi} \leq 0.70$ ) relative to the humid temperate limestone patches.

On inspection of the measured DTMs, the bed topography of all 11 gravel patches can be evaluated at two spatial scales: at the grain-scale and the meso-scale. The former describes the structure associated with individual particles and collections of grains (e.g. imbrication; cluster microforms) while the latter relates to extended patches of higher and lower bed elevation. At the grain-scale, the humid temperate patches were characterised by a coarse surface armour which largely comprised tightly packed and imbricated particles. Coarse surface grains tend to act as anchors in trapping finer sediment within cluster microforms. These depositional features are common to coarse-grained streambeds subject to perennial flows (e.g. Brayshaw, 1984; Hendrick et al., 2010) and, as discussed in Subsection 2.2.2, provide an important control in regulating bedload flux by sheltering a local neighbourhood of unclustered grains (Booth et al., 2014; Masteller and Finnegan, 2017). From a crude visual inspection of the DTMs, particle shape appeared to moderate the geometry of cluster microforms within the humid temperate patches. For instance, cluster microforms within the humid temperate gritstone patches were typically condensed into tighter, streamwise-aligned packing arrangements compared to the looser organisation of clustered grains for the humid temperate limestone patches. While Gomez (1994) observed particle shape to also affect streambed structure, the packing arrangement of surface grains appeared visually comparable between the humid temperate gritstone and humid temperate limestone patches. However, not all humid temperate patches exhibited a tightly packed armour. The  $M_1$  patch demonstrated with a looser arrangement of surface grains. This gave the impression of a poorly organised surface characterised by a relatively planar bed topography. On inspection, the dryland DTMs were similarly characterised by a relatively smooth topography in which

coarse gravels were embedded within finer sandy-granule sized material. Coarse surface grains emerged above the local surface and trapped small-to-medium sized material on their stoss side. These anchor clasts were commonly associated with downstream scour holes which extended up to c.50 mm below the mean bed level. Previous workers have noted similar patterns of scour within coarse- and fine-grained alluvial streambeds subject to ephemeral flows (Hooke and Mant, 2000; Powell et al., 2006; Storz-Peretz and Laronne, 2013). Since these regions of scour replaced the downstream wakes of bedforms, any cluster microforms that are present within the dryland patches were largely ‘incomplete’ (cf. Billi, 1987). The presence of incomplete bedforms across the dryland patches and lack of comparable features within the humid temperate patches is explained by the high rates of bedload flux, and associated scour and fill processes, during ephemeral flows (Reid and Laronne, 1995) and the short receding limb of ephemeral hydrographs which limits the opportunity for the development of bedforms (Wittenberg and Newson, 2005; Wittenberg et al., 2007).

At the meso-scale, the humid temperate gravel patches were typically characterised by extended patches of higher and lower elevations which tended to fluctuate 50–100 mm about the mean bed level. These larger topographic continuities have been observed in the laboratory (Marion et al., 2003; Cooper and Tait, 2009; Powell et al., 2016) and the field (Hodge et al., 2009b) and develop during extended phases of competent flow. By way of contrast, the  $M_1$  patch and dryland patches were devoid of meso-scale structure and inhabited only by grain-scale fluctuations in topography.

The qualitative DTM analysis described above is, however, subjective and requires verification by more objective quantitative analysis. In this regard, the structure of the gravel patches was first considered in terms of the distribution of bed elevations. In this study, the bed elevation pdfs for all the gravel patches were broadly similar and closely approximated a normal distribution. This was consistent with the findings of previous workers for gravel patches sampled from water-worked streambeds in flume- and field-based studies (Nikora et al., 1998; Smart et al., 2004; Aberle and Nikora, 2006; Cooper and Tait, 2009; Hodge et al., 2009b). The standard deviation of the bed elevation pdf,  $\sigma_z$ , was found to increase with  $D_{50}$  (Figure 4.5a) demonstrating a dependency between surface grain size and patch roughness

that has been observed by previous workers (e.g. Heritage and Milan, 2009; Hodge et al., 2009b; Brasington et al., 2012). In doing so, the finer surface grain size of the M<sub>1</sub> patch can explain the comparatively small range in bed elevations about the mean and narrow standard deviation of the bed elevation pdf relative to the other gravel patches. The finding that a single, positive linear correlation between  $\sigma_z$  and  $D_{50}$  applies across the humid temperate and dryland patches aligns with previous workers who have observed a similar, statistically significant relationship for gravel patches subject to perennial (Brasington et al., 2012) and ephemeral flows (Storz-Peretz and Laronne, 2013). Meanwhile,  $\bar{\psi}$  and  $\sigma_G$  were not found to exert significant influence on  $\sigma_z$  for all 11 patches (Figures 4.5d and 4.5g respectively) which is contrary to the assertions of previous workers that the shape and sorting of bed material will moderate grain packing arrangements and patch-averaged surface roughness; for example, a coarse-grained streambed comprised of platy, bladed sediment would be expected to display a greater tendency to imbricate and to generate a more tightly packed and topographically smoother bed than one comprising comparatively more rounded, spheroidal grains (Church et al., 1987; Gomez, 1994).

The form of the bed elevation distribution was also quantified through two additional statistical moments -  $Sk_z$  and  $Ku_z^*$  - which describe the asymmetry and tailedness and peakedness of the pdf respectively. In this study, the bed elevation pdfs were sufficiently positively skewed ( $Sk_z > 0$ ) and peaked (leptokurtic,  $Ku_z^* > 0$ ) to reject a strictly normal form. As Figure 4.18 demonstrates, these observations conform to the findings of previous workers for armoured gravel beds in natural and artificial environments (Nikora et al., 1998; Aberle and Nikora, 2006; Cooper and Tait, 2009; Curran and Waters, 2014) and are sufficiently distinct from artificial screeded gravel mixtures (i.e. where  $Sk_z < 0$ ; Coleman et al., 2011). Although  $Sk_z$  was broadly comparable between all 11 gravel patches,  $Ku_z^*$  tended to be higher for the dryland patches and toward the upper range of previous observations. The significant linear relationship between  $Ku_z^*$  and  $\sigma_G$  (Figure 4.5f) suggests this difference can be explained by the greater presence of fines within the dryland patches which infills surface pockets and leads to a reduction in elevations about the mean bed level (Coleman et al., 2011; Barzilai et al., 2013).

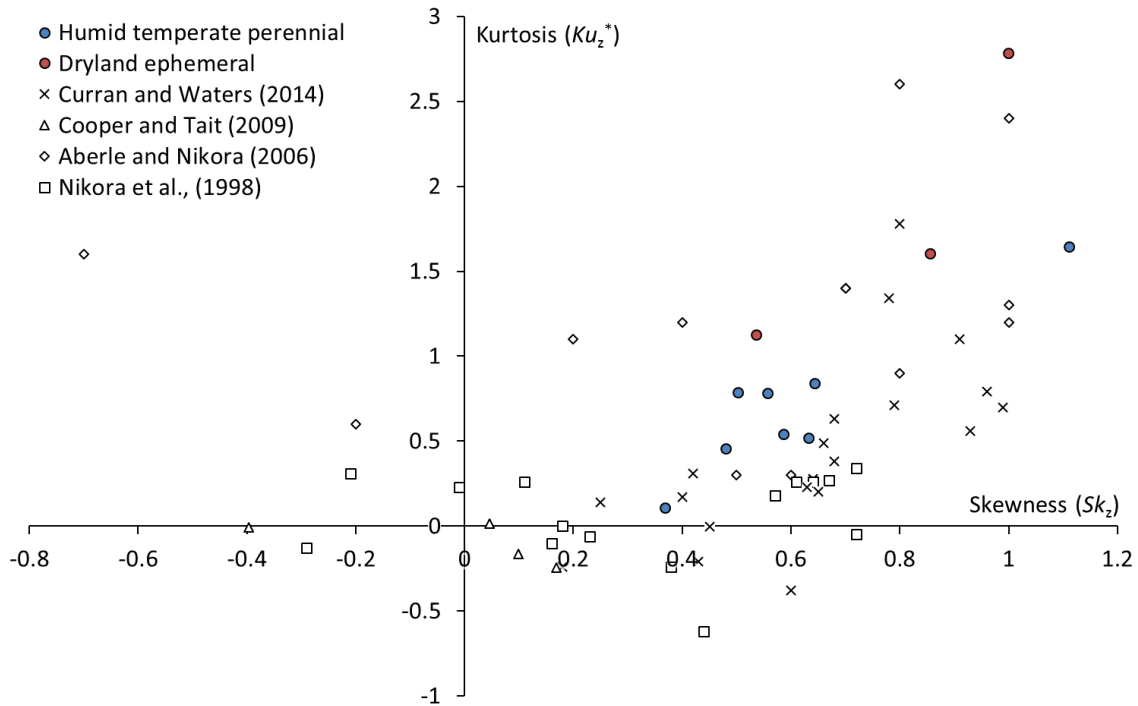


Figure 4.18 Relationship between  $Sk_z$  and  $Ku_z^*$  for the humid temperate (blue) and dryland (red) patches, plotted in relation to previous observations.

Variograms were used to provide a further view on the roughness properties and scaling characteristics of the gravel patches. For this study, the analysis first took of the form of the visual inspection of 2D variogram surfaces and the ratio of flow transverse to flow parallel standardised semivariance before moving onto the qualitative assessment of 1D variograms. On inspection of the 2D variograms, the surfaces were characterised at three scales: at the scale of grain surfaces, of individual grains and larger, meso-scale topographic elements. At subgrain- and grain-scales ( $0 < \tilde{h}_x < 3$ ), isopleth contours followed a circular pattern for all 11 gravel patches which reflects surface isotropy and no discernible preference in the orientation of surface grains for all patches considered in this study. Interestingly, the ratio of flow transverse to flow parallel standardised semivariance found the surfaces were not as isotropic as the 2D variograms suggested and that the magnitude of any smaller-scale anisotropy may be too subtle to be clearly identified from visual inspection. By way of comparison, previous workers (e.g. Hodge et al., 2009b) have similarly observed surface isotropy for the smallest lags and suggested this feature originates from noise within high resolution topographic datasets. In contrast to this study, earlier work has often observed the 2D variograms of coarse-grained water worked surfaces to exhibit elliptical contours at grain-

scales (e.g. Marion et al., 2003; Cooper and Tait, 2009; Mao et al., 2011). This indicates grain-scale surface anisotropy and was attributed to the preferential orientation of the a-axis of grains to align in a flow parallel direction (Nikora and Walsh, 2004; Aberle and Nikora, 2006; Hodge et al., 2009b; Mohajeri et al., 2015; Powell et al., 2016) and, on occasion, a flow transverse direction (Hodge et al., 2009b). Several workers have also observed a tendency for the shape of grain-scale contours to reflect particle shape, e.g. more elliptical for surfaces comprising bladed grains compared to those comprised of more rounded grains (e.g. Hodge et al., 2009b). However, in this study the pattern of grain-scale contouring was broadly comparable between the humid temperate gritstone and humid temperate limestone patches.

Over longer lags ( $3 < \widetilde{h}_x < 10$ ), the humid temperate gritstone 2D variograms were largely characterised by elliptical contours. This reflected surface anisotropy and demonstrated the flow alignment of larger-scale sedimentary structure. The figures of the ratio of flow parallel to flow transverse standardised semivariance also illustrated this shift in the organisation of grain and larger scales of structure. However, these changes were not systematic and at the largest scales considered ( $\widetilde{h}_x = 10$ ) the ratio was found to range between  $0.65 \leq \widetilde{\gamma}_x / \widetilde{\gamma}_y \leq 1.15$ . Meanwhile, the 2D variogram surfaces for the humid temperate and dryland limestone patches were characterised by broadly circular contours and the ratio of flow parallel to flow transverse standardised semivariance was close to unity over the full range of lags ( $\widetilde{\gamma}_x / \widetilde{\gamma}_y \approx 0.9$  for  $0.5 < \widetilde{h}_{x,y} < 10$ ). This indicates surface isotropy and a lack of alignment in larger-scale bed topography that is potentially, in part, mediated by particle shape. Inspection of the 2D variograms also identified differences in the magnitude of surface roughness. For example, the rate of increase in standardised semivariance with normalised lags was comparatively lower for the M<sub>1</sub> humid temperate patch and the three dryland patches than the humid temperate gritstone patches which reflects a smoother bed topography, as highlighted from the visual assessment of DTMs.

The qualitative analysis of 2D variogram surfaces was assisted by the inspection of 1D variograms extracted in flow parallel and flow transverse directions. The 1D variograms for all 11 patches were characterised by a curved form in log-log space which rejected the single fractal model of Nikora et al. (1998) owing to the systematic pattern of residuals around the

joints. The curvature in the 1D variograms indicated the presence of multiple scales of roughness, i.e. multifractal behaviour, and was an artefact of high resolution, 2½D datasets. For instance, the more recent work of Hodge et al. (2009b) recorded a similar curved form in their 1D variograms while older researchers used lower resolution bed profiles to inform log-log linear variogram models (e.g. Nikora et al., 1998). For the majority of humid temperate patches, the start of the apex of curvature of the 1D variograms occurred at  $\widetilde{h}_x \approx 1$  which was thought to reflect the large dependency of particle size on surface roughness. This feature was also evident for the 1D variograms (humid temperate facies) considered in Hodge et al. (2009b: 2033). In contrast, the start of the apex of curvature extended toward longer lags for the humid temperate M<sub>1</sub> and dryland patches. This suggests coarser clasts exert a greater influence on patch topography for these comparatively planar surfaces. In the majority of cases, the sill variance was attained over the range of lags considered which indicates the patch extents were sufficient to capture larger-scale sedimentary structure (Wang et al., 2011). Considering the humid temperate patches,  $\widetilde{\gamma}$  was typically greater for the limestone patches compared to the gritstone patches at the subgrain- and grain-scales ( $0 < \widetilde{h}_x < 3$ ). The roughness at the scale of individual grains and grain surfaces, therefore, tends to be greater for the more rounded limestone sediment. In addition, the sill variance appears to be attained at longer lags for the humid temperate gritstone patches for the flow parallel 1D variograms. Thus, the humid temperate gritstone patches exhibited larger meso-scale structure. A comparison between the limestone patches from both flow regimes reveals  $\widetilde{\gamma}_x$  was greater with  $\widetilde{h}_x$  for the humid temperate patches at the grain-scales which reflects the topographically smoother dryland patches. Furthermore, the sill variance was attained at shorter lengths for the dryland patches compared to the humid temperate patches which reflects the lack of dryland meso-scale topography.

The inclination index and slope-aspect analyses provided a final insight into the characteristics of ephemeral and perennial streambed topography. As the parameters *I* and *S* were calculated over the length of 9 mm and an area of 9 mm<sup>2</sup> respectively, these metrics describe the grain-scale properties of the gravel patches. The humid temperate and dryland patches were typically inhabited by a greater proportion of upstream facing cells than downstream facing cells and consequently the inclination index is negative. The tendency for grains to face in an upstream direction is consistent with grain imbrication and as values of *I*

are broadly comparable between the humid temperate gritstone and humid temperate limestone patches ( $-0.094 \leq I \leq 0.039$  and  $-0.039 \leq I \leq -0.015$  respectively; Figure 4.10) grain shape does not moderate particle imbrication. Furthermore, since the inclination index is broadly comparable for the humid temperate limestone and dryland limestone patches ( $-0.039 \leq I \leq -0.015$  and  $-0.051 \leq I \leq -0.004$  respectively), the extent of grain imbrication does not appear to substantially vary between the two flow regimes. Values of the inclination index recorded across all 11 patches ( $-0.094 \leq I \leq 0.039$ ) are comparatively higher than the observations of previous workers (e.g.  $-0.180 \leq I \leq -0.052$ ; Millane et al., 2006) which may reflect the use of coarser DTMs, and a wider spatial length over which  $I$  is calculated in this study.

The distributions of slope provide an indicator of grain packing arrangement. In this regard, it might be expected that streambeds comprised of bladed grains will show a greater tendency to imbricate, generate a topographically smoother surface and display a greater proportion of shallower slopes compared to patches composed of more rounded grains. However, the distributions of slope were broadly comparable between the humid temperate patches from different lithologies and exhibit a positive skew and modal slopes of  $14 \leq S_{50} \leq 25^\circ$  (Figure 4.11a). A consistency in grain-scale structure between the humid temperate and dryland patches was also evident through a comparison of the distributions of slope (Figure 4.11b). By contrast, the distribution of slope for the M<sub>1</sub> patch was highly peaked and characterised by a greater proportion of shallower slopes ( $S_{50} = 13^\circ$ ). This is consistent with the smaller surface grain size and reflects a comparatively smoother surface. Previous workers have often recorded a broader distribution of slopes with a greater proportion of steeper slopes than found in this study (e.g.  $25 \leq S_{50} \leq 50^\circ$ ; Hodge et al., 2009b). These differences between slope distributions cannot be explained by an increase in grain-scale surface roughness, since surface grain size is comparable ( $18 \leq D_{50} \leq 63$  mm; Hodge et al., 2009b), and is more likely attributed to the use of smaller experimental patches (1 m<sup>2</sup>) and an associated increase in the incidence angle of the TLS sensor. Combined with a further increase in the resolution of surface measurements (e.g. 0.002 m sampling resolution - Hodge et al., 2009b; Table 3.1), this increases the frequency of laser pulses reaching the deep interstices between grains and, in doing so, generates a more detailed, rougher DTM inhabited by steeper slopes. While these

differences in the distribution of local slopes may appear significant, the quality of the DTMs produced in this study and by Hodge et al. (2009b) are broadly comparable.

The combined distributions of slope and aspect further illustrate grain-scale structure. Following the inclination index, particle imbrication is demonstrated for all 11 gravel patches by a greater density of cells facing in an upstream direction compared to a downstream direction (Millane et al., 2006). In this study, the density patterns within the polar plots of combined slope and aspect were broadly comparable between the humid temperate gritstone and humid temperate limestone patches (Figures 4.12a-f and 4.12g-h respectively) although the qualitative analysis identifies the contrastingly smooth grain-scale topography of the M<sub>1</sub> patch (where slopes were confined within a narrow range,  $S_{50} < 30^\circ$ ; Figure 4.12e). Since no discrete lines of symmetry were observed across the humid temperate polar plots, no preference in the alignment of the a-axis of individual grains was identified between the different lithologies. Previous workers have, by contrast, found the number of lines of symmetry was a function of particle shape. For example, Hodge et al. (2009b) observed the density patterns of combined slope and aspect were characterised by a single line of symmetry for the bladed, River Feshie facies compared to the two lines of symmetry (suggesting flow-transverse a-axis alignment) for comparatively more rounded facies from Bury Green Brook. Meanwhile, the polar plots of combined slope and aspect for the dryland patches (Figure 4.12i-k) exhibit density patterns that are broadly comparable to their humid temperate counterparts. This suggests the structure at the scale of individual grain surfaces is largely similar across the gravel patches subject to perennial and ephemeral flow regimes.

#### **4.12.2. The influence of structure on bed stability**

While few previous workers have sought to relate metrics of bed surface structure with estimates of particle stability, in this study the stability of the bed was characterised using three parameters - pivoting angle ( $\Phi$ ) and two components which define grain protrusion, projection ( $p$ ) and exposure ( $e$ ) – for two humid temperate ( $W_{1.1}$  and  $W_{1.2}$ ) and three dryland patches ( $H_1$ ,  $H_2$  and  $S_1$ ). The first of these parameters,  $\Phi$ , describes the angle required to pivot and entrain a grain from its pocket within the surface. The peaked and negatively skewed distributions of  $\Phi$  for all five patches were found to reject the lognormal form that has

commonly been observed by previous workers (e.g. Johnston et al., 1998). This reflects the narrow range of high pivoting angles recorded in this study. A non-parametric Wilcoxon rank-sum test between regime-aggregated data revealed  $\Phi$  was significantly higher for the dryland patches ( $\Phi_{50} = 84^\circ$ ) compared to their humid temperate counterparts ( $\Phi_{50} = 73^\circ$ ). The increase in grain pivoting angle for the dryland patches is, in part, thought to be caused by the embedding of surface grains within a fine-grained clast-supported matrix (Buffington et al., 1992; Johnston et al., 1998). The narrower range of  $\Phi$  for the dryland patches and greater difference between distributions of  $\Phi$  for the humid temperate patches (Figure 4.13a) may also reflect differences in the size sorting of surface grains. However, while previous workers (e.g. Kirchner et al., 1990; Johnston et al., 1998) have observed poor sorting to narrow the range of  $\Phi$ , the presence of fines has also been found to reduce the depth of surface pockets and decrease  $\Phi$  (Johnston et al., 1998). Therefore, for the dryland patches, the complex interplay between particle sorting and embedding narrows the distribution of  $\Phi$  while ensuring values of  $\Phi$  were comparatively higher than the humid temperate patches.

The relationship between  $\Phi$  and  $D_i/D_{50}$  was examined for the humid temperate and dryland patches in Figures 4.13b and 4.13c respectively. For the humid temperate patches,  $\Phi$  tended to decrease with  $D_i/D_{50}$  which suggests a grain's pivoting angle was an inverse function of particle size. By contrast,  $\Phi$  was relatively consistent with  $D_i/D_{50}$  for the dryland patches which, following previous workers, is attributed to the embedding of surface grains reducing the  $D_i/D_{50}$  particle size effect (e.g. Pilgrim Creek; Johnston et al., 1998). The relationship between  $\Phi$  and  $D_i/D_{50}$  for all five gravel patches was characterised by a power law function  $\Phi = \alpha(D_i/D_{50})^{-\beta}$  (Miller and Byrne, 1966). A significant log-linear relationship between  $\Phi$  and  $D_i/D_{50}$  was rejected for the humid temperate patches owing to the large degree of scatter in  $\Phi$  with  $D_i/D_{50}$  which has similarly been observed by previous workers (Kirchner et al., 1990; Johnston et al., 1998; Hodge et al., 2013). By way of contrast, the power law function was fitted between  $\Phi$  and  $D_i/D_{50}$  for the dryland patches with a high degree of scatter ( $R^2 = 0.04-0.11$ ). The values of  $\alpha$  and  $\beta$  for the three dryland patches are presented in Table 4.3 along with the findings of previous workers. For the dryland patches,  $\alpha$  was typically higher ( $79 \leq \alpha \leq 86^\circ$ ) and  $\beta$  toward the lowermost limit of previous observations ( $0.06 \leq \beta \leq 0.19$ ). Therefore,  $\Phi$  was greater and higher values of  $\Phi$  were maintained with  $D_i/D_{50}$  for the dryland patches than found by previous workers. The most likely causes of this difference

was the greater embeddedness of grains within the dryland patches and the choice of a grid-based methodology that sampled all particles (e.g. Hodge et al., 2013), rather than an approach that relied on selecting surface grains that were readily ‘available’ (e.g. Johnston et al., 1998). However, given the relative lack of observations recorded by previous workers from natural beds or acknowledgement of local site factors (e.g. sampling from streams of different order), it is difficult to appreciate how grain pivoting angle varies with different locations in the continuum and, hence, fully contextualise these results.

Table 4.3 Summary of the power law coefficients recorded by previous workers from natural gravel streambeds. High  $R^2$  values recorded by Buffington et al. (1992) and Johnston et al. (1998) reflect the choice of sampling placed or ‘available’ grains rather than the grid-based (random) approach employed in this study and by Hodge et al. (2013).

Study	Patch info	$\Phi = \alpha(D_i/D_{50})^{-\beta}$		
		$\alpha$	$\beta$	$R^2$
<b>Buffington et al. (1992)</b>	Natural sediment, $D_{50} = 4.1\text{mm}$	60	0.26	0.99
	Natural sediment, $D_{50} = 11.4\text{mm}$	51	0.28	0.99
	Natural sediment, $D_{50} = 14.0\text{mm}$	54	0.21	0.91
	Natural sediment, $D_{50} = 14.5\text{mm}$	46	0.21	0.92
	Natural sediment, $D_{50} = 45.0\text{mm}$	52	0.24	0.93
<b>Johnston et al. (1998)</b>	Pacific Creek	61.9	0.28	0.94
	Van Duzen River	49.1	0.45	0.92
	Sagehen Creek	51.6	0.30	0.86
	Colorado River	55.5	0.14	0.98
<b>Hodge et al. (2013)</b>	Bury Green Brook (pool facies)	62		
	Bury Green Brook (pool exit)	83		
	Bury Green Brook (riffle)	76		
<b>Prancevic and Lamb (2015)</b>	Sespe Creek (Thalweg)	66.4	-0.01	
	Sespe Creek (Bar)	73.5	-0.01	
	Rose Valley Tributary	67.5	-0.01	
	Arroyo Seco	69.2	-0.01	
	Block Creek	69.9	0.18	
	San Oline Creek	67.7	0.18	
	Tumble Creek	64.3	0.18	
	Rattlesnake Creek	67.3	0.18	
<b>This study</b>	$W_{1.1}$	n/a	n/a	n/a
	$W_{1.2}$	n/a	n/a	n/a
	$H_1$	86.0	0.10	0.11
	$H_2$	78.9	0.19	0.06
	$S_1$	82.7	0.06	0.04

Note: The  $\alpha$  coefficient has been defined differently by previous workers, e.g. the mean (Hodge et al., 2013) and median pivoting angle of the median grain size (Buffington et al., 1992; Johnston et al., 1998; Prancevic and Lamb, 2015).

Particle stability was also quantified in terms of the projection ( $p$ ) and exposure ( $e$ ) of individual surface grains relative to the local bed level. In this study, the projection of grains for all five gravel patches increased with exposure which stands in agreement with the findings of Kirchner et al. (1990) and Hodge et al. (2013). Values of projection and exposure normalised by particle diameter ( $p/D$  and  $e/D$  respectively) were significantly greater for the regime-aggregated data from the dryland patches ( $\overline{p/D} = 0.34$ ,  $e/D_{.50} = 0.007$ ) compared to their humid temperate counterparts ( $\overline{p/D} = 0.27$ ,  $e/D_{.50} = 0$ ). This indicates surface grains residing within the dryland patches project further and were more exposed to the flow than similarly sized grains in the humid temperate patches. The observed differences in  $p/D$  and  $e/D$  are attributed to the smoother (poorly sorted) dryland patch topography. Previous workers have, by contrast, found the draping of the surface from fines to reduce grain protrusion (e.g. Sambrook Smith and Nicholas, 2005; Johnson and Whipple, 2007).

Bed stability was estimated using the grain entrainment model of Hodge et al. (2013) by predicting critical shear stress ( $\tau_c$ ) and dimensionless critical shear stress ( $\tau_c^*$ ). Values of  $\tau_c$  were largely dependent on surface grain size and explained differences between the humid temperate and dryland patches ( $\tau_{c,.50} = 122$  and  $52$  Pa respectively). Accounting for this grain size dependency, modelled values of  $\tau_c^*$  were significantly higher for humid temperate patches compared to the dryland patches ( $\tau_{c^*,.50} = 0.11$  and  $0.08$  respectively). Therefore, for the limited sample of sites, the humid temperate patches were comparatively more stable than their dryland counterparts which, following the observations of previous workers, can be attributed to several factors including the development of grain-scale structure (e.g. imbricated bed packing arrangement, cluster microforms) during competent and conditioning flows (Hassan and Reid, 1990; Clifford et al., 1992; Powell and Ashworth, 1995; Measures and Tait, 2008; Hodge et al., 2013; Masteller and Finnegan, 2017). The stability driven by the water-working of the humid temperate patches was sufficient to supersede the effects of particle embedding within the dryland patches which previous workers have observed generates an infilled bed structure that increases bed cohesion and entrainment thresholds (Reid et al., 1985; Reid and Hassan, 1992; Powell et al., 2001; Wilcock, 2001; Haynes and Pender, 2007; Barzilai et al., 2013).

While the humid temperate and dryland patches exhibit different characteristics in the structure of streambed material,  $\tau_c^*$  is negatively correlated with  $D_i/D_{50}$  for all five patches which ensures  $\tau_c$  shows little variation with grain size as predicted by the equal mobility hypothesis (Parker and Klingeman, 1982; Parker et al., 1982). A condition of equal mobility was also predicted for the pool, pool exit and riffle facies considered in Hodge et al. (2013). Despite the use of a neutral lift force multiplier within the grain entrainment model (i.e.  $m = 1$ , representing an un-mortared bed condition), estimates of  $\tau_c^*$  extended toward the uppermost limit of previous observations ( $0.005 \leq \tau_c^* \leq 0.096$ ; Buffington and Montgomery, 1997). This was thought to reflect the choice of coarser, potentially more stable, surface grains to drive the physically-based entrainment model. As a consequence, the mobility of smaller surface grains may be under-represented within the model which could explain the possible overestimation of values of  $\tau_c$  and  $\tau_c^*$ .

#### 4.12.3. Summary

The structure of eight humid temperate and three dryland gravel patches was evaluated using a suite of statistical techniques. The results of the statistical analysis, described through sections 4.2–11 and discussed in subsections 4.12.1-2, are summarised in Table 4.4 and quantify the variability in the structural parameters that might be seen in natural environments. These field results were compared with the observations of previous workers that have been largely derived from the laboratory.

The humid temperate gravel patches were generally comprised of a coarse, tightly packed armour in which surface grains imbricated into observable cluster bedforms (see also Brayshaw, 1984; Hendrick et al., 2010). At larger scales, the surfaces were typically characterised by a meso-scale topography that took the form of extended patches of higher and lower bed elevations. Following statistical analysis, the distribution of bed elevations for the humid temperate patches were found to adhere to a near-normal form (Aberle and Nikora, 2006),  $\sigma_z$  was statistically dependent on  $D_{50}$  (Heritage and Milan, 2009; Brasington et al., 2012) and values of  $Sk_z$  and  $Ku_z^*$  conformed to the observations for structured surfaces (Coleman et al., 2011). In addition, the curved, multifractal form of the 1D variograms was similarly observed by Hodge et al. (2009b) who used a broadly identical approach to collect

and analyse high resolution surface datasets. The choice of humid temperate patches from different lithologies and local geomorphic settings was designed to showcase the potential variability of perennial streambed structure which has largely been unaccounted for by previous research. While several workers have suggested that a gravel bed comprised of platy, bladed sediment will display a greater tendency to imbricate and tightly pack into a topographically smoother surface than one comprising of comparatively more rounded, spheroidal grains (e.g. Church et al., 1987; Gomez, 1994), this study recorded few differences in grain-scale structure between the humid temperate gritstone and humid temperate limestone patches and structural metrics (e.g.  $\sigma_z$ ,  $I$ ,  $S_{50}$ ,  $S_{k_s}$ ) were not a strict function of grain shape (i.e.  $\psi$ ). At larger scales, however, there is some evidence of slight differences in bedform-scale structure for the humid temperate patches from different lithologies. For instance, the ratio of flow transverse to flow parallel standardised semivariance was more variable within the range  $3 < \tilde{h}_x < 10$  for the humid temperate gritstone patches ( $0.65 \leq \tilde{\gamma}_x/\tilde{\gamma}_y \leq 1.15$ ) compared to their humid temperate limestone counterparts ( $\tilde{\gamma}_x/\tilde{\gamma}_y \approx 0.9$ ). This suggests larger scales of structure generated within beds comprised of bladed, gritstone grains assemble into a greater variety of forms compared to beds comprised of more rounded, limestone grains. Particle shape, therefore, appears to moderate larger scales of sedimentary structure. The potential variability in humid temperate streambed structure was also demonstrated for patches sampled from different geomorphic settings. This was most notably demonstrated by the M<sub>1</sub> patch which comprised relatively fine gravels and that, on inspection, appeared structurally quite different from the other humid temperate patches. This contrasting patch structure was highlighted through the analysis of DTMs, bed elevation pdfs (narrow, peaked distribution), variograms (lower  $\tilde{\gamma}$  with  $\tilde{h}$ ) and polar plots of combined slope-aspect (narrow, peaked distribution of shallow slopes). In this study, therefore, differences in humid temperate streambed structure generated by local geomorphic setting were, in general, more distinct than those generated from differences in particle shape.

The dryland patches were, in contrast to their humid temperate counterparts, characterised by a finer-grained, infilled bed structure. These comparatively planar surfaces were punctuated by coarse, emergent obstacle clasts and downstream scoured wakes. In addition, the dryland patch topography was limited to grain-scale topographies and devoid of the meso-scale topography found for the majority of humid temperate patches. The contrasts in bed

structure from the humid temperate patches were highlighted by the analysis of bed elevation pdfs (narrower, peaked distribution), the statistical moment  $Ku_z^*$  (higher for the dryland patches) and variograms. With regards to the latter, the contrastingly smooth grain-scale topography was demonstrated by lower  $\tilde{\gamma}$  with  $\tilde{h}$  and the lack of meso-scale topography by the attainment of a sill at shorter lags compared to the humid temperate limestone patches. Notwithstanding these highlighted differences, there were several similarities in the statistical characteristics between the humid temperate and dryland patches. For instance, the bed elevation pdfs for the dryland patches were also characterised by a positively skewed, near-normal form that was statistically different from those exhibited by unstructured surfaces, e.g. artificial screeded beds. Similarly, the standard deviation of bed elevations was a function of median particle diameter (see Storz-Peretz and Laronne, 2013) and the local metrics of inclination, slope and aspect were indistinct between the humid temperate and dryland patches. Thus, the dryland patches exhibited a water-worked bed structure that, for several of the statistical parameters could be distinguished from their humid temperate counterparts.

Table 4.4 Summary of the sedimentological and structural characteristics for the humid temperate and dryland patches.

Metric		Humid temperate	Dryland	
Sedimentology	Size	$18 \leq D_{50} \leq 78$ mm	$19 \leq D_{50} \leq 39$ mm	
	Shape	$1.6 \leq \sigma_G \leq 2.4$	$2.4 \leq \sigma_G \leq 2.8$	
	Sorting	$0.56 \leq \bar{\psi} \leq 0.71$	$0.67 \leq \bar{\psi} \leq 0.70$	
Structure	DTM	Grain	Coarse armour comprising imbricated, tightly packed grains. Cluster microforms present *	Fine-grained surface, punctuated by coarse, emergent clasts with scoured wakes, <50 mm below mean bed level
		Meso	Extended patches of higher and lower bed elevations *	n/a
	pdf	$\sigma_z$	$10.9 \leq \sigma_z \leq 32.9$	$15.0 \leq \sigma_z \leq 17.3$
		$Sk_z$	$0.37 \leq Sk_z \leq 1.08$	$0.49 \leq Sk_z \leq 0.89$
		$Ku_z^*$	$0.10 \leq Ku_z^* \leq 1.46$	$1.31 \leq Ku_z^* \leq 2.27$
	Variogram	1D and 2D approaches	Curved form with apex of curvature c. $D_{50}$ . Sill attained at limit of meso-scale roughness. Anisotropy observed across all scales (gritstone > limestone)	Curved form with apex of curvature > $D_{50}$ . Sill attained at limit of grain-scale roughness. Anisotropy observed across all scales.
	Inclination		$-0.094 \leq I \leq 0.039$	$-0.051 \leq I \leq -0.004$
	Slope		Positively skewed distribution, $14 \leq S_{50} \leq 25^\circ$ *	
Slope-Aspect		Greater proportion of upstream facing cells, highly variable density of cell aspect *		

\*The  $M_1$  patch was an exception to the described humid temperate norm.

The influence of streambed structure on particle stability was explored through three force balance parameters -  $\Phi$ ,  $p$  and  $e$  – and a grain entrainment model which estimated critical shear stress and dimensionless critical shear stress. The results of the bed stability analysis are summarised in Table 4.5. For the humid temperate patches, grain pivoting angle varied widely from pocket-to-pocket and patch-to-patch given the heterogeneity of the surfaces. The

projection and exposure of surface grains was, however, minimised from grain size sorting and the presence of bedforms which roughened the surface. By contrast, the dryland patches were characterised by an infilled bed structure in which the embedding of particles increased grain pivoting angle. The poor sorting of dryland sediment also reduced the range of pivoting angles, from pocket-to-pocket and patch-to-patch, although the infilling of interstices by fines did not lead to a decrease in pivoting angle. As a consequence, the complex interplay between particle sorting and embedding was, for the dryland patches, found to narrow the distribution of  $\Phi$  and increase values of  $\Phi$  beyond those recorded for the humid temperate patches. The contrastingly smooth dryland patch topography also increased grain protrusion sufficiently to exceed the effects of particle embedding (higher grain pivoting angles) and ensure particle stability was lower than the humid temperate patches. Despite the differences in bed stability, the humid temperate and dryland patches both exhibited an inverse log-log linear relationship between  $\tau_c^*$  and  $D_i/D_{50}$  which demonstrates a condition of equal mobility.

Table 4.5 Summary of the bed stability parameters for regime-aggregated data from the humid temperate and dryland patches. Error ranges represent 95% confidence intervals.

<b>Parameter</b>	<b>Humid temperate</b>	<b>Dryland</b>
<b>Pivoting angle (<math>\Phi_{50}</math>)</b>	73° ( $\pm 3^\circ$ )	84° ( $\pm 1^\circ$ )
<b>Grain projection (<math>\bar{p}/\bar{D}</math>)</b>	0.27 ( $\pm 0.03$ )	0.34 ( $\pm 0.02$ )
<b>Grain exposure (<math>e/D_{.50}</math>)</b>	0	0.007 ( $\pm 0.008$ )
<b>Critical shear stress (<math>\tau_{c.50}</math>)</b>	118 Pa ( $\pm 3$ Pa)	51 Pa ( $\pm 1$ Pa)
<b>Dimensionless critical shear stress (<math>\tau_c^*_{.50}</math>)</b>	0.11	0.08

The characteristics of humid temperate and dryland patches were derived from measurements gathered from single site surveys. This carries the implicit assumption that streambed structure does not vary over time and that surface measurements are representative of an unchanging, equilibrium form. To explore this further, Chapter 5 investigates the temporal dynamics of structure by assessing how quickly this condition develops from a disturbed state and whether structural conditions are maintained over competent flows.

## **Chapter 5 The temporal dynamics of sedimentary structure in coarse-grained alluvial river beds.**

### **5.1. Introduction**

This chapter explores the temporal dynamics of coarse-grained alluvial streambed structure over a series of competent flows. The chapter first investigates grain size adjustments and changes in bed character for the two humid temperate gravel patches on the River Wharfe ( $W_{1.1}$  and  $W_{1.2}$ ) over a 28-month period from November 2012 to April 2015 (Section 5.2). As Table 5.1 summaries and Figure 5.1 illustrates, the hydrograph sequence over this period is characterised by a variety of flows capable of submerging the patches and mobilising surface grains. ‘Competent flow’ is guided by repeated field site reconnaissance and defined as the minimum flow required to entrain particles from the  $W_{1.1}$  and  $W_{1.2}$  patches and local bar area. The diversity in streambed character observed over 13 repeat surveys is considered with respect to the between-site variations in structural characteristics described in Chapter 4. The temporal dynamics of streambed structure are then further studied in Section 5.3 by exploring how structure develops from a random bed condition; using three sub patches ( $W_{1.1A}$ ,  $W_{1.2A}$  and  $W_{1.1B}$ ) to characterise the short-term restructuring of the surface over a small collection of competent flows and two sub patches ( $W_{1.1A}$  and  $W_{1.2A}$ ) to characterise the longer-term development of structure over an extended series of sediment transporting events.

Table 5.1 Hydrograph statistics for the 28-month survey period from November 2012 to April 2015. Flow information supplied by the Environment Agency gauge station site at Netherside Hall (ID: 8276) where bankfull ( $= 130 \text{ m}^3 \text{ s}^{-1}$ ), moderate ( $100 - 130 \text{ m}^3 \text{ s}^{-1}$ ) and low, shoaling flows ( $< 100 \text{ m}^3 \text{ s}^{-1}$ ) are highlighted in red, orange and yellow respectively. Surveys S1 – S8 and S9 – S13 conducted using the HDS 3000/SS2 and P20 sensors respectively.

Repeat survey period (Sn, dd/mm/yr)	Peak discharge, $\hat{Q}$ ( $\text{m}^3 \text{ s}^{-1}$ )	Duration of competent flow, $T_{\text{comp}}$ (hrs)
<b>1</b>	<b>12/12/12</b>	
<b>2</b>	<b>17/02/13</b>	<b>158</b>
<b>3</b>	<b>10/06/13</b>	<b>89</b>
<b>4</b>	<b>21/08/13</b>	<b>108</b>
<b>5</b>	<b>18/09/13</b>	<b>66</b>
<b>6</b>	<b>16/10/13</b>	<b>47</b>
<b>7</b>	<b>06/11/13</b>	<b>139</b>
<b>8</b>	<b>04/02/14</b>	<b>114</b>
<b>9</b>	<b>18/11/14</b>	<b>129</b>
<b>10</b>	<b>02/12/14</b>	<b>67</b>
<b>11</b>	<b>12/02/15</b>	<b>162</b>
<b>12</b>	<b>05/03/15</b>	<b>101</b>
<b>13</b>	<b>15/04/15</b>	<b>109</b>

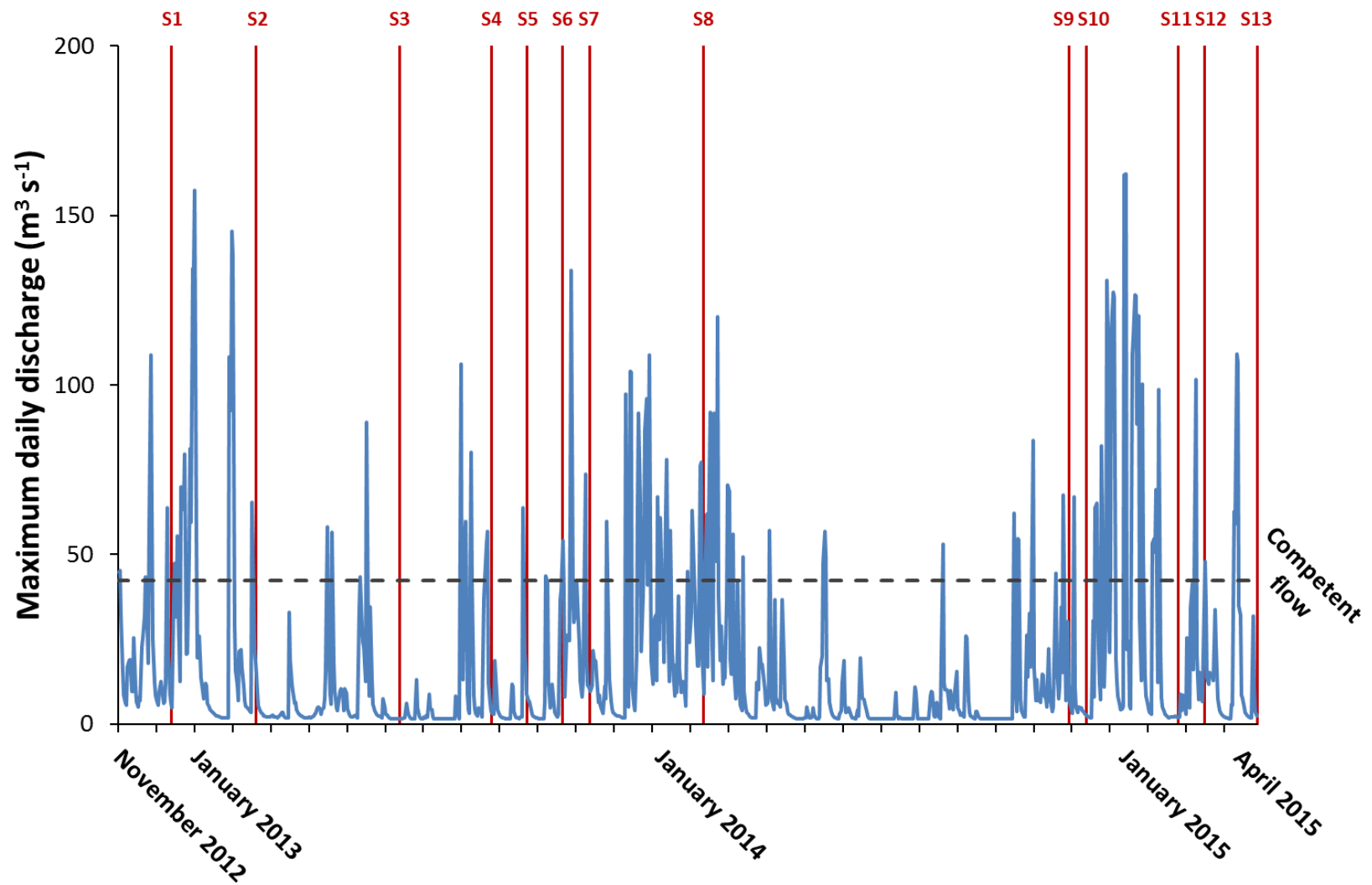


Figure 5.1 Hydrograph for the 28-month monitoring period between November 2012 and April 2015. Discharge data gathered from the EA Netherside Hall gauge station with repeat surveys (S1–S13) illustrated by the red vertical bars and text.

## 5.2. Temporal variability of streambed structure

The temporal variability of natural streambed structure was characterised for two humid temperate patches ( $W_{1.1}$  and  $W_{1.2}$ ) and sample periods, which contained 13 survey intervals, over a 28-month period between 12/12/12 and 15/04/15 ( $W_{1.1}$  S1-S13,  $W_{1.2}$  S7-S13). The patches were characterised using surface grain size (Subsection 5.2.1), DTMs (5.2.2), bed elevation pdfs and their statistical moments (5.2.3), 2D variogram surfaces and 1D variogram profiles (5.2.4) and local metrics of inclination index and slope (5.2.5).

### 5.2.1. Grain size adjustments

The adjustment in surface grain size is presented in Figure 5.2 in the form of cumulative grain size distributions and selected grain size percentiles ( $D_{16}$ ,  $D_{50}$  and  $D_{84}$ ). Regarding the former (Figures 5.2a and 5.2b), the cumulative grain size distributions over the monitoring period closely approximate one another which demonstrates no systematic changes in surface grain size occur during this period. Similarly, the surface grain size percentiles remain relatively constant ( $24.7 \leq D_{16} \leq 32.6$  mm,  $47.4 \leq D_{50} \leq 56.0$  mm,  $83.5 \leq D_{84} \leq 95.0$  mm; Figure 5.2c). The slight adjustments in  $D_{50}$  that occur over this period were unrelated to the magnitude or duration of competent flows following an acceptance of the null hypothesis of least square regression between absolute changes in  $D_{50}$  with  $\hat{Q}$  and  $T_{\text{comp}}$  ( $p > 0.05$ ).

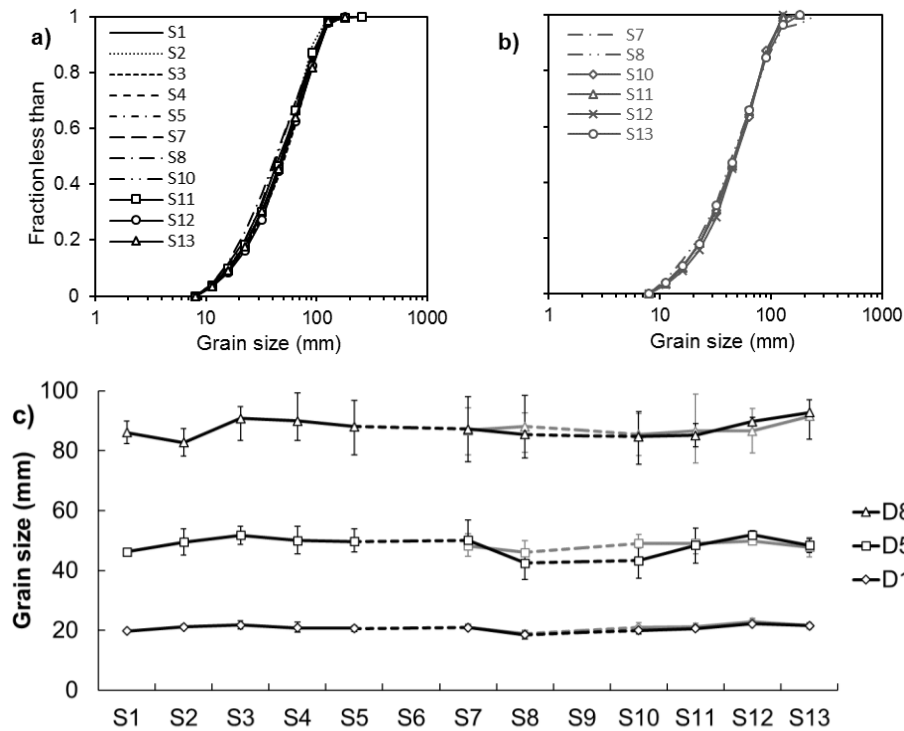
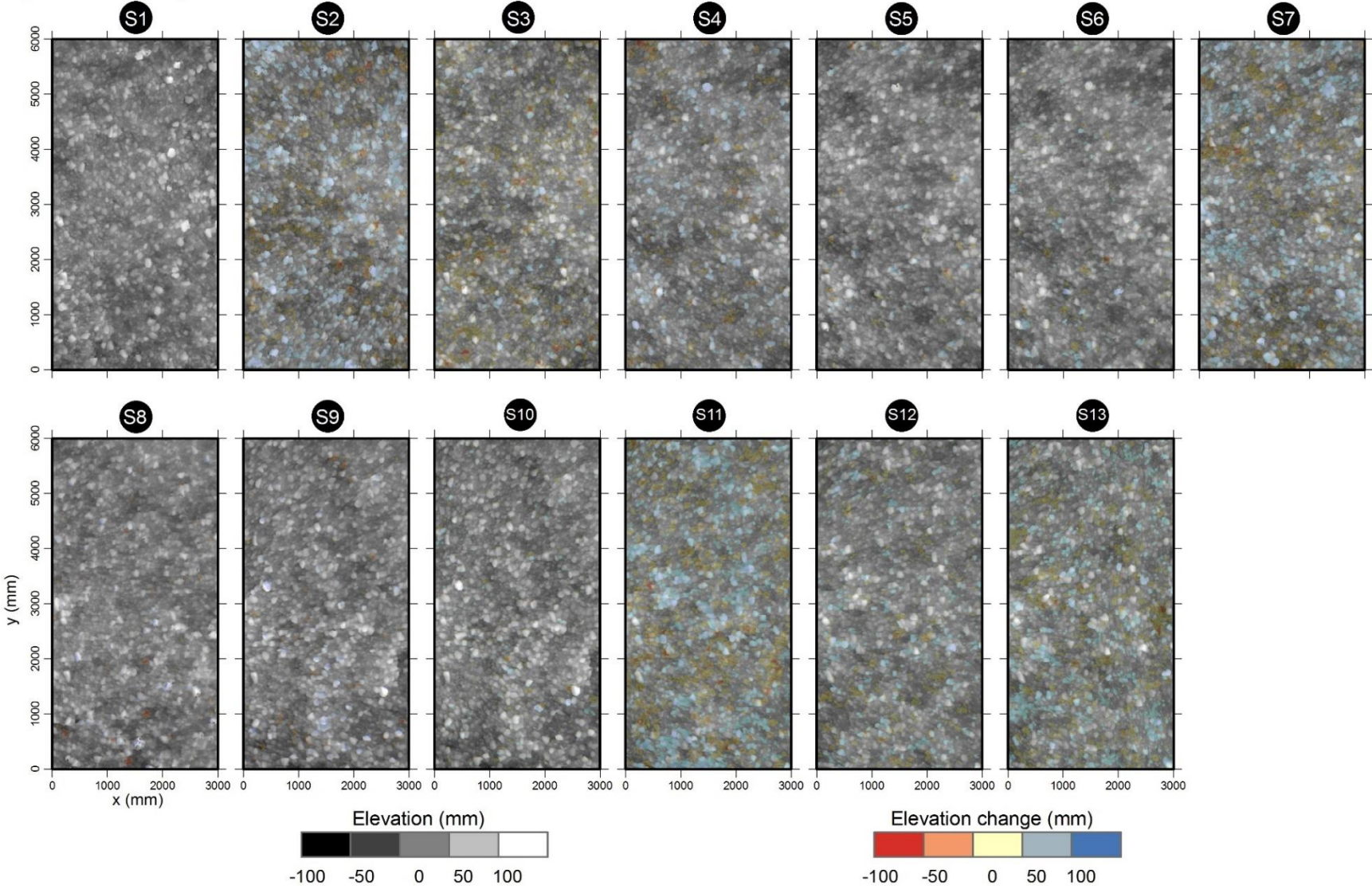


Figure 5.2 Cumulative grain size distributions for a)  $W_{1.1}$  and b)  $W_{1.2}$ . In a-c)  $W_{1.1}$  and  $W_{1.2}$  samples coloured in black and grey respectively. Digital grain size samples were not conducted for survey periods S6 and S9. In c) vertical error bars represent 95% confidence intervals.

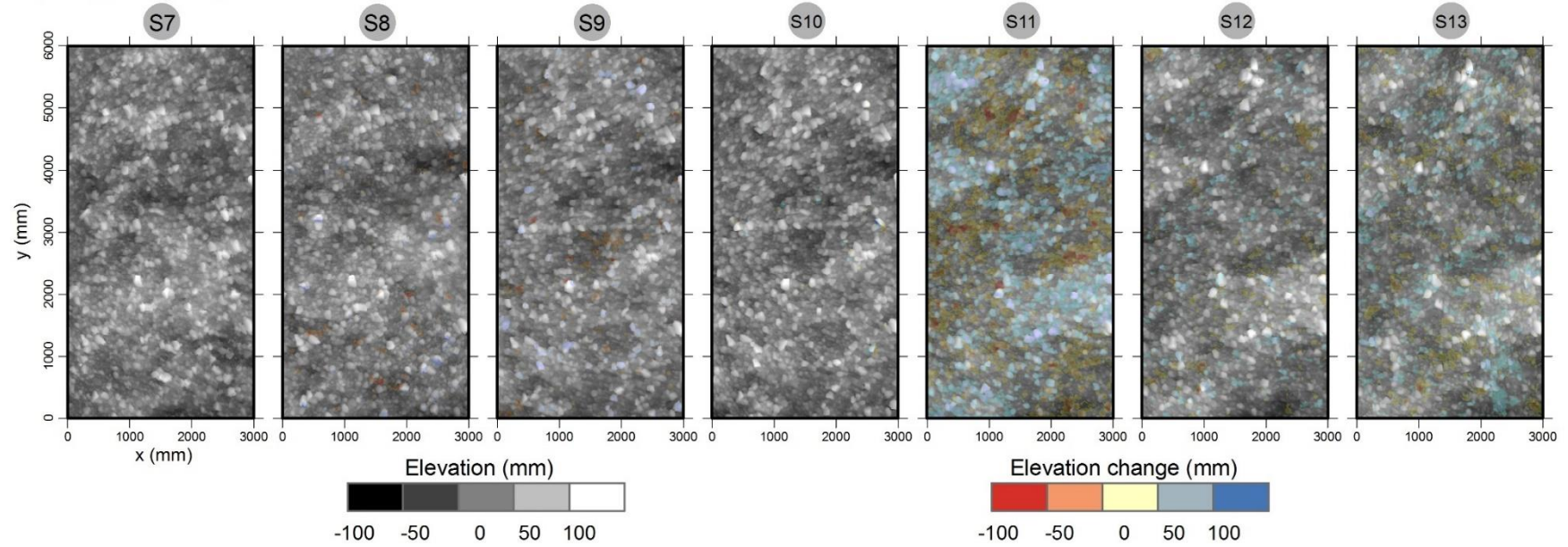
### 5.2.2. DTMs

The DTM series over the monitoring period are presented in Figures 5.3a and 5.3b for  $W_{1.1}$  and  $W_{1.2}$  respectively. As described in Section 4.3, the initial surfaces of  $W_{1.1}$  and  $W_{1.2}$  comprised an armoured layer of coarse, imbricated surface grains ( $D_{50} = 62$  mm) with randomly distributed cluster bedforms. At the meso-scale, the surfaces were characterised by extended patches of higher and lower bed elevations  $\pm 50$ – $100$  mm about the mean bed level. The greatest morphological changes (up to 150 mm vertically and 1000 mm horizontally) were associated with large flow events (e.g. S1-S2, S6-S7 and S10-S11; Figure 5.3a-d). In contrast, low flow events (e.g. S2-S3 and S4-S5; Figures 5.3a and 5.3c) generated minimal changes, e.g. only moving a few, least stable grains. This suggests only the highest flows are sufficiently capable to generate larger-scale changes in streambed topography while low flows are limited to grain-scale modifications.

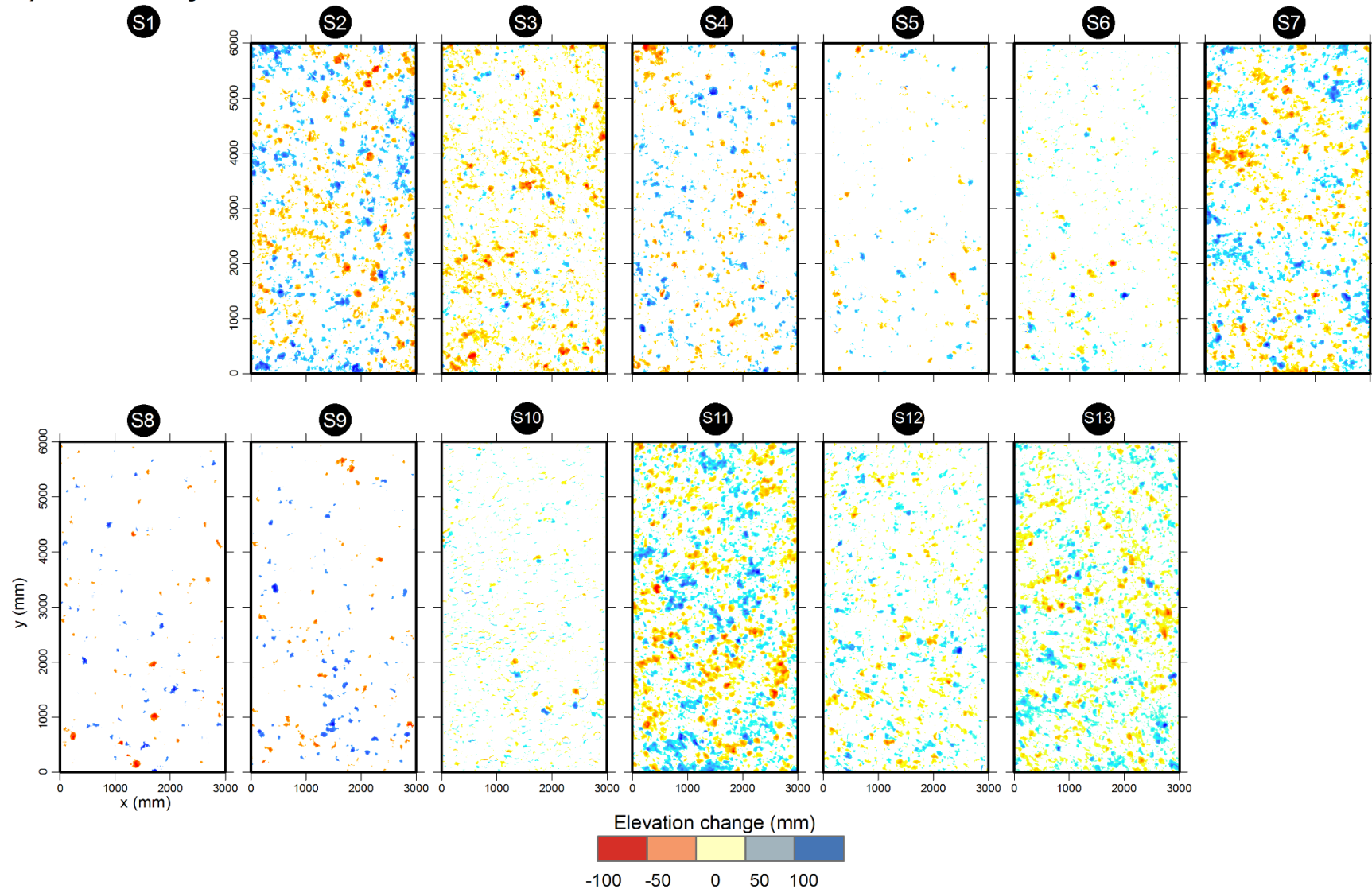
a)  $W_{1.1}$  survey series



**b)  $W_{1.2}$  survey series**



c) W<sub>1.1</sub> survey series



### d) $W_{1.2}$ survey series

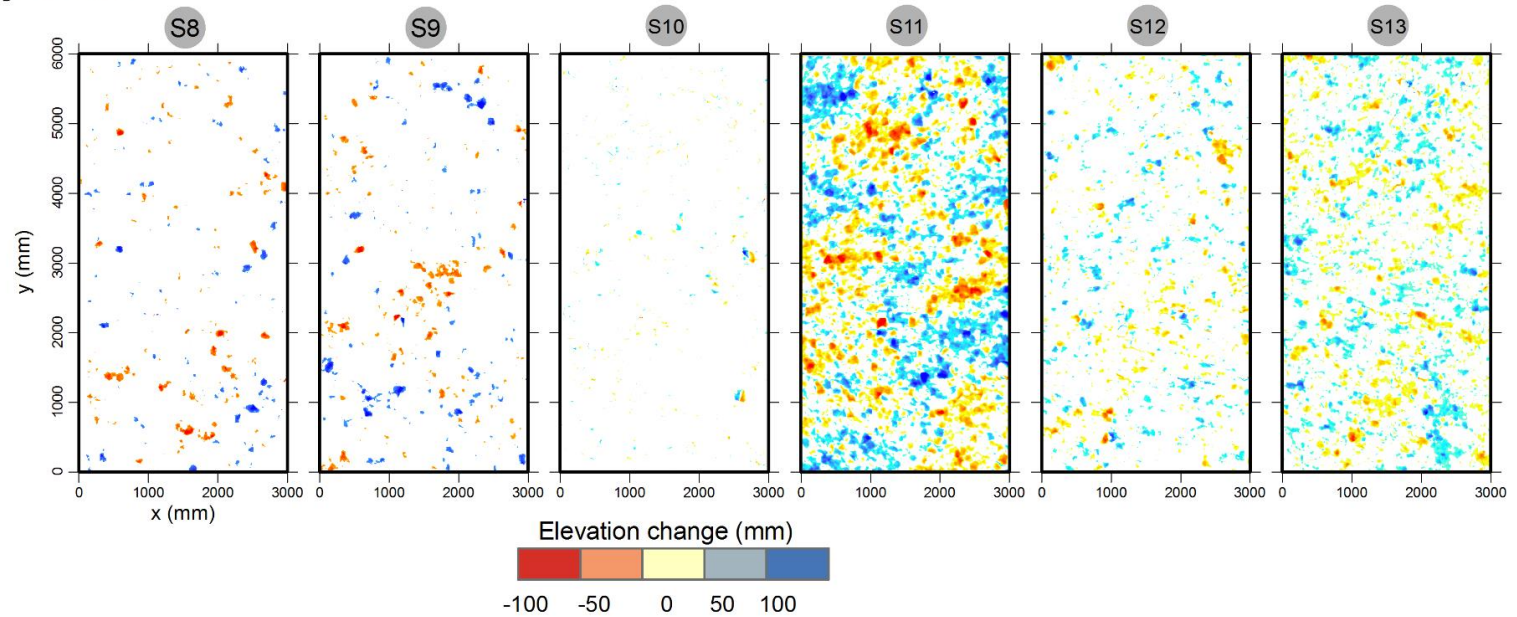


Figure 5.3 DTMs for the a)  $W_{1.1}$  S1–S13 and b)  $W_{1.2}$  S7–S13 surveys and significant changes in elevation (i.e.  $> \text{LoD}$ ; cf. Wheaton et al., 2010) between the c)  $W_{1.1}$  S1–S13 and d)  $W_{1.2}$  S7–S13 surveys. In a) and b) the monotone elevation colour map is overlain by a semi-transparent layer representing elevation change, shown in c) and d).

### 5.2.3. Bed elevation pdfs and their moments

Figure 5.4 shows the bed elevation pdfs for the 13 survey periods. As discussed in 4.4, the pdfs of the initial surfaces are characterised by near-normal, peaked ( $Ku_z^* > 0$ ) and positively skewed ( $Sk_z > 0$ ) form. Subsequent surfaces similarly fail to conform to a normal distribution as determined by a chi-squared goodness of fit test ( $p < 0.05$ ). Over the monitoring period, the pdf of  $W_{1.1}$  patch is narrower compared to the  $W_{1.2}$  patch ( $18.1 \leq \sigma_z \leq 22.4$  mm and  $23.0 \leq \sigma_z \leq 25.0$  mm respectively; Figures 5.4a and 5.4b respectively). Values of  $\sigma_z$  fluctuate within the envelope of values established for humid temperate gravel patches (Figure 5.5a). Although temporal variations in  $\sigma_z$  are small, a rejection of the null hypothesis for least squares regression for the combined data from the two patches indicates that the absolute changes in  $\sigma_z$  are positively correlated with  $\hat{Q}$  ( $R^2 = 0.49$ ;  $p < 0.003$ ) and  $T_{comp}$  ( $R^2 = 0.68$ ;  $p < 0.001$ ); this excludes the outlier (S8-S9: 512 hrs). Thus, whilst changes in  $\sigma_z$  are positively correlated with flow magnitude and duration, the streambeds did not get progressively smoother or rougher. A multiple linear regression of absolute changes in  $\sigma_z$  with  $\hat{Q}$  and  $T_{comp}$ , for the combined data sets (excluding the S8-S9 survey interval), reveals only the latter to be a significant predictor of  $\sigma_z$  ( $\sigma_z = -0.01 + 0.01 \cdot \hat{Q} + 0.01 \cdot T_{comp}$ ;  $R^2 = 0.71$ ;  $p < 0.001$ ). Therefore, the duration of flows was a more significant factor in changing  $\sigma_z$  ( $p < 0.008$ ) than the magnitude of flows ( $p > 0.05$ ).

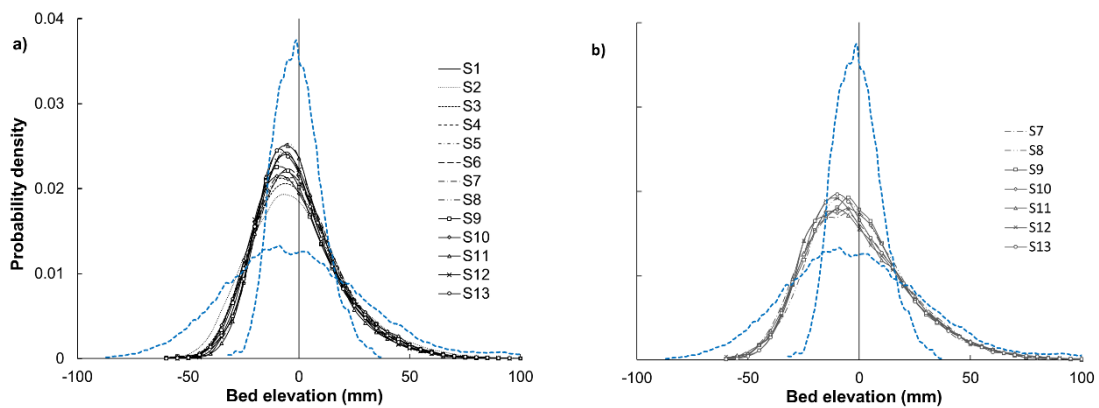


Figure 5.4 The a)  $W_{1.1}$  and b)  $W_{1.2}$  bed elevation pdfs relative to the range of pdf form established from humid temperate surface characterisation (illustrated by dashed blue lines).

Table 5.2 The bed elevation statistical moments  $\sigma_z$ ,  $Sk_z$  and  $Ku_z^*$  for the  $W_{1.1}$  and  $W_{1.2}$  patches over the monitoring period.

Patch id	Survey	Statistical moment		
		$\sigma_z$	$Sk_z$	$Ku_z^*$
W <sub>1.1</sub>	1	19.7	0.91	1.44
	2	22.4	0.65	0.60
	3	20.8	0.65	0.67
	4	20.0	0.65	0.76
	5	19.8	0.57	0.45
	6	19.4	0.60	0.57
	7	20.3	0.64	0.84
	8	18.7	0.77	1.24
	9	20.5	0.80	1.10
	10	21.1	0.77	1.00
	11	18.1	0.81	1.20
	12	18.6	0.80	1.14
	13	19.5	0.85	1.33
W <sub>1.2</sub>	7	24.4	0.63	0.52
	8	23.0	0.56	0.67
	9	23.2	0.69	0.89
	10	23.6	0.66	0.80
	11	25.0	0.74	0.81
	12	24.3	0.82	1.02
	13	23.4	0.83	1.08

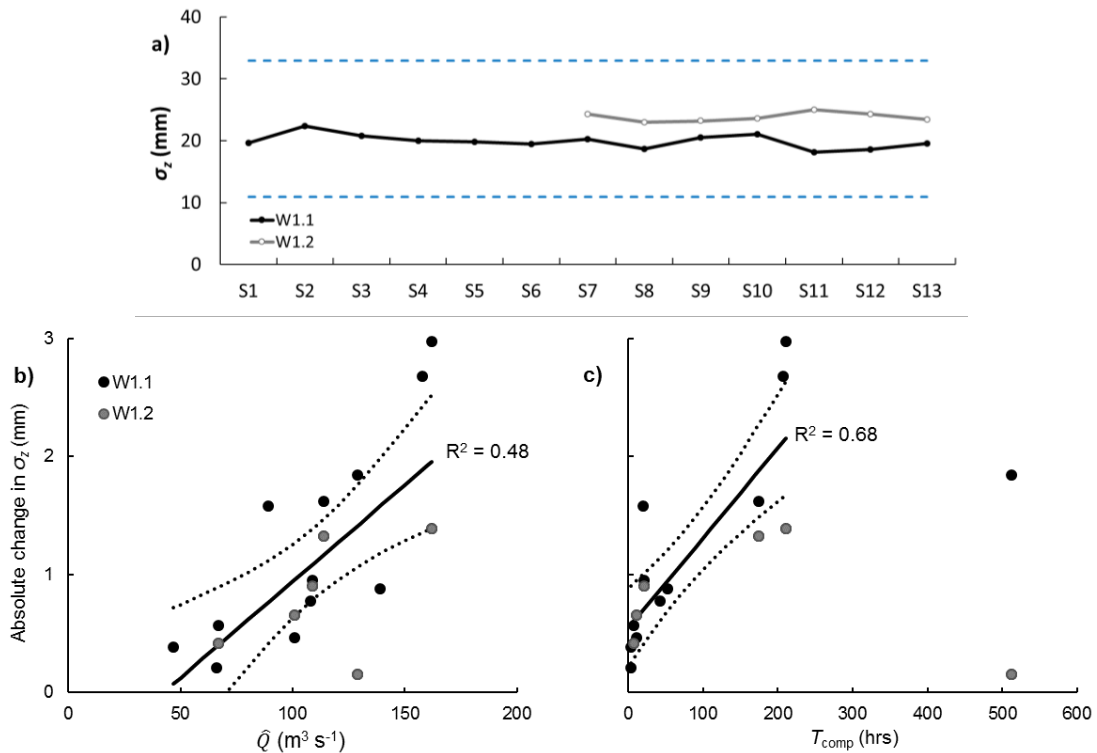


Figure 5.5 a) Variations in  $\sigma_z$  over the monitoring period and changes in  $\sigma_z$  for individual survey intervals with the b) magnitude and c) duration of competent flow. Lines of best fit determined from least squares regression for data aggregated from  $W_{1.1}$  and  $W_{1.2}$ ; 95% confidence intervals shown by the dotted lines.

The other statistical moments describing the bed elevation distribution –  $Sk_z$  and  $Ku_z^*$  – are also observed to fluctuate within the envelope of values established for humid temperate gravel patches ( $0.56 \leq Sk_z \leq 0.91$ ,  $0.45 \leq Ku_z^* \leq 1.44$ ; Figures 5.6a-b). However, in contrast to  $\sigma_z$ , absolute variations in  $Sk_z$  and  $Ku_z^*$  are not significantly controlled by peak discharge or the duration of competent flow ( $p > 0.05$ ; Figures 5.6c-f).

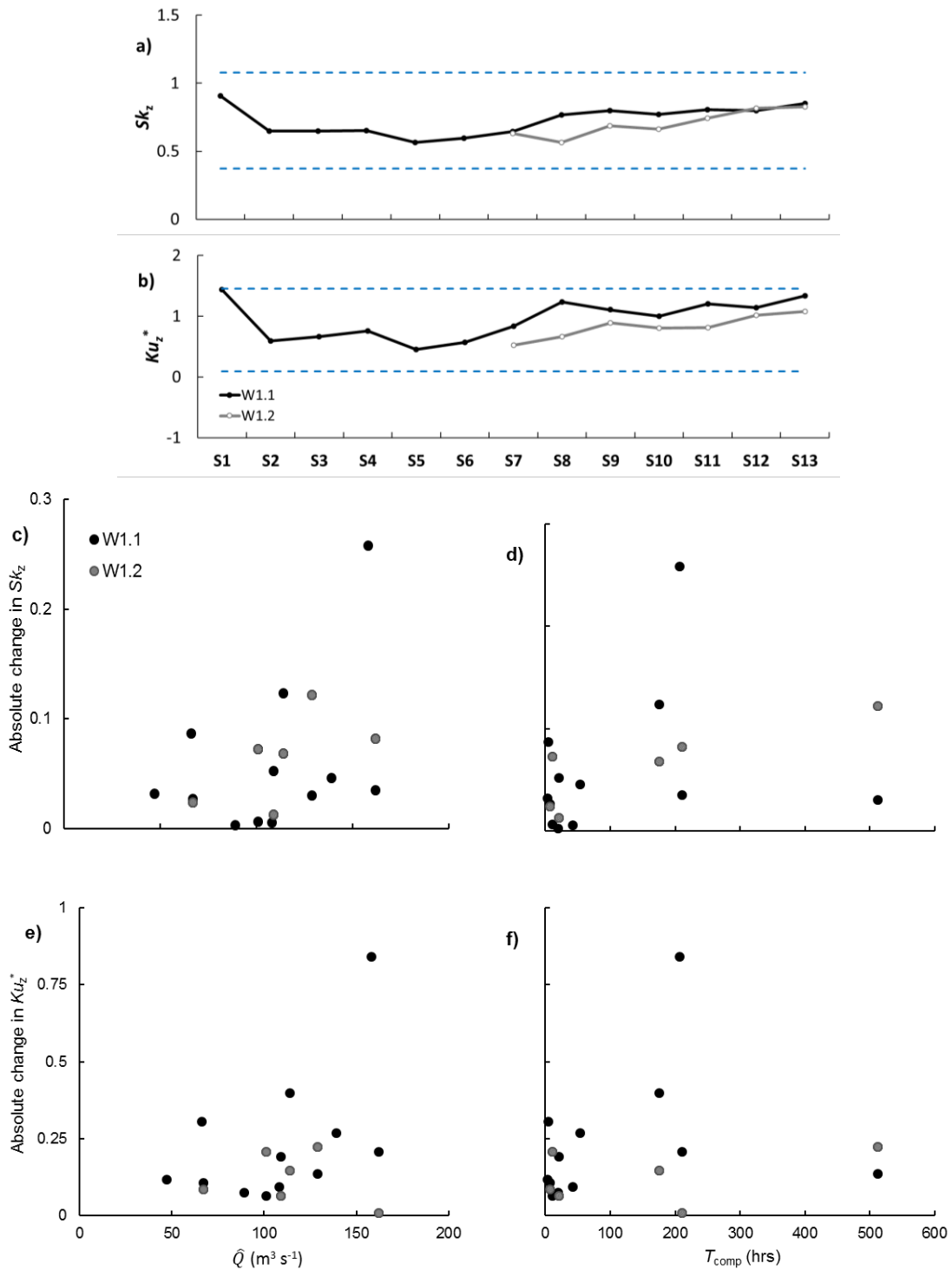


Figure 5.6 a-b) Variations in  $Sk_z$  and  $Ku_z^*$  over the monitoring period and c-f) changes in  $Sk_z$  and  $Ku_z^*$  for individual survey intervals.

## 5.2.4. Variogram analyses

The 1D flow-parallel variograms for the  $W_{1.1}$  and  $W_{1.2}$  patches over the monitoring period are presented in Figures 5.7a-b. The 1D variograms for the initial surfaces were characterised by a curved form in log-log space ( $0.04 < \tilde{h} < 10$ ) with the start of the apex of this curvature approximate to the size of individual surface grains ( $\tilde{h} \approx 1$ ). This curved form suggests the surfaces display multifractal behaviour rather than distinct fractal bands and associated scales of roughness. In the majority of cases, the sill was attained over the range of lags considered which demonstrates a statistical independence between bed elevations at larger scales. The form of the 1D variograms does not significantly alter over the monitoring period and typically remains within the bounds identified for the other humid temperate patches. Any minor changes that occur, e.g. for  $0.04 < \tilde{h} < 1$  ( $W_{1.1}$  S3-S4,  $W_{1.2}$  S10-S11,  $W_{1.2}$  S12-S13), are uncorrelated with flow magnitude or the duration of competent flows.

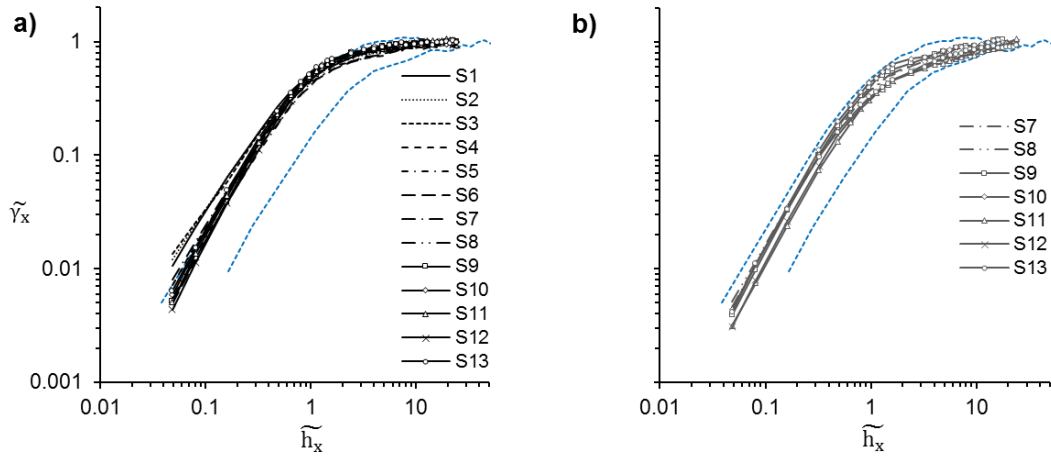


Figure 5.7 Flow-parallel variograms for the a)  $W_{1.1}$  and b)  $W_{1.2}$  patch series. In a-b) the bounds of humid temperate patch characterisation are illustrated by the dashed, blue lines.

Following Subsection 4.6.2, the ratio of  $\tilde{\gamma}$  in flow parallel and flow transverse directions was estimated over the range  $0.5 < \tilde{h} < 10$  and is presented in Figure 5.8. For the initial surfaces,  $\tilde{\gamma}$  was largely equal in flow-transverse and flow-parallel directions for all lags considered ( $\tilde{\gamma}_x/\tilde{\gamma}_y \approx 1$ ;  $0.5 < \tilde{h} < 10$ ). This indicates that grain- and meso-scale roughness is broadly isotropic. The subsequent surfaces similarly demonstrate  $\tilde{\gamma}$  is equivalent in flow parallel and flow transverse directions. While there are some slight exceptions, e.g. a relative increase in  $\tilde{\gamma}_x/\tilde{\gamma}_y$  for  $0.5 < \tilde{h} < 1$  (for  $W_{1.1}$  S1, S2 and S4) and  $1 < \tilde{h} < 10$  (for  $W_{1.1}$  S9 and S10), these adjustments are slight and do not give the impression of

significant changes in the isotropy of grain- and meso-scale bed structure over the monitoring period.

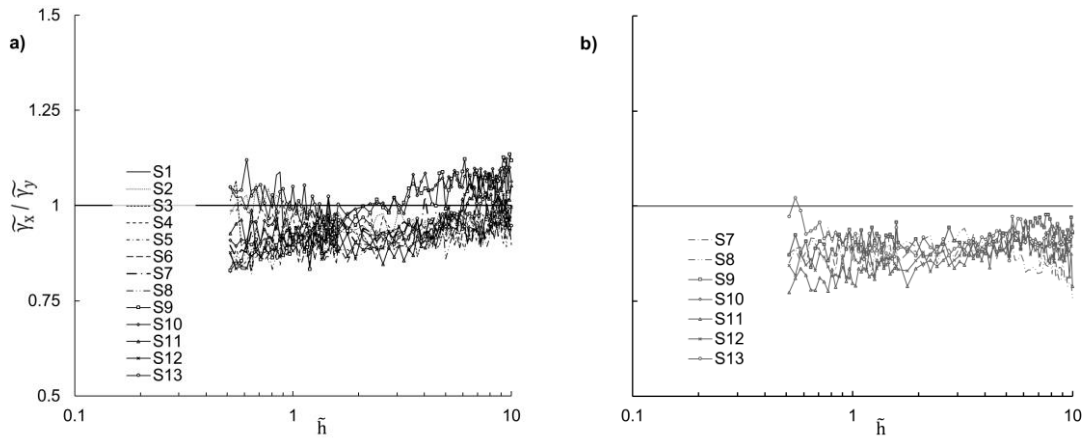


Figure 5.8 The flow-parallel:flow-transverse ratio of  $\gamma$  with  $D_{50}$ -normalised lag for the a)  $W_{1.1}$  and b)  $W_{1.2}$  patch series.

### 5.2.5. Inclination index, local slope and aspect

The inclination index for  $W_{1.1}$  and  $W_{1.2}$  patch series is displayed in Figure 5.9a. The initial surfaces were broadly characterised by a greater proportion of upstream facing grain-scale slopes to downstream facing slopes and consequently  $I$  was typically negative ( $-0.094 \leq I \leq 0.039$ ). This provides some evidence of particle imbrication. Values of  $I$  over the survey series generally remain within the bounds established from the other humid temperate patches ( $-0.089 \leq I \leq 0.062$ ), however  $I$  appears to progressively increase for the  $W_{1.1}$  over the S1-S2 to S10-S11 survey intervals and for  $W_{1.2}$  over the S7-S8 to S10-S11 survey intervals. This reflects a broadly systematic increase in the proportion of downstream facing local slopes which reflects the surfaces becoming more progressively less imbricated. Despite the indicated rearrangement of surface grains, local plots of aspect for  $W_{1.1}$  and  $W_{1.2}$  (shown for 1 x 1 m sub patches in Figures 5.10a and 5.10b respectively) do not mirror this trend. The variations in the index that occur over this period were typically invariant of the magnitude and the duration of competent flows (Figures 5.9b and 5.9c, respectively;  $p > 0.05$ ). Although a significant relationship was observed between absolute changes in  $I$  and competent flow duration for the patch-aggregated data ( $R^2 = 0.37$ ;  $p < 0.008$ ), this relationship is dictated by the S8-S9 survey interval outlier (cf. Subsection 5.2.3).

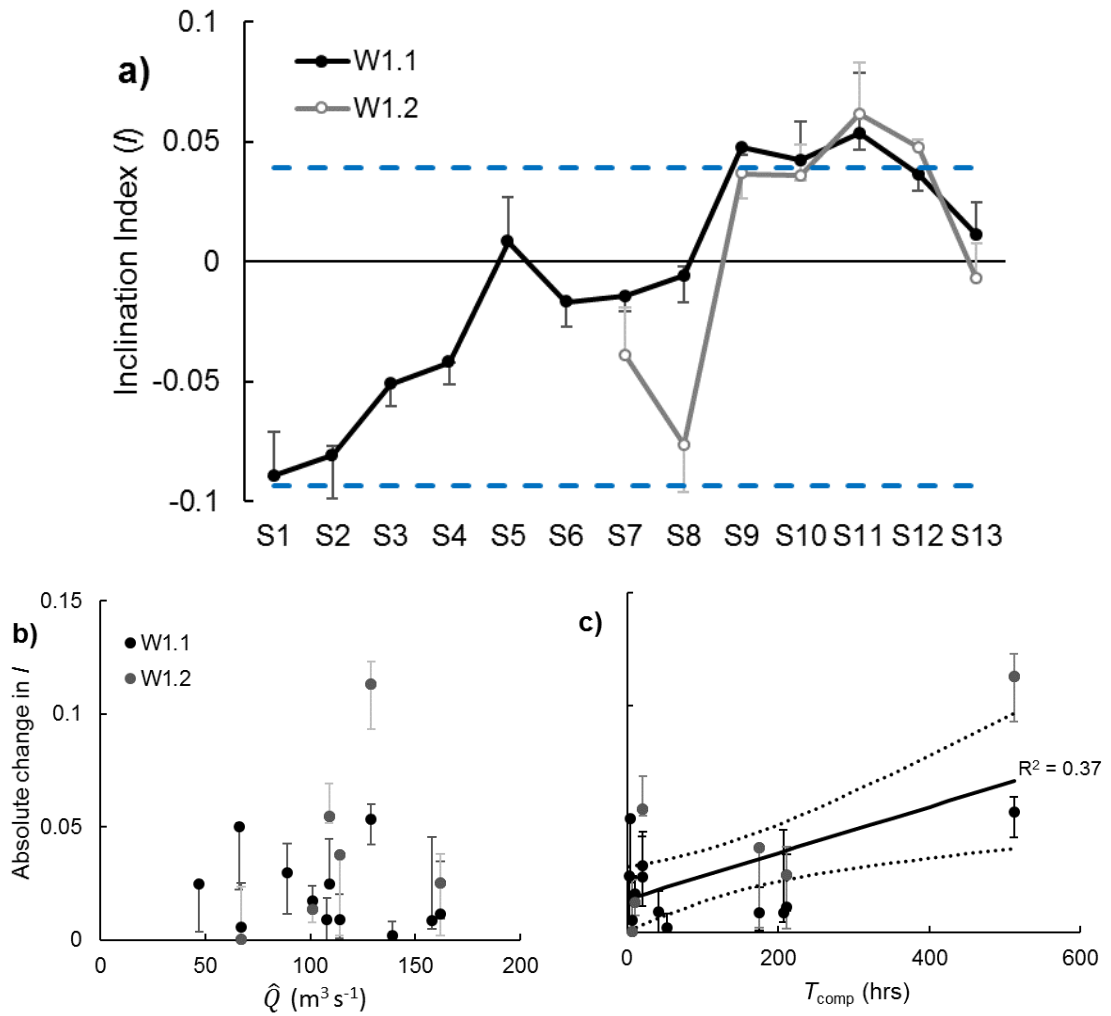
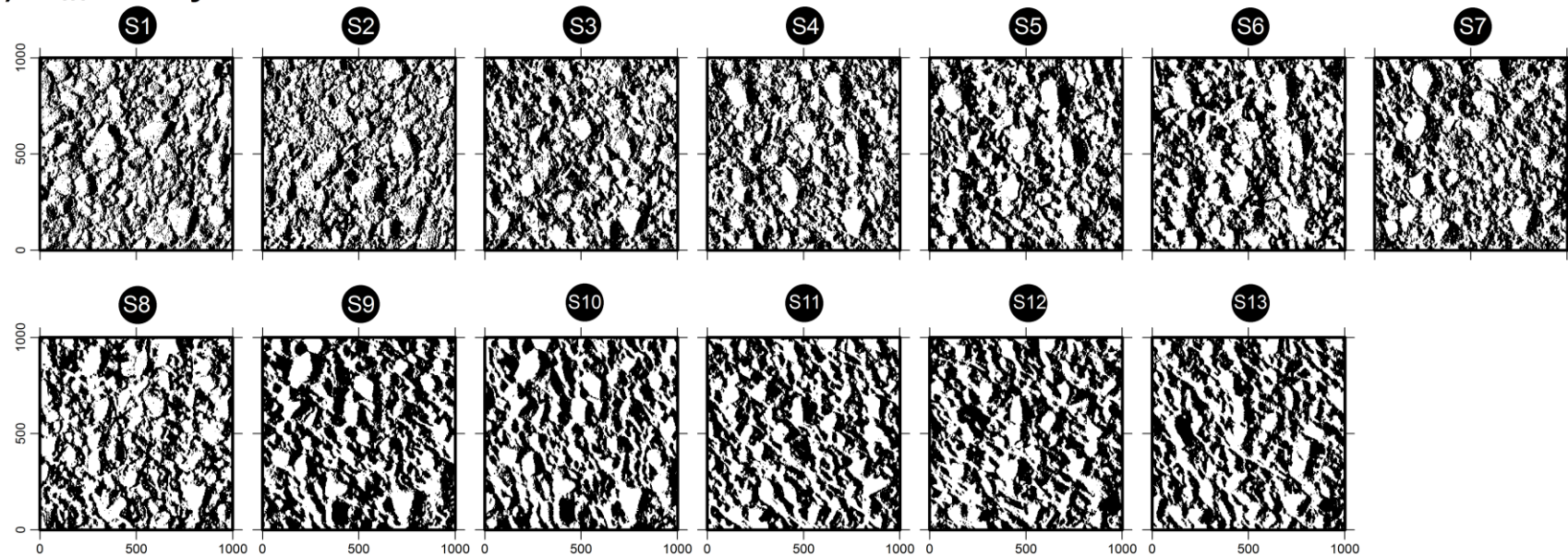


Figure 5.9 a) Changes in  $I$  over the W<sub>1.1</sub> and W<sub>1.2</sub> survey series and b-c) changes in  $I$  for individual survey intervals. In a) the dashed lines refer to the envelope of values for the other humid temperate patches and the vertical bars the range in  $I$  calculated using 8 mm and 10 mm moving windows. In b) and c) the vertical bars represent the minimum and maximum absolute changes in  $I$  for the range of values recorded for a 9 mm ( $\pm 1$  mm) moving window. Lines of best fit determined from least squares regression; 95% confidence intervals shown by the dotted lines.

**a)  $W_{1,1}$  survey series**



**b)  $W_{1,2}$  survey series**

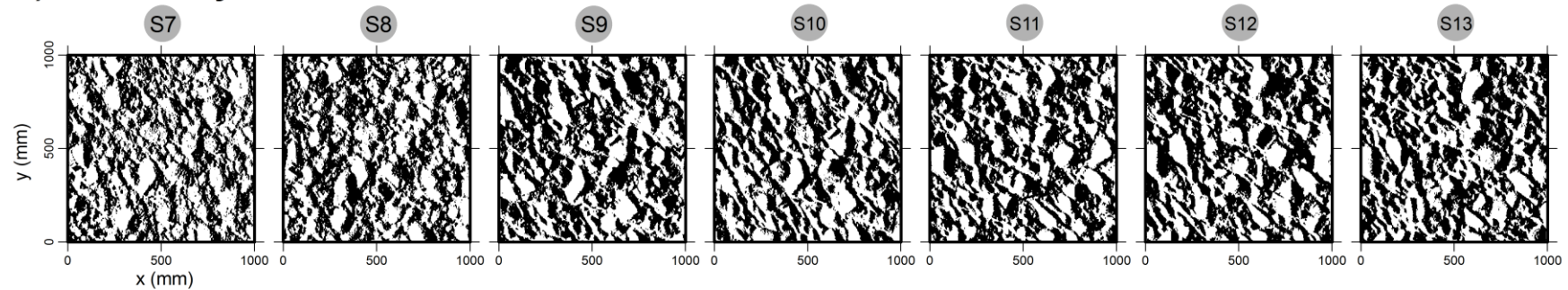


Figure 5.10 Local aspect for the a)  $W_{1,1}$  and b)  $W_{1,2}$  1 x 1m sub patch series. Direction of flow from left-to-right. In a-b) upstream and downstream facing cells are coloured in white and black respectively (see Figure 3.24).

The local slope distributions for  $W_{1.1}$  and  $W_{1.2}$  series are presented in Figures 5.11a and 5.11b respectively. As described in Section 4.8, the initial surfaces were characterised by a positively skewed distribution of, largely shallow, local slopes ( $0.37 \leq Sk_s \leq 0.76$ ;  $20.5 \leq S_{50} \leq 30.8^\circ$ ). The distributions of slope vary little over the monitoring period and are similarly characterised by a positive skew ( $0.35 \leq Sk_s \leq 0.71$ ) and shallow median slope ( $23.4 \leq S_{50} \leq 32.1^\circ$ ) that lies within the bounds for the other humid temperate patches. The slight fluctuations in the form of the slope distribution, described by  $Sk_s$  and  $S_{50}$ , that occur over the monitoring period were not dependent on peak discharge or the duration of competent flow (Figure 5.10c-e;  $p > 0.05$ ). Although a significant relationship was found between the duration of competent flow and absolute changes in  $Sk_s$  for patch-aggregated data ( $R^2 = 0.32$ ;  $p < 0.02$ ), the correlation is dictated by the outlier for S8-S9 (cf. Subsection 5.2.3).

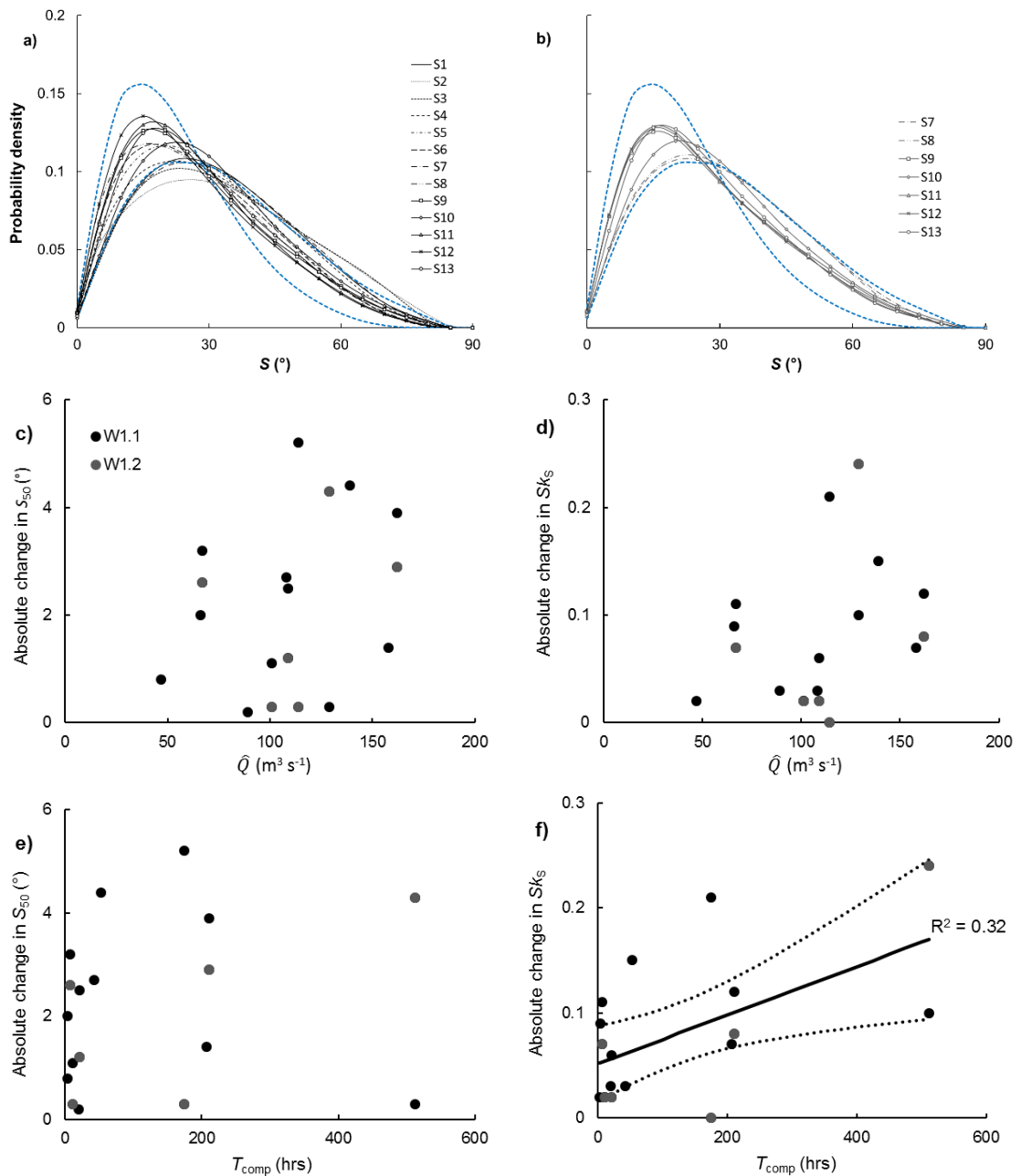


Figure 5.11 The probability distributions of local slope for a)  $W_{1.1}$  and b)  $W_{1.2}$  and c-f) changes in  $S_{50}$  and  $Sk_s$  for individual survey intervals. In a-b) the envelope of values for the other humid temperate patches are illustrated by the dashed, blue lines. Lines of best fit determined from least squares regression; 95% confidence intervals shown by the dotted lines.

### 5.3. Temporal aspects of stream bed restructuring

The temporal dynamics of streambed structure were further explored by analysing the evolution of the streambed condition from an unstructured state at  $W_{1.1A}$ ,  $W_{1.2A}$  and  $W_{1.1B}$ . As described in Subsection 3.1.4, treated surfaces devoid of structure were generated for each of the sub patches by manually turning over the surficial sediments. Each sub patch was then monitored to document how the streambed structure evolved over time. Since the timescales associated with the development of streambed structure were unknown at the outset of the experiments, the sub patches were monitored for both shorter and longer time periods. In order to study the longer-term evolution of bed structure, sub patches from experiment A were left to restructure without interference over a minimum of three survey periods. This process was repeated for the  $W_{1.1A}$  sub patch to ensure there were three replicates of the longer-term series. In addition, the short-term evolution was studied over an initial survey period after which the sub patches from experiment B were re-treated to generate additional unstructured beds (i.e. experimental replicates). This process was also repeated such that, together with sub patches from experiment A, there were six replicates of the shorter-term series. The series of surfaces analysed in this section is shown in Figure 5.12 in which the pre-treated (natural) surfaces, the unstructured (treated) surfaces and the series of restructuring surfaces are identified by the green T-1, red T0 and blue T1-T $n$  labels respectively. The effects of the surface treatment on the structural properties of the bed are considered first (Subsection 5.3.1) through a comparison of four, pre-treated (T-1; *green*) surfaces at  $W_{1.1A}$  (surveys S3 and S10),  $W_{1.2A}$  (S10) and  $W_{1.1B}$  (S3) with six, treated (T0; *red*) surfaces at  $W_{1.1A}$  (S3 and S10),  $W_{1.2A}$  (S10) and  $W_{1.1B}$  (S3, S4 and S5). The analysis then proceeds by considering the short-term evolution of bed structure (surface T0-T1; *red-blue*) at  $W_{1.1A}$  (S3-S4; S10-S11),  $W_{1.2A}$  (S10-S11) and  $W_{1.1B}$  (S3-S4; S4-S5; S5-S6) in Subsection 5.3.2. Longer-term patterns of streambed restructuring (surface T1-T $n$ ; *blue-blue*) are then explored using  $W_{1.1A}$  (T1-T4: S4-S7; T1-T3: S11-S13) and  $W_{1.2A}$  (T1-T3: S11-S13).

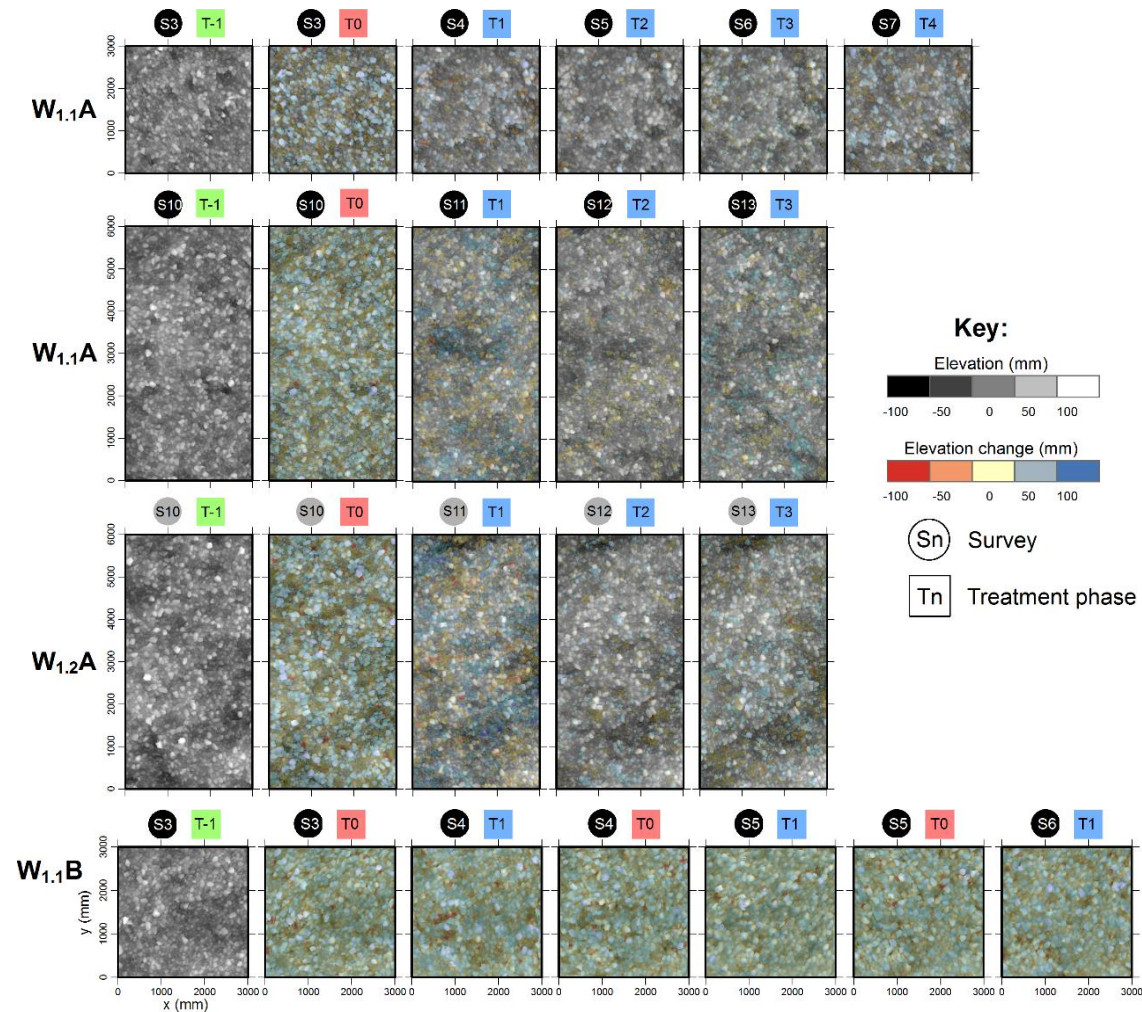


Figure 5.12 DTMs for the  $W_{1.1A}$ ,  $W_{1.2A}$  and  $W_{1.1B}$  sub patches. Pre-treated (T-1), treated (T0) and restructuring (T1-Tn) surfaces are differentiated by green, red and blue ID boxes respectively. Monotone elevation maps are overlain by a semi-transparent, coloured layer representing significant changes in elevation (i.e. > LoD; cf. Wheaton et al., 2010) between surveys.

### 5.3.1. Effects of experimental surface treatments on bed structure

To demonstrate the effects of the treatment in deconstructing the bed structure, this section compares the structural characteristics of four pre-treated surfaces (T-1, *green*; Figure 5.12) with six treated surfaces (T0, *red*; Figure 5.12). The effects of surface treatment on bed texture and structure are illustrated in Figure 5.13 using a subset of data, namely the three pre-treated and five treated surfaces at W<sub>1.1</sub>A and W<sub>1.1</sub>B (similar changes were observed at W<sub>1.2</sub>A). Summary statistics for the full dataset are presented in Table 5.3.

Table 5.3 Summary statistics describing the effects of treatment and the evolution of streambed texture and structure. Data are median values of textural and structural parameters calculated for the pre-treated (T-1), treated (T0), initial restructuring (T1) and subsequent development (T2-Tn) surfaces.

Surface	$D_{50}$ (mm)	$\sigma_z$ (mm)	$Sk_z$	$Ku_z^*$	$I$	$S_{50}$ (°)	$Sk_s$
T-1	50.2	21.8	0.65	0.71	-0.10	28.8	0.51
T0	57.2	24.5	0.63	0.43	-0.03	32.1	0.38
T1	50.7	21.7	0.59	0.53	-0.06	28.8	0.47
T2	50.0	20.9	0.58	0.51	-0.13	26.6	0.60
T3	46.6	21.0	0.66	0.61	-0.13	27.3	0.61
T4	54.0	20.7	0.74	0.59	-0.09	29.5	0.45
T2-n	50.2	20.9	0.66	0.59	-0.13	26.9	0.60

In terms of grain size, the treatment causes the surfaces to coarsen slightly ( $D_{50} = 50.2$  mm to 57.0 mm; Table 5.3; Figure 5.13a). The effects of treatment on surface character are apparent in the DTMs (four *green* T-1 surfaces vs. six *red* T0 surfaces; Figure 5.12). The treatment process generated significant (up to 150mm) and extensive (over the whole surface) changes in bed elevation that were more substantive than those generated by the largest flow events. Inspection of the treated surfaces revealed loosely packed grains lacking in imbrication, bedforms and any larger meso-scale variations in topography. The treatment was, therefore, able to modify the surface to generate treated surfaces in which the structural effects of water working had been eliminated and appeared visually distinct from their pre-treated counterparts.

In terms of bed elevation pdfs (Figure 5.13b), the effect of surface treatment was to i) increase the frequency of more extreme elevations  $\pm 50$  mm about the mean bed level and broaden the distribution of bed elevations (from  $\sigma_z = 21.8$  mm to 24.5 mm; Table 5.3), ii) decrease the peak of the distribution ( $Ku_z^* = 0.71$  to 0.43) and iii) leave the skew of the distribution

unchanged ( $Sk_z = 0.65$  to  $0.63$ ). Following surface treatment,  $\sigma_z$  increases to the upper bound and  $Ku_z^*$  falls to the lower bound of values recorded for the  $W_{1.1}$  and  $W_{1.2}$  series ( $18.1 \leq \sigma_z \leq 25.0$  and  $0.45 \leq Ku_z^* \leq 1.44$ ; Table 5.2). Little difference is observed in the form of the 1D variograms (Figure 5.12c) although there is some evidence that for  $0.04 \leq \tilde{h}_x \leq 5$  the treatment increases  $\tilde{\gamma}_x$  beyond the upper bound of  $\tilde{\gamma}_x$  recorded for the  $W_{1.1}$  and  $W_{1.2}$  series (Figure 5.7). This may reflect a roughening of the treated surfaces at grain- and meso-scales. In response to the increase in  $\tilde{\gamma}_x$ , the curved region of the variograms is narrower and the sills are attained at shorter lags ( $\tilde{h}_x \approx 5$  and  $\tilde{h}_x \approx 2$  for the T-1 and T0 surfaces respectively). This demonstrates that the treatment process was effective in removing larger scales of structure from the surfaces. The effects of treatment were further characterised by calculating the ratio  $\tilde{\gamma}_x/\tilde{\gamma}_y$  over the range  $0.5 \leq \tilde{h} \leq 10$  (Figure 5.12d). The untreated surfaces were isotropic over grain- and meso-scales ( $\tilde{\gamma}_x/\tilde{\gamma}_y \approx 1$ ;  $0.5 < \tilde{h} < 10$ ) and the treated surfaces share these properties. Therefore, surface treatment does not appear to generate changes in the directional properties of surface roughness. In terms of imbrication and slope, the effects of surface treatment were to i) reduce the frequency of upstream facing cells ( $I = -0.1$  to  $0.03$ ) and ii) generate a slight increase median slope ( $S_{50} = 28.8^\circ$  to  $32.1^\circ$ ) and a slight decrease in skewness ( $Sk_s = 0.51$  to  $0.38$ ). Following surface treatment,  $I$  remains within the bound of values of the  $W_{1.1}$  and  $W_{1.2}$  series ( $-0.09 \leq I \leq 0.06$ ; Figure 5.9a) while  $S_{50}$  increases to the upper bound and  $Sk_s$  decreases to the lower bound of values ( $23.4 \leq S_{50} \leq 32.1^\circ$  and  $0.35 \leq Sk_s \leq 0.71$ ; Figure 5.11a-b). The slight increase in  $I$  caused by surface treatment is consistent with a reduction in imbrication while the increased frequency of steep slopes is thought to reflect an increase in the depth of surface pockets caused by the breakup of particle imbrication and loosening of grain packing arrangements.

In summary, the aim of the treatment was to produce surfaces in which the structural effects of water working had been sufficiently disturbed such that they were structurally distinct from their natural counterparts. As Table 5.3 and Figure 5.13 illustrate, the surface treatment was successful generating grain- and meso-scale modifications in bed structure that were, in general, more substantive than those observed over the largest flows in the  $W_{1.1}$  and  $W_{1.2}$  series. However, while the treatment involved the wholesale rearrangement of surface grains (Figure 5.12), the shifts in the structural parameters were quite subtle and largely remain

within the bounds of values of the  $W_{1.1}$  and  $W_{1.2}$  series which make it difficult to track the restructuring of the bed over the ensuing surveys and survey intervals.

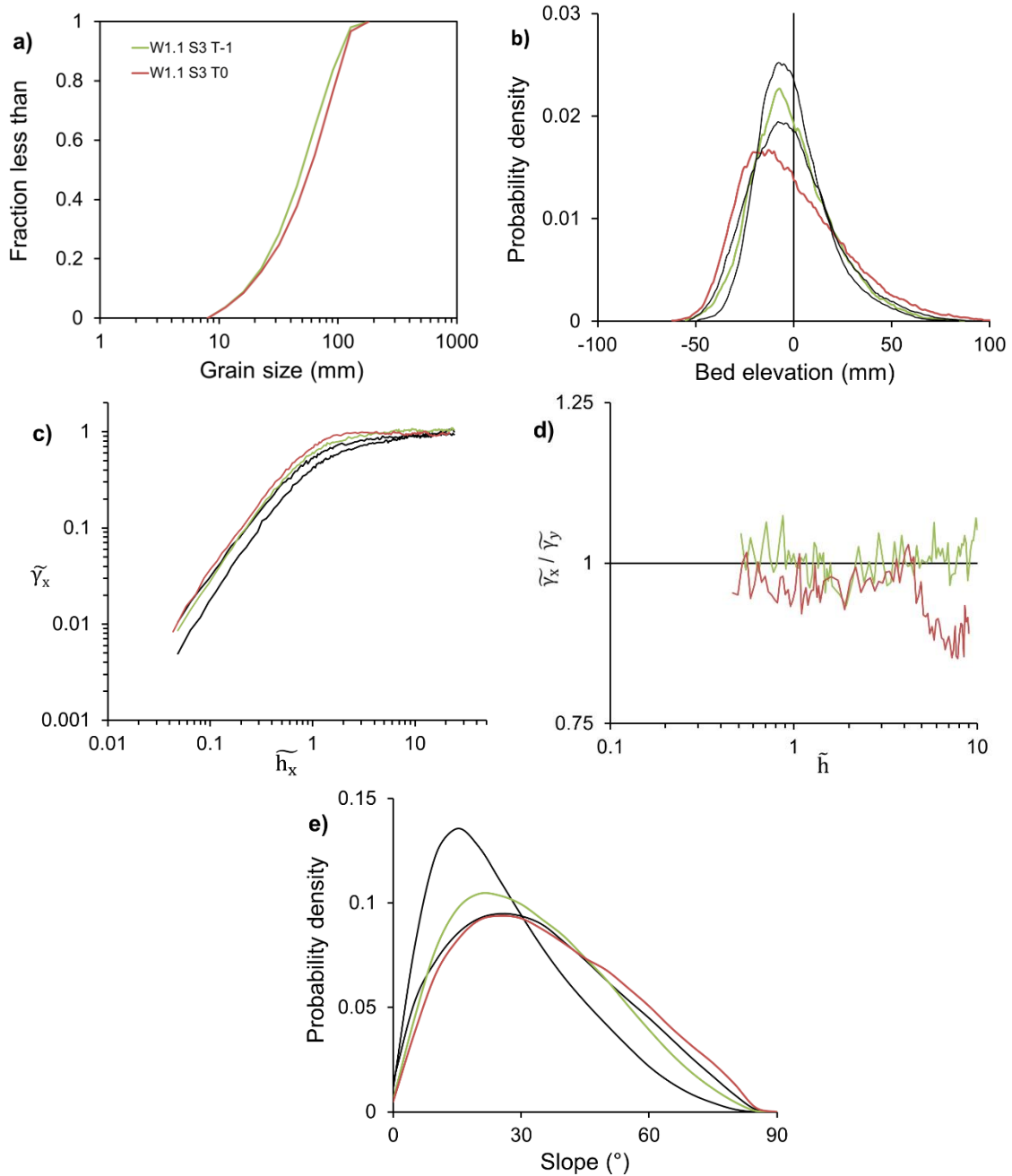


Figure 5.13 Effects of surface treatment on a) grain size distributions, b) bed elevation pdfs, c) flow parallel 1D variograms, d) ratio of flow parallel and flow transverse standardised semivariance and e) pdfs of local slope as exemplified for the pre-treated (T-1; green) and treated surfaces (T0; red) at  $W_{1.1}A S3$ . In b), c) and e) the bounds of the data for the  $W_{1.1}$  series are illustrated by the solid, black lines.

### 5.3.2. Re(development) of streambed structure from an unstructured bed state

This section compares the characteristics of the pre-treated surfaces with the surface characteristics recorded over subsequent surveys to examine how and over what timescales streambed structure develops from an unstructured state. Having compared the natural (T-1) and treated (T0) surfaces in the previous subsection, this subsection examines the short-term structural development of the treated surfaces (i.e. surface T0 to surface T1, *red to blue*; Figure 5.12) using data from three initial re-surveys conducted at W<sub>1.1</sub>A (S3-S4, S10-S11) and W<sub>1.2</sub>A (S10-S11) and from the four re-surveys conducted at W<sub>1.1</sub>B (S3-S4, S4-S5 and S5-S6). Longer-term (T1 to T<sub>n</sub>; *blue to blue*) patterns of redevelopment are analysed using data from the subsequent surfaces surveyed at W<sub>1.1</sub>A (T1-T4: S4-S7 and T1-T3: S11-S13) and W<sub>1.2</sub>A (T1-T3: S11-S13). To aid this analysis, Figure 5.14 illustrates the temporal evolution of streambed texture and structure using data from subpatch W<sub>1.1</sub>A and surfaces T-1 to T4 from surveys S3-S7 (similar changes were observed for W<sub>1.1</sub>A S10-S13 and W<sub>1.2</sub>A S10-S13). Summary statistics for all natural (T-1), treated (T0), initial (T1) and subsequent restructuring (T2-T<sub>n</sub>) surfaces are shown in Table 5.3.

The short-term effects of water working (T0 to T1; *red to blue*) were to i) slightly fine the surface ( $D_{50} = 57.0$  mm to 50.7 mm; Table 5.3; Figure 5.14a), ii) generate extensive grain and larger-scale modifications of bed topography (e.g. movement of surface grains, aggregation of particles in cluster bedforms and development of extended regions of higher and lower bed elevations 50-100 mm about the mean bed level; Figure 5.12), iii) narrow and increase the peak of the bed elevation distribution ( $\sigma_z = 24.5$  mm to 21.7 mm,  $Ku_z^* = 0.43$  to 0.53; Figure 5.14b), iv) smooth surface roughness (decrease in  $\tilde{\gamma}_x$  for the range  $0.04 \leq \tilde{h}_x \leq 5$ ) and increase the range of spatial dependency (lengthen variogram curvature from  $\tilde{h}_x \approx 2$  to  $\approx 5$ ; Figure 5.14c), v) slightly increase the frequency of upstream facing cells ( $I = -0.03$  to  $-0.06$ ) and vi) increase the frequency of shallower slopes and peak of the slope distribution ( $S_{50} = 32.1^\circ$  to  $28.8^\circ$ ,  $Sk_S = 0.38$  to  $0.47$ ; Figure 5.14e). The changes observed in the statistical parameters during initial water-working were generally more pronounced than those observed during the W<sub>1.1</sub> and W<sub>1.2</sub> series. As a result of these changes, the textural and structural characteristics of the initially water-worked surfaces were largely shared by their

pre-treated counterparts. This, therefore, demonstrates a rapid adjustment of the bed surface occurred during the initial period of restructuring (e.g. particle imbrication, tight bed packing arrangements; development of meso-scale topography) and could suggest that the surfaces have recovered much of their natural grain- and meso-scale sedimentary structure. However, these shifts in structural parameters were relatively subtle and for the initially restructured and treated surfaces remain within the bounds of values of the  $W_{1.1}$  and  $W_{1.2}$  series. Because of this, it is difficult to distinguish whether structure has fully reverted toward a pre-treated condition during the initial period of water-working. Thereafter, over subsequent periods of restructuring (T1-Tn; *blue* to *blue*), adjustments of the surfaces were less significant and largely limited to grain-scale modifications over low-to-moderate flow events which mirror those detected for the  $W_{1.1}$  and  $W_{1.2}$  series (Figure 5.12). As a result, changes in the structural parameters over successive flows were relatively modest (i.e.  $T1 \approx T2 \approx T3 \approx T4$ ) as a comparison between T1 and T2-n parameter values demonstrates (Table 5.3).

The adjustments in bed texture and bed structure observed over initial and subsequent periods of restructuring were further examined by considering absolute changes in the statistical parameters ( $D_{50}$ ,  $\sigma_z$ ,  $Sk_z$ ,  $Ku_z^*$ ,  $I$ ,  $S_{50}$  and  $Sk_s$ ) in relation to the magnitude and duration of competent flow ( $\hat{Q}$  and  $T_{comp}$ ). In this regard, the relationship between absolute changes in the metrics of streambed texture and structure between successive surveys and  $\hat{Q}$  and  $T_{comp}$  is shown in Figure 5.15. For comparison, the natural variability in streambed texture and structure is shown by mean absolute changes in parameter values recorded over the  $W_{1.1}$  and  $W_{1.2}$  series (indicated by the dotted lines in Figures 5.15a-n). In general, changes in the statistical parameters during initial restructuring were greater than those that occurred in the survey series. In addition, larger and longer flows tended to generate greater absolute changes in bed texture and structure than shorter, smaller flows; although rates of change were different between the different statistical parameters. Regarding event magnitude and duration, relatively minor flows (e.g.  $\hat{Q} = 47, 66 \text{ m}^3\text{s}^{-1}$ ;  $T_{comp} = 3, 4$  hours) were typically unable to initiate changes in bed texture and structure that exceeded the natural adjustments observed over the survey series, i.e. points broadly lie below the dotted line in Figures 5.15a-n. By contrast, changes in bed texture and structure during subsequent restructuring were largely equivalent to natural adjustments in bed character, i.e. typically rest below the dotted

lines in Figures 5.15a-n. Therefore, for a given magnitude or duration of effective flow, changes in bed texture and structure are typically greater during initial restructuring (T0-1) than subsequent restructuring (T1-4) and the latter will follow the natural temporal changes described in Section 5.2.

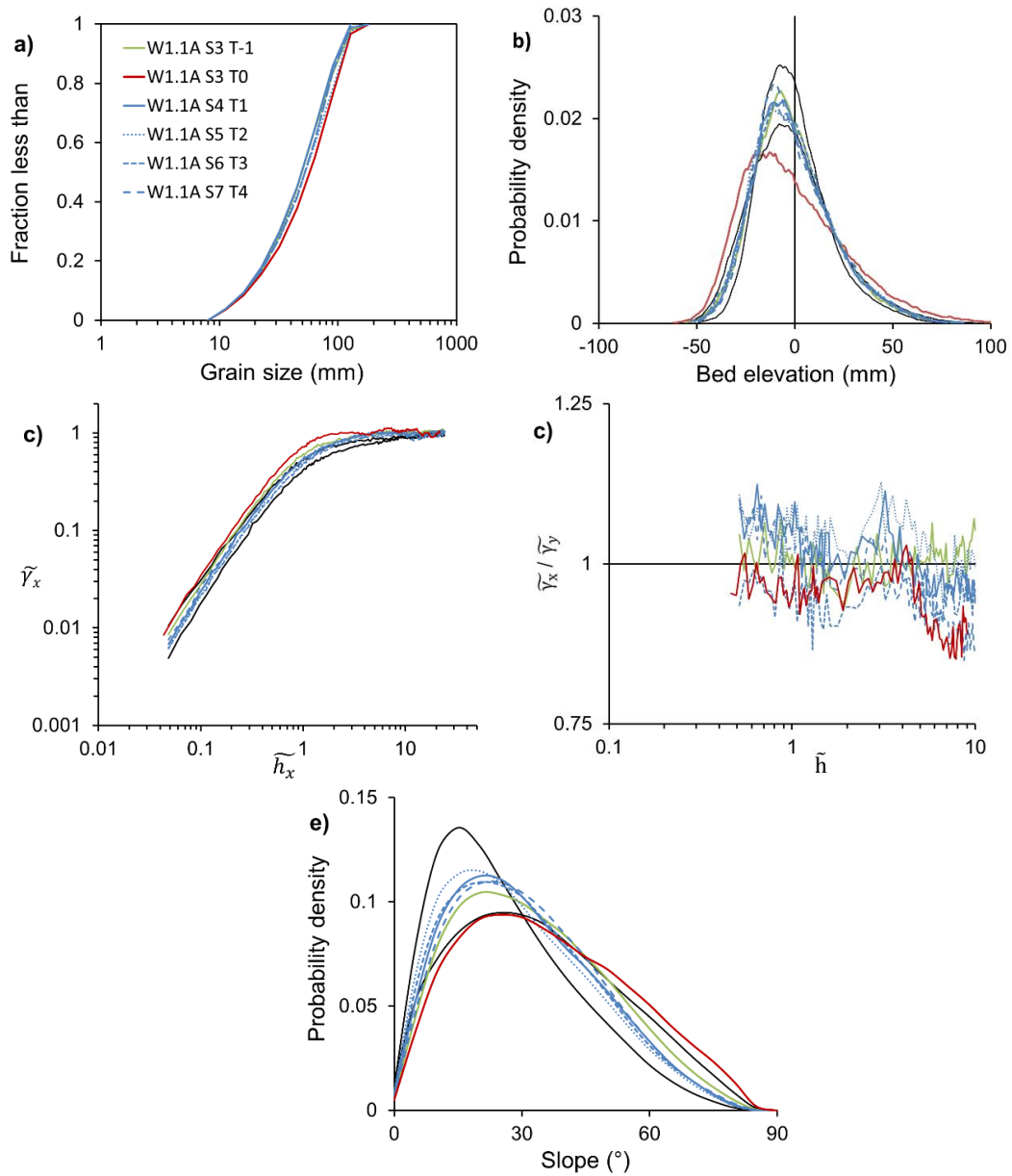
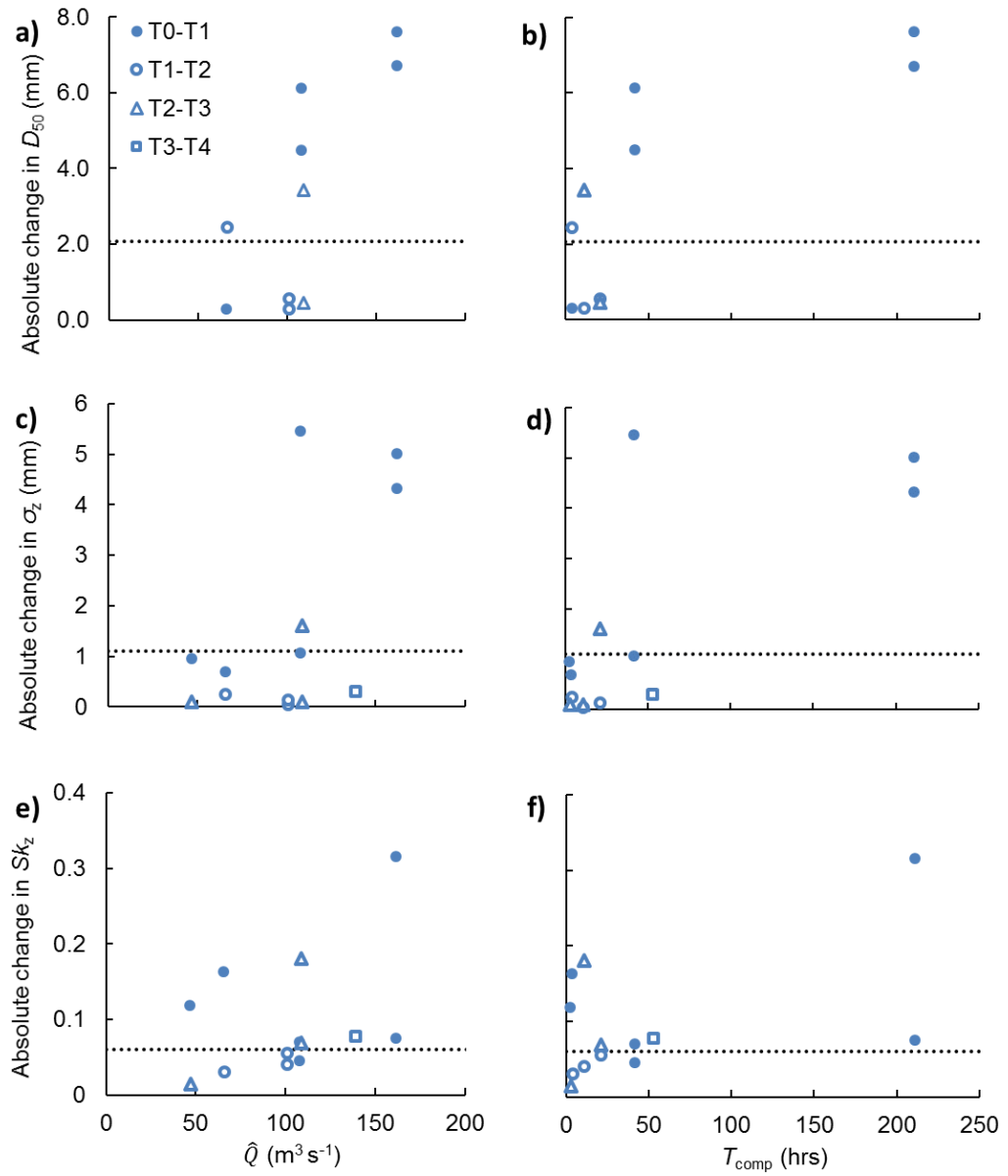


Figure 5.14 Temporal evolution of a) grain size distribution, b) bed elevation pdfs, c) flow parallel variograms, d) ratio of flow-parallel and flow-transverse standardised semivariance and e) pdfs of local slope for the pre-treated surfaces (T-1; *green*) and restructuring surfaces (T1-T4; *blue*) for  $W_{1.1}A$  S3-S7. In b), c) and e) the bounds of the data for the  $W_{1.1}$  series are illustrated by the solid, black lines.



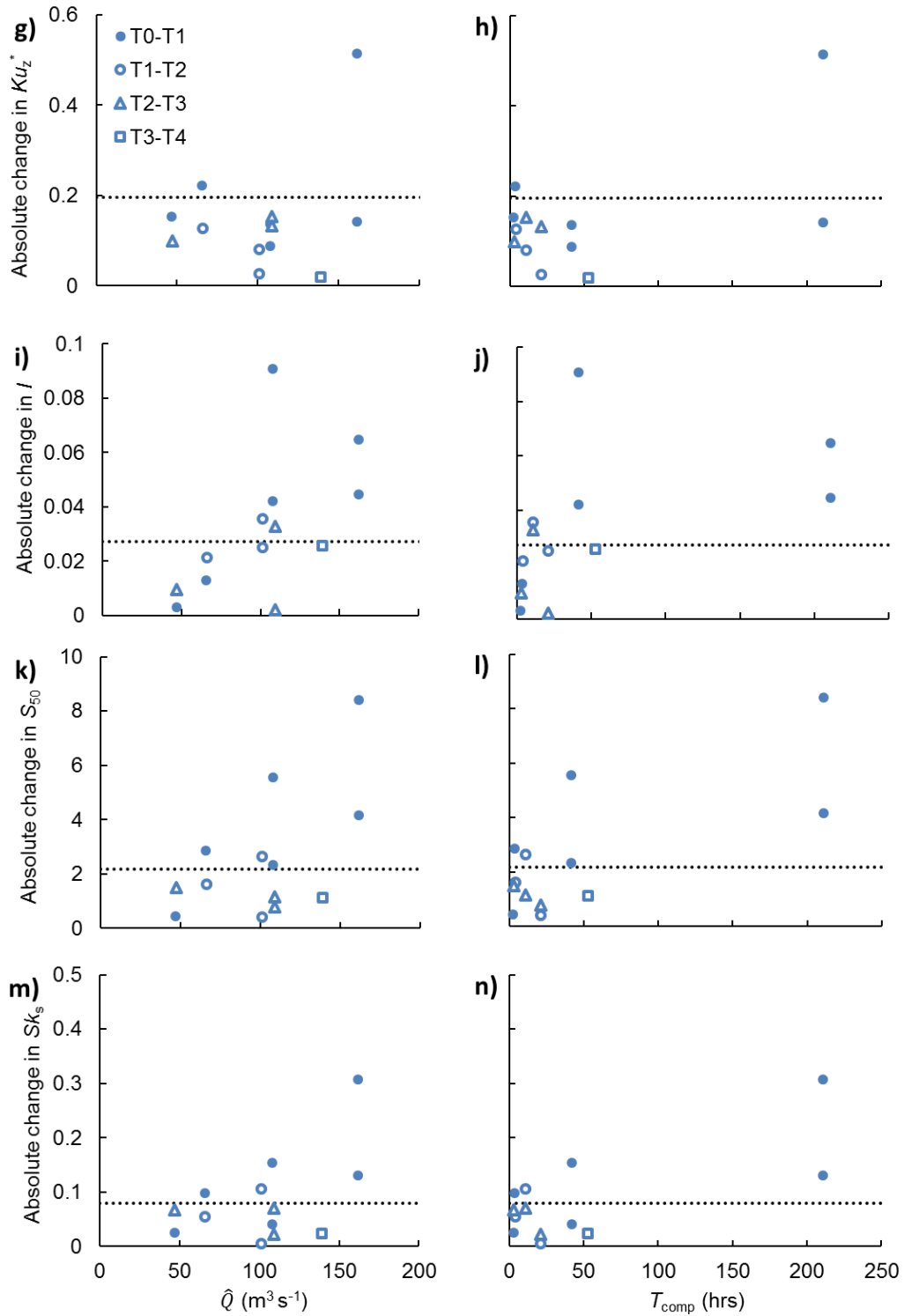


Figure 5.15 Relationship between peak discharge and duration of competent flow and absolute changes in a-b)  $D_{50}$ , c-d)  $\sigma_z$ , e-f)  $Sk_z$ . g-h)  $Ku_z$ , i-j)  $I$ , k-l)  $S_{50}$  and m-n)  $Sk_s$  between successive survey periods. Note: grain size information missing for the S6 survey (one T0-T1, T2-T3 and T3-T4 survey interval). The mean absolute changes observed over the W<sub>1.1</sub> and W<sub>1.2</sub> series are illustrated by the dotted lines.

## 5.4. Discussion

This chapter seeks to broaden our understanding of the temporal dynamics of sedimentary structure using a series of experiments. The first documented the natural variations in streambed structure over a 28-month period which involved 13 repeat surveys for the  $W_{1.1}$  patch and seven surveys for the  $W_{1.2}$  patch. Surface treatments were also applied to patches from experiments A and B in order to establish how structure re-establishes from a random bed condition. The former, Experiment A, involved monitoring the surfaces over multiple competent flows to investigate the longer-term development of structure over a series of events, while the latter, Experiment B, involved the repeated application of surface treatments to examine the short-term restructuring of the surface. As part of Experiments A and B, the treatment process was repeated a total of six times, single-event restructuring six times and multi-event sequences three times.

### 5.4.1. Temporal variability of streambed structure

The temporal dynamics of gravel bed sedimentology and structure were characterised for the  $W_{1.1}$  and  $W_{1.2}$  humid temperate patches over a range of flows which mobilised the bed surface to varying extents. These structural characteristics were compared with the range of results reported for the eight humid temperate gravel patches (Chapter 4) and are discussed against the hypothesis that humid temperate bed structure is maintained over effective flows but that slight adjustments of this water-worked condition are affected by event magnitude and duration, i.e. greater flows initiate greater changes in streambed structure.

The temporal dynamics of the patches were firstly considered in terms of textural adjustments. In this study, surface grain size for  $W_{1.1}$  and  $W_{1.2}$  remained broadly consistent over the monitoring period ( $47.4 \text{ mm} \leq D_{50} \leq 56.0 \text{ mm}$  and  $47.4 \text{ mm} \leq D_{50} \leq 51.5 \text{ mm}$  respectively; Figure 5.2) and, following an acceptance of the null hypothesis for the least squares regression between  $D_{50}$ ,  $\hat{Q}$  and  $T_{\text{comp}}$ , absolute changes in bed texture were not a function of event magnitude or duration. As a consequence, the surface grain size distributions for  $W_{1.1}$  and  $W_{1.2}$  were relatively insensitive to changes in flow and sediment regime during the monitoring period. Previous workers have similarly observed bed texture

to remain relatively constant over effective flows for water-worked beds in the flume (Wilcock and Southard, 1989; Wilcock, 2001; Mao et al., 2011) and field (Andrews and Erman, 1986; Wilcock and DeTemple, 2005; Clayton and Pitlick, 2008; Lamarre and Roy, 2008). This was explained by the likelihood of mobilised surface grains being replaced by equivalently-sized grains since pocket geometry and local flow conditions favour this exchange (Clayton and Pitlick, 2008). While there was little evidence from a visual inspection of the DTM series to support this like-for-like replacement of surface grains, the persistence of textural structure was demonstrated by the  $W_{1.1}$  and  $W_{1.2}$  DTMs (Figure 5.3) which do not appreciably coarsen or fine over time, e.g. as observed following the washing out of the surface armour (Parker and Klingeman, 1982).

In addition to these textural adjustments, this study also sought to monitor the adjustments of bed structure, which has often been disregarded by previous workers in favour of single-survey characterisation (e.g. Hodge et al., 2009b) or with a limited focus on cluster bedforms (e.g. Oldmeadow and Church, 2006). The qualitative assessment of bed structure at grain- and meso-scales was first considered through the visual inspection of DTMs (Figure 5.3). In this regard, the  $W_{1.1}$  and  $W_{1.2}$  DTMs appear to share the grain- and meso-scale structural characteristics exhibited by the humid temperate patches in section 4.3. This visual structure (e.g. coarse, tightly packed bed inhabited by cluster bedforms; extended patches of higher and lower elevations 50-100 mm about the mean bed level) was maintained over the range of effective flows, from those that are just large enough to mobilise individual grains to flows that are large enough to rework the bar surface. The near-normal form of the bed elevation pdfs for  $W_{1.1}$  and  $W_{1.2}$  (cf. Section 4.4) was similarly maintained during this period. A least squares regression found small, absolute adjustments in  $\sigma_z$  over the survey series were a function of  $\hat{Q}$  and  $T_{\text{comp}}$  (excluding S8-9). Therefore, while greater flows initiate greater changes in surface roughness, the bed does not progressively smooth or roughen in response to the magnitude or duration of water-working. Previous workers have also observed  $\sigma_z$  to be maintained for an established flume armour over low-magnitude, long-duration flow events (e.g. *L* hydrograph; Mao, 2012). In contrast,  $\sigma_z$  increased during high-magnitude, short-duration events (e.g. *M* and *H* hydrographs; Mao, 2012) which reflected a greater potential for the bed to roughen during peak flows and the limited periods of flow recession, in which the reworking of surface grains smoothed the surface. The adjustments in surface roughness

observed over low-magnitude, long-duration events are, therefore, more comparable to those recorded for  $W_{1.1}$  and  $W_{1.2}$ . Meanwhile, the bed elevation moments  $Sk_z$  and  $Ku_z^*$  remained within the envelope of values established for humid temperate gravel patches (section 4.4) and, since least squares regression is rejected between  $Sk_z$ ,  $Ku_z^*$ ,  $\hat{Q}$  and  $T_{comp}$ , any slight, absolute adjustments in the skew or the peak of the bed elevation distribution were not a function of event magnitude or duration.

Moving on to the variogram analyses, little change was observed in the 1D variograms which maintained a curved form (an indicator for multifractal behaviour) over time (Figures 5.7-8). As a consequence, the form of the 1D variograms remained within the bounds established from the other humid temperate patches and, in addition, any minor changes that occurred (e.g. in  $\tilde{\gamma}$  for  $\tilde{h} < 1$ :  $W_{1.1}$  S3-S4,  $W_{1.2}$  S10-S11 and  $W_{1.2}$  S12-S13) did not appear to be related to event magnitude or duration. In the flume experiments of Mao (2012), the scaling characteristics of artificial beds were similarly maintained over low-magnitude, long-duration events ( $M$  and  $L$  hydrographs). By contrast, high-magnitude, short-duration events ( $H$  hydrograph) led to a change in the rate of increase in  $\tilde{\gamma}$  for  $\tilde{h} < 1$  and the length of correlation which reflected the limited opportunity for grain- and larger-scale modifications during the receding limb of peaked hydrographs (Mao, 2012).

In terms of the grain-scale parameters of inclination and slope, the  $W_{1.1}$  and  $W_{1.2}$  patches were generally characterised by a greater proportion of upstream facing grain-scale slopes than downstream facing slopes ( $-0.094 \leq I \leq 0.039$ ) and the index  $I$  largely remained within the bound of values recorded for the other humid temperate patches ( $-0.089 \leq I \leq 0.062$ ). However, during the  $W_{1.1}$  S1-S11 and  $W_{1.2}$  S7-S11 survey intervals values of  $I$  appear to progressively increase (Figure 5.9) which demonstrates the frequency of downstream facing cells increase over time. Given previous workers have used this metric as a proxy for particle imbrication (e.g. Smart et al., 2004; Millane et al., 2006), this suggests grain-scale structure systematically changes during successive flow events. Since this progressive shift in particle imbrication was not reconcilable with DTMs and plots of local surface aspect (Figures 5.3 and 5.10), this suggests the inclination index is more sensitive to smaller-scale changes in grain-scale bed structure compared to the other metrics. An acceptance of the null hypothesis for the least squares regression between absolute changes in  $I$  with  $\hat{Q}$  and  $T_{comp}$  (excluding

the S8-S9 outlier) indicates shifts in local inclination were not a function of event magnitude or duration and therefore, probably, random. Grain-scale structure was also characterised through the distribution of local slopes. In this regard, the distribution of local slopes for  $W_{1.1}$  and  $W_{1.2}$  was characterised by a positive skew and shallow median slope ( $0.35 \leq Sk_S \leq 0.71$ ;  $23.4 \leq S_{50} \leq 32.1^\circ$ ) that remained relatively consistent over time and within the bounds established from the other humid temperate patches. The small changes in  $Sk_S$  and  $S_{50}$  that occurred over the survey series were largely independent of event magnitude and duration, rejecting least squares regression. Moreover, the slight shifts in the local slope distribution do not correspond to the progressive increase in  $I$  observed over the S1-S11 survey series; for example, a broadening of the distribution and an increase in the frequency of steeper slopes as might be expected following a reduction in particle imbrication. This provides further evidence that the inclination is more sensitive to adjustments in grain-scale structure than the other local metrics of slope and aspect.

#### **5.4.2. Evaluating the (re)development of structure from a treated condition**

The temporal dynamics of gravel streambed structure were further explored by investigating the restructuring of the bed from an unstructured condition over a range of effective flows. The analysis of DTMs (Figure 5.12) revealed surface treatment was relatively successful in eliminating the structural effects of water-working, through extensive changes in bed topography, and in the process generated surfaces that appeared visually distinct compared to their pre-treated counterparts. In terms of bed texture, the effect of treatment was to generate a slight coarsening of the surface (Table 5.3) which has similarly been noted by previous workers using a comparable treatment methodology (e.g. Oldmeadow and Church, 2006; Lamarre and Roy, 2008). Moving on to the parameters of bed structure, the surface treatment produced a slight shift in the near-normal form of the bed elevation pdfs that took the form of an increase in  $\sigma_z$  and a decrease in  $Ku_z^*$  (Figure 5.12). The positive skew of the bed elevation distribution remained following treatment whereas the pdfs for artificial screeded surfaces (similarly unstructured) typically exhibited a negative skew (Coleman et al., 2011). The latter reflects the smoothed topography of unstructured flume beds while the treatment, applied in this study, led to an increase in surface roughness which suggests a

point-of-difference in structural character between the two unstructured conditions. Grain-scale modifications were slight and were demonstrated by subtle increases in the proportion of downstream facing cells (reduced particle imbrication) and the frequency of steep local slopes (roughening of the surface following a breakup of grain-scale structure). The elimination of larger-scale structural effects of water-working was also demonstrated by a reduction in the length of curvature of the 1D variograms (to  $\widetilde{h}_x \approx 2$ ) which suggests the limit of spatial dependence (structure) is reached at the scale of coarse surface grains. Powell et al. (2016) similarly recorded a reduced scale of process for their artificial screeded beds.

In summary, the treatment process used for Experiments A and B generated larger adjustments in grain- and larger- scales of structure than had been observed for  $W_{1.1}$  and  $W_{1.2}$  over the sequence of interannual flows. The shifts in bed structure following treatment were, however, subtle and not sufficient to produce a surface that was clearly structurally distinct from their pre-treated counterparts, e.g. compared to the more defined division between artificially screeded and water worked beds (Coleman et al., 2011). Since only slight differences persisted between the structured and pre-treated beds, subsequent changes in bed structure toward a pre-treated state were, therefore, relatively difficult to identify over the course of the initial and extended periods of water-working.

During the initial period of restructuring, the surfaces were observed to slightly fine (Figure 5.14a) which reflected the rearrangement of surface grains to a water-worked form. The initial adjustments in grain size were accompanied by extensive changes in bed topography (Figure 5.12) that were comparable to those observed over the largest flows for  $W_{1.1}$  and  $W_{1.2}$  but less impactful than surface treatment. The short-term effects of water-working appeared, from the inspection of DTMs, to rework the surface sufficiently to develop ‘natural’ bed structure, i.e. generate a coarse surface armour inhabited by cluster bedforms and larger-scale, extended patches of higher and lower elevations. The rapid formation of a natural and stable bed structure was similarly noted by previous workers (e.g. Marion et al., 2003; Cooper and Tait, 2009). For example, a rapid adjustment in the spatial distribution of bedforms was observed for natural beds (Lamarre and Roy, 2008) and the formation of meso-scale topography for artificial beds (Powell et al., 2016) upon on the onset of water-working. However, Oldmeadow and Church (2006) found this incipient bed structure was not

sufficiently resilient to resist larger flow events and reverted toward an unstructured condition.

Further to the visual adjustments in bed character, the initial response of the surface to water-working was also characterised by an increase in the frequency of elevations <50 mm about the mean bed level and the skew of the slope distribution and associated decreases in surface roughness and median local slope (Figures 5.14b and 5.14e; Table 5.3). While larger and longer flows appeared on occasion to generate a greater smoothing of the surface during initial restructuring (and greater changes in the form of the bed elevation and slope distributions), an acceptance of the null hypothesis of least squares regression found absolute changes in the statistical parameters were not a strict function of event magnitude or duration. Previous workers, in flume-based research, have by contrast found the surfaces of mobile armours to roughen under stronger formative flows while maintaining bed texture (e.g. Mao et al., 2011). This may reflect the use of unstructured (topographically smooth) flume beds as the starting-point for restructuring compared to the treated (roughened) surfaces used in this study. In addition, the rapid response of bed structure was also illustrated by larger-scale modifications. For instance, during the initial period of restructuring the sill variance extended to lengths beyond the size of coarse surface grains which reflects the growth of meso-scale topography. The extension of the range of process was similarly noted following the water-working of artificial beds in Powell et al. (2016). However, while changes in several of the statistical parameters were more pronounced than those observed over the largest flows for  $W_{1.1}$  and  $W_{1.2}$ , they were subtle. More significantly, the structural characteristics of the initially restructured beds were not clearly distinguishable from their treated counterparts and remained within the bounds of values at  $W_{1.1}$  and  $W_{1.2}$ . Therefore, it was difficult to determine whether bed structure had reverted to a pre-treated condition over the initial period of restructuring.

Little change was observed in bed texture and structure over subsequent periods of restructuring (Figure 5.14; Table 5.3). In this regard, modifications of bed topography were comparable to those observed for  $W_{1.1}$  and  $W_{1.2}$  and largely limited to the movement of individual surface grains. Adjustments in the statistical parameters were similarly modest and remained within the bounds of values at  $W_{1.1}$  and  $W_{1.2}$ . During this period, the reversal

of bed structure toward a treated condition (cf. Oldmeadow and Church, 2006) was not observed. When compared to the more pronounced textural and structural adjustments recorded over initial restructuring, this suggests the bed has been sufficiently reworked such that it is more resilient to subsequent flows than a treated condition. The comparison of absolute changes in the statistical parameters with  $\hat{Q}$  and  $T_{\text{comp}}$  (Figure 5.15) also demonstrated that, for given magnitude and duration of effective flow, adjustments were greater during initial than subsequent periods of restructuring. A similar pattern of initial pronounced adjustments in bed structure and longer-term persistence of this adjusted form were observed in the flume and flume experiments of Powell et al. (2016) and Lamarre and Roy (2008) respectively. This reflected the rapid attainment of a stable, equilibrium surface that limited sediment transport and muted further grain- and meso-scale modifications in bed topography. However, given the subtlety of differences in bed structure between pre-treated, treated and restructured surfaces in this study, it is not possible to conclude whether and to what extent water-worked structure has ‘recovered’ toward a natural condition.

### **5.4.3. Summary**

In summary, the characteristics of bed texture and structure were broadly maintained over the range of interannual, effective flows; from those capable of moving individual surface grains to those able to rework larger scales of topography. Thus, while the bar was an active transport layer, i.e. mobile in response to flood events, the statistical characteristics of the surface were not affected by temporal flow fluctuations (i.e. a stable texture and structure were preserved; Parker, 2007). The slight changes in bed structure over time were largely independent of event magnitude or duration although larger and longer floods typically generated greater absolute changes in surface roughness, i.e. that were not cumulative over time. Surface treatment was effective in generating changes in bed texture and structure that were more pronounced than those observed for  $W_{1.1}$  and  $W_{1.2}$ . However, given the subtlety of these changes, it was not possible to clearly distinguish pre-treated and treated beds (T-1 vs. T0). A pronounced adjustment in bed texture and structure was observed in response to the initial period of water-working (T0-T1) while adjustments over subsequent periods of restructuring were relatively modest (T1-Tn), i.e. the greatest modifications in grain and

larger scales of structure occur on the onset of water-working. While this could suggest the potential for larger flows to generate a more rapid reversion of structure toward a pre-treated, ‘natural’ condition, adjustments were subtle and largely remained within the bounds of values for  $W_{1.1}$  and  $W_{1.2}$ . It was, therefore, difficult to prove whether bed structure had fully ‘recovered’.

## Chapter 6 Conclusion

The conclusions of this work are:

- Following previous workers (e.g. Hodge et al., 2009a, 2009b), terrestrial LiDAR has again been found to provide an effective approach in capturing high resolution topographic data from alluvial streambeds and in turn characterising bed structural and textural features. Through correct surveying protocol, e.g. Heritage and Hetherington (2007), the error associated with the registration of individual scans was reduced to  $\leq 1$  mm. This allowed for the production of highly precise and accurate surfaces, with an RMSE of residuals in the range  $1.8 \leq \text{RMSE} \leq 3.7$  mm, despite increasing the areal extent of the patches to  $\geq 2$  m<sup>2</sup>. This study advances the use of TLS in characterising alluvial streambed topography by conducting repeat surveys and, in doing so, was able to monitor the dynamic change of bed structure. As referencing errors to a TS-defined coordinate system were reduced to  $\leq 10$  mm, the movement of individual surface grains could be identified between DTMs which helped evaluate slight morphological changes.
- The eight gravel patches sampled from four perennial channels were characterised by a water-worked bed structure that was largely consistent (i.e. within the bounds of values for the structural parameters) with the observations made by previous workers. In this respect, the humid temperate patches comprised a coarse surface armour in which grains showed the potential to imbricate and assemble into cluster bedforms (Laronne and Carson, 1976; Brayshaw, 1984). At larger scales, the surface was characterised by a meso-scale topography which took the form of extended patches

of higher and lower bed elevations (Powell et al., 2016). In terms of the statistical parameters of bed structure, the humid temperate patches were characterised by a positively skewed and peaked, near-normal distribution of bed elevations (Aberle and Nikora, 2006; Coleman et al., 2011), the standard deviation of which was largely a function of bed texture (Heritage and Milan, 2009; Brasington et al., 2012). Since the humid temperate patches adhere to a structural ‘envelope’, their character is inherently predictable. This predictability has wider implications for geomorphologists and engineers; for instance, as Chapter 1 describes, for the effectiveness of channel management strategies and the success of river restoration schemes which rely on an understanding of bed surface character.

- The humid temperate patches from different (gritstone and limestone) lithologies and different geomorphic settings showcased the potential variability of streambed structure in perennial channels. While previous workers have suggested that grain shape plays an important role on bed packing arrangements, this study found little evidence to suggest grain-scale structure was significantly different between the gritstone and limestone patches. There was, however, some evidence that particle shape moderated larger scales of structure and, in this respect, bladed grains assemble into a greater variety of different forms compared to more rounded grains. The effect of local geomorphic setting was found to generate greater differences in bed structure than particle shape. This was most notably demonstrated by the  $M_1$  patch which comprised fine gravels, organised loosely across a relatively planar bed surface (devoid of meso-scale topography). Through the inspection of DTMs, this gave the impression of a surface that was structurally distinct from the other humid temperate patches. These contrasts in humid temperate bed structure were further illustrated through the analysis of bed elevation pdfs (narrow, peak distribution), variograms (lower  $\tilde{\gamma}$  with  $\tilde{h}$ ) and polar plots of combined slope-aspect (narrow, peaked distribution of shallow slopes). The described variability in structural character generated by geomorphic setting will not only have implications on boundary resistance and entrainment thresholds but also on local flooding and bedload flux. Moreover, this range in structural character will affect the local dynamics and

geomorphic response of the channel and must be acknowledged for the effective administration of alluvial river systems.

- The structural characteristics of alluvial streambeds from ephemeral channels were, for the first time, evaluated using a suite of statistical parameters. Through this process, the three patches sampled from two dryland ephemeral channels were found, in contrast to their humid temperate counterparts, to be characterised by infilled, finer grained surfaces. The streambed structure of these ephemeral channels was limited to grain-scale topography which was largely dictated by coarse, emergent obstacle clasts and their downstream scoured wakes. The differences in bed structure between the humid temperate and dryland patches were illustrated through the analysis of bed elevation pdfs (dryland = comparatively narrow, peaked distribution), the bed elevation moment  $Ku_z^*$  (typically higher for the dryland patches) and variograms (shorter range of influence at the scale of the largest surface grains). As Chapter 1 describes, the difference in surface character for alluvial streambeds from different environments reflects the ability for the system to attain an equilibrium. Ephemeral channels in dryland environments are shaped by sporadic, flashy flooding which generates high surface runoff which limits the ability of the system to reach a stable condition. The surface character that results from this state of disequilibrium was broadly comparable for the three dryland patches and, following the humid temperate patches, this predictability can be utilised for channel management strategies.
- Besides several differences in bed structure, there were similarities in several statistical parameters for the humid temperate and dryland patches. For instance, the bed elevation pdfs for all 11 gravel patches were characterised by a positively skewed, near-normal form that was distinct from those exhibited by unworked beds. Furthermore, the standard deviation of the bed elevation distribution was largely a function of bed texture (see also Storz-Peretz and Laronne, 2013) and the local metrics of inclination, slope and aspect were broadly comparable between the humid temperate and dryland patches. Therefore, the dryland patches were described by a

water-worked bed structure (i.e. different from an unworked bed) that could, for select structural metrics, be distinguished from their humid temperate counterparts.

- The influence of bed structure on particle stability was examined through the force balance parameters -  $\Phi$ ,  $p$  and  $e$  – and a grain entrainment model (Wiberg and Smith, 1987; Kirchner et al., 1990; Hodge et al., 2013) which estimated critical and dimensionless critical shear stresses. Through this analysis of particle stability, grain pivoting angle was found to vary widely for the humid temperate patches from pocket-to-pocket and between patches reflecting the heterogeneity of the surfaces. Grain protrusion was, however, minimised by the bed structure of the humid temperate patches. In contrast, the dryland patches were characterised by an infilled bed structure which limited the variety of surface pockets and, in doing so, reduced the range of pivoting angles from pocket-to-pocket and patch-to-patch. While it might be expected that infilling by fines reduced the depth of surface pockets, and hence pivoting angles, the presence of a relatively planar patch topography increased grain protrusion above that observed for the humid temperate patches. In addition, the higher grain protrusion for the dryland patches was sufficient to exceed the effects of particle embedding (higher pivoting angles with relative grain size) and ensured that bed stability was lower than the humid temperate patches. Despite differences in bed stability, a condition of equal mobility characterised the two humid temperate and three dryland patches (Parker and Klingeman, 1982).
- The characteristics of bed texture and structure were found to be maintained over a range of competent, perennial flows which were able to generate grain- and larger-scale modifications of the surface. The adjustments in bed structure over time were largely invariant of event magnitude or duration although longer flows were found to generate greater absolute changes in surface roughness, i.e. that were not cumulative over time. The observation that humid temperate streambed texture and structure remained within a dynamic equilibrium over the monitoring period has wider implications for geomorphologists (predictable boundary resistance and entrainment

thresholds) and river engineers (stable surface character and predictable dynamic response).

- Surface treatment (T-1 to T0) was responsible for generating greater changes in bed texture and structure than natural temporal dynamics. However, given the relative subtlety of these adjustments, it was not possible to clearly distinguish pre-treated and treated beds across all statistical parameters. Following surface treatment, pronounced adjustments in bed texture and structure were observed during the first sample period (T0 to T1) while restructuring in subsequent sample periods (T1 to T $n$ ) was comparatively modest. This could suggest a stable bed structure develops rapidly during initial restructuring, as has been observed by previous workers (e.g. Mao et al., 2011; Powell et al., 2016). This has wider implications for channel management, for instance in river restoration, where imposed changes to flow regime, sediment supply or to the channel character will generate a rapid response in streambed structure to an equilibrium state. However, while stronger flows tended to generate greater absolute changes in the metrics, and hence structural character, given the subtlety of changes (comparable to natural temporal dynamics) it was not possible to conclusively determine whether bed structure reverted toward a pre-treated, natural condition.

## **6.1. Further work**

Further to this research, subsequent work should seek to consider:

- Improvements to data processing to increase the precision of the filtered point cloud datasets and the accuracy of associated DTMs which will reduce the error associated with calculated surface statistics; particularly since changes in the structural metrics between sites and over survey series were, in most cases, relatively subtle. While the potential for increasing the accuracy of the measured surfaces will be limited by the quality of the range measurements, further improvements may be achieved by modifying the existing data processing workflow, for example, through the addition of newly developed filters. Continued advancements in methods of data capture and

the development of data cleaning algorithms (e.g. *Leica's* Mixed Pixel filter for the ScanStation P20 data) will aid this increase in data quality prior to processing.

- The structural characteristics for a wider variety of gravel patches sampled from a more diverse range of perennial and ephemeral reaches (inclusive of different types of lithology, local geomorphic setting, stream order and flow regime (Base Flow Index)). This should primarily focus on bed structure in ephemeral channels since the results presented in this study are the first of their kind and limited and so require consolidation. Further work should adopt a considered approach by using smaller patches ( $\leq 1 \text{ m}^2$ ) to capture grain scale structure (through local metrics of inclination, slope and aspect) and larger patches ( $\geq 4 \text{ m}^2$ ) to evaluate larger scales of sedimentary structure (through 1D and 2D variogram analyses).
- The link between bed structure and particle stability for a greater number of gravel patches in humid temperate and dryland environments to build on this preliminary analysis. In addition, further study should seek to investigate temporal changes in the force balance parameters (and, hence, critical and dimensionless critical shear stress) over the course of natural flows. Furthermore, the grain entrainment model should be used to evaluate differences in bed stability between the natural and treated patches (i.e. test whether sediment transport from an unstructured bed conforms to equal mobility) and monitor the stability of gravel patches during shorter- and longer-periods of restructuring.
- Increasing the frequency of survey intervals during survey series analysis to further isolate the contribution of individual flood events to adjustments in bed texture and structure. To facilitate this, recent advancements in terrestrial LiDAR technologies have led to further increases in the rate of data acquisition while improvements in Structure-from-Motion (SfM) Photogrammetry have allowed the technique to provide a low-cost alternative to TLS for capturing highly accurate and detailed topographic information from smaller gravel patches (Pearson et al., 2017; Groom et al., 2018).

## References

- Aberle, J., and Nikora, V., 2006. Statistical properties of armoured gravel bed surfaces. *Water Resources Research*, 42, W11414.
- Aberle, J., and Smart, G.M., 2003. The influence of roughness structure on flow resistance on steep slopes. *Journal of Hydraulic Research*, 41(3), 259-269.
- Aberle, J., Nikora, V., Henning, M., Ettmer, B., and Hentschel, B., 2010. Statistical characterization of bed roughness due to bed forms: A field study in the Elbe River at Aken, Germany. *Water Resources Research*, 46, W03521.
- Alho, P., Vaaja, M., Kukko, A., Kasvi, E., Kurkela, M., Hyypä, J., Hyypä, H., and Kaartinen, H., 2011. Mobile laser scanning in fluvial geomorphology: mapping and change detection of point bars. *Zeitschrift für Geomorphologie*, 55, 31-50.
- Anderson, M.G., and Richards, K.S., 1979. Statistical modelling of channel form and process. In: Wrigley, N. (Ed.), *Statistical Applications in the Spatial Sciences*, Pion: London, 205-228.
- Andrews, E.D., 1983. Entrainment of gravel from naturally sorted riverbed material. *Geological Society of America Bulletin*, 94, 1225-1231.
- Andrews, E.D., 1994. Marginal bed load transport in a gravel bed stream, Sagehen Creek, California. *Water Resources Research*, 30(7), 2241-2250.
- Andrews, E.D., and Erman, D.C., 1986. Persistence in the size distribution of surficial bed material during an extreme snowmelt flood. *Water Resources Research*, 22(2), 191-197.
- Andrews, E.D., and Parker, G., 1987. Formation of coarse surface layer as the response to gravel mobility. In: Thorne, C.R., Bathurst, J.C., and Hey, R.D. (Eds.), *Sediment transport in gravel-bed rivers*. Wiley: Chichester, 269-300.
- Angelopoulos, N.V., 2013. Identifying limitations of monitoring the success of river rehabilitation schemes for freshwater fish. PhD thesis, University of Hull.
- Ashworth, P.J., and Ferguson, R.I., 1989. Size-Selective Entrainment of Bed Load in Gravel Bed Streams. *Water Resources Research*, 25(4), 627-634.
- Barziali, R., Laronne, J.B., and Reid, I., 2013. Effects of changes in fine-grained matrix on bedload sediment transport in a gravel-bed river. *Earth Surface Processes and Landforms*, 38, 441-448.
- Bathurst, J.C., 2002. At-a-site variation and minimum flow resistance for mountain rivers. *Journal of Hydrology*, 269, 11-26.
- Behan, A., 2000. On the matching accuracy of rasterised scanning laser altimeter data. *International Archives on Photogrammetry and Remote Sensing*, XXXIII, 75-82.

- Bergeron, N.E., 1996. Scale-space analysis of stream bed roughness in coarse gravel-bed streams. *Mathematical Geology*, 27, 537-561.
- Bertin, S., and Friedrich, H., 2014. Measurement of gravel-bed topography: Evaluation study applying statistical roughness analysis. *Journal of Hydraulic Engineering*, 140, 269-279.
- Bertin, S., and Friedrich, H., 2016. Field application of close-range digital photogrammetry (CRDP) for grain-scale fluvial morphology studies. *Earth Surface Processes and Landforms*, 41, 1358-1369.
- Biggs, B.J.F., Duncan, M.J., Francoeur, S.N., and Meyer, W.D., 1997. Physical characterisation of microform bed cluster refugia in 12 headwater streams, New Zealand. *New Zealand Journal of Marine and Freshwater Research*, 31(4), 413-422.
- Billi, P., 1987. Sediment storage, bed fabric and particle features of two mountain streams at Plynlimon (mid-Wales). Wallingford, Institute of Hydrology, 39 pp. (IH Report No.97) (Unpublished)
- Billi, P., 1988. A note on cluster bedform behaviour in a gravel-bed river. *Catena*, 15(5), 473-481.
- Black, W.W., 1950. The Carboniferous Geology of the Grassington Area, Yorkshire. *Proceedings of the Yorkshire Geological Society*, 28, 29-42.
- Bluck, B.J., 1982. Texture of gravel bars in braided streams. In: Hey, R.D., Bathurst, J.C., and Thorne, C.R. (Eds.), *Gravel-bed rivers: fluvial processes, engineering and management*. Wiley: Chichester, 339-355.
- Bluck, B.J., 1987. Bed forms and clast size changes in gravel-bed rivers. In: Richards, K. (Ed.), *River Channels: Environment and process, Institute of British Geographers Special Publications*, 17, Blackwell: Oxford, 159-178.
- Boon, D.P., and Evans, H.M., 2008. Walkover survey of a landslide on the A57 (Snake Pass) road at Cowms Moor, Derbyshire in January 2008. Nottingham, UK, British Geological Survey, 19pp. (OR/08/006) (Unpublished)
- Booth, A.M., Hurley, R., Lamb, M.P., and Andrade, J.E., 2014. Force chains as the link between particle and bulk friction angles in granular material. *Geophysical Research Letters*, 41, 8862-8869.
- Bowman, D., Shechnovich-Firtel, Y., and Devora, S., 2007. Stream channel convexity by continuous base level lowering, the Dead Sea, Israel. *Geomorphology*, 114, 227-237.
- Brandt, S.A., 2000. Classification of geomorphological effects downstream of dams. *Catena*, 40, 375-401.
- Brasington, J., Rumsby, B.T., and McVey, R.A., 2000. Monitoring and modelling morphological change in a braided gravel-bed river using high resolution GPS-based survey. *Earth Surface Processes and Landforms*, 25(9), 973-990.

- Brasington, J., Langham, J., and Rumsby, B., 2003. Methodological sensitivity of morphometric estimates of coarse fluvial sediment transport. *Geomorphology*, 53(3-4), 299-316.
- Brasington, J., Vericat, D., and Rychkov, I., 2012. Modeling river bed morphology, roughness, and surface sedimentology using high resolution terrestrial laser scanning. *Water Resources Research*, 48, W11519.
- Bray, D.I., 1980. Evaluation of effective boundary roughness for gravel-bed rivers. *Canadian Journal of Civil Engineering*, 7(2), 392-397.
- Bray, D.I., 1982. Flow resistance in gravel-bed rivers. In: Hey, R.D., Bathurst, J.C., and Thorne, C.R. (Eds.), *Gravel-Bed Rivers*, Wiley: Chichester, 109-137.
- Brayshaw, A.C., 1984. Characteristics and origin of cluster bedforms in coarse-grained alluvial channels. In: Koster, E.H., and Steel, R.J. (Eds.), *Sedimentology of Gravels and Conglomerates*. Canadian Society of Petroleum Geologists: Calgary, 77-85.
- Brayshaw, A.C., 1985. Bed microtopography and entrainment thresholds in gravel-bed rivers. *Geological Society of America Bulletin*, 96, 218-223.
- Brayshaw, A.C., Frostick, L.E., and Reid, I., 1983. The hydrodynamics of particle clusters on sediment entrainment in coarse alluvial channels. *Sedimentology*, 30, 137-140.
- Brewer, P.A., Leeks, G.J.L., and Lewin, J., 1992. Direct measurement of in-channel abrasion processes. In: Bogen, J., Walling, D., and Day, T.J. (Eds.), *Erosion and sediment transport monitoring programmes in river basins*. IAHS Publication 210, 21-30.
- Bridge, J.S., and Bennett, S.J., 1992. A model for the entrainment and transport of sediment grains of mixed sizes, shapes, and densities. *Water Resources Research*, 20, 476-490.
- Brown, A., and Willetts, B., 1997. Sediment flux, grain sorting and the bed condition. In Wang, S.S.Y., and Carstens, T. (Eds.), *Environmental and Coastal Hydraulics: Protecting the Aquatic Habitat*, 2, ASCE: New York, 1469-1474.
- Buffin-Belanger, T., and Roy, A.G., 1998. Effects of a pebble cluster on the turbulent structure of a depth-limited flow in a gravel-bed river. *Geomorphology*, 25, 254-267.
- Buffington, J.M., and Montgomery, D.R., 1997. A systematic analysis of eight decades of incipient motion studies, with special reference to gravel-bedded rivers. *Water Resources Research*, 33(8), 1993-2029.
- Buffington, J.M., and Montgomery, D.R., 1999. Effects of sediment supply on surface textures of gravel-bed rivers. *Water Resources Research*, 35(11), 3523-3530.
- Buffington, J. M., Dietrich, W.E., and Kirchner, J.W., 1992. Friction angle measurements on a naturally formed gravel stream bed: Implications for critical boundary shear stress. *Water Resources Research*, 28(2), 411-425.
- Bull, W.B., 1997. Discontinuous ephemeral streams. *Geomorphology*, 19, 227-276.

- Bunte, K., and Abt, S.R., 2001. *Sampling Surface and Subsurface Particle-Size Distributions in Wadable Gravel- and Cobble-Bed Streams for Analyses in Sediment Transport, Hydraulics and Streambed Monitoring*. RMRS-GTR-74. US Forest Service, Rocky Mountain Research Station, Fort Collins, Colorado. [http://www.fs.fed.us/rm/pubs/rmrs\\_gtr74.html](http://www.fs.fed.us/rm/pubs/rmrs_gtr74.html)
- Bunte, K., Abt, S.R., Swingle, K.W., Cenderelli, D.A., and Schneider, J.M., 2013. Critical Shields values in coarse-bedded steep streams. *Water Resources Research*, 49(11), 7427-7447.
- Butler, J.B., Lane, S.N., and Chandler, J.H., 2001. Automated extraction of grain-size data from gravel surfaces using digital image processing. *Journal of Hydraulic Research*, 39, 519-529.
- Carbonneau, P.E., Lane, S.N., and Bergeron, N.E., 2003. Cost-effective non-metric close-range digital photogrammetry and its application to a study of coarse gravel river beds. *International Journal of Remote Sensing*, 24, 2837-2854.
- Charlton, F.G., Brown, P.M., and Benson, R.W., 1978. The hydraulic geometry of some gravel rivers in Britain. Report IT180, Hydraulics Research Station, Wallingford, England.
- Chepil, W.S., 1959. Equilibrium of soil grains at the threshold of movement by wind. *Soil Science Society of America Proceedings*, 23(6), 422-428.
- Church, M., 1978. Palaeohydrological reconstructions from a Holocene valley fill. In: Miall, A.D. (Ed.), *Fluvial Sedimentology*. Memoir of the Canadian Society of Petroleum Geologists: Calgary, 5, 743-72.
- Church, M.A., McLean, D.G., and Wolcott, J.F., 1987. River bed gravels: sampling and analysis. In: Thorne, C.R., Bathurst, J.C., and Hey, R.D. (Eds.), *Sediment Transport in Gravel Bed Rivers*. Wiley: New York, 43-79.
- Church, M., Hassan, M.A., and Wolcott, J.F., 1998. Stabilizing self-organized structures in gravel-bed stream channels: field and experimental observations. *Water Resources Research*, 34(11), 3169-3179.
- Clayton, J. A., and Pitlick, J., 2008. Persistence of the surface texture of a gravel bed river during a large flood. *Earth Surface Processes and Landforms*, 33(5), 661-673.
- Clifford, N.J., Robert, A., and Richards, K.S., 1992. Estimation of flow resistance in gravel-bedded rivers: a physical explanation of the multiplier of roughness length. *Earth Surface Processes and Landforms*, 17, 111-126.
- Cohen, H., and Laronne, J.B., 2005. High rates of sediment transport by flashfloods in the southern Judean Desert, Israel. *Hydrological Processes*, 19(8), 1687-1702.
- Coleman, S.E., Nikora, V.I., and Aberle, J., 2011. Interpretation of alluvial beds through bed elevation distribution moments. *Water Resources Research*, 47(11), W11505.

- Cooper, J.R., and Tait, S.J., 2009. Water-worked gravel beds in laboratory flumes – a natural analogue? *Earth Surface Processes and Landforms*, 34, 384-397.
- Coulthard, T.J., Kirkby, M.J., and Macklin, M.G., 1998. Modelling the 1686 flood of Cam Gill Beck, Starbotton, Upper Wharfedale. In: Howard, A.J., and Macklin, M.G. (Eds.), *The Quaternary of the Eastern Yorkshire Dales: Field Guide*. Quaternary Research Association: London. 11-18.
- Curran, J.C., and Waters, K., 2014. The importance of bed sediment sand content for the structure of a static armour layer in a gravel bed river. *Journal of Geophysical Research: Earth Surface*, 199, 1484-1497.
- Deal, E., Braun, J., and Botter, G., 2018. Understanding the Role of Rainfall and Hydrology in Determining Fluvial Erosion Efficiency. *Journal of Geophysical Research: Earth Science*, 123, 744-778.
- DeCarlo, L.T., 1997. On the Meaning and Use of Kurtosis. *Psychological Methods*, 2(3), 292-307.
- de Jong, C., 1991. A re-appraisal of the significance of obstacle clasts in cluster bedform dispersal. *Earth Surface Processes and Landforms*, 16(8), 737-744.
- de Jong, C., 1995. Temporal and spatial interactions between river bed roughness, geometry, bedload transport and flow hydraulics in Mountain Streams – Examples from Squaw Creek, Montana USA and Lainbach/Schmiedlaine, Upper Bavaria, Germany. PhD Thesis, Freie Universitaet Berlin, Germany. *Berliner Geographische Abhandlungen* 59, 1-229.
- de Jong, C., and Ergenzinger, P., 1995. Interrelations between mountain valley form and river bed arrangement. In: Hickin, T. (Ed), *River geomorphology*. Wiley: Chichester, UK, 55-91.
- Deutsch, C.V., and Journel, A.G., 1998. *GSLIB Geostatistical Software Library and User's Guide*. Oxford University Press: New York, 369 pp.
- Diepenbrock, M.A., and De Jong, C., 1994. Quantification of textural pattern characteristics by image analysis of sediment surfaces: Examples from active and paleo-surfaces in steep, coarse-grained mountain environments. In: Ergenzinger, P. and Schmidt, K.H. (Eds.), *Dynamics and Geomorphology in Mountain Rivers*, Springer: New York, 301-314.
- Dietrich, W.E., Kirchner, J.W., Ikeda, H., and Iseya, H., 1989. Sediment supply and the development of the coarse surface layer in gravel-bedded rivers. *Nature*, 340, 215-217.
- Diplas, P., 1987. Bedload transport in gravel-bed streams. *Journal of Hydraulic Engineering, ASCE*, 113(3), 277-291.
- Eagleson, P.S., and Dean, R.G., 1961. Wave-induced motion of bottom sediment particles. *Transactions of the American Society of Civil Engineers*, 126(1), 1162-1189.
- Egiazaroff, I.V., 1965. Calculation of nonuniform sediment concentration. *Journal of the Hydraulics Division, ASCE*, 91(4), 225-247.

- Einstein, H.A., 1950. The bed-load function for sediment transportation in open channel flow. *U.S. Department of Agriculture Technical Bulletin, 1026*, p.71.
- Entwistle, N.S., and Fuller, I.C., 2009. Terrestrial laser scanning to derive surface grain size facies character of gravel bars. In *Laser Scanning for the Environmental Sciences*. Wiley-Blackwell: Oxford, 102-114.
- Entwistle, N.S., Heritage, G.L., Johnson, K., and Hetherington, D., 2007. Repeat terrestrial laser scanner survey of pebble cluster creation and formation in response to flow change. *Proceedings RSPSoc 2007*, University of Newcastle upon Tyne, September.
- ESRI, 2011. ArcGIS Desktop: Release 10. Redlands, CA: Environmental Systems Research Institute.
- Everall, N.C., 2010. The aquatic ecological status of the rivers of the Upper Dove Catchment in 2009. *Natural England Research Reports, Number 046*, Natural England, Sheffield
- Everall, N.C., Farmer, A., Heath, A.F., Jacklin, T.E., and Wilby, R.L., 2012. Ecological benefits of creating messy rivers. *Area, 44*(4), 470-478.
- Ewen, C. 2010. Characterisation of Coarse-Grained Alluvial Bed Roughness at Multiple Scales using Geomorphic Parameters. PhD thesis, University of Leicester.
- Fenton, J.D., and Abbott, J.E., 1977. Initial movement of grains on a stream bed: The effect of relative protrusion. *Proceedings of the Royal Society of London (A), 352*, pp.523-537.
- Ferguson, R.I., 1987. Hydraulic and sedimentological controls of channel pattern. In: Richards, K.S. (Ed.), *River channels: environment and process*, Blackwell: Oxford, 129-158.
- Ferguson, R.I., Prestegard, K.L., and Ashworth, P.J., 1989. Influence of Sand on Hydraulics and Gravel Transport in a Braided Gravel Bed River. *Water Resources Research, 25*(4), 635-643.
- Folk, R.L., and Ward, W.C., 1957. Brazos River bar: A study of the significance of grain size parameters. *Journal of Sedimentary Petrology, 27*(1), 3-26.
- Franceschi, M., Teza, G., Preto, N., Pesci, A., Galgaro, A., and Girardi, S., 2009. Discrimination between marls and limestones using intensity data from terrestrial laser scanner. *ISPRS Journal of Photogrammetry and Remote Sensing, 64*(6), 522-528.
- Frey, P., and Church, M., 2009. How river beds move. *Science, 325*, 1509-1510.
- Frostick, L.E., and Reid, I., 1989. Climate versus controls of fan sequences: lessons from the Dead Sea, Israel. *Journal of the Geological Society, 146*, 527-538.
- Frumkin, A., 2001. The Cave of the Letters Sediments: Indication of an Early Phase of the Dead Sea Depression? *The Journal of Geology, 109*, 79-90.
- Gessler, J., 1970. Self-stabilizing tendencies of alluvial channels. *Journal of the Waterways, Harbors and Coastal Engineering Division, 96*(2), 235-249.

- Gessler, J., 1971. Beginning and ceasing of sediment motion. In Shen, H.W. (Ed.), *River mechanics*, Colorado State University: Fort Collins, CO, 7, 1-7:22.
- Gilat, A., 1987. The Geological Map of Israel (1:50,000), Har Hezron Sheet, 15-II. The Geological Survey of Israel, Geological and Structural maps.
- Gomez, B., 1983. Temporal variations in the particle size distribution of surficial bed material: The effect of progressive bed armouring. *Geografiska Annaler: Series A, Physical Geography*, 65, 183-192.
- Gomez, B., 1993. Roughness of stable, armoured gravel beds. *Water Resources Research*, 29, 3631-3642.
- Gomez, B., 1994. Effects of particle shape and mobility on stable armor development. *Water Resources Research*, 30, 2229-2239.
- Graf, W.H., 1991. Flow resistance over a gravel bed: Its consequence on initial sediment motion. In: Armanini, A., and DiSilvio, G. (Eds.), *Fluvial Hydraulics of Mountain Regions*, Springer-Verlag: Berlin, 17-32.
- Graham, D.J., Reid, I., and Rice, S.P., 2005ab. Automated sizing of coarse-grained sediments: Image processing procedures. *Mathematical Geology*, 37(1), 1-28.
- Graham, D.J., Reid, I., and Rice, S.P., 2005ab. A transferable method for the automated grain sizing of river gravels. *Water Resources Research*, 41, W07020.
- Gregory, K.J., 2006. The human role in changing river channels. *Geomorphology*, 79, 172-191.
- Groom, J., Bertin, S., and Friedrich, H., 2018. Assessing Intra-Bar Variations in Grain Roughness Using Close-Range Photogrammetry. *Journal of Sedimentary Research*, 88(5), 555-567.
- Gustavson, T.C., 1974. Sedimentation on gravel outwash fans, Malaspina glacier foreland, Alaska. *Journal of Sedimentary Research*, 44(2), 374-389.
- Habersack, H., M. Rinaldi, H. Piegay, 2008. *Gravel bed rivers VI: from process understanding to river restoration*, Elsevier: Amsterdam; London, 817 pp.
- Hassan, M.A. and Church, M., 2000. Experiments on surface structure and partial sediment transport on a gravel bed. *Water Resources Research*, 36, 1885-1895.
- Hassan, M.A., and Reid, I., 1990. The influence of microform bed roughness elements on flow and sediment transport in gravel bed rivers. *Earth Surface Processes and Landforms*, 15, 739-750.
- Hassan, M.A., Egozi, R. and Parker, G., 2006. Experiments on the effect of hydrograph characteristics on vertical grain sorting in gravel bed rivers. *Water Resources Research*, 42, W09408.

- Hassan, M.A., Marren, P.M., and Schwartz, U., 2009. Bar structure in an arid ephemeral stream. *Sedimentary Geology*, 221, 57-70.
- Haynes, H., and Pender, G., 2007. Stress history effects on graded bed stability. *Journal of Hydraulic Engineering*, 33, 343-349.
- Heaney, T., 2013. River Ashop & River Noe Silt Issues: improving the transfer of raw water to Bamford WTW in the Peak District. *UK Water Projects 2013*, 239-241.
- Hendrick, R.R., Ely, L.L., and Papanicolaou, A.N., 2010. The role of hydrologic processes and geomorphology on the morphology and evolution of sediment clusters in gravel-bed rivers. *Geomorphology*, 114, 483-496.
- Heritage, G. and Hetherington, D., 2007. Towards a protocol for laser scanning in fluvial geomorphology. *Earth Surface Processes and Landforms*, 32, 66-74.
- Heritage, G.L., and Milan, D.J., 2009. Terrestrial Laser Scanning of grain roughness in a gravel-bed river. *Geomorphology*, 113, 4-11.
- Heritage, G.L., Milan, D.J., Large, A.R.G., and Fuller, I.C., 2009. Influence of survey strategy and interpolation model on DEM quality. *Geomorphology*, 112(3-4), 334-344.
- Hey, R.D., 1979. Flow resistance in gravel-bed rivers. *Journal of the Hydraulic Division, ASCE*, 105(HY4), 365-379.
- Hey, R.D., and Winterbottom, A.N., 1990. River Engineering in National Parks: the case of the River Wharfe, U.K. *Regulated Rivers: Research and Management*, 5, 35-44.
- Higgs, G., 1997. Fluvial geomorphology of Wales. In: Gregory, K.J. (Ed.), *The Fluvial Geomorphology of Great Britain*, Chapman and Hall: London, 115-172.
- Hodge, R.A., 2010. Using simulated Terrestrial Laser Scanning to analyse errors in high-resolution scan data of irregular surfaces. *ISPRS Journal of Photogrammetry and Remote Sensing*, 65, 227-240.
- Hodge, R., Brasington, J., and Richards, K., 2009a. *In-situ* characterisation of grain-scale fluvial morphology using Terrestrial Laser Scanning. *Earth Surface Processes and Landforms*, 34(7), 954-968.
- Hodge, R., Brasington, J., and Richards, K., 2009b. Analysing laser-scanned Digital Terrain Models of gravel bed surfaces: Linking morphology to sediment transport processes and hydraulics. *Sedimentology*, 56(7), 2024-2043.
- Hodge, R., Sear, D.A., and Leyland, J., 2013. Spatial variations in surface sediment structure in riffle-pool sequences: A preliminary test of the Differential Sediment Entrainment Hypothesis (DSEH). *Earth Surface Processes and Landforms*, 38, 449-465.
- Hohenthal, J., Alho, P., Hyypä, J., and Hyypä, H., 2011. Laser scanning applications in fluvial studies. *Progress in Physical Geography*, 35(6), 782-809.

- Hooke, J.M., and Mant, J.M., 2000. Geomorphological impacts of a flood event on ephemeral channels in SE Spain. *Geomorphology*, 34, 163-180.
- Howard, A.J., Macklin, M.G., Black, S., and Hudson-Edwards, K.A., 2000. Holocene river development and environmental change in Upper Wharfedale, Yorkshire Dales, England. *Journal of Quaternary Science*, 15(3), 239-252.
- Howe, G.M., Slaymaker, H.O., and Harding, D.M., 1967. Some Aspects on the Flood Hydrology of the Upper Catchments of the Severn and Wye. *Transactions of the Institute of British Geographers*, 41, 33-58.
- Huang, G.H., and Wang, C.K., 2009. Semivariogram analysis of gravel bed roughness with ground-based lidar data. Asian Conference on Remote Sensing 2009, Beijing, China.
- Huang, G.H., Wang, C.K., Wu, F.C., and Atkinson, P.M., 2016. Anisotropy Characteristics of Exposed Gravel Beds Revealed in High-Point-Density Airborne Laser Scanning Data. *IEEE Geoscience and Remote Sensing Letters*, 13(8), 1044-1048.
- Ibisate, A., Ollero, A., and Díaz, E., 2011. Influence of catchment processes on fluvial morphology and river habitats. *Limnetica*, 30(2), 169-182.
- Iseya, F., and Ikeda, H., H., 1987. Pulsations in Bedload Transport Rates Induced by a Longitudinal Sediment Sorting: A Flume Study Using Sand and Gravel Mixtures. *Geografiska Annaler. Series A, Physical Geography*, 69(1), 15-27.
- Johnson, J.P.L., 2016. Gravel threshold of motion: a state function of sediment transport disequilibrium? *Earth Surface Dynamics*, 4, 685-703.
- Johnson, J.P. and Whipple, K.X., 2007. Feedbacks between erosion and sediment transport in experimental bedrock channels. *Earth Surface Processes and Landforms*, 32, 1048-1062.
- Johnson, M.F., Wilby, R.L., and Toone, J.A., 2014. Inferring air-water temperature relationships from rivers and catchment properties. *Hydrological Processes*, 28(6), 2912-2928.
- Johnston, C.E., Andrews, E.D., and Pitlick, J., 1998. *In situ* determination of particle friction angles of fluvial gravels. *Water Resources Research*, 34(8), 2017-2030.
- Journel, A.J., and Huijbregts C.J., 1978. *Mining geostatistics*. Academic Press: New York, 600 pp.
- Kellerhals, R., and Bray, D.I., 1971. Sampling procedures for coarse fluvial sediments. *Journal of Hydraulics Division, ASCE*, 97(8), 1165-1180.
- Keulegan, G.H., 1938. Laws of turbulent flow in open channels. *Journal of Research of the National Bureau of Standards*, 21, Research Paper, RP1151, 707-741.
- Kirchner, J. W., Dietrich, W.E., Iseya, F., and Ikeda, H., 1990. The variability of critical shear stress, friction angle, and grain protrusion in water-worked sediments. *Sedimentology*, 37(4), 647-672.

- Klingemann, P.C., and Emmett, W.W., 1982. Gravel bedload transport processes. In: Hey, R.D., Bathurst, J.C., and Thorne, C.R., (Eds.), *Gravel-bed Rivers*. Wiley: Chichester; 141–169.
- Klinkenberg, B., 1994. A review of methods used to determine the fractal dimensions of linear features. *Mathematical Geology*, 26, 23-46.
- Knighton, A.D., 1982. Longitudinal changes in the size and shape of stream bed material: Evidence of variable transport conditions. *Catena*, 9(1-2), 25-34.
- Komar, P. D., and Li, Z., 1986. Pivoting analyses of the selective entrainment of sediments by size and shape with application to gravel threshold. *Sedimentology*, 33, 425-436.
- Kondolf, G.M., Piégay, H., and Landon, N., 2002. Channel response to increased and decreased bedload supply from land use change: contrasts between two catchments. *Geomorphology*, 45, 35-51.
- Kozłowski, B., and Ergenzinger, P., 1999. Ring structures – a specific new cluster type in steep mountain torrents. *XXVII IAHR Congress Proceedings, Graz*, 410.
- Krumbein, W.C., 1941. The effects of abrasion on the size, shape, and roundness of rock fragments. *Journal of Geology*, 49, 482-520.
- Kuhnle, R.A., 1992. Bed-load transport during rising and falling stages on 2 small streams. *Earth Surface Processes and Landforms*, 17(2), 191-197.
- Lamarre, H., and Roy, A.G., 2008. A field experiment on the development of sedimentary structures in a gravel-bed river. *Earth Surface Processes and Landforms*, 33, 1064-1081.
- Lane, S.N., and Milledge, D.G., 2012. Impacts of upland open drains upon runoff generation: a numerical assessment of catchment-scale impacts. *Hydrological Processes*, 27(12), 1701-1726.
- Lane, S.N., Tayefi, V., Reid, S.C., Yu, D., and Hard, R.J., 2007. Interactions between sediment delivery, channel change, climate change and flood risk in a temperate upland environment. *Earth Surface Processes and Landforms*, 32, 429-446.
- Lane, S.N., Reid, S.C., Tayefi, V., Yu, D., and Hardy, R.J., 2008. Reconceptualising coarse sediment delivery problems in rivers as catchment-scale and diffuse. *Geomorphology*, 98, 227-249.
- Laronne, J.B., and Carson, M.A., 1976. Interrelationship between bed morphology and bed-material transport for a small, gravel-bed channel. *Sedimentology*, 23, 67-85.
- Laronne, J.B., and Reid, I., 1993. Very high rates of bedload sediment transport by ephemeral desert rivers. *Nature*, 366(6451), 148-150.
- Laronne, J.B., Reid, I., Yitshak, Y., and Frostick, L.E., 1994. The non-layering of gravel streambeds under ephemeral flood regimes. *Journal of Hydrology*, 159(1-4), 353-363.

- Lee, A.J., 1998. The hydraulics of steep streams. PhD thesis, Sheffield University.
- Leica Geosystems, 2006. Leica HDS 3000 Datasheet, [Online]. Available at: <[http://hds.leica-geosystems.com/hds/en/Leica\\_HDS3000.pdf](http://hds.leica-geosystems.com/hds/en/Leica_HDS3000.pdf)> [Accessed March 11, 2011].
- Leica Geosystems, 2007. Leica ScanStation 2 Datasheet, [Online]. Available at: <[http://hds.leica-geosystems.com/downloads123/hds/hds/ScanStation/brochures-datasheet/Leica\\_ScanStation%202\\_datasheet\\_en.pdf](http://hds.leica-geosystems.com/downloads123/hds/hds/ScanStation/brochures-datasheet/Leica_ScanStation%202_datasheet_en.pdf)> [Accessed July 30, 2012].
- Leica Geosystems, 2013. Leica ScanStation P20 Datasheet, [Online]. Available at: <[http://w3.leica-geosystems.com/downloads123/hds/hds/scanstation\\_p20/brochures-datasheet/leica\\_scanstation\\_p20\\_dat\\_en.pdf](http://w3.leica-geosystems.com/downloads123/hds/hds/scanstation_p20/brochures-datasheet/leica_scanstation_p20_dat_en.pdf)> [Accessed April 3, 2014].
- Leopold, L.B., Wolman, M.G., and Miller, J.P., 1964. *Fluvial Processes in Geomorphology*, W.H. Freeman: New York, 522 pp.
- Lewin, J., and Brindle, B., 1977. Confined meanders. In: Gregory, K.J. (Ed.), *River Channel Changes*, Wiley: Chichester, 221-233.
- Li, Z., 1985. Pivoting angles of gravels and its application in sediment threshold studies. MSc thesis, Oregon State University, Corvallis, 90 pp.
- Li, Z., and Komar, P.D., 1986. Laboratory measurements of pivoting angles for applications to selective entrainment of gravel in a current. *Sedimentology*, 33, 413-423.
- Lichti, D.D, Gordon, S.J., Tipdecho, T., 2005. Error models and propagation in directly georeferenced terrestrial laser scanner networks. *Journal of Surveying Engineering*, ASCE, 131(4), 135-142.
- Lindsay, J.B., and Evans, M.G., 2008. The influence of elevation error on the morphometrics of channel networks extracted from DEMs and the implications for hydrological modelling. *Hydrological Processes*, 22, 1588-1603.
- Maddock, I.P., Bickerton, M.A., Spence, R., and Pickering, T., 2001. Reallocation of compensation releases to restore river flows and improve instream habitat availability in the Upper Derwent catchment, Derbyshire, UK. *Regulated Rivers: Research & Management*, 17, 417-441.
- Mao, L., 2012. The effect of hydrographs on bed load transport and bed sediment spatial arrangement. *Journal of Geophysical Research*, 117, F03024.
- Mao, L., Uyttendaele, G.P., Iroumé, A., and Lenzi, M.A., 2008. Field based analysis of sediment entrainment in two high gradient streams located in Alpine and Andine environments. *Geomorphology*, 93, 368-383.
- Mao, L., Cooper, J.R. and Frostick, L.E., 2011. Grain size and topographical differences between static and mobile armour layers. *Earth Surface Processes and Landforms*, 36(10), 1321-1334.

- Marion, A., Tait, S.J., and McEwan, I.K., 2003. Analysis of small-scale gravel bed topography during armouring. *Water Resources Research*, 39(12), 1334.
- Martini, I.P., 1977. Gravelly flood deposits of Irvine Creek, Ontario, Canada. *Sedimentology*, 24, 603-622.
- Masteller, C.C., and Finnegan, N.J., 2017. Interplay between grain protrusion and sediment entrainment in an experimental flume. *Journal of Geophysical Research: Earth Surface*, 122, 274-289.
- McDonald, B.C., and Banerjee, I., 1971. Sediments and bedforms on a braided outwash plain. *Canadian Journal of Earth Sciences*, 8, 1282-1301.
- Measures, R., and Tait, S., 2008. Quantifying the role of bed surface topography in controlling sediment stability in water-worked gravel deposits. *Water Resources Research*, 44, W04413.
- Merrett, S.P., and Macklin, M.G., 1999. Historic river response to extreme flooding in the Yorkshire Dales, Northern England. In: Brown, A.G., and Quine, T.A. (Eds.), *Fluvial Processes and Environmental Change*, Wiley: Chichester, 345-360.
- Milan, D.J., Heritage, G.L., and Hetherington, D., 2007. Application of a 3D laser scanner in the assessment of erosion and deposition volumes and channel change in a proglacial river. *Earth Surface Processes and Landforms*, 32, 1657-1674.
- Milhous, R.T., 1973. Sediment transport in a gravel-bottomed stream. PhD thesis, Oregon State University.
- Millane, R.P., Weir, M.I., and Smart, G.M., 2006. Automated analysis of imbrication and flow direction in alluvial sediments using laser-scan data. *Journal of Sedimentary Research*, 76(8), 1049-1055.
- Miller, R. L. and Byrne, R.J., 1966. The angle of repose for a single grain on a fixed rough bed. *Sedimentology*, 6, 303-314.
- Miller, M.C., McCave, I.N., and Komar, P.D., 1977. Threshold of sediment motion under unidirectional currents. *Sedimentology*, 24, 507-527.
- Mohajeri, S.H., Grizzi, S., Righetti, M., Romano, G.P., and Nikora, V., 2015. The structure of gravel-bed flow with intermediate submergence: A laboratory study. *Water Resources Research*, 51(11), 9232-9255.
- Monteith, H., and Pender, G., 2005. Flume investigations into the influence of shear stress history on a graded sediment bed. *Water Resources Research*, 41(12), W12401.
- Montgomery, D.R., and Buffington, J.M., 1997. Channel-reach morphology in mountain drainage basins. *GSA Bulletin*, 109(5), 596-611.
- Moody, L.F., 1944. Friction Factors for Pipe Flow. *Transaction of the American Society of Civil Engineers*, 66, 671-678.

- Naden, P.M., and Brayshaw, A.C., 1987. Small and medium scale bedforms in gravel-bed rivers. In: Richards, K.S. (ed.), *River Channels: Environment and Process*. Basil Blackwell: Oxford, 249-271.
- Nanson, G.C., and Huang, H.Q., 2008. Least action principle, equilibrium states, iterative adjustment and the stability of alluvial channels. *Earth Surface Processes and Landforms*, 33, 923-942.
- National River Flow Archive, 2012a. 28001 – *Derwent at Yorkshire Bridge*, [online]. Available at: < <http://nrfa.ceh.ac.uk/data/station/info/28001> >
- National River Flow Archive, 2012b. 55032 – *Elan at Caban Dam*, [online]. Available at: < <http://nrfa.ceh.ac.uk/data/station/info/55032> >
- National River Flow Archive, 2012c. 28031 – *Manifold at Ilam*, [online]. Available at: < <http://nrfa.ceh.ac.uk/data/station/info/28031> >
- National River Flow Archive, 2012d. 27043 – *Wharfe at Addingham*, [online]. Available at: < <http://nrfa.ceh.ac.uk/data/station/info/27043> >
- Nikora, V., and Walsh, J., 2004. Water-worked gravel surfaces: high-order structure functions at the particle scale. *Water Resources Research*, 40, W12601.
- Nikora, V., Goring, D., and Biggs, B., 1998. On gravel-bed roughness characterization. *Water Resources Research*, 34(3), 517-527.
- Nikuradse, J., 1933. Strömungsgesetze in rauhen Röhren. *Forschungs-Arbeit des Ingenieurwesens*, Forschungsheft 361. VDI Verlag: Berlin (in German). (English translation: Law of flow in rough pipes, NACA TM 1292, 1950).
- Nitsche, M., Rickenmann, D., Kirchner, J.W., Turowski, J.M., and Badoux, A., 2012. Macroroughness and variations in reach-averaged flow resistance in steep mountain streams. *Water Resources Research*, 48, W12518.
- Ockelford, A., and Haynes, H., 2013. The impact of stress history on bed structure. *Earth Surface Processes and Landforms*, 38, 717-727.
- Ockelford, A., Haynes, H., Haynes, R., and Hodge, R., 2010. Using high resolution laser scanning to indicate mechanisms of stabilisation under varying sub threshold flow exposures. In: Proceedings of the 17<sup>th</sup> Congress of Asia and Pacific Division of International Association of Hydraulic Engineering and Research (IAHR-APD 2010), Auckland, New Zealand.
- Oldmeadow, D.F., and Church, M., 2006. A field experiment on streambed stabilization by gravel structures. *Geomorphology*, 78, 335-350.
- Pandžić, J., Erić, V., Božić, B., and Pejić, M., 2014. The Accuracy Analysis of Leica ScanStation P20 Data by Means of Point Cloud Fitting Algorithm. INGENEO 6<sup>th</sup> International Conference on Engineering Surveying, Prague, Czech Republic, April.

- Paola, C., 1988. Subsidence and Gravel Transport in Alluvial Basins. In: Kleinspehn, K.L., and Paola, C. (Eds.), *New Perspective in Basin Analysis*, Springer-Verlag: New York, 231-243.
- Papanicolaou, A.N., Strom, K., Schuyler, A., and Talebbeydokhti, N., 2003. The role of sediment specific gravity and availability on cluster evolution. *Earth Surface Processes and Landforms*, 28(1), 69-86.
- Paphitis, D., and Collins, M.B., 2005. Sand grain threshold, in relation to bed 'stress history': an experimental study. *Sedimentology*, 52(4), 827-838.
- Parker, G., 2007. Transport of gravel and sediment mixtures. *Sedimentation Engineering, ASCE Manual 54*, Chapter 4. In press. Available at: [http://hydrolab.illinois.edu/people/parkerg/\\_private/Man54/Man54Chap3WholeText.pdf](http://hydrolab.illinois.edu/people/parkerg/_private/Man54/Man54Chap3WholeText.pdf)
- Parker, G., and Klingeman, P.C., 1982. On why gravel bed streams are paved. *Water Resources Research*, 18, 1409-1423.
- Parker, G., and Sutherland, A.J., 1990. Fluvial armour. *Journal of Hydraulic Research*, 28(5), 529-544.
- Parker, G., Klingeman, P.C., and McLean, D.G., 1982. Bedload and size distribution in paved gravel-bed streams. *Journal of the Hydraulics Division, ASCE*, 108(4), 544-571.
- Parker, G., Wilcock, P.R., Paola, C., Dietrich, W.E., and Pitlick, J., 2007. Physical basis for quasi-universal relations describing bankfull hydraulic geometry of single-thread gravel bed rivers. *Journal of Geophysical Research*, 112, F04005.
- Pawson, R.R., Evans, M.G., and Allott, T.E.H.A., 2012. Fluvial carbon flux from headwater peatland streams: significance of particulate carbon flux. *Earth Surface Processes and Landforms*, 37, 1203-1212.
- Pearson, E., Smith, M.W., Klaar, M.J., and Brown, L.E., 2017. Can high resolution 3D topographic surveys provide reliable grain size estimates in gravel bed rivers? *Geomorphology*, 293(A), 143-155.
- Pender, G., Hoey, T.B., Fuller, C., and McEwan, I., 2001. Selective bedload transport during the degradation of a well sorted grade sediment bed. *Journal of Hydraulic Research*, 39(3), 1-9.
- Petit, F., 1994. Dimensionless critical shear stress evaluations from flume experiments using different gravel beds. *Earth Surface Processes and Landforms*, 19, 565-576.
- Petts, G.E., and Gurnell, A.M., 2005. Dams and geomorphology: Research progress and future directions. *Geomorphology*, 71, 27-47.
- Piedra, M.M., Haynes, H., and Hoey, T.B., 2011. The spatial distribution of coarse surface grains and the stability of gravel river beds. *Sedimentology*, 59(3), 1014-1029.

- Polak, S., 1988. Maximal peak discharges following the rainstorm of the 17 – 18/10/197. Jerusalem, Israel: Israel Hydrological Service Report HYD/2/1988, 23 pp. [Hebrew].
- Powell, D.M., 1998. Patterns and processes of sediment sorting in gravel-bed rivers. *Progress in Physical Geography*, 22, 1-32.
- Powell, D.M., 2014. Flow resistance in gravel-bed rivers: Progress in research. *Earth-Science Reviews*, 136, 301-338.
- Powell, D.M., and Ashworth, P.J., 1995. Spatial pattern of flow competence and bed load transport in a divided gravel bed river. *Water Resources Research*, 31(3), 741-752.
- Powell, D.M., Reid, I., and Laronne, J.B., 2001. Evolution of bed load grain size distribution with increasing flow strength and the effect of flow duration on the calibre of bed load sediment yield in ephemeral gravel bed rivers. *Water Resources Research*, 37, 1463-1474.
- Powell, D.M., Brazier, R., Wainwright, J., Parsons, A., and Nichols, M., 2006. Spatial patterns of scour and fill in dryland sand bed streams. *Water Resources Research*, 42(8), W08412.
- Powell, D.M., Ockelford, A., Rice, S.P., Hillier, J.K., Nguyen, T., Reid, I., Tate, N.J., and Ackerley, D., 2016. Structural properties of mobile armours formed at different flow strengths in gravel-bed rivers. *Journal of Geophysical Research: Earth Surface*, 121, 1494-1515.
- Prancevic, J.P., and Lamb, M.P., 2015. Unraveling bed slope from relative roughness in initial sediment motion. *Journal of Geophysical Research: Earth Surface*, 120, 474-489.
- Prestegard, K.L., 1983. Bar resistance in gravel bed streams at bankfull stage. *Water Resources Research*, 19, 472-476.
- Proffitt, G. T., and Sutherland, A.J., 1983. Transport of non-uniform sediments. *Journal of Hydraulical Research*, 21, 33-43.
- Qin, J., and Ng, S.L., 2011. Multifractal characterization of water-worked gravel surfaces. *Journal of Hydraulic Research*, 49(3), 345-351.
- Qin, J., Zhong, D., Wang, G., and Ng, S.L., 2012. On characterization of the imbrication of armoured gravel surfaces. *Geomorphology*, 159-160, 116-124.
- Qin, J., Zhong, D., Wang, G., and Ng, S.L., 2013. Influence of particle shape on surface roughness: Dissimilar morphological structures formed by man-made and natural gravels. *Geomorphology*, 190, 16-26.
- Raven, E., Lane, S.L., Ferguson, R.I., and Bracken, L.J., 2009. The spatial and temporal patterns of aggradation in a temperate, upland, gravel-bed river. *Earth Surface Processes and Landforms*, 34, 1181-1197.
- Raz, E., 1986. The Geological Map of Israel (1:50,000), 'En-Gedi Sheet, 16-I. The Geological Survey of Israel, Geological and Structural maps.

- Recking, A., 2009. Theoretical development on the effects of changing flow hydraulics on incipient bed load motion. *Water Resources Research*, 45, W04401.
- Recking, A., 2012. Influence of sediment supply on mountain stream bedload transport. *Geomorphology*, 175, 139-150.
- Reid, I., and Frostick, F.E., 1984. Particle interaction and its effect on the threshold of initial and final bedload motion in coarse alluvial channels. In: Koster, E.H., and Steel, R.J. (Eds.), *Sedimentology of Gravels and Conglomerates*. Canadian Society of Petroleum Geologists: Calgary, 61-68.
- Reid, I., and Hassan, M.A., 1992. The influence of microform bed roughness elements on flow and sediment transport in gravel bed rivers: A reply. *Earth Surface Processes and Landforms*, 17, 535-538.
- Reid, I., and Laronne, J.B., 1995. Bed-load sediment transport in an ephemeral stream and a comparison with seasonal and perennial counterparts. *Water Resources Research*, 31(3), 773-781.
- Reid, I., Frostick, L.E., and Layman, J.T., 1985. The incidence and nature of bedload transport during flood flows in coarse-grain alluvial channels. *Earth Surface Processes and Landforms*, 10, 33-44.
- Reid, I., Frostick, L.E., and Brayshaw, A.C., 1992. Microform roughness elements and the selective entrainment and entrapment of particles in gravel-bed rivers. In: Billi, P., Hey, R.D., Thorne, C.R., and Tacconi, P. (Eds.), *Dynamics of Gravel-bed Rivers*, Wiley: Chichester, 253-276.
- Reid, I., Laronne, J.B., and Powell, D.M., 1995. The Nahal Yatir bedload database: sediment dynamics in a gravel-bed ephemeral stream. *Earth Surface Processes and Landforms*, 20, 845-857.
- Reid, I., Laronne, J.B., and Powell, D.M., 1998. Flash-flood and bedload dynamics of desert gravel-bed streams. *Hydrological Processes*, 12(4), 543-557.
- Reid, S., 2002. Sediment delivery, river dynamics and ecological impacts in upland floodplains. PhD thesis, University of Leeds.
- Reid, S.C., Lane, S.N., Berney, J.M., and Holden, J., 2007. The timing and magnitude of coarse sediment transport events within an upland, temperate gravel-bed river. *Geomorphology*, 83, 152-182.
- Renwick, W.H., 1992. Equilibrium, disequilibrium, and nonequilibrium landforms in the landscape. *Geomorphology*, 5, 265-276.
- Reschetyuk, T., 2006. Investigation on the influence of surface reflectance on the measurements of the terrestrial laser scanner Leica HDS 3000, *Zeitschrift für Geodäsie, Geoinformation und Landmanagement*, 131(2), 96-103.

- Rice, S., and Church, M., 1996. Sampling surficial fluvial gravels: the precision of size distribution percentile estimates. *Journal of Sedimentary Research*, 66(3), 654-665.
- Rice, S., and Church, M., 1998. Grain size along two gravel-bed rivers: Statistical variation, spatial pattern and sedimentary links. *Earth Surface Processes and Landforms*, 23, 345-363.
- Rice, S.P., and Toone, J.A., 2011. Fluvial audit of the Upper Dove Catchment, Loughborough University.
- Richards, K.S., 1982. *Rivers: Form and Process in Alluvial Channels*. Methuen: London.
- Richards, K.S., 1990. Fluvial geomorphology: the initial entrainment of gravel bed material. *Progress in Physical Geography*, 14, 395-415.
- Robert, A., 1988. Statistical properties of sediment bed profiles in alluvial channels. *Mathematical Geology*, 20(3), 205-223.
- Robert, A., 1991. Fractal properties of simulated bed profiles in alluvial channels. *Mathematical Geology*, 23, 367-382.
- Rosgen, D.L., 1994. A classification of natural rivers. *Catena*, 22, 169-199.
- Rothwell, J.J., Evans, M.G., and Allott, T.E.H., 2006. Sediment-water interactions in an eroded and heavy metal contaminated peatland catchment, Southern Pennines, UK. *Water, Air, and Soil Pollution: Focus*, 6, 669-676.
- Rouse, H., 1965. Critical analysis of open-channel flow resistance. *Journal of the Hydraulics Division ASCE*, 91, 1-25.
- Rychkov, I., Brasington, J., and Vericat, D., 2012. Computational and methodological aspects of terrestrial surface analysis based on point clouds. *Computers and Geosciences*, 42, 64-70.
- Sambrook Smith, G.H., and Nicholas, A.P., 2005. Effect on flow structure of sand deposition on a gravel bed: Results from a two-dimensional flume experiment. *Water Resources Research*, 41, W10405.
- Sanguinito, S., and Johnson, J., 2012. Quantifying gravel overlap and dislodgement forces on natural river bars: implications for particle entrainment. *Earth Surface Processes and Landforms*, 37, 134-141.
- Schneider, J.M., Rickenmann, D., Turowski, J.M., Bunte, K., and Kirchner, J.W., 2015. Applicability of bed load transport models for mixed-size sediments in steep streams considering macro-roughness. *Water Resources Research*, 51, 5260-5283.
- Schumm, S.A., 1981. Evolution and response of the fluvial system, sedimentologic implications. In: Ethridge, F.G., and Flores, R.M. (Eds), *Recent and ancient nonmarine depositional environments*. Society of Economic Palaeontologists and Mineralogists Special Publication, 31, 19-29.

- Schumm, S.A., and Lichty, R.W., 1965. Time, Space and Causality in Geomorphology. *American Journal of Science*, 263, 110-119.
- Schumm, S.A., and Stevens, M.A., 1973. Abrasion in Place: A Mechanism for Rounding and Size Reduction of Coarse Sediments in Rivers. *Geology*, 1(1), p.37-40.
- Scullion, J., and Sinton, A., 1983. Effects of artificial feshets on substratum composition, benthic invertebrate fauna and invertebrate drift in two impounded rivers in mid-Wales. *Hydrobiologia*, 107, 261-269.
- Sear, D.A., 1992. Sediment transport processes in riffle-pool sequences in a river experiencing hydropower regulation. In: Hey, R.D., Billi, P., Thorne, C.R., and Tacconi, P. (Eds.), *Dynamics of Gravel-bed Rivers*, Wiley: Chichester, 629-650.
- Sear, D.A., 1995. Morphological and sedimentological changes in a gravel-bed river following 12 years of flow regulation of hydropower. *River Research and Applications*, 10(2-4), 247-264.
- Sear, D.A., 1996. Sediment transport processes in pool-riffle sequences. *Earth Surface Processes and Landforms*, 21, 241-262.
- Shamir, E., Ben-Moshe, L., Ronen, A., Grodek, T., Enzel, Y., Georgakakos, K.P., and Morin, E., 2013. Geomorphology-based index for detecting minimal flood stages in arid alluvial streams. *Hydrology and Earth System Sciences*, 17, 1021-1034.
- Shentsis, I., Meirovich, L., Ben-Zvi, A., and Rosenthal, E., 1999. Assessment of transmission losses and groundwater recharge from runoff events in a wadi under shortage of data on lateral inflow, Negev, Israel. *Hydrological Processes*, 13, 1649-1663.
- Shields, A., 1936. Application of the theory of similarity and turbulence research to the bed load movements, Mitt. Preuss. *Versuch-sanst. Wasserbau Schiffbau*, 26, 5-24.
- Smart, G., Aberle, J., Duncan, M. and Walsh, J., 2004. Measurement and analysis of alluvial bed roughness. *Journal of Hydraulic Research*, 42(3), 227-237.
- Smith, M., Vericat, D., and Gibbins, C., 2012. Through-water terrestrial laser scanning of gravel beds at the patch scale. *Earth Surface Processes and Landforms*, 37, 411-421.
- Sohag, M.A., 1993. Sediment tracing, bed structure and morphological approaches to sediment transport estimates in a gravel-bed river: the River South Tyne, Northumberland, UK. PhD Thesis, University of Newcastle upon Tyne.
- Soudarissanane, S., Lindenberg, R., Menenti, M., and Teunissen, P., 2011. Scanning geometry: Influencing factor on the quality of terrestrial laser scanning points. *ISPRS Journal of Photogrammetry and Remote Sensing*, 66, 389-399.
- Storz-Peretz, Y., and Laronne, J.B., 2013. Morphotextural characterization of dryland braided channels. *Geological Society of America Bulletin*, 125(9-10), 1599-1617.

- Storz-Peretz, Y., Laronne, J.B., Surian, N., and Lucía, A., 2016. Flow recession as a driver of the morpho-texture of braided streams. *Earth Surface Processes and Landforms*, 41, 754-770.
- Strahler, A., 1957. Quantitative Analysis of Watershed Geomorphology. *Transactions, American Geophysical Union*, 38, 913-920.
- Strom, K.B., and Papanicolaou, A.N., 2008. Morphological characterization of cluster microforms. *Sedimentology*, 55, 137-153.
- Strom, K., Papanicolaou, A.N., Evangelopoulous, N., and Odeh, M., 2004. Microforms in gravel-bed rivers: Formation, disintegration and effects on bedload transport. *Journal of Hydraulic Engineering*, 130, 554-567.
- Surian, N., and Rinaldi, M., 2003. Morphological response to river engineering and management in alluvial channels in Italy. *Geomorphology*, 50, 307-326.
- Tallis, J.H., 1973. Studies on Southern Pennine Peats: V. Direct Observations on Peat Erosion and Peat Hydrology at Featherbed Moss, Derbyshire. *Journal of Ecology*, 61(1), 1-22.
- Tallis, J.H., 1985. Mass Movement and Erosion of a Southern Pennine Blanket Peat. *Journal of Ecology*, 73(1), 283-315.
- The Met. Office, 1986. Monthly and annual totals of RAINFALL 1986 for the United Kingdom. The Meteorological Office: Bracknell. 112pp.
- Thorne, C.R., 1995. Chapter 8: Channel Types and Morphologic Classification. In: Thorne, C.R., Hey, R.D., and Newson, M.D. (Eds.), *Guidebook of Applied Fluvial Geomorphology for River Engineering and Management*, River Dynamics Group, UK, 8-1 – 8-55.
- Trimble, S.W., and Mendel, A.C., 1995. The cow as a geomorphic agent – A critical review. *Geomorphology*, 13, 233-253.
- Turowski, J.M., Badoux, A., and Rickenmann, D., 2011. Start and end of bedload transport in gravel-bed streams. *Geophysical Research Letters*, 38, L04401.
- van den Berg, J.H., 1995. Prediction of alluvial channel pattern of perennial rivers. *Geomorphology*, 12, 259-279.
- Vericat, D., Batalla, R.J., and Gibbins, C., 2006. Breakup and reestablishment of the armour layer in a large gravel-bed river below dams: the lower Ebro. *Geomorphology*, 76, 122-136.
- Walling, D.E., Owens, P.N., and Leeks, G.J.L., 1999. Rates of contemporary overbank sedimentation and sediment storage on the floodplains of the main channel systems of the Yorkshire Ouse and River Tweed, UK. *Hydrological Processes*, 13, 993-1009.
- Wang, C.K., Wu, F.C., Huang, G.H., and Lee, C.Y., 2011. Meso-scale terrestrial laser scanning of fluvial gravel surface. *IEEE Geoscience Remote Sensing Letters*, 8(6), 1075–1079.

- Ward, J.V., and Stanford, J.A., 1995. Ecological connectivity in alluvial river ecosystems and its disruption by flow regulation. *River Research and Applications*, 11(1), 105-119.
- Ward, J.V., Tockner, K., Uehlinger, U., and Malard, F., 2001. Understanding natural patterns and processes in river corridors as the basis for effective river restoration. *Regulated Rivers: Research and Management*, 17, 311-323.
- Wheaton, J.M., Brasington, J., Darby, S.E., and Sear, D.A., 2010. Accounting for uncertainty in DEMs from repeat topographic surveys: improved sediment budgets. *Earth Surface Processes and Landforms*, 35, 136-156.
- Whitaker, A.C., and Potts, D.F., 2007. Analysis of flow competence in an alluvial gravel bed stream, Dupuyer Creek, Montana. *Water Resources Research*, 43(7), W07433.
- Wiberg, P.L., and Smith, J.D., 1985. A Theoretical Model for Saltating Grains in Water. *Journal of Geophysical Research*, 90(C4), 7341-7354.
- Wiberg, P.L., and Smith, J.D., 1987. Calculations of critical shear stress for motion of uniform and heterogenous sediments. *Water Resources Research*, 23(8), 1471-1480.
- Wilcock, P.R., 1992. Experimental investigation of the effect of mixture properties on transport dynamics. In: Billi, P., Hey, R.D., Thorne, C.R., and Tacconi, P. (Eds.), *Dynamics of Gravel-bed Rivers*, John Wiley: New York, 109-139.
- Wilcock, P.R., 2001. The flow, the bed, and the transport: Interaction in the flume and field. In: Mosley, P. (ed), *Gravel-Bed Rivers V*, New Zealand Hydrological Society Inc.: Wellington, 183-219.
- Wilcock, P.R., and DeTemple, B.T., 2005. Persistence of armor layers in gravel-bed streams. *Geophysical Research Letters*, 32, L08402.
- Wilcock, P.R., and Southard, J.B., 1989. Bed-load transport of mixed-size sediment: fractional transport rates, bed forms and the development of a coarse bed-surface layer. *Water Resources Research*, 25, 1629-1641.
- Wilcock, P.R., Kenworthy, S.T., and Crowe, J.C., 2001. Experimental study of the transport of mixed sand and gravel. *Water Resources Research*, 37(12), 3349-3358.
- Wittenberg, L., 2002. Structural Patterns in Coarse Gravel River Beds: Typology, Survey and Assessment of the Roles of Grain Size and River Regime. *Geografiska Annaler*, 84A(1), 25-37.
- Wittenberg, L., and Newson, M.D., 2005. Particle clusters in gravel-bed rivers: an experimental morphological approach to bed material transport and stability concepts. *Earth Surface Processes and Landforms*, 30, 1351-1368.
- Wittenberg, L., Laronne, J.B., and Newson, M.D., 2007. Bed clusters in humid perennial and Mediterranean ephemeral gravel-bed streams: The effect of clast size and bed material sorting. *Journal of Hydrology*, 334, 312-318.

- Wolcott, J.F., 1989. Flume studies of coarse gravel bed surfaces response to flowing water. PhD thesis, University of British Columbia.
- Wolman, M.G., 1954. A method of sampling coarse river-bed material. *Transactions of the American Geophysical Union*, 35(6), 951-956.
- Wooldridge, C.L., and Hickin, E.J., 2002. Step-pool and cascade morphology, Mosquito Creek, British Columbia: a test of four analytical techniques. *Canadian Journal of Earth Sciences*, 39(4), 493-503.
- Wright, D.B., and Herrington, J.A., 2011. Problematic standard errors and confidence intervals for skewness and kurtosis. *Behavior Research Methods*, 43(1), 8-17.
- Yair, A., and Kossovsky, A., 2002. The relationship between annual rainfall and sediment yield in arid and semi-arid areas. The case of the northern Negev. *Catena supplement*, 10, 122-136.
- Yalin, M.S., 1977. *Mechanics of Sediment Transport*, Pergamon Press: Oxford, 298 pp.
- Yen, B.C., 2002. Open Channel Flow Resistance. *Journal of Hydraulic Engineering*, 128(1), 20-39.
- Zingg, T., 1935. Beitrag zur Schotteranalyse. *Schweizerische Mineralogische und Petrologische Mitteilungen*, 15, 39-140.

## Appendix A: Instrument Specifications

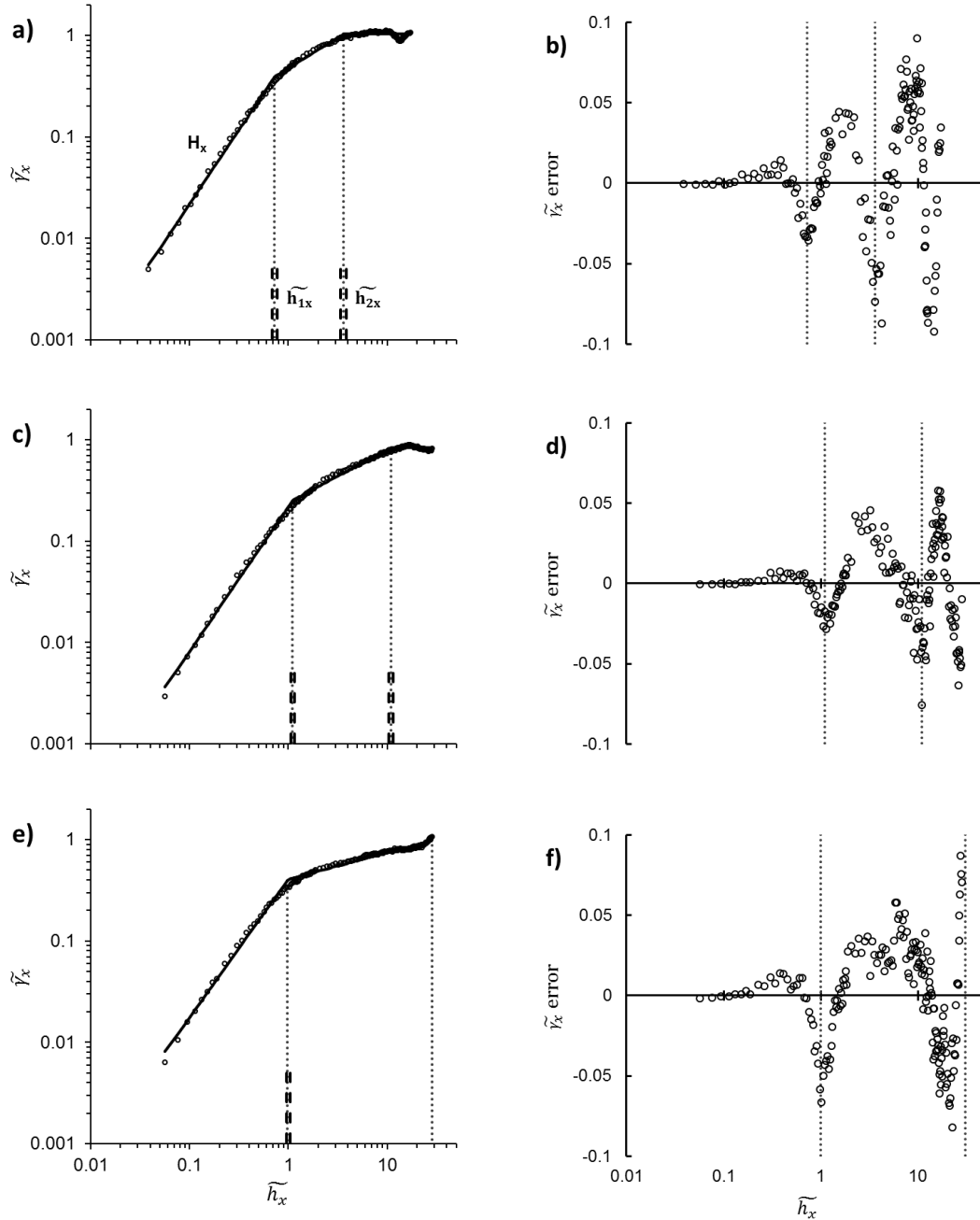
Table A.1 Specifications for the Leica HDS 3000, ScanStation 2 and ScanStation P20 TLS sensors

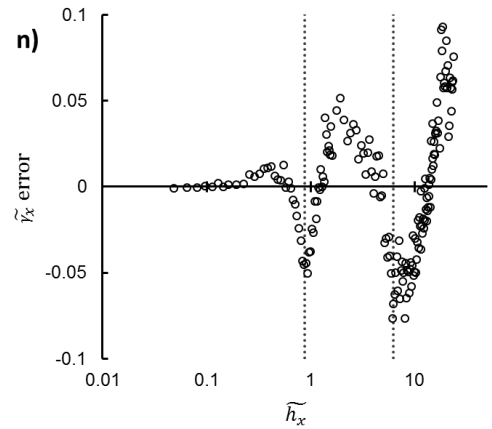
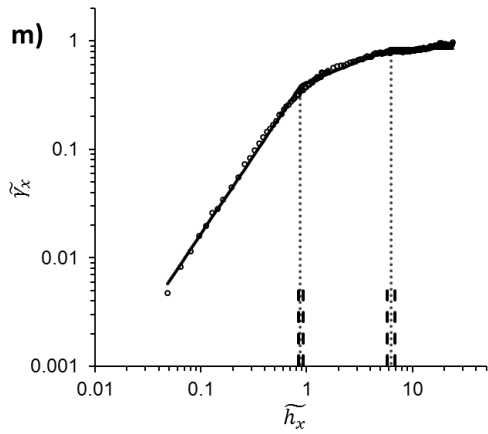
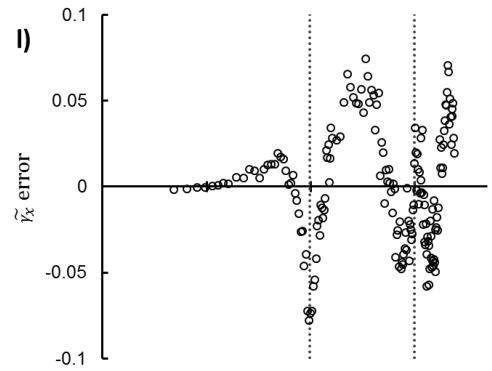
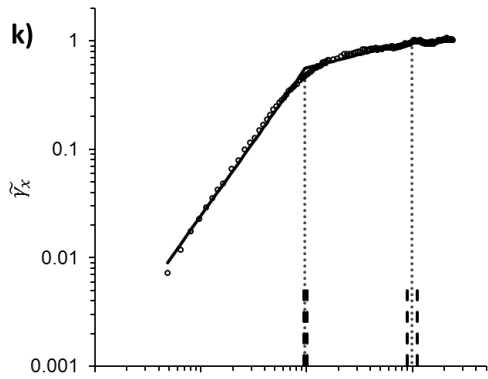
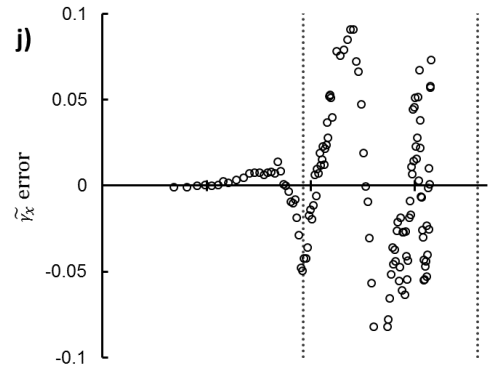
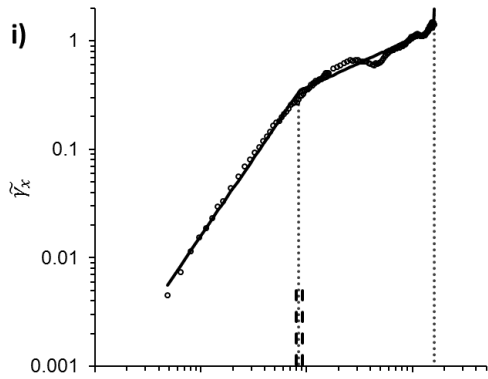
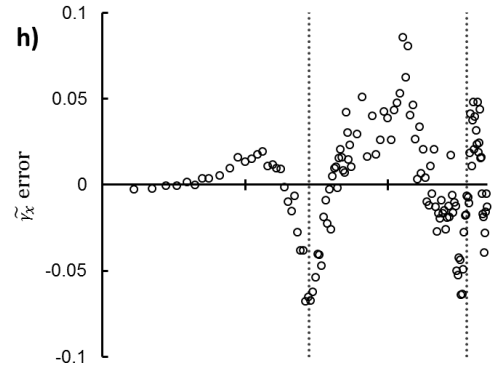
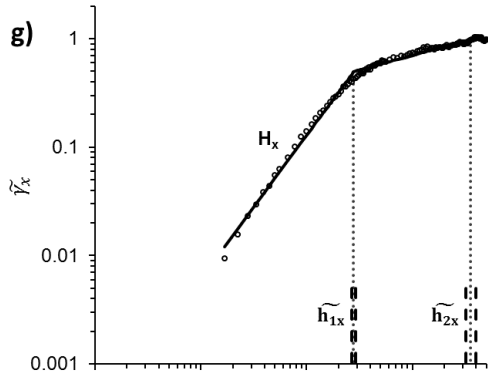
	<b>HDS 3000</b>	<b>ScanStation 2</b>	<b>ScanStation P20</b>
<b>Sensor Type</b>	Time-of-flight (ToF)		Waveform Digitising (WFD) enhanced ToF
<b>Wavelength</b>	532 nm		808nm
<b>Laser class</b>	3R		1
<b>Maximum scan rate</b>	4,000 points/sec	50,000 points/sec	1,000,000 points/sec
<b>Positional accuracy of single measurement *</b>	6 mm at 50 m		3 mm at 50 m; 6 mm at 100 m
<b>Range</b>	300 m		120 m
<b>Spot size</b>	0 – 50 m: 4 mm (FWHH – based); 6 mm (Gaussian – based)		≤2.8 mm **

\* one sigma

\*\* Beam diameter at front window (beam divergence = 0.2 mrad)

**Appendix B: Flow-parallel and flow-transverse 1D variogram model assessment for the remaining humid temperate and dryland gravel patches.**





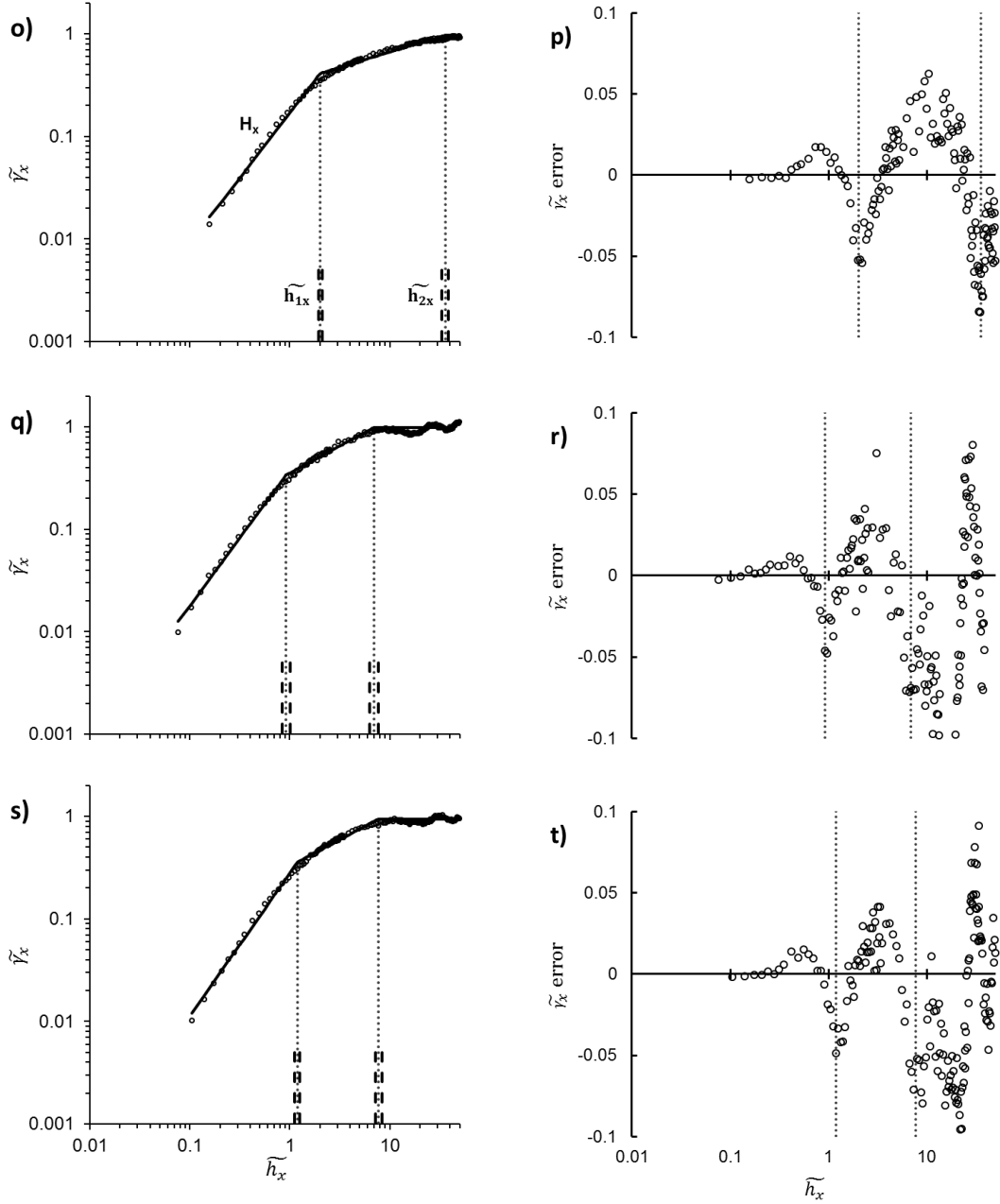
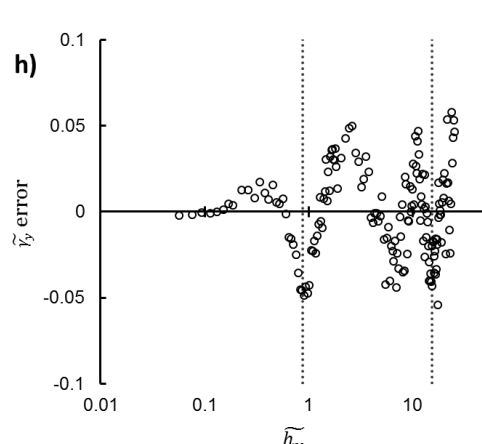
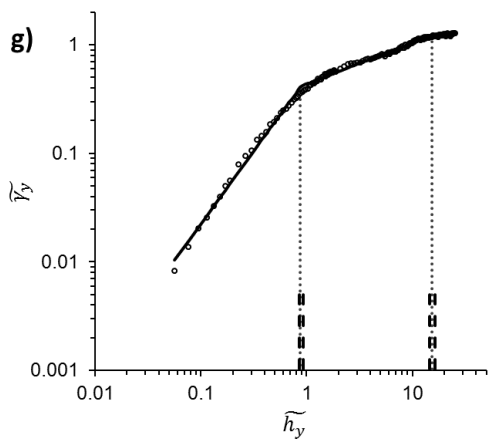
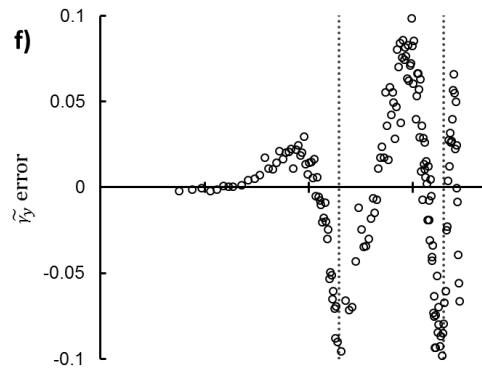
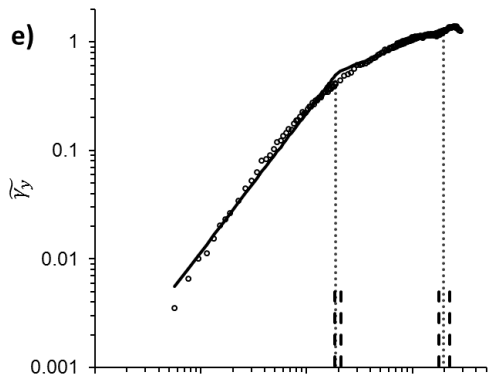
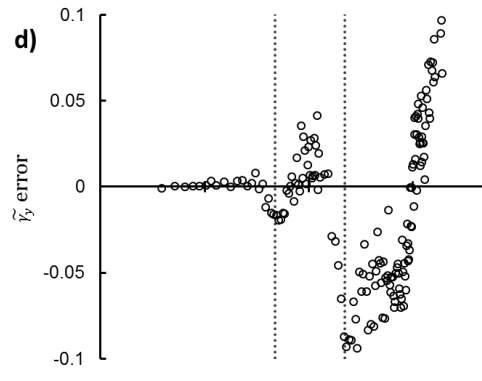
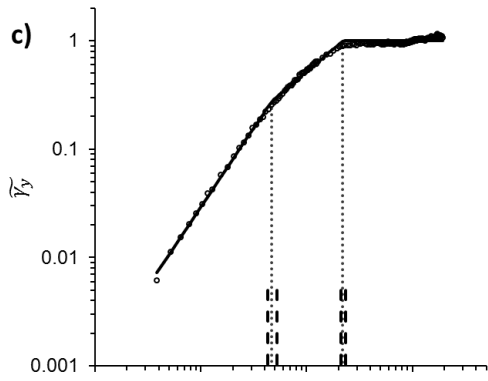
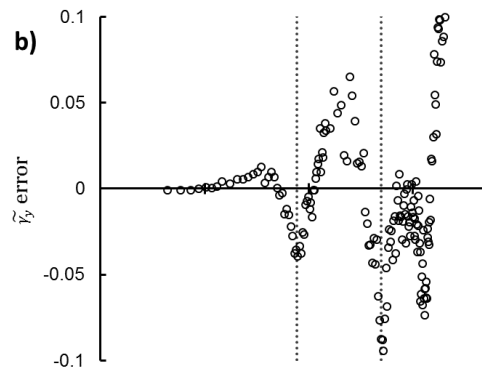
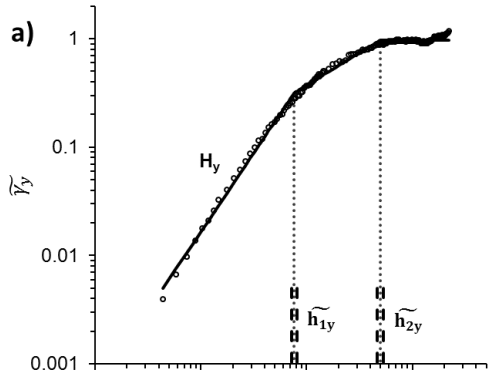
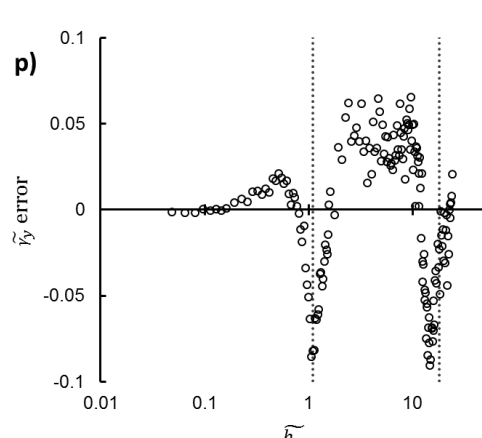
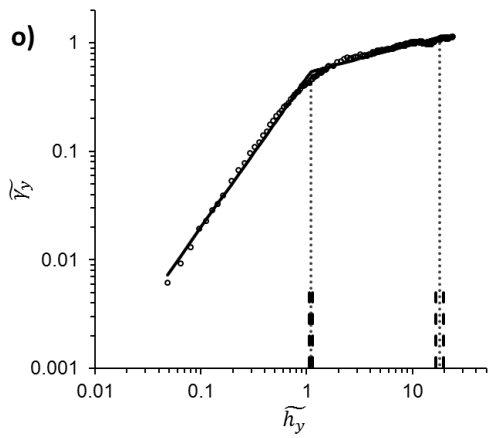
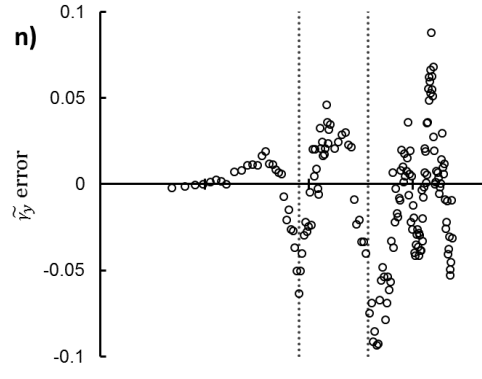
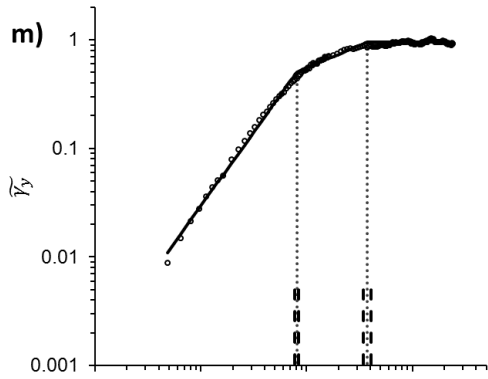
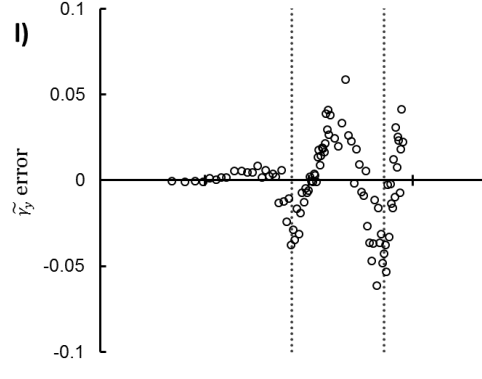
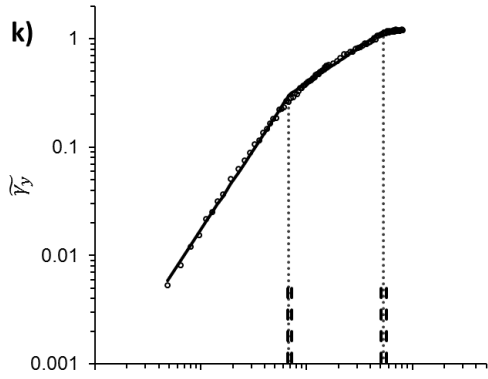
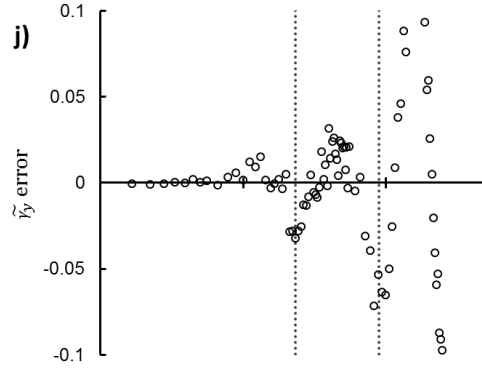
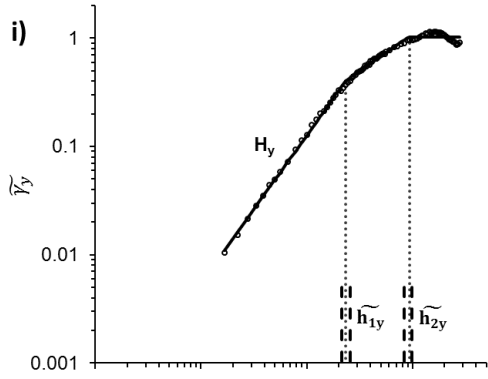


Figure B.1 Flow-parallel variograms and fitted spline models and residual between the observed and expected  $\tilde{\gamma}_x$  for the (a-b) A<sub>2</sub>, (c-d) E<sub>1.1</sub>, (e-f) E<sub>1.2</sub>, (g-h) M<sub>1</sub>, (i-j) M<sub>2</sub>, (k-l) W<sub>1.1</sub>, (m-n) W<sub>1.2</sub>, (o-p) H<sub>1</sub>, (q-r) H<sub>2</sub> and (s-t) S<sub>1</sub> gravel patches. In a), c), e), g), i), k), m), o), q) and s) the dotted lines refer to the length of the  $\tilde{h}_{1x}$  and  $\tilde{h}_{2x}$  scales of roughness and the dashed lines represent the 95% confidence intervals around  $\tilde{h}_{1x}$  and  $\tilde{h}_{2x}$ . Note log  $\tilde{h}_x$  and  $\tilde{\gamma}_x$  scales.





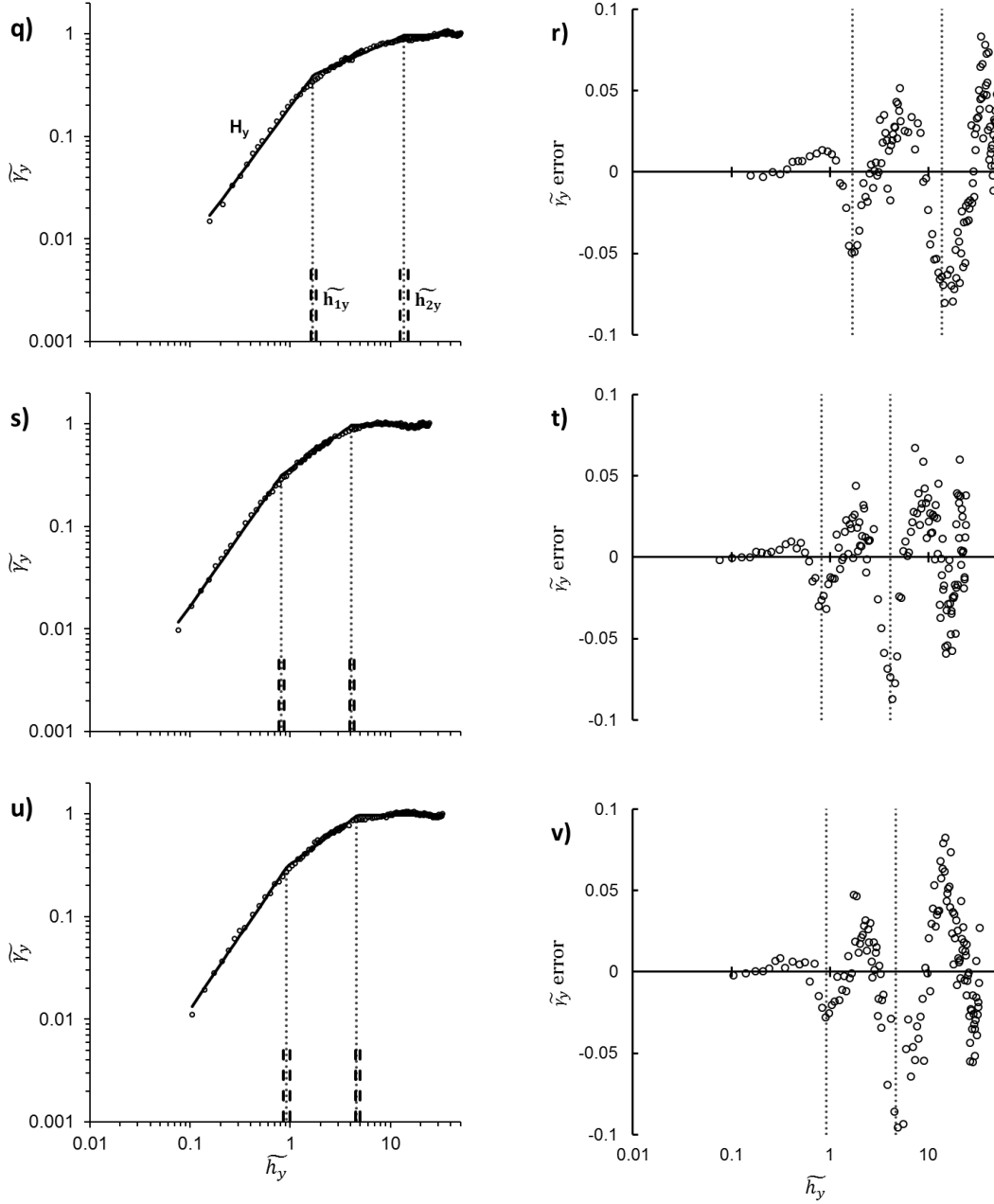


Figure B.2 Flow-transverse variograms and fitted spline models and residual between the observed and expected  $\tilde{\gamma}_x$  for the (a-b) A<sub>1</sub>, (c-d) A<sub>2</sub>, (e-f) E<sub>1.1</sub>, (g-h) E<sub>1.2</sub>, (i-j) M<sub>1</sub>, (k-l) M<sub>2</sub>, (m-n) W<sub>1.1</sub>, (o-p) W<sub>1.2</sub>, (q-r) H<sub>1</sub>, (s-t) H<sub>2</sub> and (u-v) S<sub>1</sub> gravel patches. In a), c), e), g), i), k), m), o), q), s) and u) the dotted lines refer to the length of the  $\tilde{h}_{1x}$  and  $\tilde{h}_{2x}$  scales of roughness and the dashed lines represent the 95% confidence intervals around  $\tilde{h}_{1x}$  and  $\tilde{h}_{2x}$ . Note log  $\tilde{h}_x$  and  $\tilde{\gamma}_x$  scales.

## Appendix C: Grain entrainment model preliminary analysis

The distributions of the residuals (Figure C.1) from least squares regression between dimensionless projection ( $p/D$ ) and dimensionless exposure ( $e/D$ ; Figure 4.15) for the two humid temperate and three dryland patches conform to a normal distribution (described by a mean and standard deviation:  $\mu_{\text{res}}$  and  $\sigma_{\text{res}}$ , respectively) as determined by a chi-square goodness of fit test ( $p > 0.05$ ).

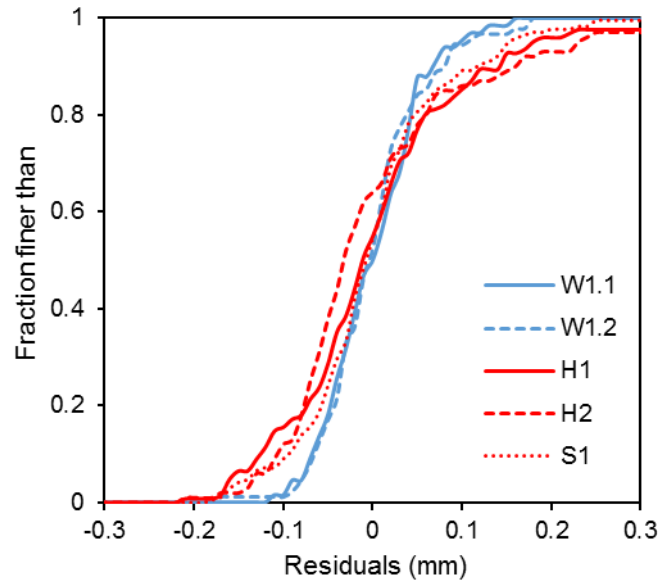


Figure C.1 Cumulative frequency distributions of (normally distributed) residuals from the relationship between dimensionless projection ( $p/D$ ) and dimensionless exposure ( $e/D$ ; Figure 4.15) for the  $W_{1.1}$  ( $\mu_{\text{res}} = 0$ ,  $\sigma_{\text{res}} = 0.06$ ),  $W_{1.2}$  ( $\mu_{\text{res}} = 0$ ,  $\sigma_{\text{res}} = 0.06$ ),  $H_1$  ( $\mu_{\text{res}} = 0$ ,  $\sigma_{\text{res}} = 0.10$ ),  $H_2$  ( $\mu_{\text{res}} = 0$ ,  $\sigma_{\text{res}} = 0.12$ ) and  $S_1$  patches ( $\mu_{\text{res}} = 0$ ,  $\sigma_{\text{res}} = 0.09$ ).